Chapter 1

Introduction

In this chapter the scene is set by giving a brief introduction to the two radio source populations to be studied in this thesis, star-forming galaxies and those powered by an active galactic nucleus (AGNs). A brief outline of the major goals of this thesis is also given.

1.1 Preamble

All galaxies in the universe are sources of radio emission at some level. The brightest radio sources are the result of compact active nuclei within galaxies and form a population which includes the most luminous and most distant objects in the universe. These objects are useful cosmological probes because in all radio source surveys they can be seen over a redshift range which spans more than 90% of the history of the universe. In current radio surveys, less than 1% of powerful radio sources fuelled by active nuclei are found in the *local*[1] universe and these are predominantly found in the brightest host galaxies. Another population of fainter radio sources is found almost exclusively in the local universe with the current generation of radio surveys: those are powered by recent star formation in normal galaxies. Star formation often occurs in dusty parts of galaxies which are opaque at optical wavelengths, meaning that radio and far-infrared emission from these galaxies yield a more robust estimate of the amount of star formation within them. An accurate census of radio sources in the local universe is important as a *benchmark* for understanding the cosmological evolution of galaxies harbouring a compact active nucleus and those which have undergone recent star formation.

This thesis presents such a census, by examining the statistical properties of a population of radio sources hosted by galaxies in the local universe. In this introduction the scene is set by giving a brief introduction to cosmology in Section 1.2. The nature of radio source populations is introduced in Section 1.3 and a brief introduction to the surveys used in constructing the dataset upon which this thesis is based is given in Section 1.4. Section 1.5 outlines the aims of this thesis.

1.2 Cosmology

Our current understanding of the universe is based on the standard 'hot big bang model'. Within the framework of this model the universe has expanded to its present day form from a singularity some 13 billion years ago and is homogeneous (meaning that matter is uniformly spread through space) and isotropic (meaning that the universe looks the same in any direction). This model, which is heavily reliant upon Einstein's laws of general relativity, has provided the framework which provides much of our current understanding of the evolution of the universe. This section will provide a brief introduction to those areas of the hot big bang model which are relevant to this thesis. Most of the equations mentioned here have been taken from Peacock (1999); the reader is referred to this book for more detail.

[1] Here and throughout this thesis the term 'local universe' is understood to mean the part of the universe contained within a volume centred on our own Galaxy in which the cosmological evolution of objects and structures is negligible. Specifically for the 6dFGS-NVSS sample presented in this thesis, this means the volume enclosed within a distance corresponding to a redshift of approximately 0.15.

1.2.1 A brief history of the universe

In the hot big bang model the universe has expanded and cooled to the present day from a hot dense gas of radiation and elementary particles. During this expansion the elementary particles condensed into atoms and matter and radiation decoupled after which the universe became transparent to radiation. This radiation has continued to cool to a temperature of about 3 K at the present day, it is known as the Cosmic Microwave Background Radiation (CMB). The CMB carries with it a snapshot of the physical conditions in the universe at the epoch at which matter and radiation decoupled. Measurements of temperature fluctuations made with instruments such as the Wilkinson Microwave Anisotropy Probe (WMAP; Bennett *et al.*, 2003) are a powerful tool for understanding the state of the universe 300 000 years after it came into existence. These measurements of the CMB have found it to be extremely uniform with temperature variations of $\Delta T/T \sim 10^{-5}$ on angular scales of $1' - 10^{\circ}$ which implies that the universe consisted of an almost featureless gas of particles in thermodynamic equilibrium at the epoch of decoupling.

The present day universe is anything but featureless. Hubble Space Telescope (HST) observations imply that the universe contains more than a hundred billion galaxies which formed some time after the decoupling of matter and radiation. These galaxies are clustered on hierarchical scales, from small groups less than 1 Mpc across, such as our own local group of galaxies, through clusters and rich clusters (on scales of 1-10 Mpc) which are in turn contained within superclusters of galaxies such as the nearby Shapley Supercluster. Superclusters are the largest known gravitationally bound objects known in the universe and exist on scales up to 100 Mpc and above. One of the central problems in cosmology is how these structures seen today formed from the uniform distribution of matter at the moment of decoupling when the universe was around 300 000 years old. Studies of the distribution and properties of galaxies in the *local* universe, such as the one presented in this thesis, are important as an accurate benchmark describing the present state of the universe and constraining models of the properties of galaxy evolution over the history of the universe.

1.2.2 Measuring the universe

The standard hot big bang model assumes a space-time metric known as the Robertson-Walker metric which defines the invariant space-time interval ds between two observers who are moving away from one another due to the expansion of the universe.

$$ds^2 = c^2dt^2 - R(t)^2 \left[\frac{dr^2}{1 - kr^2} + r^2(d\theta^2 + \sin^2\theta d\phi^2) \right]. \tag{1.1}$$

This expansion is parametrised by the scale factor, $R(t)$ at time t; θ, ϕ and r define the co-ordinate system of the universe. These are known as comoving co-ordinates because they expand with the expansion of the universe. The parameter k in the Robertson-Walker metric parametrises the geometry of the universe such that it is closed ($k = 1$), open ($k = -1$) or flat ($k = 0$).

The scale factor $R(t)$ is used to define the expansion rate of the universe $H(t)$ such that

$$H(t) = \frac{\dot{R}(t)}{R(t)}. \tag{1.2}$$

Edwin Hubble discovered in the 1920s that nearby galaxies are receding from us with a velocity v proportional to their proper distance d from us. The constant of proportionality is known as the Hubble constant H_0 such that the "Hubble law" is $v = H_0 d$. H_0 is the present-day expansion rate of the universe or $H(0)$ in equation 1.2. General relativity tells us that there is a direct connection between the mass density of the universe (ρ_M) and the geometry of the universe which is given by the Friedmann equation

$$\left(\frac{\dot{R}}{R}\right)^2 = \frac{8\pi G\rho_M}{3} + \frac{\Lambda}{3} - \frac{k}{R^2} \tag{1.3}$$

which describes the time evolution of the scale factor R in natural units (such that the speed of light $c = 1$). Here Λ is the cosmological constant and G is the gravitational constant. This equation shows that there are three terms which drive the expansion of the universe, a matter term, a cosmological constant term and a curvature term. The relative contributions of the matter term (Ω_M) and cosmological constant term (Ω_Λ) at the present epoch are given by the density parameters

$$\Omega_M \equiv \frac{8\pi G\rho_M}{3H_0^2} \tag{1.4}$$

and

$$\Omega_\Lambda \equiv \frac{\Lambda}{3H_0^2} \tag{1.5}$$

The contribution of the curvature of space term (Ω_k) can be found from the relation

$$\Omega_M + \Omega_\Lambda + \Omega_k = 1 \tag{1.6}$$

These parameters completely determine the geometry of the universe if it is homogeneous, isotropic and matter-dominated. For a complete description of Λ-based cosmology see the review by Carroll *et al.* (1992) and references therein.

The expansion of the universe is measured via the cosmological redshift, z. This redshift is caused by photons which have been emitted in distant galaxies having their wavelength stretched by the expansion of the universe from their emitted wavelength λ_0 to a longer observed wavelength λ and is defined by the equation

$$z = \frac{\lambda - \lambda_0}{\lambda_0}. \tag{1.7}$$

Measured cosmological redshift is directly related to the ratio of scale factors at $t_{\rm obs}$ (the time of observation) and $t_{\rm em}$ (the time of emission) by

$$1 + z = \frac{R(t_{\rm obs})}{R(t_{\rm em})}. \tag{1.8}$$

Cosmological redshift should not be interpreted as a classical Doppler shift as it arises from the stretching of the wavelength of light by the expansion of the universe.

Equation 1.8 shows that observed redshifts are directly related to the scale factor at time $t_{\rm em}$. This means it is possible to convert redshifts directly into distances for a given set of cosmological parameters. In cosmology, distances are governed by the curved space-time of the Robertson Walker metric and are therefore dependent upon how one wants to measure "distance". The most common distance measures used in this thesis for a flat ($k = 0$) universe are outlined in the following paragraphs.

The *comoving distance* d_M is the distance between two objects which remains constant if they are moving with the Hubble flow, which can be interpreted as the distance between them which would be measured by rulers at the time they are observed, divided by the ratio of the scale factors between the times of emission and observation (ie. the $(1 + z)$ factor given in equation 1.8) (Hogg, 1999). For a flat universe d_M is given by

$$d_M = \frac{c}{H_0} \int_0^z \frac{dz'}{\sqrt{(1+z')^2(1+\Omega_M z') - z'(2+z')\Omega_\Lambda)}}, \tag{1.9}$$

where Ω_M and Ω_Λ are the density parameters defined by Equations 1.4 & 1.5 above. d_M is used in this thesis for the calculation of the two-point correlation function $\xi(r)$.

Another commonly used cosmological distance is the *luminosity distance*, d_L. It is defined by the inverse square relationship between the bolometric flux S of an object and its bolometric luminosity L

$$d_L = \sqrt{\left(\frac{L}{4\pi S}\right)}. \tag{1.10}$$

d_L is related the comoving distance d_M by the relation

$$d_L = (1 + z)d_M \tag{1.11}$$

and is used throughout this thesis to calculate luminosities and absolute magnitudes.

The *angular diameter distance* d_A is also frequently used in cosmology to calculate areas of space from a solid angle Ω. It is defined as the ratio of an object's physical transverse size to its projected angular size on the sky. d_A is easily calculated from

$$d_A = \frac{d_M}{1+z}. \tag{1.12}$$

Angular diameter distances have the counter-intuitive property that they turn over at $z \approx 1$, which means that objects of fixed physical size beyond this redshift start to appear increasingly large in projected angular size on the sky.

Chapter 5 of this thesis is largely concerned with the calculation of volumes of space. The cosmological *comoving volume* V_C is a volume measure in which the number density of non-evolving comoving objects stays constant with redshift. The comoving volume is found by calculating a volume element element dV_C by converting the solid angle element $d\Omega$ into a comoving area of space using the angular diameter distance multiplied by two

factors of $(1+z)$ and then converting this comoving area element into a volume element by multiplying by the comoving distance d_M in a redshift element dz

$$dV_C = \frac{c}{H_0} \frac{(1+z)^2 d_A^2}{\sqrt{(1+z)^2(1+\Omega_M z) - z(2+z)\Omega_\Lambda)}} d\Omega dz \tag{1.13}$$

in Mpc^3. Integrating this in a sphere from the earth out to a redshift z for a flat universe gives the simple geometric volume of the entire sky out to redshift z,

$$V_C = \frac{4\pi}{3} d_M^3 \tag{1.14}$$

in Mpc^3. V_C is not so straightforward to calculate for a universe which is not flat, see Carroll *et al.* (1992) for the more generalised result.

One last measurement which is often discussed throughout this thesis is the *look-back time* τ, defined as the difference between the age of the universe now and the age of the universe at redshift z. τ (in seconds) is defined by

$$\tau = \frac{1}{H_0} \int_0^z \frac{dz'}{(1+z')\sqrt{(1+z')^2(1+\Omega_M z') - z'(2+z')\Omega_\Lambda)}} \tag{1.15}$$

after converting H_0 from km s^{-1} Mpc^{-1} to s^{-1}.

1.2.3 The concordance paradigm

Much work in observational cosmology in the past decade has been aimed at measuring the values of the cosmological parameters H_0, Ω_M and Ω_Λ. In the past few years results of studies of supernovae type Ia (Perlmutter *et al.*, 1999; Schmidt *et al.*, 1998), measurements of the cosmic microwave background radiation (Spergel *et al.*, 2003) and studies of the matter distribution in the universe (Tegmark *et al.*, 2002) via large scale redshift surveys such as the 2 degree Field Galaxy Redshift Survey (2dFGRS; Colless *et al.*, 2001) have been used in conjunction to constrain these cosmological parameters to a high degree of accuracy.

Supernovae of type Ia have emerged as extremely powerful "standard candles" in a cosmological context because their luminosity normalised by the shape of their light curve does not vary between objects (see review by Leibundgut, 2001). This means that SNe Ia can be used as distance indicators independent of cosmological parameters. Two independent teams, Perlmutter *et al.* (1999) and Schmidt *et al.* (1998) discovered from surveys of high redshift SNe Ia that more distant objects appear fainter than their local counterparts, indicating that the cosmological expansion of the universe is accelerating. Models explaining this acceleration require that the cosmological constant Λ in the Friedmann equation (equation 1.3) is non-zero.

There is remarkable consistency between the latest results from CMB measurements by the WMAP satellite (Spergel *et al.*, 2003) and measurements of the matter distribution in the local universe using redshift surveys such as the 2dFGRS (Tegmark *et al.*, 2002).

The fluctuations in the power spectrum of the CMB temperature measure the coherent acoustic oscillations of the photon-baryon fluid at the epoch of decoupling at $z \approx 1065$; these fluctuations provide strong constraints on the values of cosmological parameters. Also, the power spectrum of the distribution of matter in the universe measured from redshift surveys can be related via a transfer function to the primordial matter density field from which large scale structures seen today grew, giving further constraints on cosmological parameters. The latest results from the combination of WMAP satellite data and 2dFGRS data show that the universe is flat (or very close to it) with baryon fraction (ie. the fraction of "observable" matter) $\Omega_{\rm b} = 0.044 \pm 0.004$, total matter fraction $\Omega_{\rm M} = 0.27 \pm 0.04$ (this implies that 23% of the matter in the universe is "dark" matter) and Hubble constant $H_0 = 71 \pm 4\,{\rm km\,s^{-1}\,Mpc^{-1}}$ (Spergel *et al.*, 2003). The values of the cosmological parameters commonly adopted in this thesis are $\Omega_{\rm M} = 0.3$, $\Omega_\Lambda = 0.7$ and $H_0 = 70\,{\rm km\,s^{-1}\,Mpc^{-1}}$; any deviation from this will be clearly stated in the text.

1.3 Radio source populations

By comparison with optical astronomy, radio astronomy has a brief history. However, since the first detection of radio emission it has proved to be a useful tool for understanding the properties of structures within our own galaxy and the nature of external galaxies. Extragalactic radio sources fall into two main categories, those whose radio emission is fuelled by processes related to star formation (star-forming galaxies) and those whose radio emission is fuelled by an active nucleus powered by a super-massive black hole (Active Galactic Nuclei or AGNs). The radio properties of both these classes are discussed in this section.

1.3.1 A brief history of radio astronomy

The first detection of radio emission from space was made by Karl Jansky in the early 1930s (his name has been given to the unit of radio flux density, $1\,{\rm Jansky} = 10^{-26}\,{\rm W\,Hz^{-1}\,m^{-2}}$). Working at Bell Labs he was investigating the levels of radio interference at 20.5 MHz, and found a slowly varying background noise which was varying on the time-scale of a sidereal day. This led him to conclude that this radio "noise" was extra-terrestrial in origin. Jansky pinpointed this background noise as coming from the constellation of Sagittarius. He had made the first detection of the centre of the Milky Way at radio wavelengths. Not long after this Grote Reber, hearing of Janskys discovery, built a parabolic radio dish in his own backyard. This was the first radio telescope used exclusively for astronomical research and is the prototype for modern reflecting radio telescopes. Reber, in 1944 published the first radio frequency maps of large parts of the sky. It was not until after World War II that antenna technology improved enough to further understand the nature of extra-terrestrial radio emission. In 1949 Bolton, Stanley and Slee, working at Australia's CSIRO Radiophysics Laboratory identified the radio sources Centaurus A and Virgo A with the nearby optical galaxies NGC 5128 and NGC 4486 (M87) (Bolton *et al.*, 1949). This was the first optical identification of extragalactic ra-

dio sources and the subsequent identifications of other radio sources with distant galaxies established a new class of object known as "radio galaxies".

The earliest radio source surveys began soon after. During 1951 and 1952 Graham Smith at the Cavendish Laboratory, Cambridge University and Bernard Mills at Sydney University, in collaboration with Walter Baade and Rudolf Minkowski at Mt Wilson Observatory, attempted to improve the accuracy in the positions of radio sources to allow identifications with faint optical objects. Their observations pushed radio astronomy to higher resolution to increase the positional accuracy with the aim of identifying the optical counterparts of bright radio sources. By the 1960s the accuracy achieved in radio source positions was such that radio sources were being identified with objects on optical plates that did not appear like galaxies at all but looked more like Galactic stars. The optical spectra of these stellar objects had broad emission lines which were not identifiable with any atomic transitions seen before in galaxy or stellar spectra. In 1963 Maarten Schmidt realised while working on the spectrum of 3C 273, that its emission lines could be identified with the Balmer series of hydrogen at a redshift of 0.16, larger than any previously obtained. Subsequently, spectra of other "stellar" radio sources were investigated and all were identified with moderately large redshifts. These objects were known as "quasi-stellar radio sources" or quasars.

By the end of the 1960s and 1970s a wealth of new types of radio source had been discovered, both Galactic and extra-galactic. Radio telescopes were being built capable of much higher resolution and sensitivity. In the 1970s, aperture synthesis interferometry had advanced far enough that a new telescope was built near Socorro, New Mexico called the Very Large Array (VLA). This telescope is composed of 27 movable antennas, each 25m in diameter, whose signals were combined by a state-of-the-art correlator. These telescope dishes are configured in a "Y" shape over 40 km in diameter on over 136 km of railroad track such that the telescope can be steered into different configurations to allow a trade-off between sensitivity and resolution.

Here, discussion turns to the physical properties of two classes of extragalactic radio source which are of importance to this thesis: active galactic nuclei and star-forming galaxies.

1.3.2 Active Galactic Nuclei

The brightest extragalactic radio sources ($P_{1.4} > 10^{24}\,\mathrm{W\,Hz^{-1}}$) generally harbour an active galactic nucleus (AGN). AGNs often have enhanced levels of emission at X-ray, far-infrared (FIR) and optical wavelengths. They are broadly grouped into two distinct categories, 'radio loud' and 'radio quiet' based on their level of radio emission. The host galaxies of radio-loud and radio-quiet AGN are are essentially indistinguishable. The spectral energy distribution of radio-loud AGN at radio frequencies implies that the radio emission is non-thermal in origin; it comes from synchrotron emission from ultra-relativistic electrons spiralling in the magnetic field of the galaxy and the intergalactic medium. The enhanced emission from AGN is due to the presence of a very compact and energetic nuclear object, believed to be a super-massive black hole accreting matter. In many radio loud AGN, jets of radio emission extend for up to thousands of kilo-parsecs

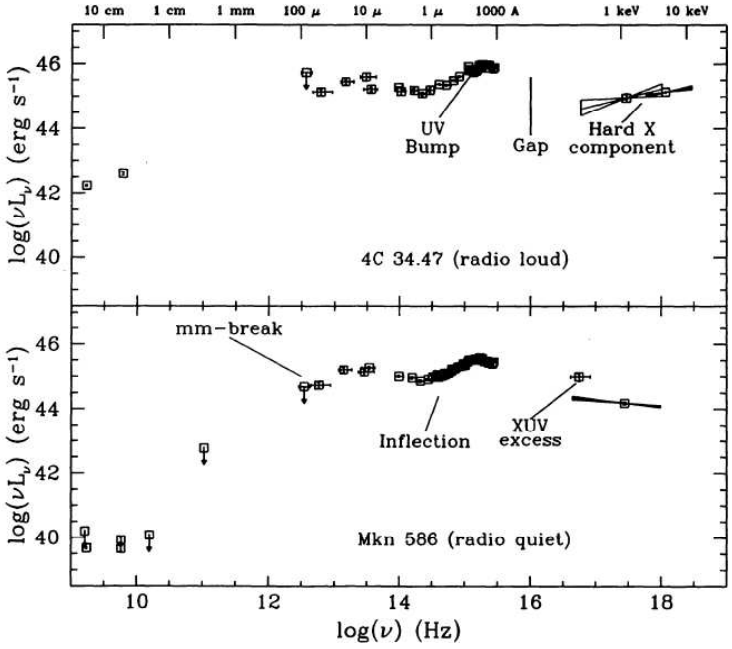

Figure 1.1 The spectral energy distribution of a radio-loud (4C 34.47, *top*) and a radio-quiet (Mrk 586, *bottom*) quasar with characteristic features labelled. Note the distinct drop in intensity at wavelengths shorter than 60μm in the case of the radio-quiet quasar. This figure was obtained from Elvis *et al.* (1994).

from the nucleus and into the surrounding intergalactic medium. Typical spectral energy distributions of radio loud and radio quiet AGN are compared in Figure 1.1.

Optical spectra of AGN essentially have two different forms: Type I and Type II. Type I AGN are characterised by both broad and narrow emission lines whereas Type II AGN only have narrow emission lines. Examples of Type I and Type II spectra are shown in Figure 1.3. Differences in spectral properties are explained by a unification scheme in which the observed properties of an AGN are due to its orientation relative to the observer's line of sight (Antonucci, 1993). Such a scheme is shown in Figure 1.2. In these schemes matter is accreting onto a super-massive black hole from an accretion disk surrounded by a dusty torus and energy is transported via jets into the intergalactic medium. The broad-line region lies within 1 pc of the central engine and the narrow-line region lies further out, about 1 kpc from the nucleus. Type I AGN are viewed closer to face on, such that both the broad and narrow line regions are visible whereas Type II are viewed closer to edge on, with the dusty torus obscuring the broad line region. For a thorough review of unification schemes see Antonucci (1993).

The reason some AGN are radio loud and some radio quiet is not explained in terms of AGN unification schemes. Work on the broad-line region in active galaxies and quasars has established that there are no obvious differences between the broad-line regions associated with radio-selected AGN and those selected optically (Heckman, 1980). Much debate recently has centred on the possibility of a relationship between the mass of the central black hole and the strength of the radio emitting AGN. Magliocchetti *et al.* (2004)

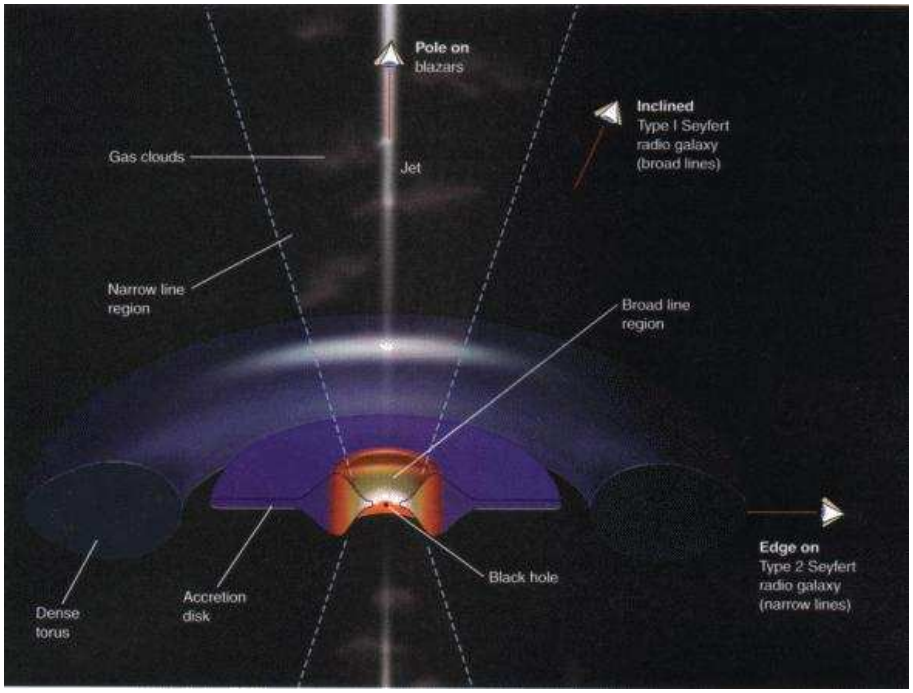

Figure 1.2 An illustration of AGN unification schemes. Type 2 galaxies which have only narrow spectral lines are viewed edge on and Type 1 galaxies with broad and narrow lines are viewed at inclinations $< 45^\circ$ to the pole. This image was obtained from http://cassfos02.ucsd.edu/public/tutorial/AGN.html.

have suggested, from studies of the clustering of radio-loud AGN, that there is a minimum halo mass which can support a radio AGN which in turn implies that there must be a minimum black-hole mass of $10^9\,\mathrm{M}_\odot$ for the onset of radio loudness. Furthermore, above this black-hole mass Metcalf & Magliocchetti (2005) have suggested that there appears to be no correlation between black-hole mass and radio luminosity. Examining a population of nearly 2 500 radio loud AGN with measured black-hole masses Best *et al.* (2005a) found that the *fraction* of radio-loud AGN increases strongly as a function of black-hole mass but that the *distribution* of radio luminosities does not generally depend on black-hole mass. On the other hand, using a large sample of black-hole masses measured from the velocity dispersion of the broad line region in optical spectra of both radio-loud and radio-quiet objects, McLure & Jarvis (2004) found a strong correlation between black-hole mass and radio power, though they noted that the range in radio power for a given black-hole mass is several orders of magnitude. It is possible that other physical mechanisms such as the efficiency of accretion onto the black hole may cause differences in the radio power of different objects. It is believed that all AGN are radio sources at some level including the radio-quiet ones. There is a compact low luminosity ($P_{1.4} \approx 10^{18}\,\mathrm{W\,Hz^{-1}}$) radio source at the centre of our own Milky Way Galaxy (Sgr A*) associated with a $3 \times 10^6\,\mathrm{M}_\odot$ black hole. Also, by stacking radio images which show no detectable radio source at the position of optically-selected quasars Glikman *et al.* (2004) found an average 1.4 GHz flux density of radio-quiet quasars of $25\,\mu$Jy.

Radio-loud AGN are divided into two morphological classes: Fanaroff-Riley (FR)

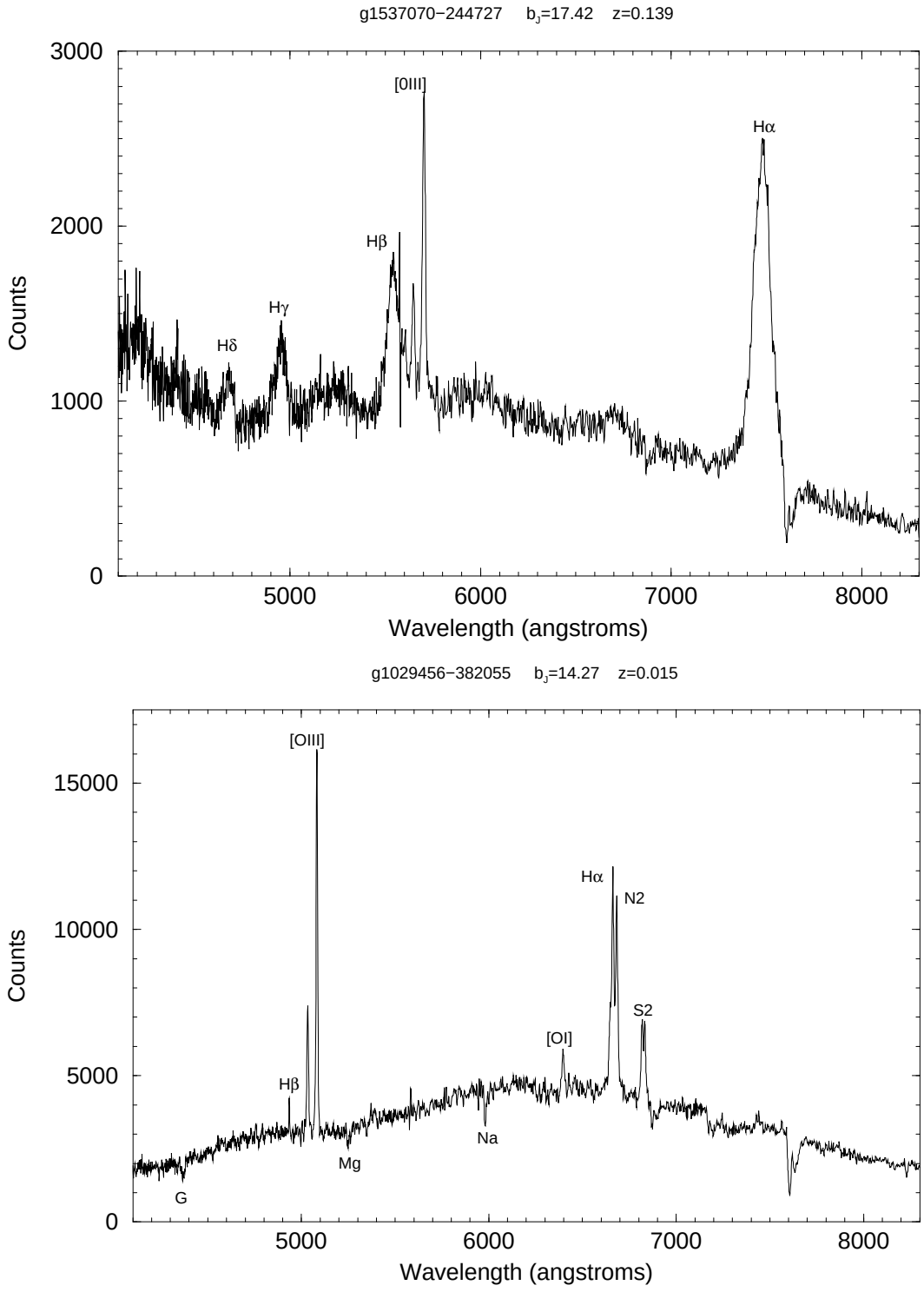

Figure 1.3 **Top:** An example of a Type I AGN spectrum. Note the strong broad Hydrogen Balmer lines which come from the broad line region close to the black hole and the narrow [OIII] lines which come from the narrow line region further away from the black hole. **Bottom:** An example spectrum of a Type II AGN. This only has narrow lines. Both spectra are from the 6dFGS (Jones *et al.*, 2004).

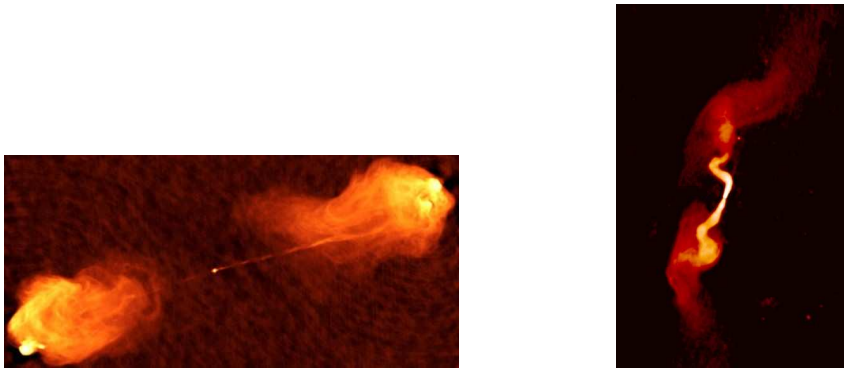

Figure 1.4 **Left image:** A radio image at $1''$ resolution of the FRII type radio galaxy Cygnus A. Two bright hot-spots are clearly visible at the extremities of the long thin jets that originate from the core of the host galaxy. **Right Image:** A radio image of the FRI type radio galaxy 3C31. This galaxy is distinct from the FRII type galaxy with well collimated jets emerging from a bright nucleus becoming increasingly turbulent further away. Both images were made with the Very Large Array and were obtained from http://www.nrao.edu/imagegallery courtesy of NRAO/AUI.

type I and type II (Fanaroff & Riley, 1974). Examples of these two classes are shown in Figure 1.4. The radio emission from FRI galaxies is brightest close to the nucleus of the host galaxy, with poorly collimated extended emission becoming more diffuse further out. FRII radio galaxies, on the other hand, have well-collimated jets terminating in bright lobes, with hot-spots at their outer edges. FRI and FRII class AGN show a division in 1.4 GHz radio power with FRI objects having $P_{1.4} < 10^{25}\,\mathrm{W\,Hz^{-1}}$ and FRII objects brighter than this (Ledlow & Owen, 1995). These two types of radio loud AGN are often described by AGN unification models. Radio loud quasars are assumed to be the same objects as FRII radio galaxies but are viewed close to the line of sight of the jet axis resulting in their observed broad spectral lines. BL Lac objects, which exhibit strong, rapid variability and a featureless spectrum, are FRI radio galaxies in which the jet is Doppler boosted along our line of sight (Urry & Padovani, 1995).

Radio-loud AGN are potential tracers of large-scale structure. Most radio sources at low redshift are found in groups or clusters of galaxies (Hill & Lilly, 1991), and there is some evidence that distant radio-loud AGN are associated with the densest environments (Brand *et al.*, 2003). Analysis of samples of radio-loud AGN at low redshift (Peacock & Nicholson, 1991; Magliocchetti *et al.*, 2004; Brand *et al.*, 2005) has shown that these sources have clustering amplitudes in excess of the clustering amplitude of normal galaxies. This implies that radio-loud AGN are biased tracers of the galaxy distribution, which means that they are preferentially located in regions of high galaxy density. Radio source catalogues contain almost exclusively AGN above $z \sim 0.1$ and sample the universe to median redshifts $z \approx 0.8$ and are therefore powerful tools for investigating the clustering properties of galaxies at cosmological redshifts.

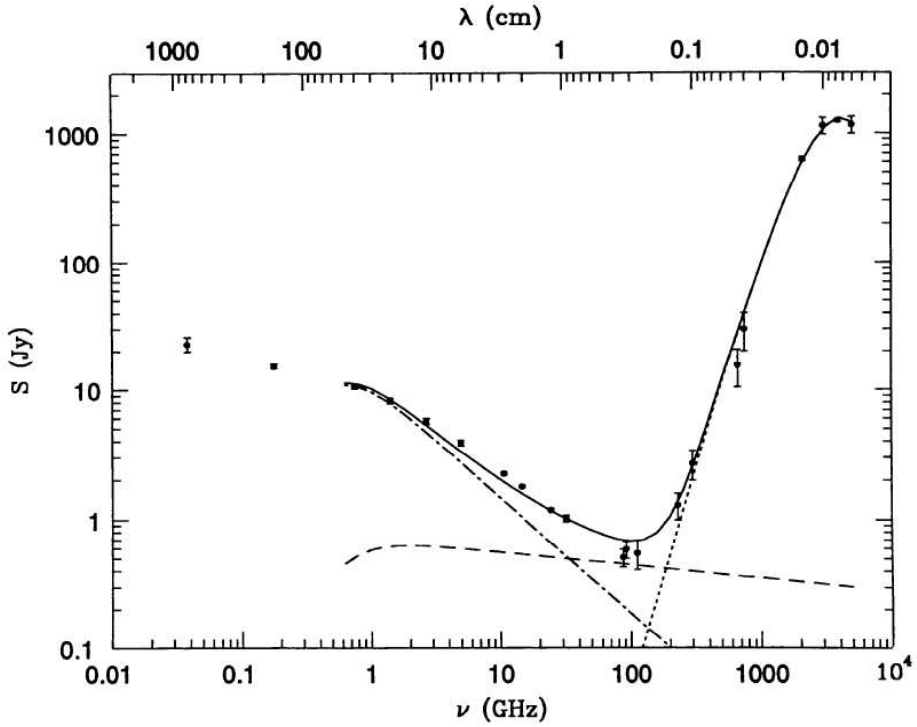

Figure 1.5 The radio-Far-Infrared spectral energy distribution of M82. The data shown is well approximated by the solid line which is the sum of contributions from non-thermal synchrotron emission (*dot-dashed line*), thermal bremsstrahlung (*dashed line*) and reradiation by 45 K dust (*dotted line*). Figure from Condon (1992).

1.3.3 Star-forming galaxies

Star-forming galaxies on average have lower radio powers than AGNs and dominate the radio source population below $P_{1.4} = 10^{23}\,\mathrm{W\,Hz^{-1}}$ (Sadler *et al.*, 2002). They are characterised by their blue optical colours which are indicative of a young stellar population, their high level of far-infrared emission and strong and narrow hydrogen Balmer emission lines in their spectra. At wavelengths near 1 GHz most of the emission ($\sim 90\%$) is from non-thermal synchrotron radiation from relativistic electrons accelerated in shocks associated with the expanding supernova remnants of the most massive stars ($M > 8M_{\odot}$) (Condon, 1992). The remaining $\sim 10\%$ is from thermal bremsstrahlung in HII regions. The same population of massive stars that produces the ultra-relativistic electrons in shocks will also ionise the HII regions. These massive stars have lifetimes ($t < 10^7$ yr) much shorter than the typical age of a galaxy at the present epoch ($t > 10^9$ yr), which implies that radio observations are probing very recent star formation activity. Figure 1.5 shows the spectral energy distribution of a typical star-forming galaxy (M82) from radio to far-infrared wavelengths. It shows that the spectrum can be modelled as the sum of contributions from thermal bremsstrahlung (*dashed line*), non-thermal synchrotron radiation (*dot-dashed line*) and thermal reradiation by 45 K dust (*dotted line*).

A remarkable, though poorly-understood correlation exists between emission in the

far-infrared (FIR) and radio parts of the spectrum of star-forming galaxies. In the 1980s large samples of spiral galaxies observed in the far-infrared by the Infrared Astronomical Satellite (IRAS) were combined with radio data to establish the correlation (eg, Helou *et al.*, 1985; Condon & Broderick, 1988). Most emission at far-infrared wavelengths occurs due to thermal re-radiation by cool dust (10-50 K) which has been heated by UV-emitting short-lived massive stars, the same massive stars which are thought to be responsible for the radio emission from star-forming galaxies. Though it is well established that short-lived stars are responsible for the radio-FIR correlation the process that relates the thermally dominated FIR emission and the non-thermally dominated radio emission is poorly understood. A substantial review of radio-emission from star-forming galaxies and the radio-FIR correlation is given by Condon (1992).

Star formation in galaxies is also measured by the strength of Hα and far-UV emission within them. Estimates of the amount of star formation in galaxies made at both these wavelengths is uncertain because of absorption of photons by dust in star-forming regions. Dust is transparent to radio and FIR photons which means that observed flux densities are accurately proportional to intrinsic luminosities (Condon, 1992). However, at radio wavelengths there are significant steps between star formation and the production of non-thermal synchrotron electrons. In particular, the relationship between the rate of type II and Ib supernovae and the non-thermal radio luminosity is not well understood. The radio-FIR correlation has been an important constraint on models relating star formation to radio luminosity (eg. Condon & Yin, 1990).

In large radio surveys it is important to disentangle the star-forming galaxy population from the AGN population because they arise from completely different physical processes. This is not a straightforward process as radio data alone cannot easily distinguish between these two classes of galaxy. A useful diagnostic for distinguishing between star-forming galaxies and AGNs has been the radio-FIR correlation whereby galaxies with a radio "excess" above that expected from the correlation are classed as AGN and the remainder as star-forming (eg. Condon & Broderick, 1988; Machalski & Condon, 1999; Condon *et al.*, 2002). High resolution Very Long Baseline Interferometry (VLBI) images of radio sources may also be used to distinguish the AGN component from galaxies whose radio emission is a composite mixture of both star formation and AGN activity. AGN typically have parsec-scale radio cores with brightness temperature $\sim 10^8$ K which are easily observed at high angular resolution, whereas star-forming galaxies typically have kpc scale radio structure with lower brightness temperature ($\sim 10^4$ K) which VLBI observations lack the surface brightness sensitivity to detect. Such VLBI observations are essentially "blind" to star formation making them a powerful method of extracting the AGN component of galaxies whose emission is fuelled by a superposition of both AGN activity and star formation (eg. Norris *et al.*, 1992). In recent years, radio samples constructed from large optical redshift surveys (Sadler *et al.*, 2002; Magliocchetti *et al.*, 2002; Best *et al.*, 2005b) have had the advantage of having optical spectra available for each source. Classification based on spectral line ratios provides an extremely robust method for distinguishing between star-forming galaxies and AGNs.

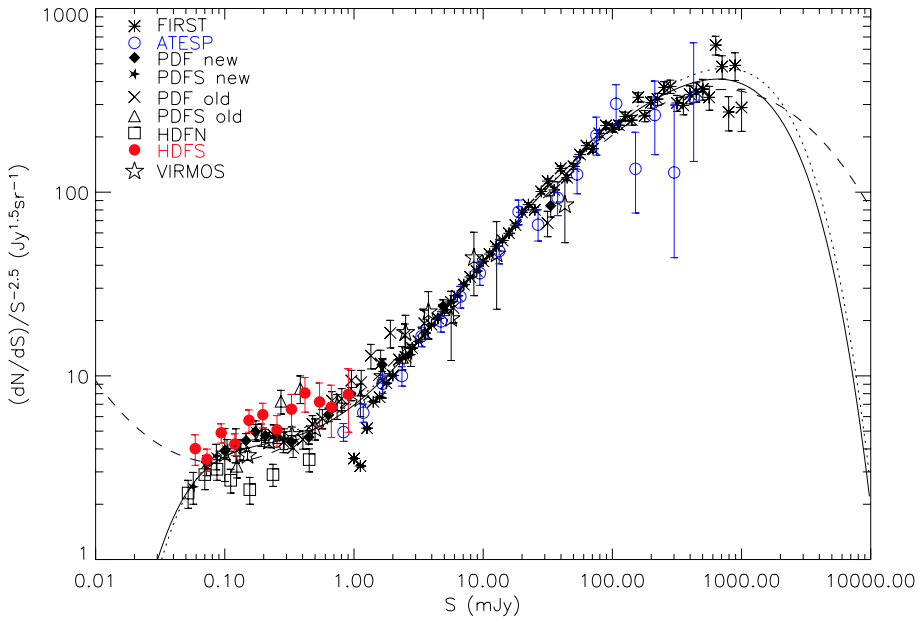

Figure 1.6 The radio source counts at 1.4 GHz normalised such that counts in a static Euclidean universe would lie on a straight line. The data points labelled in the top left of the plot refer to different radio source surveys as defined by Huynh *et al.* (2005).The curves plotted are polynomial fits to the radio source counts used to quantify evolution.

1.3.4 Radio Source counts

Source counts are a way of categorising the populations of objects in a survey. They are visually presented as a plot of the surface density of objects as a function of their flux density. Radio source counts are commonly plotted in a form in which each bin of flux density is weighted by $S^{-2.5}$ such that the source counts in a static Euclidean universe would lie on a horizontal line. The universe is neither static nor Euclidean so in general radio source counts are not horizontal. Radio source counts are powerful cosmological probes because radio surveys probe an enormous range in redshift (the median redshift of most deep radio surveys is $z \approx 0.8$) though their interpretation is highly model dependent. Recent radio source counts from a number of deep 1.4 GHz radio surveys are shown in Figure 1.6.

Changes in the shape of the observed source counts with flux density are indicative of changes in the underlying population of radio sources contributing to them. The radio source counts shown in Figure 1.6 are Euclidean at about 1 Jy and then steadily decrease below about 100 mJy, indicative of the flattening of the underlying true source count. Steepening in the radio counts at high flux density levels has been used to show that radio sources were more common at higher redshift (Ryle, 1968). The counts then flatten again at 1-2 mJy down to the faintest observable flux densities. Condon (1989) suggested that the distribution of radio source counts can be explained by the two populations of radio sources described in the previous sections, namely star-forming galaxies and AGNs. The flattening of the source counts at lower flux density is due to the population of star-forming

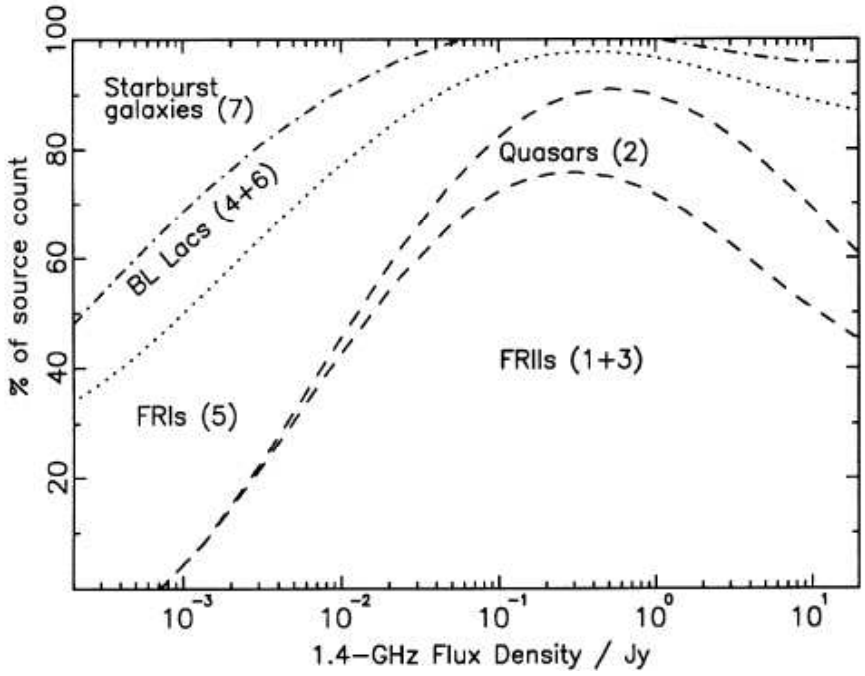

Figure 1.7 The predicted integral population mix at 1.4 GHz from the source count models of (Jackson & Wall, 1999). (Figure 17 of Jackson & Wall (1999)).

galaxies, which start to dominate the radio source counts below 1 mJy. Figure 1.7 shows the predicted population mix of radio sources with 1.4 GHz flux density, derived from models fitted to the radio source counts by Jackson & Wall (1999).

Radio source count models can be used to predict the amount of cosmological evolution undergone by the different radio source populations. This evolution is usually parametrised into two distinct types: *luminosity evolution* in which the radio luminosity of sources changes with epoch and *density evolution* in which the comoving space density of a population changes with epoch. Fitting the radio source counts with evolutionary models is done by generalising the *local* radio luminosity function (see chapter 5 for a definition of the local radio luminosity function) by an evolution function to give the radio luminosity function at any epoch z (Wall *et al.*, 1980; Jackson & Wall, 1999).

1.4 Survey astronomy

When studying the demographics of any population it is necessary to have a good understanding of the selection effects of a sample to extract robust and meaningful results. This is true across a wide range of scientific pursuits from human population studies to the radio source populations presented in this thesis. In an astrophysical context, uniform and accurate surveys of a large volume of space are important tools for studying population demographics, not only because large volumes yield better statistics, but because the homogeneity of surveys made with a single telescope minimises the biases which might

be introduced into samples through combining data from different telescopes. The past decade has seen an explosion in the size and accuracy of astronomical surveys across the entire electromagnetic spectrum. This section will provide a brief introduction to the optical, near-infrared and radio surveys upon which this thesis is based.

1.4.1 Optical and Near-infrared surveys

The earliest optical sky surveys which are of relevance to this thesis are the photographic surveys done with the UK Schmidt telescope (UKST) in the southern hemisphere and the Palomar Schmidt telescope in the northern hemisphere. Surveys have been undertaken with these telescopes at blue (Cannon, 1984; Reid *et al.*, 1991), red (Morgan *et al.*, 1992; Reid *et al.*, 1991) and near-infrared (Hartley & Dawe, 1981; Reid *et al.*, 1991) passbands. In the past two decades the scientific return from these photographic surveys has greatly increased since they have been digitised into machine readable catalogues. The COSMOS/UKST catalogue of the southern sky (Yentis *et al.*, 1992) digitised all the UKST blue photographic plates at $|b| > 10^{\circ}$ with $1.1''$ resolution and produced an object catalogue with positions, morphological classifications ("stellar" or "extended") and photometric information (b_J magnitude). The COSMOS/UKST survey has recently been superseded by the SuperCOSMOS Sky Survey (Hambly *et al.*, 2001b). SuperCOSMOS has scanned photographic plates with $0.67''$ pixels in the b_J, r_F and I bands. The SuperCOSMOS sky survey catalogue contains magnitudes, morphological classification, positions and proper motions (from repeated r_F band surveys of the entire sky more than 10 years apart) for about 100 million objects.

Recently the advent of direct CCD imaging has made possible all-sky surveys which probe deeper and have more accurate photometric information than the previous generation of photographic surveys. The Sloan Digital Sky Survey (York *et al.*, 2000) aims to image 10 000 deg^2 of the northern sky in five separate passbands to a depth of $g' \sim 23$ mag. The 2-micron All Sky Survey (2MASS; Kleinmann *et al.*, 1994) has imaged the entire celestial sphere in the near-infrared (H, J, K passbands) down to $K \sim 14.5$. Near-infrared surveys are very useful because dust is almost transparent to near-infrared light meaning that magnitude limited surveys will not be biased away from dusty galaxies with high star-formation rates or obscured AGN. Throughout this thesis radio sources have been identified from the 2MASS eXtended Source Catalogue (2MASS XSC; Jarrett *et al.*, 2000) and the SuperCOSMOS Sky Survey (Hambly *et al.*, 2001a).

1.4.2 Radio Surveys

The early history of radio surveys includes the 3C (Edge *et al.*, 1959), 4C (Gower *et al.*, 1967; Pilkington & Scott, 1965), 6C (Baldwin *et al.*, 1985) and 7C (Visser *et al.*, 1995) surveys all of which cover much of the northern sky at at frequencies below 200 MHz. The lowest frequency Cambridge survey, the 8C (Rees, 1990) covered only the northern polar cap ($\delta > 70^{\circ}$) at 38 MHz. In the south the Molonglo radio telescope operating at a frequency of 408 MHz surveyed the entire sky with $19^{\circ} > \delta > -85^{\circ}$ to a limiting

Table 1.1 Major large-area radio surveys.

Survey name	Year Completed	ν MHz	Resolution arcmin	$S_{\rm lim}$ mJy	Area steradians	Sources per deg^2
3C[1]	1959	159	10	7000	6	0.02
4C[2]	1967	178	11.5	2000	6	0.2
8C[3]	1990	38	4.5	1000	1	0.3
MRC[4]	1981	408	3	700	7.9	0.47
87GB[5]	1991	4850	3.5	25	6	2.8
PMN[6]	1994	4850	3.5	20	7.4	2.1
NVSS[7]	1997	1400	0.75	2.3	10	55
WENSS[8]	1998	325	0.9	18	3.1	20
FIRST[9]	2002	1400	0.08	1	2.7	90
SUMSS[10]	2005	843	0.75	6	2.4	30
AT20G[11]	2006	20000	0.17	40	6	1
VLSS[12]	2006	74	1.3	500	9	2

NOTES:
[1] Third Cambridge radio survey (3C; Edge *et al.*, 1959)
[2] Fourth Cambridge radio survey (4C; Gower *et al.*, 1967; Pilkington & Scott, 1965)
[3] Eighth Cambridge radio survey (8C; Rees, 1990)
[4] Molonglo Reference Catalogue of radio sources (Large *et al.*, 1981, MRC;)
[5] 1987 Green Bank radio survey (87GB; Condon *et al.*, 1989)
[6] Parkes-MIT-NRAO radio surveys (PMN; Griffith & Wright, 1993)
[7] NRAO VLA Sky Survey (NVSS; Condon *et al.*, 1998)
[8] Westerbork Northern Sky Survey (WENSS; Rengelink, 1998)
[9] Faint Images of the Radio Sky at Twenty-one cm (FIRST; Becker *et al.*, 1995)
[10] Sydney University Molonglo Sky Survey (SUMSS; Bock *et al.*, 1999) & This thesis
[11] Australia Telescope 20 GHz Survey (AT20G; Ricci *et al.*, 2004)
[12] VLA Low-frequency Sky Survey (VLSS; Cohen *et al.*, 2004)

flux density of 700 mJy to produce the Molonglo Reference Catalogue of Radio Sources (MRC; Large *et al.*, 1981).

The next major advance in sensitivity for large area radio surveys came when the Green Bank telescope was used to produce the GB87 survey of the entire northern sky at 4.85 GHz (Condon *et al.*, 1989). The southern equivalent came soon after and was called the Parkes-MIT NRAO survey (PMN; Griffith & Wright, 1993) which was done with the Parkes radio telescope at a frequency of 4.85 GHz. These surveys remain the deepest and most uniform high frequency radio surveys ever completed.[2] The limiting factor of all these early surveys was that they lacked the angular resolution required to make unambiguous optical identifications of most sources for further study. Obtaining

[2]Recently a new and more sensitive high-frequency imaging survey at 18 GHz is being undertaken using the Australia Telescope Compact Array (ATCA) (Ricci *et al.*, 2004).

large samples of radio sources with optical identifications was a lengthy process requiring repeat observations of individual sources at better angular resolution with interferometric telescopes.

It has only been in recent years that some of the most sensitive radio telescopes in the world, the VLA, the Westerbork Synthesis Radio Telescope (WSRT) and the Molonglo Observatory Synthesis Telescope (MOST) have been used to cover much of the northern and southern sky with milliJansky sensitivity and sufficient angular resolution to allow unambiguous identifications of large numbers of radio sources with objects from optical catalogues. The VLA has recently produced two surveys: the high resolution Faint Images of the Radio Sky at Twenty-one centimetres (FIRST; Becker *et al.*, 1995) and the lower resolution NRAO VLA Sky Survey (NVSS; Condon *et al.*, 1998) both at 1.4 GHz. This thesis makes much use of the NVSS, which covers the entire sky north of $\delta = -40^\circ$ with angular resolution of $45''$. At the same time as the NVSS and FIRST surveys the WSRT was used to produce a complementary survey covering the northern sky at 325 MHz (WENSS; Rengelink, 1998). The southern complement to these northern sky surveys has been the Sydney University Molonglo Sky Survey (SUMSS; Bock *et al.*, 1999). The Molonglo Radio Telescope used to make the MRC was upgraded between the early 1980s and mid 1990s to have a wider field of view and reincarnated as the Molonglo Observatory Synthesis Telescope (MOST) operating at a frequency of 843 MHz. SUMSS, when complete in late 2005, will have imaged the sky south of $\delta = -30^\circ$ with $45''$ resolution and an rms noise of 1-2 mJy. Chapter 2 of this thesis is concerned with the creation of the SUMSS catalogue.

Table 1.1 summarises the properties of the radio surveys mentioned in this section.

1.4.3 Redshift surveys

Since Hubble's discovery of the redshift-distance relationship for galaxies, measuring the redshifts of large numbers of galaxies as a means of understanding their 3-dimensional distribution has been a major branch of observational astronomy. Up until the mid 1990s, redshift surveys were extremely arduous. Thousands of galaxies, had their redshifts measured one at a time using long slit spectrographs. Collections of (extremely inhomogeneous) redshift surveys were combined to form maps which revealed galaxies to be very clustered, large clusters of galaxies are linked by filaments stretching for hundreds of megaparsecs. One of the largest of these early maps was the IRAS Point Source Catalogue redshift survey (IRAS PSCz; Saunders *et al.*, 2000) for which 15 000 galaxies in the IRAS-PSC had their redshifts measured.

Advances in optical fibre technology in the mid 90s has brought about a new era in redshift surveys. Optical fibre-fed spectrographs, capable of observing hundreds of galaxies at a time, have been used to observe large homogeneous samples of hundreds of thousands of galaxies in much larger volumes of space than any hitherto achieved. The basic properties of some of the largest of these are shown in Table 1.2. The 6dF Galaxy Survey (Jones *et al.*, 2004) which is most relevant to this thesis is described in detail in Chapter 3.

Table 1.2 Summary of some recent redshift surveys (data from Colless, 2000)

Survey name	$N_{\rm galaxies}$	Band	Magnitude limit	Median redshift
PSCz[1]	15 000	$S_{60\,\mu m}$	0.6 Jy	0.03
LCRS[2]	26 000	R	17.7	0.1
2dFGRS[3]	250 000	b_J	19.4	0.1
SDSS[4]	700 000	g	18.3	0.1
6dFGS[5]	150 000	K	12.75	0.05

NOTES:
[1] IRAS Point Source Catalogue z (PSCz; Saunders *et al.*, 2000)
[2] Las Campanas Redshift Survey (LCRS; Shectman *et al.*, 1996)
[3] 2dF Galaxy Redshift Survey (2dFGRS; Colless *et al.*, 2001)
[4] Sloan Digitized Sky Survey (SDSS; York *et al.*, 2000)
[5] 6dF Galaxy Survey (6dFGS; Jones *et al.*, 2004)

1.4.4 Radio-selected multiwavelength surveys

Much of our current understanding of radio source populations has come from samples of objects for which optical counterparts have been found and redshifts measured. Finding optical counterparts for radio sources is extremely important as optical morphology and line spectra of radio source populations are of vital importance in understanding their host galaxy properties. In the past this was a difficult process, requiring high resolution radio observations to secure optical counterparts for each object which could then be observed spectroscopically one at a time. Early work on radio sources in elliptical galaxies (eg. Auriemma *et al.*, 1977; Sadler *et al.*, 1989) showed that bright radio sources in elliptical galaxies were equally likely to reside inside and outside of clusters and also that the probability of an elliptical galaxy to be a radio source increased as a function of the luminosity of the galaxy. This means that powerful radio sources preferentially reside in the most luminous and hence most massive elliptical galaxies. Condon (1989) obtained a sample of 176 radio identifications of galaxies in the *Uppsala General Catalog of Galaxies* (UGC; Nilson, 1973) and found that local radio source populations were made up of two distinct classes of objects which he termed "starbursts" (here called star-forming galaxies) and "monsters" (here called AGN) and that the vast bulk of objects in radio catalogues are AGN at a median redshift of $z \approx 0.8$. Only about 1% of objects in radio source catalogues above 10 mJy are nearby ($z < 0.1$), in stark contrast to optical galaxy catalogues for which the median redshift is $z \approx 0.15$.

Recent large fibre-spectrograph redshift surveys, coupled with accurate and deep radio surveys, have spawned a new generation of multiwavelength datasets which contain thousands of objects. Machalski & Condon (1999) crossmatched the NVSS catalogue with objects in the Las Campanas Redshift Survey and derived the radio luminosity function. Sadler *et al.* (2002) have crossmatched the NVSS catalogue with the 2dF Galaxy Redshift

Survey and derived the radio luminosity function of 242 star-forming and 420 AGNs at a median redshift of $\bar{z} \approx 0.1$. Condon *et al.* (2002) crossmatched the UGC with the NVSS catalogue, finding more than 2 000 identifications of mostly star-forming galaxies in the local universe ($\bar{z} \approx 0.02$). Recently Best *et al.* (2005b) have used both the NVSS and FIRST radio catalogues to find optical identifications for $\sim 3\,000$ (about 90% AGN) radio sources in the Sloan Digital Sky Survey (SDSS) at a median redshift of $z \approx 0.1$. This thesis present results from identifications of NVSS and SUMSS radio sources in the 6dF Galaxy survey at a median redshift of $z \approx 0.05$, an intermediate redshift between SDSS, 2dFGRS samples and the UGC sample.

1.5 Outline of thesis

The goal of this thesis is to understand the radio properties of galaxies in the local universe through followup spectroscopy with the 6 degree Field (6dF) fibre spectrograph of radio sources identified with galaxies on optical plates. Results will be presented from a study of radio sources in the Sydney University Molonglo Sky Survey (SUMSS; Bock *et al.*, 1999; Mauch *et al.*, 2003) and the NRAO VLA Sky Survey (NVSS; Condon *et al.*, 1998) which are identified with galaxies observed in the 6 Degree Field Galaxy Survey (6dFGS; Jones *et al.*, 2004) primary sample. The 6dFGS primary sample is a near-infrared ($K < 12.75$) selected spectroscopic survey of all galaxies in the $\sim 17\,000\,\mathrm{deg}^2$ of the celestial sphere with galactic latitude $|b| > 10^\circ$ and declination $\delta < 0^\circ$. The sample of SUMSS radio sources in the 6dFGS primary sample will hereafter be referred to as the 6dFGS-SUMSS primary sample and NVSS radio sources in the 6dFGS will be referred to as the 6dFGS-NVSS primary sample. Selecting radio sources at milliJansky flux densities ($S > 3 - 6\,\mathrm{mJy}$) with a relatively bright near-infrared magnitude limit of $K < 12.75$ ensures that the 6dFGS-NVSS and 6dFGS-SUMSS primary samples are optimised for selecting both star-forming galaxies and AGN at low ($z < 0.15$) redshifts, making the primary sample essentially a study of the *local* universe.

The near-infrared selection of the primary sample may miss populations of galaxies which are present in other radio samples selected from optical catalogues. In order to quantify this "missing" population, results will be presented from serendipitous (ie. randomly selected) 6dF observations of NVSS and SUMSS radio sources identified with objects in the same region of sky as the primary sample, but which are either too blue in colour or stellar in appearance to be part of it. These objects are selected from the SuperCOSMOS catalogue (Hambly *et al.*, 2001b) with $b_J < 18\,\mathrm{mag}$ and should comprise a population of galaxies with blue colours, such as Seyfert and starburst galaxies, as well as radio sources whose optical host galaxies appear stellar such as quasars. These objects are referred to throughout this thesis as "additional targets".

The structure of this thesis is as follows. Chapter 2 will give an introduction to the current generation of radio imaging surveys by outlining the creation of the SUMSS catalogue, which is similar in angular resolution and flux density limit to the NVSS catalogue. Chapter 3 will present a brief introduction to the 6dF instrument and the 6dFGS survey strategy, including the observations and data reduction pipeline. This chapter will also

discuss the technique for identification of SUMSS and NVSS radio sources in the 6dFGS primary sample as well as the method for selecting additional target galaxies. Finally, Chapter 3 will give an overview of the spectral classification of the 6dFGS-SUMSS/NVSS primary and additional target samples. In Chapter 4 the additional targets will be examined in more detail, including the quasar sample and the population of objects which may have been "missed" in the primary sample. Chapter 5 looks at the primary sample in some detail, including identifications of 6dF-NVSS primary targets in the IRAS-FSC, a determination of both the local radio luminosity function and the local fractional luminosity function of star-forming galaxies and AGNs. Chapter 6 will contain a brief study of the large-scale structure of 6dFGS-NVSS primary targets through a clustering analysis via the two-point correlation function. The thesis will be concluded in Chapter 7.

Chapter 2

The SUMSS Catalogue

The following chapter is a reproduction of the article *SUMSS: a wide-field radio imaging survey of the southern sky - II. The source catalogue*, T. Mauch, T. Murphy, H. J. Buttery, J. Curran, R. W. Hunstead, B. Piestrzynska, J. G. Robertson and E. M. Sadler, *Monthly Notices of the Royal Astronomical Society*, **342**, 1117-1130, 2003. The article was wholly written by me and I was primarily responsible for this work, the other authors contributions are as follows:

- T. Murphy wrote some early code which formed a part of the catalogue construction and helped train the decision tree.
- H. J. Buttery helped to test the catalogue and produced Figure 2.15.
- J. Curran supplied the decision tree learner and helped train the decision tree.
- R.W. Hunstead supervised the work, helped train the decision tree and meticulously edited the text.
- B. Piestrzynska reduced the survey images, ran the archive and helped train the decision tree.
- J. G. Robertson computed the model curve in Figure 2.4.
- E. M. Sadler supervised the work and helped train the decision tree.

The text is as it appears in the published article with minor changes for consistency of spelling and style.

Abstract

This paper is the second in a series describing the Sydney University Molonglo Sky Survey (SUMSS) being carried out at 843 MHz with the Molonglo Observatory Synthesis Telescope (MOST). The survey will consist of ~ 590 $4.3^\circ \times 4.3^\circ$ mosaic images with $45'' \times 45''\mathrm{cosec}|\delta|$ resolution, and a source catalogue. In this paper we describe the initial release (version 1.0) of the source catalogue consisting of 107,765 radio sources made by fitting elliptical gaussians in 271 SUMSS $4.3^\circ \times 4.3^\circ$ mosaics to a limiting peak brightness of 6 mJy beam^{-1} at $\delta \leq -50^\circ$ and 10 mJy beam^{-1} at $\delta > -50^\circ$. The catalogue covers approximately 3500 deg^2 of the southern sky with $\delta \leq -30^\circ$, about 43 per cent of the total survey area. Positions in the catalogue are accurate to within $1'' - 2''$ for sources with peak brightness $A_{843} \geq 20$ mJy beam^{-1} and are always better than $10''$. The internal flux density scale is accurate to within 3 per cent. Image artefacts have been classified using a decision tree, which correctly identifies and rejects spurious sources in over 96 per cent of cases. Analysis of the catalogue shows that it is highly uniform and is complete to 8 mJy at $\delta \leq -50^\circ$ and 18 mJy at $\delta > -50^\circ$. In this release of the catalogue about 7000 sources are found in the overlap region with the NRAO VLA Sky Survey (NVSS) at 1.4 GHz. We calculate a median spectral index of $\alpha = -0.83$ between 1.4 GHz and 843 MHz. This version of the catalogue will be released via the World Wide Web with future updates as new mosaics are released.

2.1 Introduction

Paper I of this series (Bock *et al.*, 1999) described the survey design and science goals of the Sydney University Molonglo Sky Survey (SUMSS). SUMSS is imaging the southern ($\delta < -30^\circ$) radio sky at 843 MHz with similar sensitivity and resolution to the northern NRAO VLA Sky Survey (NVSS; Condon *et al.*, 1998) at 1.4 GHz.

SUMSS uses the Molonglo Observatory Synthesis Telescope (MOST; Mills, 1981; Robertson, 1991), a 1.6 km-long cylindrical paraboloid reflector which has the largest collecting area of any telescope in the southern hemisphere. The MOST was upgraded in 1996–97 to give it a 2.7° diameter field of view (Large *et al.*, 1994; Bock *et al.*, 1999), and since mid-1997 over 90 per cent of MOST observing time has been devoted to SUMSS. The survey will be completed by the end of 2005.

In this paper, we present the first part of the SUMSS source catalogue, covering 3500 deg^2 of the southern sky. The catalogue will be updated regularly as the survey progresses, and a version is available online at www.astrop.physics.usyd.edu.au/sumsscat/.

The structure of the paper is as follows. In Section 2 we describe the software used to construct the catalogue and the procedures to construct the source list. In Section 3 we describe our technique for removing spurious responses from the catalogue. In Sections 4 and 5 we describe the uncertainties in the catalogue and its format. Finally, Section 6 contains our analysis of the catalogue.

2.2 Catalogue Construction

The individual 2.7° diameter fields of the survey are cleaned and then combined to form $4.3^\circ \times 4.3^\circ$ mosaics. The field centres are located on a grid of overlapping pointing centres such that, when combined, sensitivity is recovered in the overlap regions making the noise in the resulting mosaics almost uniform (Bock *et al.*, 1999). The mosaic centres are located on a grid which matches that for the NVSS mosaics, but is extended to the south celestial pole. This initial release of the SUMSS catalogue was built on 2003 February 25 using 271 of the ~ 590 mosaics in the complete survey. Figure 2.1 shows the positions of all 107,765 sources currently in the catalogue and gives a representation of the sky coverage of this release.

Extracting sources from astronomical images is a well documented problem and there are currently many computer programs which will find and characterise sources in images such as those in SUMSS. We decided to use the AIPS task VSAD, written for the NVSS survey (Condon *et al.*, 1998), which locates sources in an image and fits elliptical gaussians to them. This was to ensure uniformity between SUMSS and NVSS, and also because our tests showed that VSAD fitted sources more reliably than other programs such as IMSAD in the MIRIAD package (Sault *et al.*, 1995).

Most of the sources in the SUMSS survey are well fitted by an elliptical gaussian model because the majority of extragalactic radio sources are smaller than the MOST restoring beam of $45'' \times 45''\mathrm{cosec}|\delta|$ (Windhorst *et al.*, 1990). The current release of the SUMSS catalogue does not cover the Molonglo Galactic Plane Survey (MGPS-2; Green 1999) region ($|b| < 10^\circ$) because complex source structures in the Galactic plane make elliptical gaussian fits unsatisfactory. However, there is little contamination by complex Galactic sources in MGPS-2 mosaics as close to the Galactic plane as $|b| = 2^\circ$, so in the future it will be possible to visually inspect regions closer to the Galactic plane to decide those which can be included in the catalogue using current methods. In extremely complex regions we intend to crossmatch the MGPS-2 mosaics with source catalogues at other frequencies (eg. IRAS PSC; Beichman *et al.* 1988 & RASS; Voges 1993).

2.2.1 Source Fitting

VSAD was used to find radio sources in each of the $4.3^\circ \times 4.3^\circ$ mosaics in the SUMSS survey and fit an elliptical gaussian to them. The parameters of each gaussian returned by VSAD are the J2000 right ascension α and declination δ (both in degrees), peak brightness A_{843} (mJy beam^{-1}), total flux density S_{843} (mJy), FWHM fitted source major and minor axes $\theta_{\rm M}, \theta_{\rm m}$ (arcseconds) and the fitted position angle of the major axis (degrees east from north). VSAD also creates a residual image by subtracting each fitted gaussian from the input image.

Figure 2.2 shows a small region of an illustrative SUMSS mosaic (J0000M84[1]) overlaid with the gaussians fitted by VSAD. Most sources in the original mosaic are well fitted

[1]The naming scheme for SUMSS mosaics is J$hhmm$Mdd where J signifies J2000 coordinates, $hhmm$ is the RA in hours and minutes of the mosaic centre, M signifies southern declination and dd is the declination of the mosaic centre in degrees. This is similar to the NVSS mosaic naming convention

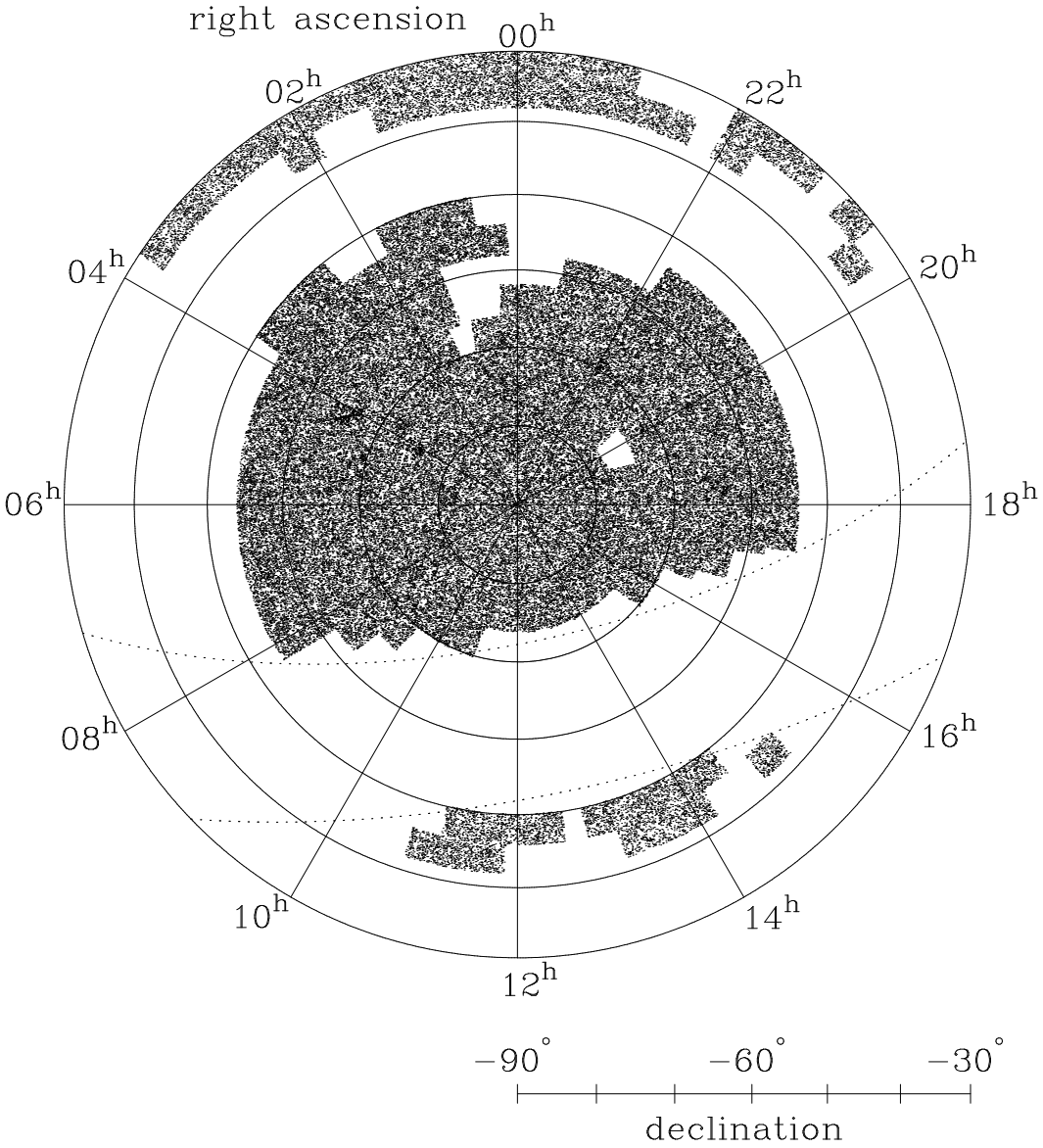

Figure 2.1 A plot in the equal-area Lambert projection of all 107,765 sources in the 271 mosaics in version 1.0 of the SUMSS catalogue. The total sky coverage is 3500 deg^2. Dotted lines are drawn at $b = \pm 10^\circ$ to indicate the location of the Galactic plane. The source density is lower at declinations north of -50° due to the higher flux density limit ($S_{843\mathrm{MHz}} \geq 10\,\mathrm{mJy}$). There is a significant underdensity of sources around $\delta = -45^\circ, \alpha = 13h$; this is because of the large number of artefacts in the vicinity of Centaurus A, which obscure weak sources.

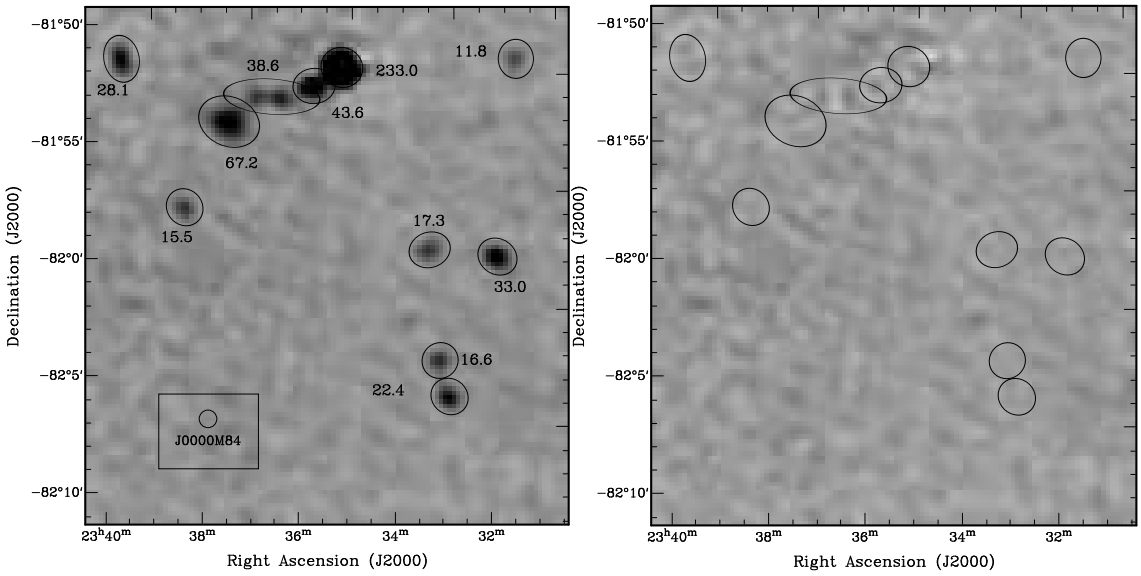

Figure 2.2 Left: A small section of the mosaic J0000M84 with ellipses fitted by VSAD. The total flux density (in mJy) of each source is printed beside it. The beam is shown as a small circle on the bottom left of the image. One close double is fitted as a single gaussian, while another is fitted as two. Right: The residual image of the same region after subtraction of the fitted gaussians. The improperly fitted source in the north has resulted in residual flux in this image.

by gaussians, though some artefacts close to stronger sources are also fitted. It can be seen from the complex structure in Figure 2.2 that in extreme cases VSAD can be unreliable for close pairs of sources. Occasionally two distinct sources are fitted incorrectly as a single gaussian with major axis greater than the true separation of the sources (eg. the 38.6 mJy extended source in Figure 2.2.). Almost all close doubles remain in the final version of the catalogue as separate sources.

2.2.2 Noise

Even though the field tiling patterns were designed to make the resulting noise in the mosaics uniform, background noise is higher in localised regions close to strong sources. We determined the rms noise in the SUMSS survey to establish a threshold below which sources are discarded from the catalogue. The residual images created by VSAD were kept and used to estimate the local rms noise for each source. Two estimates of the rms noise were obtained:

1. First the noise was estimated over each residual image by fitting a normal curve to the pixel distribution giving an estimate of the average noise over the area of each entire mosaic. Figure 2.3 shows the distribution of rms values obtained in this way. The median rms noise of the mosaics at $\delta \leq -50^\circ$ is 1.27 mJy beam^{-1}. For $\delta > -50^\circ$ the scatter is much greater as the rms noise increases strongly with declination north of -50° (see Figure 2.4). The median value of rms noise at $\delta >$

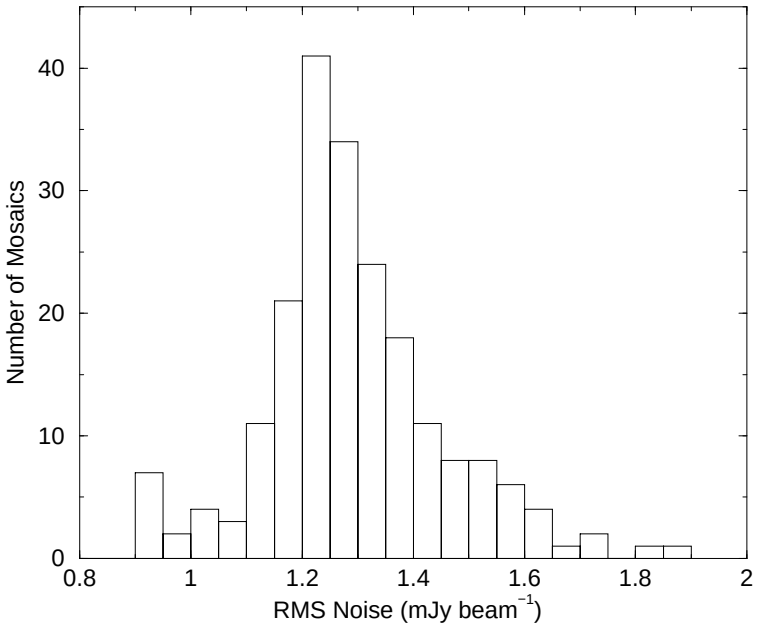

Figure 2.3 A histogram of the rms noise measured in the mosaics at $\delta \leq -50^\circ$. Most of the mosaics have rms values $\sim 1.2 - 1.3$ mJy beam^{-1}; the mode is 1.25 mJy beam^{-1}. The tail at higher rms values is due to mosaics containing bright sources which tend to increase the local rms noise.

-50° is 1.9 mJy beam^{-1}. Hereafter we refer to regions at $\delta \leq -50^\circ$ as southern and those $\delta > -50^\circ$ as northern.

2. Secondly, a local rms for each source was determined by computing a pixel histogram in a box of 100×100 pixels ($\sim$600 beams) in the residual image and fitting a normal curve to this distribution. The distribution was clipped so as to only include pixels within ± 5 times the rms noise measured in the mosaics. Residual artefacts from strong sources tend to increase the estimate of local rms noise. By this method we have an estimate of the local rms noise for each source which takes into account increases in the noise level close to bright sources. Values of local rms noise close to bright sources are 3–4 times greater than those in other regions, because of the limited dynamic range $(\sim 100 : 1)$ of the MOST (Bock *et al.*, 1999).

Figure 2.4 shows the variation in local rms noise with declination for stronger sources $(S_{843} > 50\,\mathrm{mJy})$ in the present survey release. The gain of the MOST varies with Meridian Distance[2] (MD) due to a number of factors arising from the structure of the telescope. For example the $\mathrm{cosec}|\delta|$-shaped rise toward northern declinations is due to the foreshortening of the MOST at large $|\mathrm{MD}|$. A model of the rms noise variation with declination is plotted. This was determined by summing the noise variance as a function of hour angle, taking into account the variation of noise due to the MOST MD gain curve. This curve matches the observed rms noise variation quite well.

[2]The Meridian Distance (MD) at declination δ and hour angle H is given by $\sin(\mathrm{MD}) \approx \cos\delta \sin H$. This is explained in more detail in Paper I (Bock *et al.*, 1999).

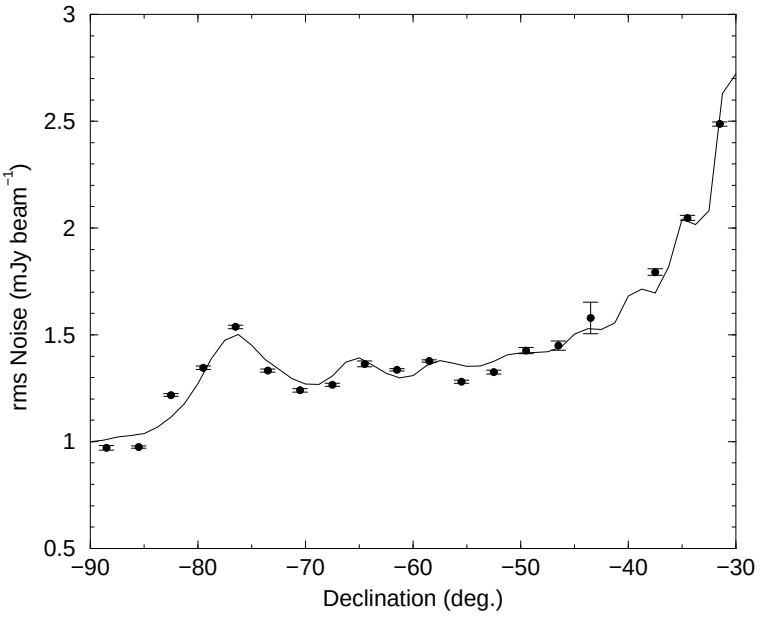

Figure 2.4 A plot of median rms noise computed around brighter sources ($S_{843} > 50\,\mathrm{mJy}$) vs. declination. The line drawn is a model based on the MOST MD gain curve. It is shown to indicate the effect of the variation of the MOST gain with declination. The noise peak at $\delta = -76^\circ$ is explained by this curve. The rms noise increases sharply north of $\delta \sim -50^\circ$, which is the declination above which we increase the brightness limit of the catalogue to $10\,\mathrm{mJy\,beam^{-1}}$.

VSAD was used to fit all peaks brighter than 5 mJy beam^{-1} at $\delta \leq -50^\circ$ and 10 mJy beam^{-1} at $\delta > -50^\circ$. Typically about 400 gaussians were fitted in each northern mosaic and about 700 in each southern one. VSAD fitted many noise peaks and artefacts in the southern mosaics between 5 and 6 mJy beam^{-1}. We decided to set the catalogue limit at 6 mJy beam^{-1} at $\delta \leq -50^\circ$ and 10 mJy beam^{-1} at $\delta > -50^\circ$. This limit represents a $\sim 4.7\sigma$ to $\sim 5.3\sigma$ cutoff for the catalogue. A limit of less than 5σ can lead to unreliable radio source identifications (Murdoch *et al.*, 1973). Our method of dealing with unreliable identifications is outlined in section 2.3.2.

2.2.3 Duplicate Sources

The VSAD routine was run separately on each mosaic resulting in a total list of 171,846 responses over the 3500 deg^2 of survey area currently complete. This list was then pruned to remove multiple entries and spurious sources arising from image artefacts. The SUMSS survey was designed such that the mosaics created from the individual observations overlapped slightly (Bock *et al.*, 1999). This overlap changes with declination from about 50 per cent at $\delta = -88^\circ$ to 1–2 per cent at $\delta = -32^\circ$. Therefore some entries in the total list are multiple occurrences of sources which have appeared in overlapping mosaics.

Figure 2.5 is a plot of the distribution of source separations for a subset of about 40,000 sources in the raw catalogue. The distribution has a minimum at $45''$ after which

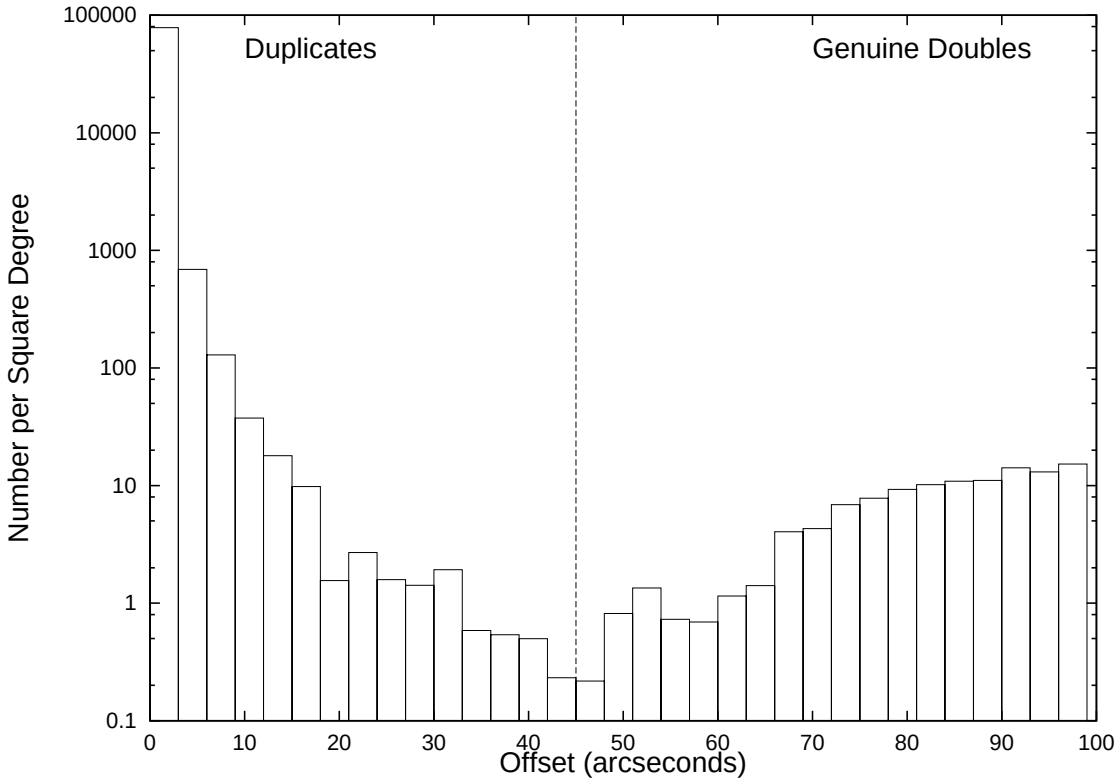

Figure 2.5 The distribution of source separations for the raw version of the SUMSS catalogue. The number of sources found at different radii has been divided by the sky area to obtain the source density versus separation. The minimum at about 45″ is taken as the separation beyond which the number of close doubles dominates over the number of duplicates. There is a small number of sources with separations between $45''$ and $75''$; these are the result of overlapping gaussians fitted by VSAD. Above $80''$ the distribution flattens as expected.

the contribution of genuine close doubles causes it to rise again. This minimum is not surprising given that the beamwidth of the survey is $\sim 45''$. Sources appearing in different mosaics with position differences less than 45″ were flagged as possible duplicates.

Once a group of duplicate sources has been identified the following criteria are used to select which source to retain from that group:

1. If there are more than two sources then the peak amplitudes of all the sources are compared and those with peak amplitude greater than twice or less than half the average are ignored. This can occur when some artefacts are fitted at the position of another source.
2. Sources closer than 10 pixels from the edge of a mosaic are ignored to ensure that extended sources are not fitted over the edge of the image. If all sources are further than 10 pixels from the edge then option (3) is used.
3. If there is still more than one source to select, the source with the lowest local rms noise has its fitted parameters recorded in the catalogue.

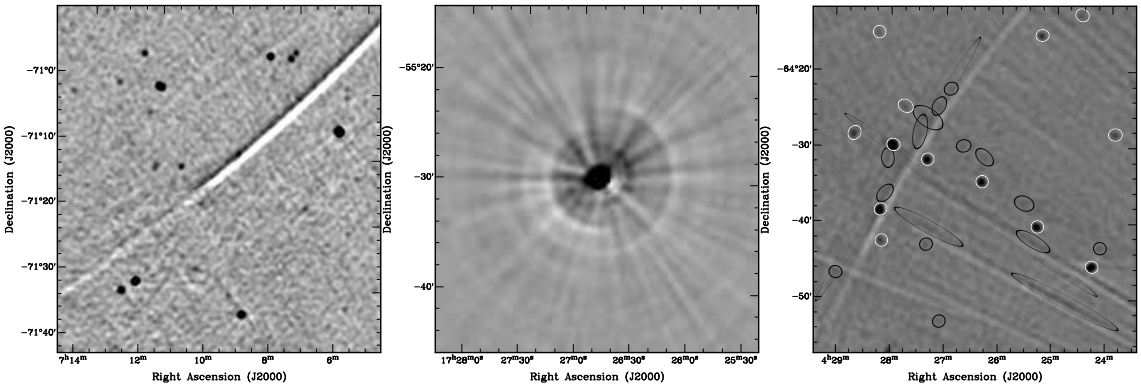

Figure 2.6 Three images showing the variety of artefacts present in SUMSS mosaics which are fitted as spurious sources by VSAD. The left image shows part of a grating ring associated with a 5.46 Jy source (PKS B0743–673) at RA $= 07^{\rm h}\,43^{\rm m}\,32\overset{\rm s}{.}67$, Dec. $= -67^\circ\,26'\,28\overset{''}{.}4$ (J2000). Its sudden weakening occurs because the ring appears in different parts of two 2.7° fields which make up the mosaic. The middle image shows a 1.8 Jy source and the radial spikes associated with it. The spikes here have peak amplitude of 10 mJy beam^{-1} and extend about $30'$ away from the source. The right image shows a small area of the SUMSS mosaic J2100M72 with many artefacts. Radial spokes of average peak amplitude ~ 6 mJy beam^{-1} are visible, as is a weak grating ring. Ellipses fitted by VSAD are overlaid on the image. Sources classified by the decision tree as artefacts are shown as black ellipses and sources classified as genuine are shown as white ellipses.

These criteria ensure that one source is selected out of a set of multiple detections. Fits to duplicate sources are not independent as they all have the same underlying 2.7° fields contributing to them. Therefore no signal-to-noise increase will be gained by simply averaging their fitted parameters. Generally only two sources need to be compared and the one with the lower local rms noise is placed in the catalogue. A flag telling how many other mosaics the selected source appears in is included in the final catalogue. The source which is listed in the catalogue can be considered the best-fitting source from VSAD. In compiling the current version of the catalogue, about 45,000 sources were removed because they appear more than once in the raw catalogue.

2.3 Image Artefacts

The images in SUMSS are affected by a number of artefacts, many of which are fitted by the VSAD routine as sources. Classification of artefacts is a difficult problem, as they vary enough in shape and strength that no simple method can be used to separate them from real sources. The images in Figure 2.6 show the variety of artefacts in SUMSS images and some examples of elliptical gaussians which VSAD has fitted to them. About 10 per cent of sources in the raw SUMSS catalogue are fits to artefacts.

2.3.1 Types of Artefacts

There are two common artefacts which are fitted as genuine sources by VSAD, *grating rings* and *radial spokes*.

Grating rings arise from the periodic structure of the MOST array. They appear as ellipses of semi-diameter $n(1.15^\circ \times 1.15^\circ \mathrm{cosec}|\delta|)$ where n is an integer denoting the order of the grating ring. Grating rings increase in strength up to the fourth order ring. While grating rings are not uniquely a problem of the MOST, it is not possible to remove them using the standard CLEAN routine. This is because the effective primary beam of the MOST varies with time and is not azimuthally symmetric. Also individual baseline visibilities are not recorded during MOST observations (Mills, 1981; Robertson, 1991). It is possible that in future an improved CLEAN routine might be written to remove grating rings by accurately modelling the MOST primary beam. The future upgrade of the telescope as an SKA demonstrator (SKAMP; Green *et al.*, 2001) will eliminate this problem, as all the baseline visibilities will be retained with each observation and application of self calibration algorithms will be possible. The amplitude of grating rings is also dependent on the position of the source in the original SUMSS field so the mosaicing process can cause abrupt steps in their strength. This effect can be seen in the leftmost image of Figure 2.6, where a strong fourth-order grating ring associated with a 5.4 Jy source abruptly becomes weaker.

Radial spokes appear as long thin bands stretching away radially from a source. They are believed to be caused by random shifts of order $1''$ in the position of the comb of MOST fan beams, on a time-scale of minutes (Bock *et al.*, 1999). The shifts are believed to occur due to weather related anomalies in the local oscillator phase or irregularities in ionospheric or tropospheric refraction. Some radial spokes are shown in the middle image of Figure 2.6 and almost always appear as highly elongated sources in the output of VSAD. Generally such artefacts are only fitted close to sources with peak brightness greater than 500 mJy beam^{-1}, because the peak amplitude of radial spokes then becomes stronger than 6 mJy beam^{-1}. The source density close to extremely bright sources in SUMSS can decrease substantially as radial spokes can raise the local rms noise level by up to 3-4 times.

2.3.2 Response Classification with a Decision Tree

The variety and complexity of artefacts fitted as sources make it difficult to classify sources as genuine or spurious in a simple way. We have employed the *decision tree* program C4.5 (Quinlan, 1993) to aid in the classification of sources in the mosaics. A decision tree encodes a classification function as a hierarchy of tests which classify examples into different classes. Each example consists of a set of attributes, each with an associated value.

The tree represents the classification function as follows:

1. Every internal node corresponds to a test examining one or more attributes of the example to be classified.

Table 2.1 Confusion matrices comparing decision tree classification with hand classification. Left: Results of southern decision tree on test data. Right: Results of northern decision tree on test data.

Southern				Northern			
Class	(decision tree)			Class	(decision tree)		
(hand)	(1)	(2)	(3)	(hand)	(1)	(2)	(3)
(1)	12		5	(1)	3	1	1
(2)	1	2		(2)	2	1	
(3)	1	3	618	(3)	3		415

2. Each branch descending from the node corresponds to a particular outcome of the test.
3. Finally, the leaf nodes in the tree are labelled with the class to assign.

C4.5 is a popular, freely available decision tree learner. Another application of a decision tree to radio source catalogues can be found in the FIRST survey (White *et al.*, 1997).

The raw output from VSAD includes about 39 source characteristics which can be used as attributes for the decision tree; these include the fitted and deconvolved source sizes and the raw fitting uncertainties quoted by VSAD. We have also included some extra parameters mainly relating each fitted source to the nearest strong source, including separation and relative position angle. Because of the different properties of the MOST beam in the two regions, we made two separate decision trees, one for the southern catalogue $\delta \leq -50^\circ$ and one for the northern catalogue $\delta > -50^\circ$.

The decision tree program was trained by hand on a subset of mosaics with many artefacts. About 3000 sources in the south and about 1500 sources in the north were hand classified. To ensure that the training was reliable, each source was examined separately by at least two of us, and the final decision on each source was made by one of us (Mauch) comparing the two human classifications, thereby minimising the subjective judgement of each human classifier. About 10 per cent of human classifications were changed during comparison. The objects contained in the raw output of VSAD were classified using a numbering scheme from 1-3 with the following definitions.

(1). The source is an artefact.

(2). The source is in a region of high noise.

(3). The source is real.

The decision tree was then run and the result for both the northern and southern decision trees was tested on a small independent sample of hand classified sources from one mosaic. Table 2.1 shows the results from this test. It can be seen from analysis of the training data that artefacts tend to be correctly identified. In some cases a hand classified type 1 source is machine classified as type 2 and vice versa but it is rare for sources

hand classified as 1 or 2 to be machine classified as genuine. Conversely only a small number of type 3 sources have been classified as artefacts. This does have an effect on the completeness of the survey at flux densities of 6–10 mJy (Figures 2.11 & 2.15 in Section 2.6 show this more clearly). Overall the accuracy of the decision tree on the testing data is conservatively estimated to be 96 per cent. The accuracy for the entire catalogue is probably a little lower, but most of the misclassified sources are real sources which were classified as artefacts. This implies that the final version of the catalogue should be very reliable.

The decision tree was found to be least reliable for extended sources with major axis length greater than five times their minor axis length. Every such source classified as genuine by the decision tree was double checked by hand. About 10 per cent of these classifications were found to be incorrect.

The final released catalogue only contains sources classified as genuine by the decision tree. The unmodified catalogue contains 10 per cent extra sources, most of which are artefacts. This larger (but less reliable) catalogue with an extra column containing decision tree classifications, will be available on request.

2.4 Accuracy

All of the uncertainties calculated in the catalogue are a combination of both fitting and calibration uncertainties of the MOST. In general the calibration uncertainties of the MOST are small and the fitting uncertainties tend to dominate. Fitting uncertainties for the SUMSS catalogue were determined using equations derived in Condon (1997) (hereafter C97). The noise in SUMSS mosaics is correlated at the length scale of the restoring beam of MOST. As this beam is elliptical, the axis length of the restoring beam was taken as the noise correlation length in SUMSS, $\theta_{\rm N}^2 = b_{\rm M} b_{\rm m} = 45'' {\rm cosec}|\delta| \times 45''$; where $b_{\rm M}, b_{\rm m}$ are widths of the MOST beam major and minor axes respectively. This implies that the effective signal-to-noise ratio (ρ) is given by:

$$\rho^2 = \frac{\theta_{\rm M}\theta_{\rm m}}{4\theta_{\rm N}^2}\left[1+\left(\frac{\theta_{\rm N}}{\theta_{\rm M}}\right)^2\right]^{\alpha_{\rm M}}\left[1+\left(\frac{\theta_{\rm N}}{\theta_{\rm m}}\right)^2\right]^{\alpha_{\rm m}}\frac{A_{843}^2}{\sigma^2}, \tag{2.1}$$

where $\theta_{\rm M}$ is the fitted major axis size and $\theta_{\rm m}$ is the fitted minor axis size. A_{843} is the peak brightness of the fitted Gaussian and σ is the rms noise of each mosaic (C97); σ is taken to be the local rms noise as derived in Section 2.2.1. For the uncertainties in each fitted parameter we have used the same empirical values for the exponents $\alpha_{\rm M}$ and $\alpha_{\rm m}$ taken from C97 and also used in the NVSS source catalogue (Condon *et al.*, 1998).

2.4.1 Position Uncertainties

The fitting variances in the source positions are given by:

$$\sigma_\alpha^2 = \sigma_{\rm M}^2 \sin^2({\rm PA_F}) + \sigma_{\rm m}^2 \cos^2({\rm PA_F}), \tag{2.2}$$

$$\sigma_\delta^2 = \sigma_{\rm M}^2 \cos^2\left({\rm PA_F}\right) + \sigma_{\rm m}^2 \sin^2\left({\rm PA_F}\right), \tag{2.3}$$

where the rms noiselike uncertainties of the fitted major and minor axes $\sigma_{\rm M}$ and $\sigma_{\rm m}$ are derived as in equation 25 of C97. $\rm PA_F$ is the fitted position angle of the source in degrees east of north. The fitting uncertainties become quite large ($\sim 5''$) for weaker extended sources ($A_{843} < 10\,{\rm mJy\,beam^{-1}}$).

For sources with $S_{843} \geq 50\,{\rm mJy}$ the calibration uncertainty of the MOST is greater than the fitting uncertainties. We have determined the calibration uncertainty for stronger sources ($S_{843} > 200\,{\rm mJy}$) by comparison with positions in the NVSS catalogue in the overlap region between SUMSS and NVSS ($-40^\circ < \delta < -30^\circ$; $464\,{\rm deg^2}$ in the current release). The positions of strong sources in the NVSS catalogue are known to be accurate to within ($\epsilon_\alpha, \epsilon_\delta$)=($0\farcs45, 0\farcs56$) (Condon *et al.*, 1998). Only point sources in SUMSS were used in this comparison to avoid the larger position uncertainties associated with extended sources. There are about 500 SUMSS sources which meet these criteria in the overlap region, all of which have a counterpart in the NVSS catalogue. Figure 2.7 contains a plot of the offsets in Right Ascension ($\Delta\alpha$) and Declination ($\Delta\delta$) between NVSS and SUMSS. The mean offsets are $\langle\Delta\alpha\rangle = -0\farcs59 \pm 0\farcs07$ and $\langle\Delta\delta\rangle = -0\farcs30 \pm 0\farcs08$. These offsets are caused by a combination of both calibration errors in individual fields and fitting errors. It is unknown if the offsets are caused by errors in the NVSS or SUMSS catalogues and it is most likely that they are a combination of errors in both. Therefore no correction has been applied to positions in the final version of the catalogue. For more information about SUMSS position uncertainties, see Paper I (Bock *et al.*, 1999).

The rms of the offsets between the SUMSS and NVSS catalogues have been used to determine the SUMSS position calibration uncertainties. These are $\epsilon_\alpha = 1\farcs5$ for Right Ascension and $\epsilon_\delta = 1\farcs7$ for Declination. The elongation of the MOST beam at $\delta \geq -40^\circ$ means the rms in declination is larger than in the southern catalogue, implying that these values are a conservative estimate of the MOST position uncertainty in declination. The calibration uncertainties quoted here have been added in quadrature to the fitting uncertainties for each source to obtain the position uncertainties in the catalogue.

2.4.2 Source Sizes

The uncertainties in the axes of the elliptical gaussians fitted by VSAD ($\sigma(\theta_{\rm M}), \sigma(\theta_{\rm m})$) are determined by combining in quadrature equation 21 of C97 and the calibration uncertainty in the major and minor axes of the MOST beam shape. The MOST beam calibration uncertainty has been determined by examining fits to moderately strong sources believed to be unresolved. Because fits to the strongest sources with $S_{843} > 500\,{\rm mJy}$ could be contaminated by image artefacts, only moderately strong (100 mJy$< S_{843} <$500 mJy) sources were chosen. From this analysis we have conservatively estimated the beam calibration uncertainty to be $\epsilon_\theta \leq 3$ per cent in both axes. The uncertainty is worst in the northern mosaics in which the beam is considerably elongated. The probability that the fitted size of a point source would be larger than the beam by more than $2.33\sigma(\theta_{\rm M,m})$ is 2 per cent so we compare the beam plus $2.33\sigma(\theta_{\rm M,m})$ with the major and minor fitted axis lengths to determine if a source is resolved along either axis.

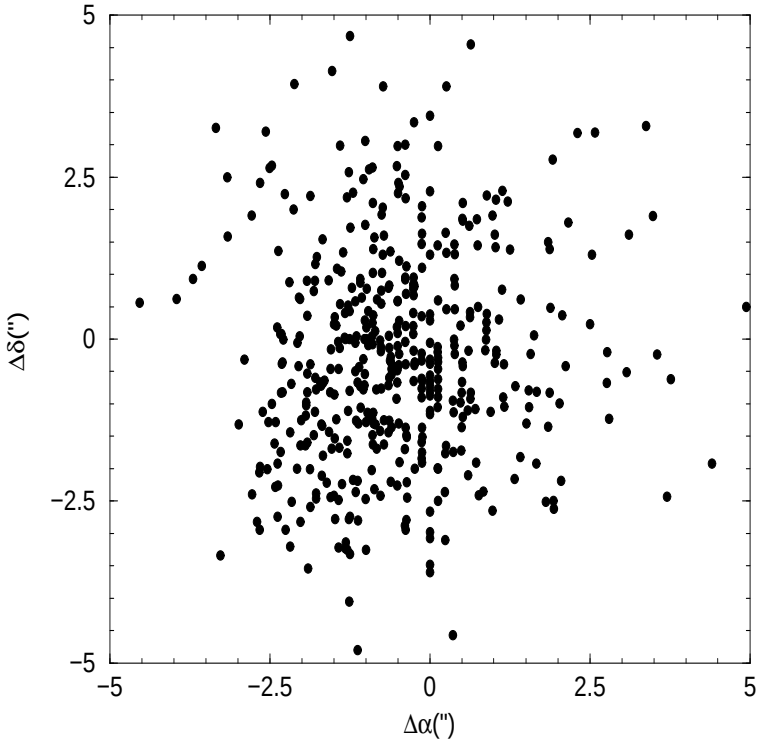

Figure 2.7 A plot of the offset (SUMSS position minus NVSS position) in both Right Ascension (α) and Declination (δ) between 500 bright point sources in the overlap region between SUMSS and NVSS.

Sources for which either the major axis or both fitted axes are believed to be resolved are then deconvolved along each resolved axis. The fitted gaussians in the raw output of VSAD are the convolution of the MOST elliptical beam with the true source shape. The deconvolved major and minor axis widths of each fitted source $(\phi_{\rm M}, \phi_{\rm m})$ were found using

$$2\phi_{\rm M}^2 = (\theta_{\rm M}^2 + \theta_{\rm m}^2) - (b_{\rm M}^2 + b_{\rm m}^2) + \beta, \tag{2.4}$$

$$2\phi_{\rm m}^2 = (\theta_{\rm M}^2 + \theta_{\rm m}^2) - (b_{\rm M}^2 + b_{\rm m}^2) - \beta, \tag{2.5}$$

where $\theta_{\rm M}, \theta_{\rm m}$ are the fitted major & minor axes of the source, $b_{\rm M}, b_{\rm m}$ are the beam major & minor axes and β is given by

$$\begin{aligned}\beta^2 = {} & (\theta_{\rm M}^2 - \theta_{\rm m}^2)^2 + (b_{\rm M}^2 - b_{\rm m}^2)^2 - \\ & 2(\theta_{\rm M}^2 - \theta_{\rm m}^2)(b_{\rm M}^2 - b_{\rm m}^2)\cos 2\left({\rm PA_F} - {\rm PA_B}\right),\end{aligned} \tag{2.6}$$

where $\rm PA_F$ and $\rm PA_B$ are the position angles of the fitted source and the MOST beam (Wild, 1970). The MOST beam is oriented north-south so ${\rm PA_B} = 0$ always.

The ellipticity of the MOST beam causes the fitted position angle to differ from the true source position angle ($\rm PA_S$). We find the deconvolved major axis position angle using

$$\tan\left(2{\rm PA_S}\right) = \left[\frac{(\theta_{\rm M}^2 - \theta_{\rm m}^2)\sin 2{\rm PA_F}}{(\theta_{\rm M}^2 - \theta_{\rm m}^2)\cos 2{\rm PA_F} - (b_{\rm M}^2 - b_{\rm m}^2)}\right]. \tag{2.7}$$

Table 2.2 Measurements of Molonglo Calibrators.

Calibrator[a] Name	α (B1950)[a] $h\ m\ s$	δ (B1950)[a] $^\circ\ '\ ''$	S_{843} Nominal[a] (Jy)	S_{843} Measured[b] (Jy)	$\sigma_{\rm rms}$[c] per cent of Measured
0252–712	02 52 26.63	−71 16 47.3	9.21	9.13 ± 0.01	2.1
0409–752	04 09 58.45	−75 15 05.7	19.80	20.21 ± 0.03	2.4
0420–625	04 20 18.61	−62 30 40.9	5.62	5.49 ± 0.02	2.8
1814–519	18 14 07.92	−51 59 20.0	6.51	6.55 ± 0.02	3.7
1814–637	18 14 45.94	−63 47 03.1	20.22	20.04 ± 0.05	3.6
1827–360	18 27 36.86	−36 04 38.1	13.86	13.72 ± 0.06	3.6
2323–407	23 23 51.69	−40 43 48.8	5.21	5.16 ± 0.03	3.8

NOTES:
[a]The source names, positions and values of nominal flux density are taken from Campbell-Wilson & Hunstead (1994).
[b]The values of measured flux density have been corrected for effects described in Gaensler & Hunstead (2000) and are average measured values for the 12-year period.
[c]The rms in flux density measurements as a percentage of measured flux density from observations, used to define the calibration uncertainty of the MOST.

A deconvolved source size is quoted for each resolved source in the catalogue. No source sizes are given for unresolved sources. It should be noted that the fitted source sizes and deconvolved source sizes in the catalogue are only intended to be indicative of the true source structure. Sometimes more extended sources are the result of a poor fit by the VSAD program (see Figure 2.2) and the original images are the best guide in determining whether or not a given radio source is resolved.

2.4.3 Flux Density

The uncertainties in the fitted peak brightness in SUMSS images are calculated as the quadratic sum of the MOST internal flux density calibration uncertainty and the local noise uncertainty. The local noise uncertainty is calculated using

$$\sigma^2_{A_{843}} = \frac{A^2_{843}}{\rho^2}, \tag{2.8}$$

where $\alpha_M = \alpha_m = 3/2$ was used in the calculation of ρ^2 from Equation 2.1 (Condon *et al.*, 1998).

To calculate the flux density calibration uncertainty of the MOST we used results from a detailed analysis of the Molonglo calibrators (Gaensler & Hunstead, 2000). Before and after every 12-hour observation the MOST measures the flux densities of $\sim$5 compact sources, chosen from a list of 55 calibrators. Observations of the calibrators in the period 1984 to 1996 have been extracted from the MOST archive and used to determine the calibration uncertainty of the MOST. Gaensler & Hunstead (2000) examined the variability of the calibrators in this period and found that 19 of these showed no variability in this

time. We have chosen 7 of the non-variable calibrators with flux densities > 5 Jy which were observed at a meridian distance $|\mathrm{MD}| < 30^\circ$ to ensure that errors resulting from fan-beam confusion and uncertainty in the meridian distance gain curve at higher MD were minimised. Table 2.2 shows the results of this analysis.

The average scatter in flux density measurements $\epsilon_{A_{843}}$ is around 3 per cent. We have adopted this value as the internal calibration uncertainty of MOST peak brightness measurements. Peak brightness uncertainties in the catalogue are obtained by adding $\epsilon_{A_{843}} A_{843}$ and $\sigma_{A_{843}}$ in quadrature.

The integrated flux density of each source is calculated from the parameters of the gaussian fit and depends on whether or not the source is significantly resolved. We use the same equations to derive the total flux density as those described for NVSS (Condon *et al.*, 1998). The fitting uncertainties in integrated flux density are the same as those quoted in C97.

The quoted flux density uncertainties do not take account of the errors which arise from fitting an extended gaussian to a source with complex structure. Extended sources are often fitted poorly by an elliptical gaussian model and this can lead to unreliable estimates of the true integrated flux density. Users should therefore note that for some extended sources the quoted flux density and source sizes will be incorrect by more than the quoted uncertainties.

The flux density scale at 843 MHz was determined partly by absolute measurements and partly by interpolation between measurements at 408 MHz (Molonglo) and 2700 MHz (Parkes) (Hunstead, 1991). To check the accuracy of the total flux densities quoted in the SUMSS catalogue we have examined the distribution of spectral indices between the SUMSS catalogue at 843 MHz and the NVSS catalogue at 1.4 GHz. Flux densities in the NVSS catalogue are known to be accurate to 2 per cent, given the same caveats associated with VSAD explained in this paper (Condon *et al.*, 1998). Figure 2.8 shows the distribution of spectral index (α)[3] between SUMSS and NVSS in three flux density bins. This was determined by crossmatching all sources in the SUMSS-NVSS overlap region ($-40^\circ \leq \delta \leq -30^\circ$) with position offset no greater than $30''$ and only a single match within $100''$. This resulted in 7643 matches. The overall median spectral index is -0.83, which is consistent with previous determinations of spectral index at frequencies below 1.4 GHz (Oort *et al.*, 1988; Hunstead, 1991; De Breuck *et al.*, 2000). A tail of flat spectrum ($\alpha \sim 0$) sources (probably QSOs) can be seen in the top panel. The FWHM of the distributions increases from 0.7 in the upper panel to 1.2 in the lower panel reflecting the increasing uncertainty in flux density for $S_{843} < 20$ mJy. The steep and flat spectrum tails ($\alpha < -2.0$ and $\alpha > 1.0$ respectively) in the bottom panel were checked visually and found to be due to fitting errors and erroneous flux densities in both NVSS and SUMSS.

[3]In this paper we define spectral index α to be $S_\nu \propto \nu^\alpha$

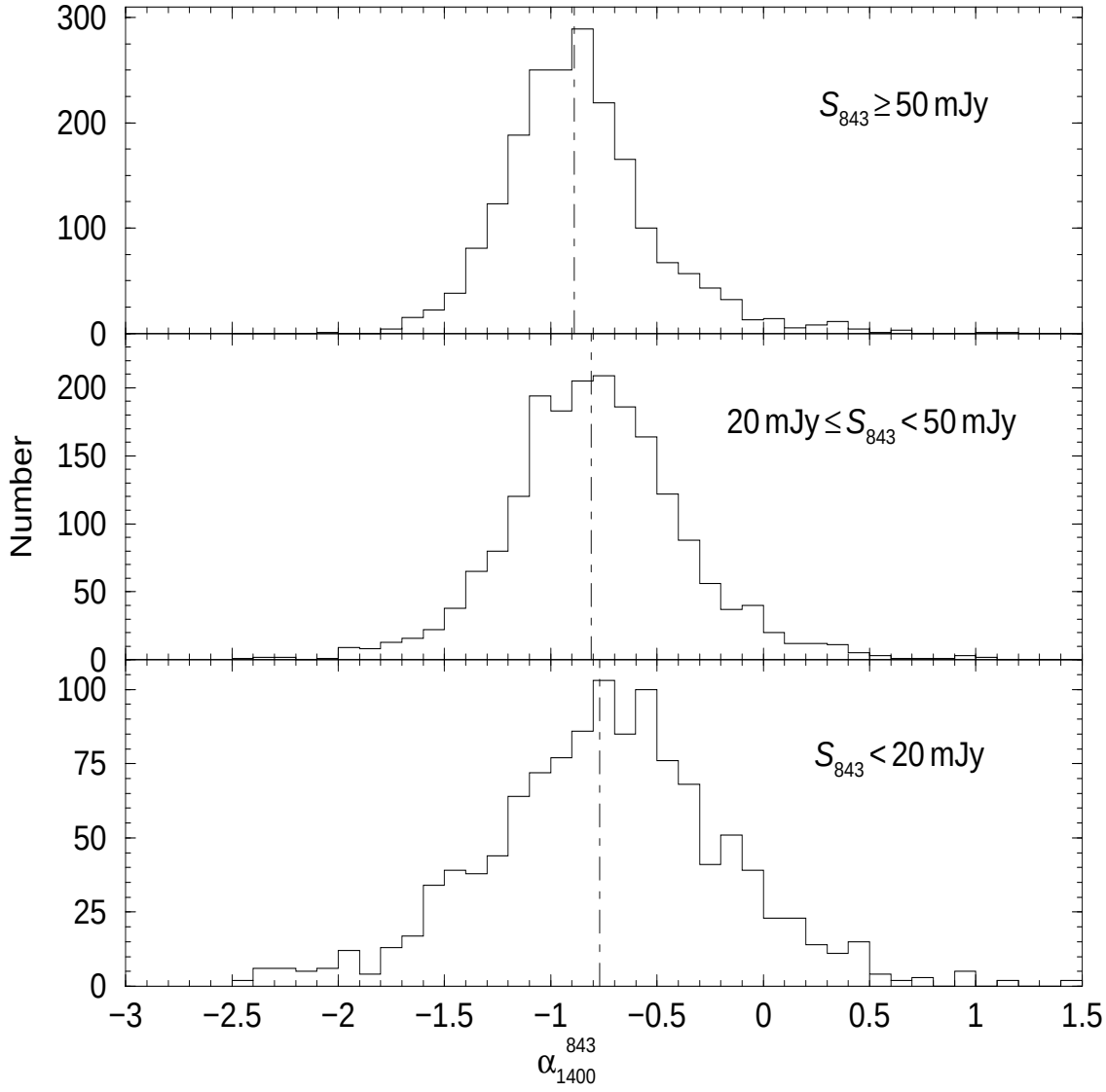

Figure 2.8 The spectral index distribution in the NVSS-SUMSS overlap region binned into three flux density ranges. A dotted line showing the median spectral index in each flux density bin is shown. The median spectral index increases from -0.89 at $S_{843} \geq 50$ mJy to -0.77 at $S_{843} < 20$ mJy. A tail of flat spectrum sources can be seen for $S_{843} \geq 50$ mJy. The scatter in the spectral index increases with decreasing flux density.

2.5 Catalogue Format

Table 2.3 shows the format of the SUMSS catalogue. The catalogue will be available as a large text file accessible via the web. A short description of each of the columns of the catalogue follows.

Columns (1) & (2): The right ascension (α) and declination (δ) of the source in J2000 coordinates.
Column (3): The uncertainty in Right Ascension in seconds of arc, calculated from the quadratic sum of the MOST Right Ascension calibration uncertainty $(1\farcs1)$ and equation 2.2.
Column (4): The uncertainty in Declination in seconds of arc, calculated from the quadratic sum of the MOST Declination calibration uncertainty $(1\farcs6)$ and equation 2.3.
Column (5): The peak brightness in units of mJy beam^{-1} and its associated uncertainty calculated from the quadratic sum of equation 2.8 and the MOST flux density calibration uncertainty of 3 per cent.
Column (6): The total flux density in units of mJy and its associated uncertainty, calculated from the equations described in C97.
Columns (7) & (8): The fitted major & minor axes of the source in arcseconds.
Column (9): The fitted major axis position angle of the source in degrees east of north. Most unresolved sources would have PA values close to 0° or 180° since the MOST elliptical beam has PA=0.
Column (10): If the fitted major axis size exceeds the beam size by more than $2.33\sigma(\theta_{\rm M})$, the major axis size after deconvolution from the MOST beam is given in arcseconds.
Column (11): If the major axis is resolved the minor axis is subsequently checked using the same criterion. If the minor axis is found to be resolved the deconvolved minor axis size is given in arcseconds.
Column (12): If the major axis is resolved, its deconvolved position angle in degrees east from north is given.
Column (13): The name of the mosaic in which the source appears. The original mosaics are available online at http://www.astrop.physics.usyd.edu.au/mosaics. In the case of duplicate matches the mosaic name quoted is that used for the fit which is chosen to be included in the catalogue.
Column (14): The number of mosaics in which the source appears. This is included to let the user know when the source appears in more than one image. The source parameters which appear in the catalogue are those for the most reliable fit.
Columns (15) & (16): The X & Y pixel positions of the source on the quoted mosaic.

Please refer to SUMSS catalogue sources by their full IAU designations (Lortet *et al.*, 1994). These are of the form SUMSS *JHHMMSS−DDMMSS* where SUMSS is the survey acronym, *J* specifies J2000.0 coordinate equinox, *HHMMSS* are the hours, minutes and truncated seconds of right ascension, $-$ is the sign of declination and *DDMMSS* are the degrees, minutes and truncated seconds of declination. For example the SUMSS source in Table 2.3 at J2000.0 coordinates $\alpha = 00^h00^m08\fs89,\ \ \delta = -71°00'19\farcs76$ is called SUMSS J000008−710019.

Table 2.3 The First Page of the SUMSS Catalogue.

(1) α (J2000) $h\ m\ s$	(2) δ (J2000) $^\circ\ '\ ''$	(3) $\Delta\alpha$ $''$	(4) $\Delta\delta$ $''$	(5) A_{843}^{a} mJy beam^{-1}	σ_A	(6) S_{843}^{b} mJy	σ_S	(7) $\theta_{\rm M}{}^{c}$ $''$	(8) $\theta_{\rm m}{}^{c}$ $''$	(9) $\rm PA_F{}^{c,d}$ $^\circ$	(10) $\phi_{\rm M}{}^{e}$ $''$	(11) $\phi_{\rm m}{}^{e}$ $''$	(12) $\rm PA_S{}^{d,e}$ $^\circ$	(13) Mosaic[f]	(14) #[f]	(15) X-Pixel	(16) Y-Pixel
00 00 00.00	−31 09 52.24	4.4	4.6	12.1	1.4	13.8	1.6	84.9	58.4	41.3	0.0	0.0	- - -	J0000M32	1	705.0	518.9
00 00 02.31	−37 08 00.38	2.3	3.4	13.2	1.2	13.3	1.2	76.6	45.3	177.2	0.0	0.0	- - -	J0000M36	1	702.5	197.0
00 00 03.28	−75 01 02.93	1.8	2.1	29.4	1.5	33.0	1.7	58.6	45.0	5.4	35.8	0.0	5.9	J0000M76	1	703.8	996.0
00 00 03.29	−66 05 43.51	1.7	1.8	25.6	1.0	25.7	1.0	50.1	45.0	90.7	0.0	0.0	- - -	J0000M64	2	703.2	17.8
00 00 04.14	−64 19 06.06	3.5	3.9	7.4	0.9	7.4	0.9	50.1	45.1	173.1	0.0	0.0	- - -	J0000M64	1	702.6	540.4
00 00 04.61	−75 12 43.42	4.3	4.8	9.7	1.4	11.4	1.6	57.4	50.1	16.1	0.0	0.0	- - -	J0000M76	1	703.4	934.2
00 00 06.14	−29 55 10.49	4.5	7.6	11.8	2.1	13.1	2.3	93.0	51.0	169.4	0.0	0.0	- - -	J0000M32	1	697.7	734.7
00 00 06.39	−34 19 06.49	4.0	5.8	10.4	1.6	10.9	1.7	76.6	49.5	11.6	0.0	0.0	- - -	J0000M36	1	697.8	738.4
00 00 06.39	−63 11 52.08	1.8	1.8	34.0	1.3	43.8	1.7	75.9	49.5	67.2	60.6	0.0	69.9	J0000M64	1	701.1	870.0
00 00 06.43	−69 25 35.54	1.5	1.7	118.9	3.6	118.9	3.6	48.6	45.0	91.6	0.0	0.0	- - -	J0000M68	1	701.9	221.2
00 00 07.78	−70 21 10.15	1.9	2.1	18.2	0.9	18.2	0.9	47.3	45.3	17.9	0.0	0.0	- - -	J0000M72	1	701.4	1182.6
00 00 07.96	−72 36 43.24	2.2	2.3	14.2	0.9	14.5	0.9	48.0	46.0	38.7	0.0	0.0	- - -	J0000M72	1	701.8	479.5
00 00 08.22	−37 38 19.61	3.1	3.3	18.1	1.5	20.8	1.7	76.6	59.9	41.6	0.0	0.0	- - -	J0000M36	1	696.1	99.8
00 00 08.89	−71 00 19.76	2.3	2.5	13.2	0.9	13.3	0.9	47.3	45.6	151.2	0.0	0.0	- - -	J0000M72	1	701.1	979.5
00 00 09.90	−31 33 30.53	1.6	2.1	44.7	2.0	44.7	2.0	84.9	45.1	0.9	0.0	0.0	- - -	J0000M32	1	693.5	450.6
00 00 10.70	−63 04 14.09	2.8	2.9	11.3	1.0	13.0	1.1	62.4	47.6	42.1	0.0	0.0	- - -	J0000M64	1	698.4	907.4
00 00 10.86	−72 12 53.71	1.7	1.9	25.0	1.1	25.2	1.1	47.3	45.5	119.1	0.0	0.0	- - -	J0000M72	1	700.5	603.1
00 00 11.43	−85 39 20.09	1.5	1.7	101.6	3.1	102.9	3.2	46.3	45.2	65.9	0.0	0.0	- - -	J0000M84	3	703.8	162.2
00 00 11.82	−82 47 32.39	1.7	1.8	74.4	2.7	101.0	3.7	69.0	54.4	66.9	52.3	30.2	67.2	J0000M84	1	703.0	1094.0
00 00 11.93	−66 30 45.94	1.5	1.7	93.5	2.9	98.2	3.1	53.0	45.4	5.7	21.4	0.0	10.1	J0000M68	1	698.5	1105.2
00 00 13.15	−63 34 57.29	3.6	3.5	10.3	1.0	13.4	1.4	79.8	48.2	48.8	0.0	0.0	- - -	J0000M64	1	697.0	756.8
00 00 13.17	−72 59 54.71	1.8	1.9	28.1	1.2	29.9	1.3	51.2	47.2	103.6	0.0	0.0	- - -	J0000M72	1	699.7	359.2
00 00 13.29	−35 55 20.96	3.8	3.1	12.2	1.3	12.6	1.3	76.6	48.3	63.2	0.0	0.0	- - -	J0000M36	1	690.3	429.9
00 00 14.02	−34 10 00.23	1.7	2.0	65.4	2.5	77.0	3.0	76.6	62.4	150.2	0.0	0.0	- - -	J0000M36	1	689.2	767.6
00 00 15.68	−76 56 30.59	1.5	1.7	84.5	2.7	86.3	2.8	48.3	45.1	11.9	0.0	0.0	- - -	J0000M76	1	700.2	384.9
00 00 15.77	−33 12 21.60	3.2	2.3	17.0	1.4	17.1	1.4	84.9	45.7	78.0	0.0	0.0	- - -	J0000M32	1	687.0	164.9
00 00 15.86	−70 49 28.88	2.8	3.2	10.0	1.0	10.5	1.0	52.0	45.2	14.1	0.0	0.0	- - -	J0000M72	1	697.9	1035.8
00 00 17.30	−82 40 59.16	2.2	2.3	23.8	1.5	23.8	1.5	45.2	45.0	65.8	0.0	0.0	- - -	J0000M84	1	702.0	1129.6
00 00 17.37	−37 28 25.07	2.8	4.2	11.2	1.3	11.3	1.3	76.6	45.7	4.3	0.0	0.0	- - -	J0000M36	1	686.2	131.6
00 00 17.76	−34 10 40.26	1.6	1.7	126.4	4.1	132.4	4.3	76.6	49.4	116.7	0.0	0.0	- - -	J0000M36	1	685.0	765.5
00 00 17.84	−35 18 07.16	4.0	3.7	14.5	1.5	16.3	1.7	76.6	57.1	122.0	0.0	0.0	- - -	J0000M36	1	685.1	549.3
00 00 17.94	−37 21 00.68	3.0	3.5	16.7	1.4	19.3	1.6	76.6	59.9	154.1	0.0	0.0	- - -	J0000M36	1	685.6	155.3

NOTES:

[a] The peak brightness of the gaussian fit in units of mJy beam^{-1}. This value may be in error by more than the quoted error for extended sources.

[b] The total flux density of the gaussian fit in units of mJy. $S = A$ for point sources.

[c] The widths and position angle of the fitted gaussian. The fit is constrained so that $\theta_{\rm m} \geq 45''$ (the beam minor axis width).

[d] The position angle of the major axis is measured in degrees East from North.

[e] The deconvolved widths and position angle of the source. A value is given only if the fitted axis exceeds the beam by more than $2.33\sigma_\theta$

[f] The name of the mosaic the quoted source can be found in. If the number in the next column is greater than 1 it can also be found in neighbouring mosaics.

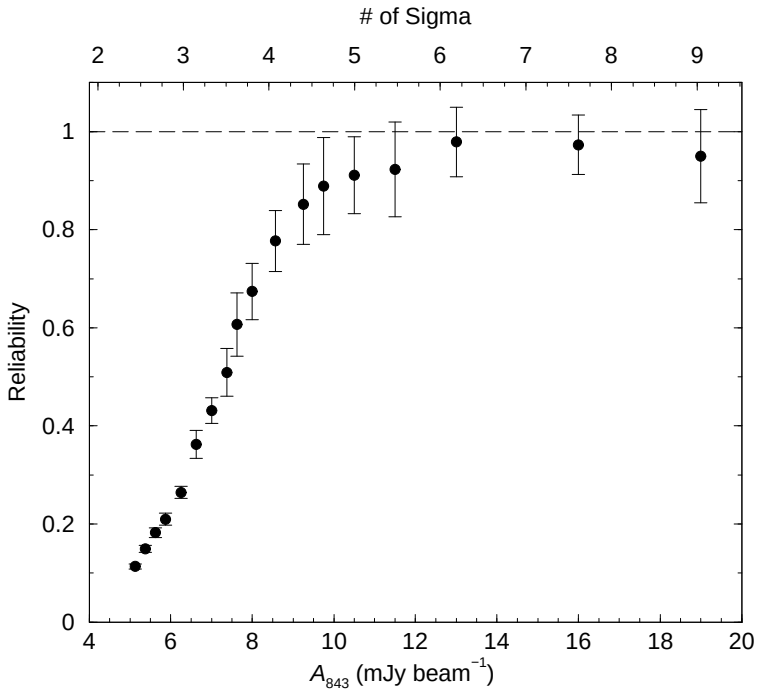

Figure 2.9 The fraction of SUMSS sources detected in the NVSS catalogue vs. peak flux density. At the catalogue limit of 10 mJy beam^{-1} about 90 per cent of SUMSS sources are detected in NVSS. Sigma has been calculated as the median local rms noise of all sources in this plot (1σ=2.1 mJy beam^{-1}). At these flux densities the NVSS is also about 90 per cent reliable.

2.6 Analysis

The following section contains results of our analysis of the catalogue. Our goal in producing the SUMSS catalogue has been to create a source list which is as reliable as possible. This implies that all the sources which appear should be genuine. In this section we also examine the uniformity of the catalogue. An adequate determination of 843 MHz source counts and the two-point angular correlation function will require a catalogue with uniform source density (Blake & Wall, 2002). Finally the SUMSS catalogue is compared with catalogues at other frequencies as an independent check of the accuracy of quoted source characteristics.

2.6.1 Reliability and Completeness

The rms noise level in SUMSS mosaics is not uniform across the survey. It can increase substantially close to bright sources and changes strongly with declination (see Figure 2.4). In surveys with uniform noise levels a 5σ limiting amplitude is applied to catalogues made from them (Murdoch *et al.*, 1973). As the noise is not uniform in SUMSS the limiting peak amplitude varies from 4σ to 6σ depending on the position of each source in the survey.

To estimate how the SUMSS catalogue reliability varies with amplitude we have searched 5 northern mosaics down to 2σ and crossmatched all fitted sources with the NVSS. The NVSS is believed to be better than 90 per cent reliable at flux densities above 5 mJy at 1.4 GHz (Condon *et al.*, 1998) and so should be a good independent check of the reliability of SUMSS. We define the reliability at amplitude A_{843} as the number of SUMSS sources with an NVSS counterpart within $50''$ divided by the total number of SUMSS sources. There is about a 3 per cent chance of an NVSS position being within $50''$ of a random SUMSS noise peak.

Figure 2.9 shows a plot of the reliability of SUMSS as a function of peak flux density. At the 4σ level, the catalogue is still around 80 per cent reliable and this increases to 90 per cent at around 4.5σ. The SUMSS catalogue is therefore still reliable below 5σ, predominantly because the decision tree is trained to remove spurious responses.

Fitting errors and confusion in the MOST beam can affect the completeness of the catalogue at fainter flux densities. The decision tree is geared toward removing poorly fitted sources at lower flux density and this may also affect the completeness. We have attempted to determine the completeness of the SUMSS catalogue by running simulations. We placed 1000 artificial point sources of varying flux density into a selection of mosaics and performed the normal cataloguing procedures on them.

Figure 2.10 shows the fraction of artificial point sources which were catalogued vs. flux density. In fitting the 1000 point sources no particular biases were evident. The shape of the distributions is quite different for northern and southern mosaics. For southern mosaics the plot shows that the SUMSS catalogue is ~ 60 per cent complete at the limiting flux density of 6 mJy and this increases to 100 per cent at 8 mJy. For northern mosaics the catalogue is ~ 40 per cent complete at 10 mJy and 100 per cent complete at 18 mJy. The more extended distribution in the northern catalogue is because the mosaics here are noisier and the beam is larger, resulting in greater confusion. The decision tree has had no significant detrimental effect on the completeness for point sources. This is because artefacts generally mimic extended sources and the decision tree tends to remove extended sources at lower flux density rather than point sources.

2.6.2 Source Density

Table 4 of Paper I (Bock *et al.*, 1999) shows integral source counts at 843MHz taken from (Large, 1990) and we are now able to compare the source counts in that table with those derived in the SUMSS survey. The source density has been determined from a selection of non-overlapping mosaics in the catalogue and the results of this analysis are shown in Figure 2.11. To examine the effect of the decision tree on the source density, we have plotted the source density both before and after its application. The source density derived from the raw catalogue will contain artefacts as well as real sources while the classified catalogue should only have real sources, although some real sources may have been erroneously removed by the decision tree.

For $S_{843} \geq 6$ mJy Large (1990) estimated an 843 MHz source density of 31 ± 3 sources deg^{-2}. Figure 2.11 (left) shows the source density in southern mosaics limited to peak brightness $A_{843} \geq 6\,\mathrm{mJy\,beam^{-1}}$. The distribution before application of the deci-

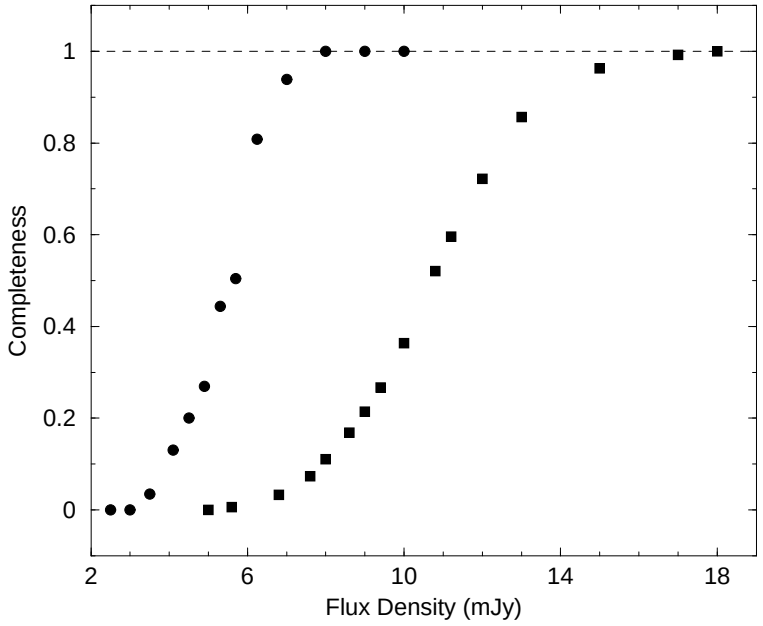

Figure 2.10 The fraction of artificial point sources which are catalogued vs. Flux Density. The circles are for southern mosaics ($\delta \leq -50°$) and the squares are for northern ones ($\delta > -50°$). A dashed line at 100 per cent is shown. At 6mJy (the limit of the southern catalogue) the completeness for southern mosaics is around 60 per cent and this rises rapidly to 100 per cent at 8 mJy. At 10 mJy the completeness for the northern catalogue is about 40 per cent. The northern catalogue is 100 per cent complete above about 18 mJy.

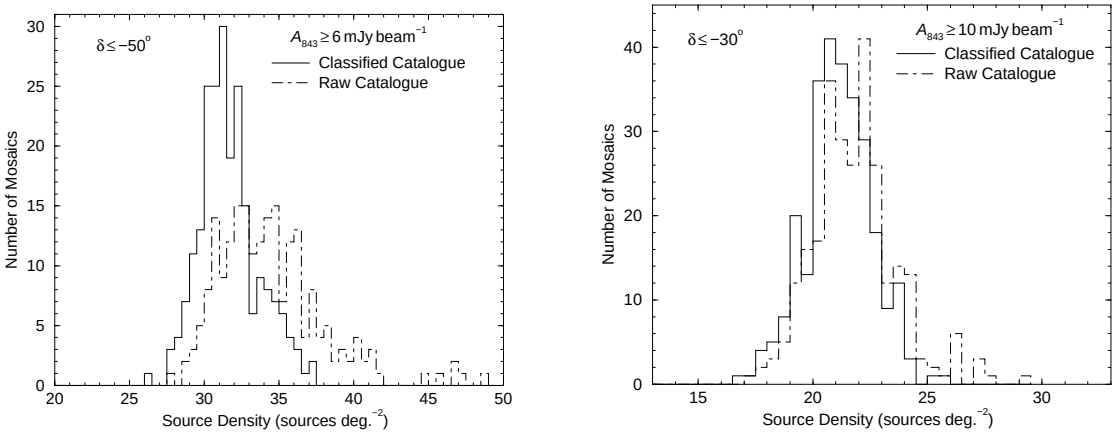

Figure 2.11 Histograms showing the source density of the SUMSS catalogue before and after the application of the decision tree. The source density was calculated for each mosaic and a random selection of non-overlapping mosaics was chosen so as to keep the data independent. The plot on the left is for southern sources with $A_{843} \geq 6$ mJy beam^{-1}. Northern and southern sources are grouped in the plot on the right, which shows the source density for sources with $A_{843} \geq 10$ mJy beam^{-1}.

sion tree has an average of 36.3 ± 0.6 sources deg^{-2} and, after classification, 31.6 ± 0.1 deg^{-2}. Outliers in the distribution are attributed to mosaics with strong sources which produce many artefacts. In the raw catalogue these artefacts are fitted as sources, producing an increased source density for that mosaic. In the classified catalogue, the source density is not uniform because the local rms noise close to strong sources is higher than in other regions.

The effect of the decision tree is less pronounced at $A_{843} \geq 10$ mJy beam^{-1}. Large (1990) determined a source density of 21 ± 2 deg^{-2}. The plot on the right in Figure 2.11 shows the distribution of source densities in the same set of southern mosaics with the addition of non-overlapping northern mosaics with $A_{843} \geq 10\,\mathrm{mJy\,beam^{-1}}$. For $A_{843} \geq 10$ mJy beam^{-1} the distribution is very similar for both the raw and classified catalogues and indicates that our decision tree is predominantly affecting sources of peak brightness less than 10 mJy beam^{-1} (see Figure 2.15). The average source density for the raw catalogue is 22.1 ± 0.2 deg^{-2} and the average for the classified catalogue is 21.1 ± 0.1 deg^{-2}.

Our results are in good agreement with those derived by Large (1990) from a much smaller survey area. One important aspect of the distribution of source density in the classified catalogue is that there is less scatter between mosaics after the application of the decision tree. This indicates that the decision tree is making the catalogue more uniform.

The rms scatter about the mean of 21.1 deg^{-2} for the surface densities of the 190 $4.3^\circ \times 4.3^\circ$ mosiacs in the right panel of Figure 2.11 is 1.42 deg^{-2}. The expected Poisson statistical error in the surface density is 1.54 deg^{-2}, only slightly greater than the observed value. This result is indicative of the homogeneity of radio sources over the 4.3° scale of SUMSS mosaics.

Figure 2.12 shows the variation of source density in the catalogue with declination. This has been determined for three different flux density cutoffs ($A_{843} \geq$6 mJy beam^{-1}, $A_{843} \geq$10 mJy beam^{-1} & $S_{843} \geq$20 mJy). The lines in the plot are the values of source density from Large (1990) for the three flux density cutoffs. We expect the SUMSS catalogue to be 100 per cent complete above 20 mJy so we directly compare the counts for integrated flux density with those quoted by Large (1990). We believe the source counts quoted by Large (1990) may have been underestimated due to the small area of sky used (about 28 deg^2).

Figure 2.12 is similar to that made for the NVSS survey by Blake & Wall (2002) but does not show the same scatter evident in their results. Blake & Wall (2002) attributed their results to the change from the DnC to the D configuration of the VLA for the NVSS survey at different declinations. No such change takes place on the MOST, thereby resulting in a survey which is more uniform with declination, especially at flux densities greater than 10mJy.

2.6.3 SUMSS–MRC Crossmatch

As a separate check of the catalogue completeness for brighter sources, the SUMSS catalogue was crossmatched with the Molonglo Reference Catalogue (MRC; Large *et al.* 1981, 1991). The MRC was made from $2\farcm62 \times 2\farcm86 \sec(\delta + 35\fdg5)$ resolution observa-

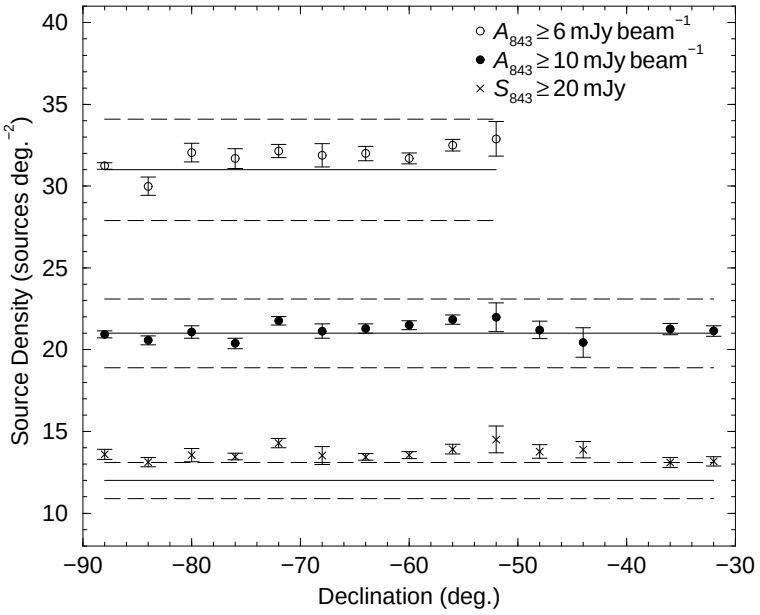

Figure 2.12 The variation in source density with declination for different flux density limits shows little scatter across the survey. This is primarily because the telescope does not change its configuration at different declinations. The lines are the values of source count values from Large (1990) with their associated 10 per cent uncertainty. A peak brightness cutoff was applied at both 10 and 6 mJy beam^{-1} and a total flux density cutoff was applied at 20 mJy, where we expect the catalogue to be complete.

Table 2.4 MRC sources missing from the SUMSS catalogue

MRC Name	α (J2000)	δ (J2000)	S_{408}
	$h\ m\ s$	$^\circ\ '\ ''$	Jy
MRC B0536−692[1]	05 36 20.7	−69 12 15	1.03
MRC B0540−697[1]	05 39 58.5	−69 45 00	2.22
MRC B1737−602	17 42 02.9	−60 15 54	0.80
MRC B1754−577[2]	17 59 05.2	−57 42 20	1.21
MRC B1817−632[2]	18 22 16.0	−63 10 41	0.90
MRC B2220−700	22 24 39.6	−69 47 42	0.73

NOTES:
[1] H II regions located in the LMC.
[2] Spurious north-south sidelobes of the Mills Cross.

tions at 408 MHz using the Molonglo Cross Radio Telescope (Mills *et al.*, 1963), the previous incarnation of the MOST. The MRC is complete to $S_{408} = 1\,\mathrm{Jy}$ at 408 MHz and has a (non-uniform) limiting flux density of $S_{408} = 0.7\,\mathrm{Jy}$. Given a spectral index of $\alpha = -0.8$ we expect the faintest MRC sources to appear in the SUMSS catalogue at around $S_{843} = 400$ mJy and certainly no fainter than $S_{843} = 150\,\mathrm{mJy}$. This implies that all MRC sources should appear in the SUMSS catalogue.

There are 1670 MRC sources in the area covered by the SUMSS catalogue. Of these only 46 were found not to have a match within 60″ in SUMSS. Upon closer inspection it was revealed that many of these initial non-detections were actually sources which were resolved into doubles in SUMSS; for these sources there are two entries in the SUMSS catalogue around 100″ from the single source in the MRC. Of the sources which are detected, we determine a median spectral index between 408 MHz and 843 MHz of $\alpha = -0.95$.

Two of the missing MRC sources (Centaurus A & NGC 5090) were found to be fitted quite badly by VSAD. Fits to these sources were modified. They have not been assigned a peak amplitude or source size, only a position and total flux density. The total flux density of these sources has been determined by summing the pixels inside a hand defined source area using the CGCURS routine in MIRIAD. We may add other complex sources by hand in future releases of the catalogue.

The MRC other sources not detected in SUMSS are tabulated in Table 2.4. Some of the sources are H II regions in the Large Magellanic Cloud which, although point sources in the MRC, appear quite complex in the smaller MOST beam. Elliptical gaussians fitted to these sources were automatically removed by the decision tree and have been left out of the catalogue.

The four sources away from the Clouds are particularly interesting. The positions of these sources have been inspected in the original SUMSS images and are not detected at even a 3σ limit. Two of the sources, MRC B1817–632 and MRC B1754–577 were observed with the Australia Telescope Compact Array at 1.4 GHz and no source was detected to a 3σ limit of 0.5 mJy at the MRC positions. All of the original 408 MHz data obtained with the Molonglo Cross telescope are currently being reprocessed by D. Crawford (private communication) and from this reprocessing a new deeper 408 MHz catalogue is being produced. Examination of the reprocessed data has revealed that both MRC B1817−632 and MRC B1754−577 appear to be anomalous north-south sidelobes. However, the other two sources (MRC B1737−602 and MRC B2220−700) appear to be genuine in the 408 MHz catalogue. A $b_J = 16.75$ magnitude galaxy is located at the position of MRC B2220−700. Given that no feasible radio spectrum could result in a flux density of ~ 1 Jy at 408 MHz dropping to less than ~ 10 mJy at 843 MHz it is probable that these objects are transient phenomena.

2.6.4 Resolved Sources

In the current release of the SUMSS catalogue about 10 per cent of sources are found to be resolved. This fraction varies from 25 per cent at $\delta = -88^\circ$ to 2 per cent at $\delta = -32^\circ$ where the beam area is almost doubled. Almost all resolved sources are extended in only

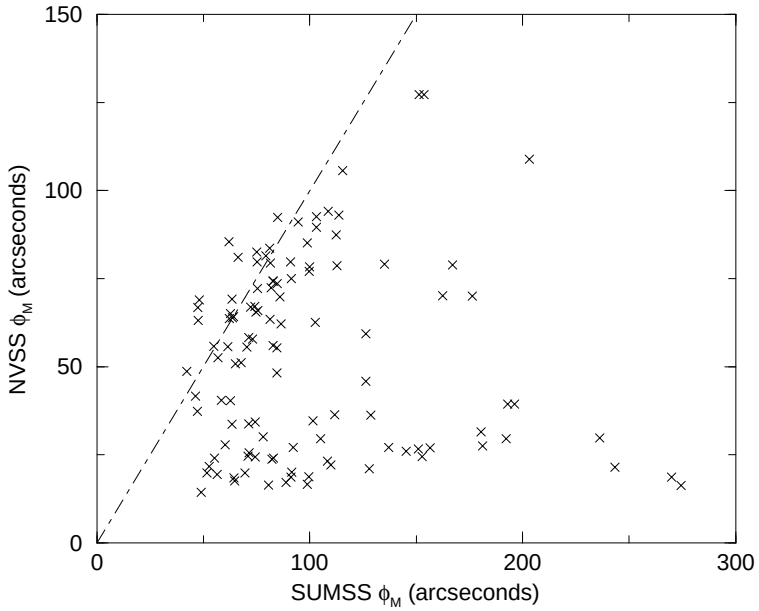

Figure 2.13 The distribution of major axis lengths in SUMSS and NVSS. There is a class of SUMSS sources with large angular sizes which appear to be barely resolved in NVSS. This is due to a mixture of fitting problems in VSAD and the increased surface brightness sensitivity of the MOST. A small number of sources which are fitted as one elongated gaussian in SUMSS are fitted as two separate unresolved components in the NVSS, this is because of the larger MOST beam.

one direction; only 1 per cent of sources are resolved in both axes.

To check the accuracy of deconvolved source sizes in the SUMSS catalogue, sizes and position angles of resolved sources were compared with the sizes of resolved sources in the NVSS catalogue. Almost all sources found to be resolved in SUMSS were also resolved in the NVSS; the small fraction that were not were attributed to the effects described below.

A comparison of the source widths in SUMSS and NVSS is shown in Figure 2.13. For about half of the sources the major axis widths agree well between the two surveys. However, there is a substantial group of sources which has a larger major axis in SUMSS. Many of these sources seem to be fitted accurately by VSAD and probably form a class of objects in which much of their structure has been resolved out in the NVSS images, but is preserved in the SUMSS survey. This is because of the continuous UV coverage of the MOST (Bock *et al.*, 1999). Visual inspection of other sources reveals some of them are poorly fitted by the VSAD program, as illustrated in Figure 2.2. These sources are all genuinely resolved close doubles but VSAD has fitted a gaussian of major axis much longer than the source. Figure 2.14 shows the distribution of position angles between sources in the two surveys, these are generally in reasonable agreement given the very different raw beamshapes.

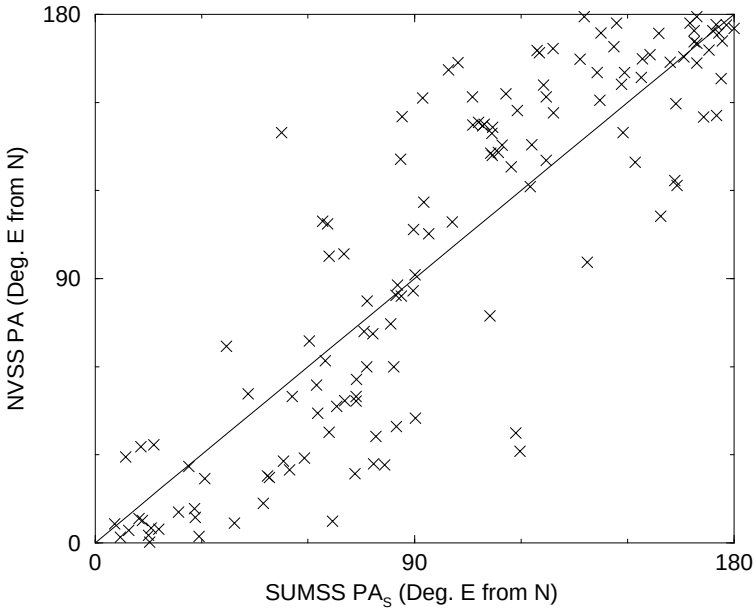

Figure 2.14 The distribution of position angles of resolved sources in SUMSS and NVSS. There is a general agreement in position angle between the two surveys. Sources with position angles close to 0° in one survey can sometimes be found close to 180° in the other.

2.6.5 Source Counts

Figure 2.15 shows the differential source counts in the southern part of the SUMSS catalogue normalised to a euclidean universe. The source counts shown here are plotted using peak amplitudes and are used to show the effectiveness of the decision tree. The true source counts at 843 MHz should resemble those shown here fairly closely as only 10 per cent of sources in the catalogue are resolved. Also, no account is made here for the decrease in source density close to brighter sources. A more thorough source count determination will follow in a later paper.

The effect of the decision tree is quite pronounced in this plot. Artefacts cause the source counts to tail upwards below about 10 mJy beam^{-1}. The decision tree is affecting the counts below this level, causing the counts to flatten to the same slope as that above 10 mJy beam^{-1}. This suggests that the decision tree is doing an excellent job of removing artefacts. Users should note that the decision tree is having its greatest effect below 10 mJy beam^{-1}, so above this level the catalogue is mostly unaltered from its raw state.

2.7 Summary

We have created a catalogue of 107,765 sources over the 3500 deg^2 of the SUMSS survey currently available. It is expected the survey will be complete by early 2006. We will endeavour to update the catalogue as new mosaics are released. The survey is currently progressing at the rate of $1500\,\mathrm{deg}^2$ per year and we expect the coverage of the catalogue

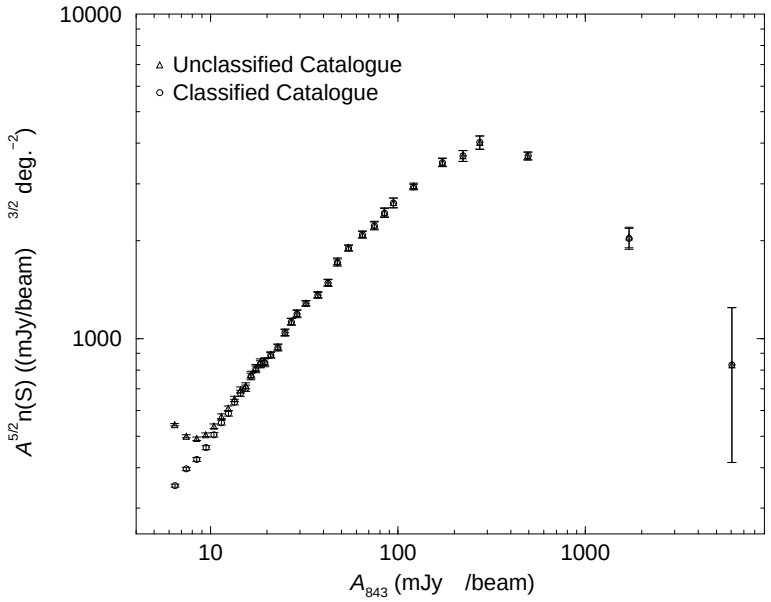

Figure 2.15 The normalised source counts derived from peak amplitude for the southern part of the catalogue. As most sources in the survey are unresolved this determination should closely resemble the counts for total flux density. The counts in the catalogue before and after application of the decision tree are presented. Artefacts are affecting the decision tree at flux density levels below 10 mJy beam^{-1} and the decision tree is restoring the counts to the slope which is expected in this region.

to increase at a similar rate. As coverage gaps in the survey are filled positions and flux densities at the edges of currently released regions may change due to the increased sensitivity from overlapping fields. We will maintain backups of each release of the catalogue so that users may continue to have access to versions of the catalogue they may previously have used.

We believe the southern catalogue to be close to 100 per cent complete above $\sim$8 mJy and the northern catalogue to be complete above $\sim$18 mJy. Below these flux densities, confusion, noise and the decision tree have affected the completeness, but we expect the catalogue to be highly reliable. The catalogue has a source density of 32 deg^{-2} above 6 mJy beam^{-1} and 21 deg^{-2} above 10 mJy beam^{-1}. Users should note that some sources (especially those which are resolved) may have positions and flux densities outside the quoted uncertainties. Users are encouraged to check the $4.3^\circ \times 4.3^\circ$ mosaics if in doubt.

The catalogue is publicly available and the current version as well as future updates can be found at www.astrop.physics.usyd.edu.au/sumsscat/.

Acknowledgements

The Molonglo Observatory site manager, Duncan Campbell-Wilson, and the staff, Jeff Webb, Michael White and John Barry are responsible for the smooth operation of the MOST telescope and the day to day observing program of the SUMSS survey. For this

we give them heartfelt thanks. Bruce McAdam and Tony Turtle provided valuable information on artefacts in MOST images and deconvolution. Tony Turtle is also responsible for SUMSS scheduling. The SUMSS survey is dedicated to Michael Large whose expertise and vision made the project possible. We would also like to thank the referee J. Condon for some useful suggestions. The MOST is operated with the support of the Australian Research Council and the Science Foundation for Physics within the University of Sydney.

Chapter 3

Radio Sources in the 6 degree Field Galaxy Survey

This chapter presents a short introduction to the 6 degree Field observing facility on the UK Schmidt Telescope. It also introduces the sample selection methodology for primary and additional targets from SUMSS and NVSS. Finally the spectral classification criteria are presented. The 6dF instrument was commissioned by Dr Will Saunders during 2001-2002 and subsequent survey observations have been carried out by the observing team at the UK Schmidt telescope which consists of Dr Fred Watson, Malcolm Hartley, Paul Cass, Dionne James, Ken Russell and Kristin Fiegert. Data is reduced using the `6dfdr` package and redshifts of the observed objects determined using the `runz` package. The data reduction is performed by a team led by Dr Heath Jones at the Research School of Astronomy and Astrophysics at the Australian National University. Reduced 6dFGS data have all been obtained from the public 6dFGS database hosted at the Wide Field Astronomy Unit at the Institute for Astronomy, University of Edinburgh and maintained by Dr Mike Reid (www-wfau.roe.ac.uk/6dFGS/). NVSS catalogue data and images have been obtained from the public database at www.cv.nrao.edu/nvss. Over the course of my PhD my contribution as a member of the 6dF team is as follows.

- I spent 2 months at the UK Schmidt telescope first in May 2001 and again in November 2001 helping with the commissioning of the 6dF instrument.
- During my second stay at the UK Schmidt in November 2001 I helped with testing of the reduction packages `6dfdr` and `runz`.
- Over the course of my PhD leading up to the 6dFGS first data release I redshifted about 100 6dFGS fields, corresponding to about 10 000 redshifts which have formed a part of the 6dFGS first public data release.
- I provided a list of some 10 000 identifications of NVSS and SUMSS radio sources which form the additional target sample discussed in this thesis. This data is available from the 6dFGS public database under programme ID 125.

Also, much of the text in Section 3.5.3 was published in the February 2002 Anglo Australian Observatory Newsletter (Mauch, 2002), an article for which I was the sole author.

3.1 Introduction

The last five to ten years has seen an explosion in the amount of redshift survey data coming from optical telescopes. The 2 degree Field Galaxy Redshift Survey (2dFGRS) has measured more than 240 000 spectra over a small region of sky (Colless *et al.*, 2001) and the Sloan Digitised Sky Survey (SDSS) will measure more than 700 000 galaxy redshifts in the northern hemisphere (York *et al.*, 2000). The scientific return from studying the large scale structure of galaxies in the local universe using large scale redshift surveys has been enormous. Accurate measurements of galaxy clustering via the 2-point correlation function as a function of galaxy class (Norberg *et al.*, 2002) and the galaxy power spectrum (Tegmark *et al.*, 2002) have been made. Also, the most accurate measurements of the local galaxy luminosity function have been made in a number of different wavebands (eg. Cole *et al.*, 2001, J, H, & K-bands). Data from the 2dFGRS and SDSS have also, in concert with studies of the CMB power spectrum, heralded a new era of 'precision cosmology' and have been used to constrain cosmological parameters to a high degree of accuracy independent of other methods such as the CMB power spectrum and high-z SNe (Spergel *et al.*, 2003; Schmidt *et al.*, 1998; Perlmutter *et al.*, 1999).

The current generation of radio imaging surveys now probe much of the sky to mJy levels, and generally have source catalogues containing hundreds of thousands of radio sources (NVSS: Condon *et al.* 1998; FIRST: White *et al.* 1997; SUMSS: Mauch *et al.* 2003). These surveys probe a population of two distinct classes of extragalactic source. Most of these ($> 90\%$) are classical radio galaxies and QSOs whose radio emission is powered by the presence of an accreting super-massive black hole (known as Active Galactic Nuclei or AGN). These galaxies are found in radio surveys at a median redshift of $z \sim 0.8$ and dominate the population of radio sources with flux density $S_{1.4} > 10$ mJy. The remainder are associated with star-forming galaxies. This is a much more nearby population (median $z \sim 0.1$) and begins to dominate the radio source population below $S_{1.4} < 10$ mJy (see Figure 1.7). Understanding the cosmic evolution of these two classes of radio source has come about through studies of radio source counts (eg. Jackson & Wall, 1999). Unfortunately proper interpretation of radio source counts is strongly model dependent and requires knowledge of the redshift distribution of these sources out to $z \approx 1$.

The scientific value of the radio surveys mentioned above is much increased by finding optical counterparts for radio sources and obtaining spectra of them using optical telescopes. This is a difficult process and until recently has only been done for small subsamples of radio sources in small areas of the sky. However, with the release of the redshift surveys mentioned above, obtaining spectra of large numbers of radio sources has never been easier. Combining radio data with the redshift surveys yields a wealth of information about host galaxies and allows classification of the physical cause of emission of each radio source as coming from star formation or an AGN. Redshift information from the spectra also allows the properties of these two classes of radio source to be examined in some detail (eg. Ivezić *et al.*, 2002; Sadler *et al.*, 2002).

The increased size of these datasets has created a new problem, in that it is difficult with such large datasets for a single person to inspect all the data manually. For this reason

novel techniques have had to be implemented for identifying radio sources in optical surveys and classifying their spectra (eg. Principal Component Analysis (PCA); Folkes *et al.*, 1999; Madgwick *et al.*, 2002). In this chapter I will give a brief introduction to the 6dF instrument and the 6dF Galaxy survey and describe the procedure by which a 6dFGS-SUMSS/NVSS dataset was constructed. I will also describe how a useful database was constructed from such a large amount of data.

3.2 The 6dF Instrument

The 6 degree Field (hereafter 6dF) instrument is a multi-object fibre spectroscopic observing facility for the UK Schmidt Telescope (UKST) at Siding Spring Observatory. The 6dF instrument is modelled on the 2 degree Field (or 2dF) instrument on the Anglo-Australian Telescope (Lewis *et al.*, 2002) with the major difference being that the robotic fibre positioner of 6dF operates off-telescope in a special enclosure in the UKST dome. The general specifications of the 6dF instrument are outlined here; for further information consult the 6dF web-page at www.aao.gov.au/ukst/6df.html and links therein.

The 6dF instrument operates by having a robot place fibres on a field plate at the positions of galaxies to be observed. The field plate is then loaded into the telescope and pointed to the correct position in the sky. During observing, light travels down each fibre to the spectrograph which is located off telescope. Spectra are recorded on a 1032×1056 pixel CCD and reduced using the `6dfdr` reduction package.

3.2.1 The Robotic Positioner

Figure 3.1 shows the fibre positioning robot for 6dF. The robot is located off telescope in a small enclosure close to the UKST. The robot uses an r-θ positioning system, meaning that it has two degrees of freedom: r indicates how far the robot is from the centre of the field plate and θ indicates the angle of the robot from this point. Using this system any position on the 5.9° diameter field plate can be accessed.

The robot is capable of positioning the fibre buttons to an accuracy of $\sim 10\,\mu\mathrm{m}$ using a small inbuilt CCD camera which measures the centroid of a back illuminated image of each fibre. This positional accuracy on the field plate corresponds to $0.7''$ on the sky. It takes about 40 minutes to configure a single field plate, meaning that using 2 field plates, one may be used for observing while the other is being set up by the robot.

3.2.2 The Field Plate

The field plate (pictured in Figure 3.2) contains 154 fibre buttons: 150 spectroscopic fibres and four 7-fibre guide bundles. The guide fibres are placed at the position of guide stars and used to position the telescope correctly during observing. Each of the 150 spectroscopic fibres has a diameter of $100\,\mu\mathrm{m}$ which corresponds to $6.7''$ on the sky. The buttons themselves are 5mm in diameter, this means that targets closer than $5.7'$ on the sky cannot be observed simultaneously. The field plate has a curved steel surface, matching the

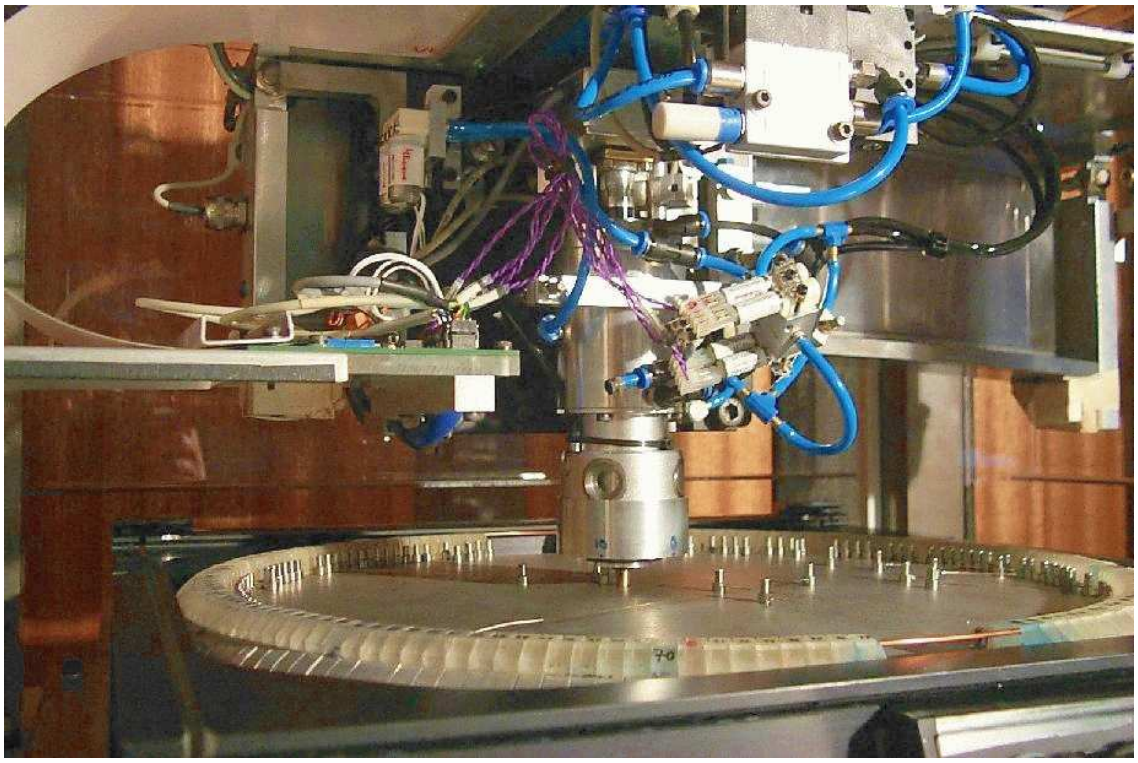

Figure 3.1 The 6dF robot pictured just as it is gripping a button on the field plate. The metal tracks above the robot move it moves in the r direction and the whole enclosure can spin around to move it in the θ direction.

curved focal surface of the Schmidt telescope. Each button carries a 90° prism which is attached to an optical fibre and used to direct starlight from the button into the fibre. Each fibre is attached to a retractor, loaded with a spring, which can be seen around the edge of the field plate in Figure 3.2, and which is used to keep the fibres taut during observing as well as making it safe to park the fibres by the robot after observing. The field plate can be rotated within its enclosure, this is used to compensate for the rotational offset of the telescope during observing.

3.2.3 The Spectrograph

Once the 6dF field plate is placed in the UKST for observing, light from the 150 science fibres are sent via a cable to an optical bench in a separate enclosure in the UKST dome. This is where the spectrograph is located. Placing the spectrograph on a separate bench from the telescope ensures the final spectra are stable and free of the effects of motion of the telescope. The spectrograph is essentially the same as that of the FLAIR (Watson & Parker, 1994) instrument which the 6dF replaced, with the addition of a new 1032×1056 pixel Marconi CCD.

For galaxy survey observing, two separate observations are made using blue and red gratings and these are then spliced together during data reduction. Before October

Figure 3.2 The 6dF field plate. The buttons are all in the park position. The retractors can be seen as a metal ring around the outside of the plate. One of the cables leading out to the right take 150 science fibres to the spectrograph and the other cable contains 4 guide fibre bundles.

2002 6dF observations were made with conventional 600V (covering 4000–5600Å) and 316R (covering 5500–8400Å) reflection gratings. Since October 2002 the spectrograph has used 580V (covering 3900–5600Å) and 425R (covering 5400–7500Å) Volume-Phase transmissive Holographic (VPH) gratings, which have improved efficiency and data uniformity. On average, the spectral resolution is ~ 7Å with the red grating and ~ 5Å with the blue one. The optimum total system efficiency of the 6dF instrument is 11% (including atmospheric losses and the quantum efficiency of the CCD detector) but this can often deteriorate in bad conditions (Jones *et al.*, 2004).

3.2.4 Observing with 6dF

6dF survey observations are done by the astronomer on duty at the Schmidt Telescope. Preparations for observing with the 6dF instrument begin well before the sky becomes dark enough to observe. Firstly, the fibres must be assigned positions on the field plate. This is done using the program `configure` which takes a list of possible target positions and determines the optimal use of the 150 science fibres to acquire as many of these targets as possible; ~ 10 fibres are usually reserved to observe random sky positions useful for data reduction later. The four guide stars are also determined at this stage. Figure 3.8 shows the typical output of the `configure` software.

Once a field is correctly configured the configuration file is loaded onto a computer in an enclosure in the dome. This computer then runs the robot, telling it where to position each fibre. The robot generally works from the middle of the field plate to the edge, but leaving the longest distances until the very end. This method is used to minimise fibre tangling and breakages. The order in which the fibres are placed is saved and the robot then defibres a field after observation in the exact reverse order. The robot takes about 1 hour to totally defibre and then fibre up a new field. There are two field plates with 6dF which means this procedure can be carried out on one field plate while the other is being used for observing.

When the fibres are configured for observing, the field plate is loaded into the telescope and the fibres are fed into the spectrograph. First flat field exposures are taken using a quartz lamp in the dome, and then both Ne + HgCd arc exposures for red gratings or He + HgCd arc exposures for blue gratings are taken. Flat field observations are made so as to remove signatures introduced into the spectra by pixel-to-pixel variations on the CCD and throughput variations between fibres. Arc observations are made for the purpose of wavelength calibration; the known positions of lines for each arc lamp are compared with their CCD pixel positions to define a function which maps between pixel space on the CCD and wavelength space. After these calibration exposures the dome is opened and the telescope pointed to the correct position on the sky. The field is then rotated within the telescope until the guide stars are seen in the acquisition camera. Once the telescope pointing and field rotation are correct, the telescope will auto-guide off a nearby bright star and the observation can begin. Typical exposure times are 1 hour for blue grating observations and 30 minutes for red grating observations. Figure 3.3 shows the raw output of a typical 6dF observation.

3.3 The 6dF Galaxy Survey

The 6 degree Field Galaxy Survey (6dFGS) is a near-infrared-selected survey which covers 17,000 $\deg^2$ of the southern sky. This section will only give a brief overview of the survey; for a more complete description see Jones *et al.* (2004).

3.3.1 The Primary Sample

The 6dFGS aims to measure redshifts of a number of different samples of extragalactic objects most of which are selected to be complete at various wavebands. Each of these samples has a 'priority' for survey observations which denotes its importance within the survey design. The primary (and therefore highest priority) sample consists of all galaxies in the 2MASS XSC (Jarrett *et al.*, 2000) with total K magnitude brighter than 12.75, declination south of 0° and galactic latitude $|b| > 10^\circ$. The final input catalogue of primary targets consists of 113 988 galaxies which satisfy these criteria. As the K-selected sample has the highest priority, the way in which fields have been tiled across the sky is strongly dependent on the distribution of these objects. An adaptive tiling algorithm was employed to distribute the fields across the sky to maximise uniformity and completeness

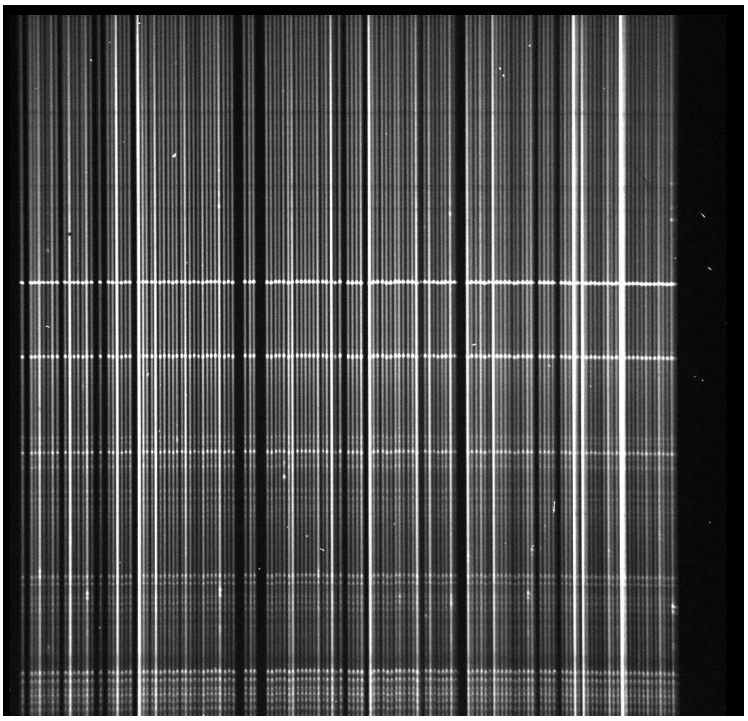

Figure 3.3 The raw output from a 6dF observation. The dispersion axis of each spectrum runs from top to bottom (bluer wavelengths at the top and redder wavelengths at the bottom). The positions of major sky emission lines can be seen in all spectra as horizontal lines of small white dots. Other small dots in the spectra are galaxy emission features or cosmic rays.

(Campbell *et al.*, 2004). Because of angular clustering on small scales in the 2MASS XSC (and, indeed of all galaxies in the local universe) this has resulted in some areas of sky having overlapping fields placed on them up to 3–4 times. This has a significant effect on the completeness of targets observed serendipitously (which have the lowest priority), and will be discussed further in Section 4.2.2.

The K-band selection of the 6dFGS primary sample makes this survey quite distinct from previous redshift surveys covering large areas of sky. The near-infrared spectral energy distributions (SEDs) of galaxies are dominated by light from old stellar populations, whose photometry provides the best estimator of a galaxy's stellar mass. Most large scale redshift surveys have been selected at optical wavebands where galaxies tend to be dominated by light from younger, bluer stars whose photometry provides an estimator of star-formation rate. This implies that galaxies in the 6dFGS primary sample will not be biased toward higher star-formation rates, and are selected purely on the basis of galaxy stellar mass. Also, at near-infrared wavelengths dust extinction within galaxies is much less than optical, meaning that dustier galaxies (often those with the highest star-formation rates) will be included in the sample.

A major aim of this thesis is to study the population of radio sources identified from this primary sample. The method of identifying radio sources with primary targets is

described in Section 3.4 and results from analysis of 6dFGS observations of these radio selected primary targets are described in Chapters 5 and 6.

3.3.2 Additional Targets

As the sky coverage of the primary sample is such that there are many fewer than 150 primary targets per field, provision has been made to observe targets from 15 other extragalactic samples. For a complete description of these see Jones *et al.* (2004). Most of them are selected to make the redshift survey complete in other wavebands (e.g. secondary 2MASS XSC targets down to $H = 13.05$ and $J = 13.75$ or targets selected from the ROSAT Bright Source Catalogue). A list of additional targets was provided for 6dF observing as a part of the work for this thesis. They were chosen to be radio source identifications of b_J-selected objects which were missing from the primary sample, either because they are stellar in appearance (e.g. QSOs, compact galaxies, Galactic planetary nebulae) or because they are very blue in colour (e.g. starburst galaxies, BL-Lacs). These targets will characterise the properties of local radio sources which are not part of the primary sample.

Because the additional target sample is aimed purely at characterising the nature of the population of radio sources, 100% completeness is not necessary. This means that it is possible to piggy-back onto the 6dFGS by having these radio-source identifications observed serendipitously, meaning that a fibre is only placed onto a target if it is available after all other potential targets have been allocated. Section 3.5 will discuss the selection criteria of the additional target sample and Chapter 4 will discuss results from analysis of 6dFGS observations of them.

3.3.3 Observing

On a typical clear night about 3–5 survey fields can be observed, depending on season. Usually a field is prepared before twilight and loaded onto the telescope for observing. Whilst observing one field, the other field is set up for the next observation. Calibration observations are repeated with each change of field. Usually fields are observed with the blue grating first and then ending with the red grating.

Guide stars for the four guide fibre bundles are selected from the Tycho-2 catalogue (Høg *et al.*, 2000) and are selected with magnitudes in the range $8 < V < 11$. Guide stars are normally chosen near the edge of a field so as to optimise the alignment of the telescope during observing. They are used both to align the telescope correctly on the sky and to rotate the field plate to the correct position angle. During survey observing, after correct alignment, 3×20 minute observations of the blue field (for a total of 1 hour) and 3×10 minute observations of the red field (for a total of 30 minutes) are made. Observations are made in shorter blocks to aid in removal of cosmic rays (such as those seen in Figure 3.3) from the data when the images are co-added. In good conditions this observation time yields spectra with a typical S/N of around 5 to 10 pixel^{-1}.

3.3.4 Data reduction

6dF Galaxy survey data is sent from the telescope to a group led by Heath Jones at Mt. Stromlo observatory where it is reduced and redshifted. The primary team members responsible for this have been Matthew Colless, Lachlan Campbell, Will Saunders, Heath Jones and Tom Mauch. Given that there are on average more than 100 objects per 6dF field and that fields are observed at a rate of about 4 per night, more than 400 raw 6dF spectra are obtained after each night of observing. It is impossible to reduce such a large amount of data by hand, so much of the data reduction process is done automatically. The reduction package used is called `6dfdr` which is a modified version of `2dfdr` used for the 2dF Galaxy Redshift Survey. Only a brief overview of the data reduction process is given here; for a complete description of the `6dfdr` package and 6dF data reduction see Jones *et al.* (2004) and references therein. The `6dfdr` package takes as input a flat field observation, an arc observation and the object observations. It uses the flat field observation to locate the positions of each spectrum on the CCD and then flat fields, wavelength calibrates, sky subtracts and extracts all of the spectra automatically. Sky subtraction is made by averaging the spectra of ~ 10 fibres which are placed at random positions without object contamination on the field plate, and is in general quite good. Spectra are then crudely flux calibrated using observations of the spectrophotometric standard stars Feige 110 and EG 274 and then the red and blue frames are spliced together to form a single spectrum.

After the spectra have been reduced the next step is redshift determination, which is carried out using a modified form of the `runz` software used for the 2dF spectra. `runz` determines redshifts via a combination of the cross-correlation technique and emission-line fitting. In general only the cross-correlation redshift was examined and this was then checked visually to decide whether the `runz` estimate was reliable. Sometimes the redshifting software can be misled by residual sky lines or patterns from fibre interference, whereas the experienced human eye can readily pick up these mistakes. Sometimes the examiner must intervene and refit the spectrum to an alternative redshift, though this happens only rarely. After visual inspection the redshift is assigned a quality (Q) between 1 and 4. $Q \geq 3$ redshifts are considered genuine, $Q = 4$ means a reliable redshift and $Q = 3$ means a probable redshift. $Q = 1$ values are reserved for failed redshifts, where neither the redshifter nor the software can make a judgement. $Q = 2$ values are reserved for stars and other galactic objects, usually assumed to be those with redshift $z < 0.002$, and also objects which have a tentative redshift estimate. This visual assessment technique was also employed for the 2dF Galaxy Redshift Survey and was checked by repeat measurements on a sample of $\sim 15\,000$ spectra by two operators; they were only discrepant in 0.4% of cases (Colless *et al.*, 2001). As part of work for this thesis and as a member of the 6dFGS team, I redshifted around 100 fields of the 6dFGS, corresponding to about 10 000 redshifts which formed part of the first data release.

3.3.5 The 6dFGS First Data Release

In March 2004 the First Data Release of the 6dFGS was made publicly available online at www-wfau.roe.ac.uk/6dFGS/. This contains 52 048 spectra from which 46 474 unique galaxy spectra were obtained; 39 649 of these unique galaxy spectra had $Q \geq 3$. 524 fields contribute to this data release, the majority of which occupy the survey's central declination strip $-42^\circ < \delta < -23^\circ$. Of the $Q \geq 3$ spectra in the first data release there are 32 156 unique galaxy spectra in the K-selected primary sample. The remainder are from the additional target samples. Section 3.4 describes how radio sources were identified in the primary sample, and which of these are in the first data release. Section 3.5 will discuss the method by which the additional target sample was constructed and which of these were in the first data release.

3.4 Finding Radio Sources in the Primary Sample

One of the goals of this thesis is to study the radio properties of objects in the K-selected primary 6dFGS sample. In order to do this a database of radio identifications was created which is as complete and reliable as possible. The primary radio catalogues used in this thesis are the NRAO VLA Sky Survey (NVSS; Condon *et al.*, 1998, $-40^\circ < \delta < 0^\circ$) and the Sydney University Molonglo Sky Survey (SUMSS; Chapter 2 of this thesis, $\delta \leq -50^\circ$). As discussed in Chapter 2 these surveys are well matched in terms of positional accuracy and flux density limit. Therefore the same techniques are used for crossmatching both the SUMSS and NVSS catalogues with the 6dFGS primary target sample.

3.4.1 The Radio Source Catalogues

In this section a brief introduction is given to the two radio catalogues as applied to the crossmatching process. For thorough descriptions of both catalogues see Condon *et al.* (1998) for the NVSS and Chapter 2 of this thesis for SUMSS.

The NRAO VLA Sky Survey (NVSS)

The NVSS is a radio imaging survey of the entire sky north of $\delta = -40^\circ$ at 1.4 GHz. Its principal data products are a set of 2326 $4^\circ \times 4^\circ$ continuum images and a catalogue of about 2×10^6 discrete sources stronger than $S = 2.3\,\mathrm{mJy}$, the NVSS catalogue is incomplete at its flux limit but becomes $> 90\%$ complete above 2.5 mJy. The images have $\theta = 45''$ FWHM resolution with position accuracy $\leq 1''$ for sources stronger than 15 mJy, increasing to $7''$ at the survey limit. The resolution and positional accuracy of the NVSS makes identification of radio sources with objects on optical survey plates straightforward. The NVSS images and associated source catalogue covering the region of sky studied in this thesis were obtained from the public database at www.cv.nrao.edu/nvss. There are 572 777 NVSS catalogue sources which overlap with the region bounded by $0^\circ > \delta > -40^\circ, |b| > 10^\circ$. These sources form the primary 1.4 GHz-selected radio input catalogue for this sample.

The Sydney University Molonglo Sky Survey (SUMSS)

SUMSS is described fully in Chapter 2 of this thesis, therefore no discussion of the survey characteristics is given here. For the purposes of the 6dFGS-SUMSS sample, version 1.3 of the SUMSS catalogue compiled on 2003 October 27 was used. This version covers $> 95\%$ of the celestial sphere south of $\delta = -50^\circ$ with $|b| \geq 10^\circ$ and contains 116 349 radio sources with flux density $S \geq 6$ mJy. These sources form the primary 843 MHz-selected input catalogue for this sample.

3.4.2 Crossmatching

When searching for NVSS and SUMSS radio sources in the 6dFGS primary target sample a method was employed which maximises both the completeness (ie. all potential radio sources are included) and the reliability (ie. all included radio identifications are genuine) of the database. The best way to ensure completeness and reliability of radio-optical identifications is to determine a maximum position offset which includes all possible identifications, construct a list of these identifications and then verify each of them by visually inspecting overlays of radio contours on optical images. Although checking all identifications by eye is time consuming, it is the best way to minimise the number of false identifications, as at all separations some radio identifications selected by position offset alone will be chance coincidences.

Figure 3.4 shows the distribution of offsets between the NVSS catalogue and the 6dFGS primary input catalogue. The solid line overplotted shows the differential distribution which would be expected if all identifications of 2MASS sources in the NVSS were chance coincidences. This is made by assuming that the (poisson) probability that at least one unrelated NVSS source lying within an angular separation r of any position is

$$P(< r) = 1 - \exp(-\pi\rho r^2) \tag{3.1}$$

(Condon *et al.*, 1998), where $\rho = 50\,\mathrm{deg.}^{-2}$ is the approximate surface density of the NVSS catalogue. The peak at around $200''$ is higher for the model distribution because in the distribution of the data, real identifications of radio sources with 2MASS XSC objects dominate at smaller offsets, meaning that fewer random identifications are made at offsets greater than $30''$. The number of chance identifications exceeds the number of genuine identifications for offsets $> 30''$ so it was any identifications with offsets $> 30''$ were discarded. All 2MASS XSC objects with separations $< 30''$ from an NVSS radio source were checked by eye.

As can be seen from the solid line in Figure 3.4, even at separations less than $30''$ some random associations of NVSS radio sources with 2MASS XSC objects are expected. Figure 3.5 shows the distribution of offsets for the sample of 5120 NVSS catalogue objects which have been inspected visually. Visual classification of these identifications are shown in different colours in the plot in Figure 3.5. It is clear from this plot that there is no simple NVSS-2MASS offset cutoff which separates real identifications from false identifications. The vast majority of real identifications have offsets $< 15''$ though there

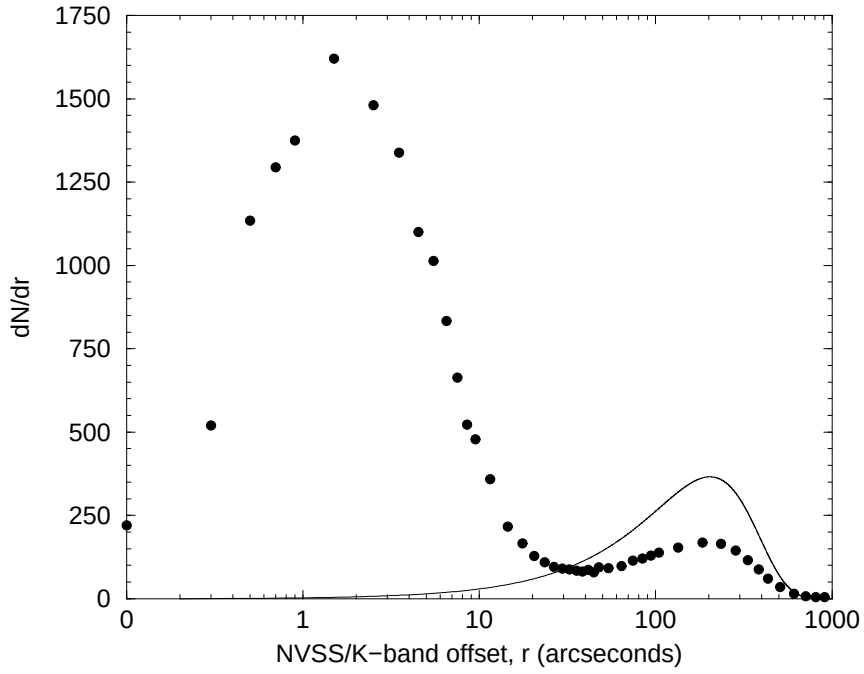

Figure 3.4 The distribution of NVSS/2MASS position offsets (filled circles). The solid line shows the theoretical distribution of offsets expected by chance from a sample of 74 609 6dFGS primary sample galaxies assuming NVSS sources are randomly distributed on the sky with a surface density of $\rho = 50\,\mathrm{deg.}^{-2}$. At the adopted separation cutoff of $30''$ the number of matches found declines to that expected by chance.

is still about 2% contamination by false identifications at these separations. This is due to a number of factors:

- Some radio sources can appear extended and have positions quoted in the NVSS catalogue which differ from the actual centroid of the extended source, though the centroid coincides with the optical host galaxy. This can lead to true identifications of radio sources with offsets $> 15''$.
- Some galaxies can appear at the position of one of the lobes of a double radio source whose centroid is associated with another galaxy. This can lead to false identifications of radio sources with offsets $< 15''$.
- One of a pair of 2MASS galaxies with small separation can be identified with a radio source which should be identified with the other galaxy. This can lead to false identifications of radio sources with offsets $< 15''$.

8.5% of the objects in Figure 3.5 were considered too uncertain to make a definitive visual classification. All such objects with separations closer than $15''$ were accepted as genuine and those with separations greater than $15''$ were discarded. This is because of the small number of false identifications in the complete sample with separations $< 15''$ ($\sim$ 2%). Given the distribution of genuine identifications, only about 1% of objects in the complete sample are expected to be misidentified by applying this cutoff to unsure identifications.

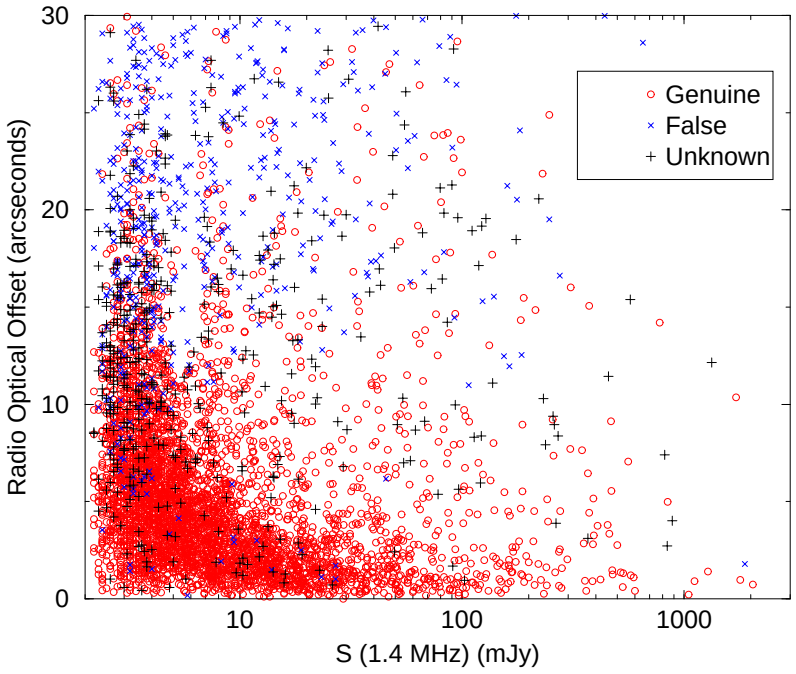

Figure 3.5 The results of hand identification of $\sim$ 5000 radio sources in the primary sample. The red circles denote objects whose identification was genuine (82% of candidates), blue crosses denote mis-identifications (9.5% of candidates) and black plus symbols denote uncertain identifications (8.5% of candidates).

A population of Giant Radio Galaxies (GRGs) (Schoenmakers *et al.*, 2001) which have linear sizes in excess of 5′ in radio images are missed by this classification technique. Many of these objects have lobes that are detected in the SUMSS and NVSS radio catalogues but cores that are not (Saripalli *et al.*, 2005). A detection of a core is required to make an unambiguous identification of such objects with galaxies on optical plates using the identification procedure outlined here. In a recent search for such objects in SUMSS Saripalli *et al.* (2005) found 22 such objects in 2100 deg.^{2} of sky implying that GRGs are extremely rare. They contribute less than 1% to the incompleteness of the 6dFGS-NVSS/SUMSS sample.

Table 3.1 shows the detection rates of the NVSS and SUMSS samples with a 30″ matching radius. These are all only candidate NVSS/SUMSS/2MASS detections, as each candidate detection must be verified by the method outlined in the previous paragraphs. Given that about 12% of the subsample shown in Figure 3.5 were discarded after visual inspection, a similar fraction should be found for the complete SUMSS/NVSS/2MASS database. This means that the actual NVSS detection rate of the complete 2MASS XSC will be $\sim$ 16% and the SUMSS detection rate will be close to $\sim$ 9%. The next section describes the detection rates of sources observed as part of the 6dFGS first data release.

Table 3.1 Candidate radio source detections of the complete list of K-selected 6dFGS objects.

Sample name	Region[a]	Bands	Survey limit	N total	N $< 30''$	det. rate[b]
NVSS-2MASS	$-40^\circ < \delta < 0^\circ$	1.4 GHz K band	≥ 2.3 mJy < 12.75	572 777 74 609	13 771	2.4% 17.9%
SUMSS-2MASS	$\delta \leq -50^\circ$	843 MHz K band	≥ 6 mJy < 12.75	116 349 25 389	2764	2.4% 10.9%

NOTES:
[a] $|b| > 10^\circ$ and all right ascensions are assumed for all entries in this column.
[b] This is the detection rate in the various samples of all sources with offset $< 30''$. The actual values will be smaller after visual inspection of all radio/optical overlays (as shown in Table 3.2).

Table 3.2 Detection rates of radio sources observed in the 6dFGS primary sample.

Sample name	# 2MASS observed	% Observed	N $< 30''$	# radio id	Detection rate
NVSS-2MASS	28 928	38.8%	5 120	4 506	15.6%
SUMSS-2MASS	1 443	5.7%	131	109	7.6%

3.4.3 Radio Sources in the First Data Release

5120 NVSS and 131 SUMSS catalogue objects were found to have offsets from primary targets in the 6dF First Data Release of less than $30''$. These candidate identifications were verified using the method outlined in Section 3.4.2, resulting in 4506 NVSS identifications and 109 SUMSS identifications in the first data release. This corresponds to a detection rate of 15.6% of $K < 12.75$ objects for NVSS and 7.6% for SUMSS. Table 3.2 summarises the detection rates of radio sources in the first data release. Analysis of these detections is presented in Chapters 5 and 6.

3.5 Finding Additional Targets

This section describes how the master input list for the serendipitously observed NVSS and SUMSS additional target sample was constructed. The aims of the additional target sample are to characterise the population of radio sources which are not part of the primary sample, including radio identifications of objects which appear stellar on optical plates and extended objects which are not in the primary sample because they are blue in colour. To do this an input list of candidates for observation must be constructed by crossmatching the radio catalogues with an appropriate optical catalogue. The SuperCOSMOS database was deemed to be ideal for this purpose.

Section 3.5.1 discusses the optical catalogue used for selecting additional targets. Section 3.5.2 describes the crossmatching process and Section 3.5.3 describes a test observation made during 6dF commissioning time of a field of additional targets.

3.5.1 Selecting additional targets

The additional targets have been selected by crossmatching radio sources in NVSS and SUMSS with objects in the SuperCOSMOS catalogue (Hambly *et al.*, 2001b). SuperCOSMOS is a facility run by the Wide Field Astronomy Unit at the University of Edinburgh and is the successor to the COSMOS facility (Yentis *et al.*, 1992). SuperCOSMOS has scanned and digitised the plates from the UK Schmidt photographic survey with 0.67 arcsecond pixels and a position accuracy of about 0.2 arcseconds. A database of pixel images and an object catalogue covering the entire southern sky with a limiting magnitude of $b_J \sim 23$ is available online at www-wfau.roe.ac.uk/sss/. Data for each object in the catalogue consist of J2000 Right Ascension and Declination, proper motion measures and error estimates calculated from repeat observations in different wavebands taken more than ~ 10 years apart and quoted in units of mas yr^{-1}, b_J,r_F & I magnitudes and a classification flag (1=extended, 2=stellar, 3=unclassifiable and 4=noise) determined from the optical morphology of the object.

To create an input list of additional targets, a preliminary database of all NVSS and SUMSS catalogue objects found in SuperCOSMOS and covering the same area of sky as the primary sample (see Table 3.1 for the sky coverage) was constructed. The vast majority of identifications will overlap with the primary sample as most 2MASS XSC galaxies are also present in the SuperCOSMOS database. These overlapping objects were subsequently removed when the preliminary database of NVSS/SUMSS/SuperCOSMOS identifications was merged with the 6dFGS master catalogue (Jones *et al.*, 2004). At galactic latitudes $|b| < 20^\circ$ the surface density of foreground stars is extremely high so it was decided that only stellar identifications with $|b| \geq 20^\circ$ should be included in the final list.

3.5.2 Crossmatching

Unlike the radio sources in the primary sample, which are all observed as part of the redshift survey, genuine radio identifications of SuperCOSMOS objects must be selected before observation. About 3% of all NVSS radio sources are identified with optical galaxies in SuperCOSMOS with $b_J < 19$. This means that visual verification of each candidate identification in the input list is impossible (there are $\sim 15\,000$ such identifications). A Monte-Carlo method of crossmatching is outlined here which maximises the number of genuine radio-optical identifications without requiring visual verification of each identification.

A subsample of genuine radio-optical identifications was selected at moderate galactic latitude and each position was offset by $5'$ to $10'$ ten times in a random direction to create a random distribution of radio positions which mimics the spatial distribution of the genuine radio positions. The probability of a chance coincidence as a function of separation can then be determined by taking the ratio of the average number of matches at the random positions to the number of matches at the true positions. This analysis was done separately for stellar identifications (SuperCOSMOS class 2) and extended identifications (SuperCOSMOS class 1) as the surface density of stellar objects on optical plates is much

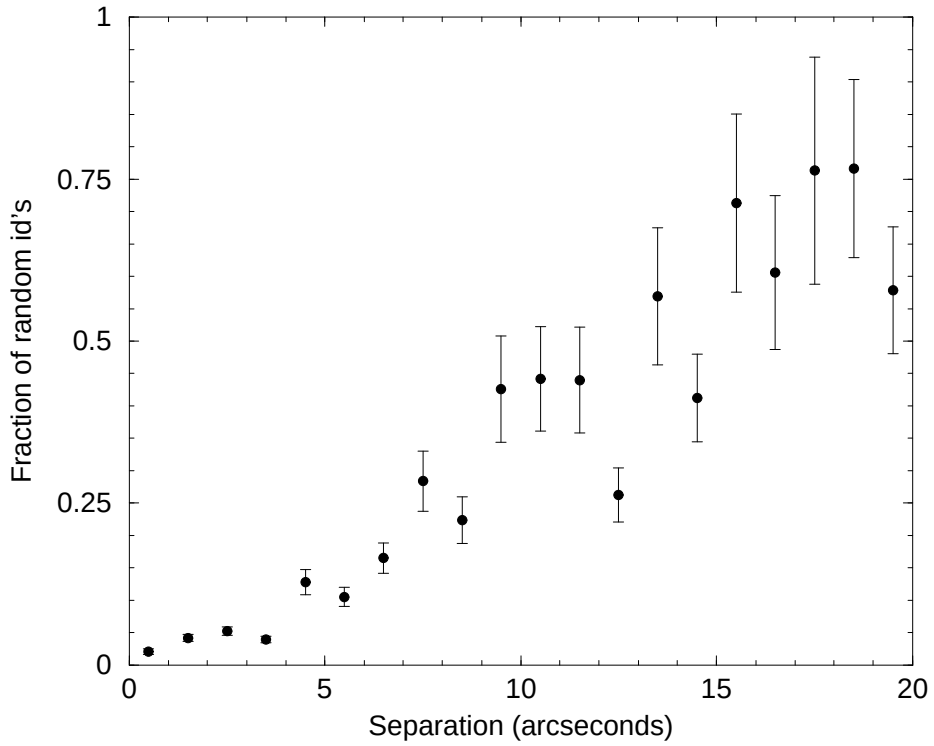

Figure 3.6 The probability of a chance coincidence of NVSS/SuperCOSMOS identifications vs. increasing separation for extended objects (SuperCOSMOS class 1). This was found by dividing the average of the number of identifications found in 5 random samples by the number of true identifications. Above $10''$, 50% of sources are expected to be chance identifications. This was the radio-optical separation cutoff adopted for 'extended' additional targets.

greater than that for extended objects at $b_J < 19$, meaning that the probability of a chance coincidence between radio sources and stellar objects is much greater. Figure 3.6 shows the results of this analysis for extended objects and Figure 3.7 shows the results for stellar objects. The probability of a chance coincidence rises to 50% for extended objects for a radio-optical separation of $10''$, which was chosen as an acceptable cutoff. For stellar identifications the probability of a chance coincidence rises to 100% at $5''$, which was chosen as an acceptable cutoff. This method may miss objects (especially extended objects) with separations greater than the chosen cutoff, but this is not a problem as the sample is only serendipitously observed and will not be complete in any case.

6dFGS-NVSS/SUMSS additional targets which have been observed in the first data release have had their identifications visually checked. About 100 radio source identifications were rejected after visual inspection.

3.5.3 Pilot study of radio sources

This section describes the reduction and analysis of a 6dF observation made on 2001 May 13. This observation was made during commissioning time, and analysis of the data

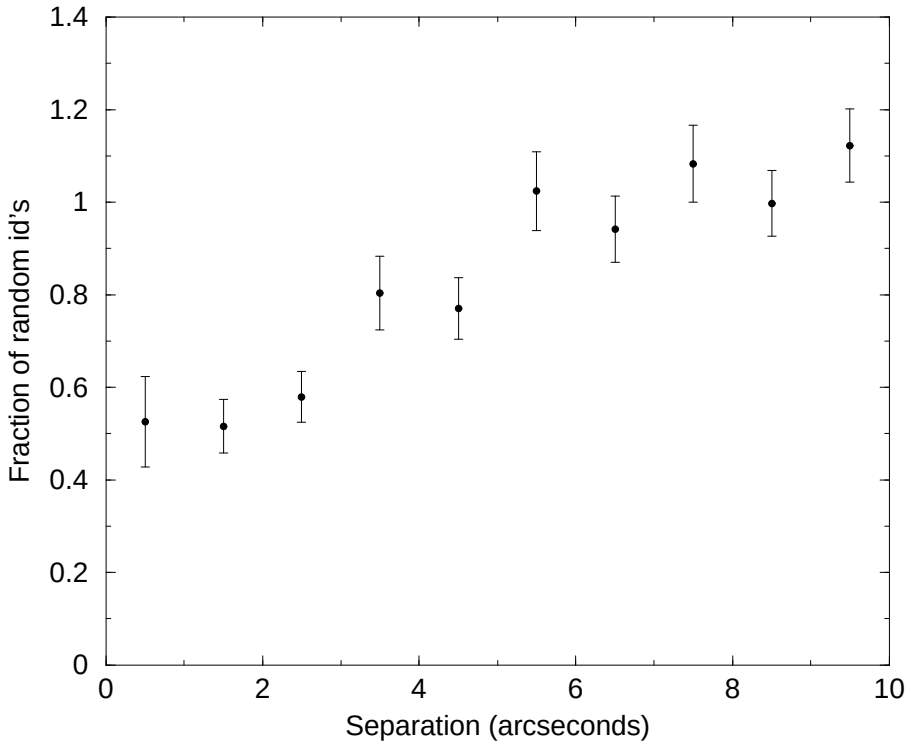

Figure 3.7 The probability of a chance coincidence of NVSS/SuperCOSMOS identifications vs. increasing separation for stellar objects (SuperCOSMOS class2). This was found by dividing the average of the number of identifications found in 5 random samples by the number of true identifications. Above $5''$, 100% of sources are expected to be chance identifications. This was the radio-optical separation cutoff adopted for 'stellar' additional targets.

obtained was intended to give insight into whether the selection process for additional targets will yield useful results, as well as determining a useful b_J magnitude limit for the additional targets. Much of the work presented in this section was published as an article in the Feb 2002 AAO Newsletter (Mauch, 2002).

The Input Catalogue

The objects observed were 105 stellar and extended objects selected from SuperCOSMOS with NVSS radio identifications and lying within a circle of 6 degrees diameter centred on $\alpha = 14h$, $\delta = -30°$. These objects were selected in the same manner as described in the previous section (i.e. extended objects with radio-optical separation $< 10''$ and stellar objects with separations less than $< 5''$). Objects fainter than $b_{\rm J} = 19$ and brighter than $b_{\rm J} = 14$ were removed from the input list. The brightness limit was made fainter than that intended for the survey in order to determine an appropriate magnitude limit for the spare fibre targets.

The distribution of sources across the 6dF field plate is shown in Figure 3.8. 152 matches were found in a circle of diameter $6°$ centred at $\alpha = 14$h, $\delta = -30°$. 104 (65%)

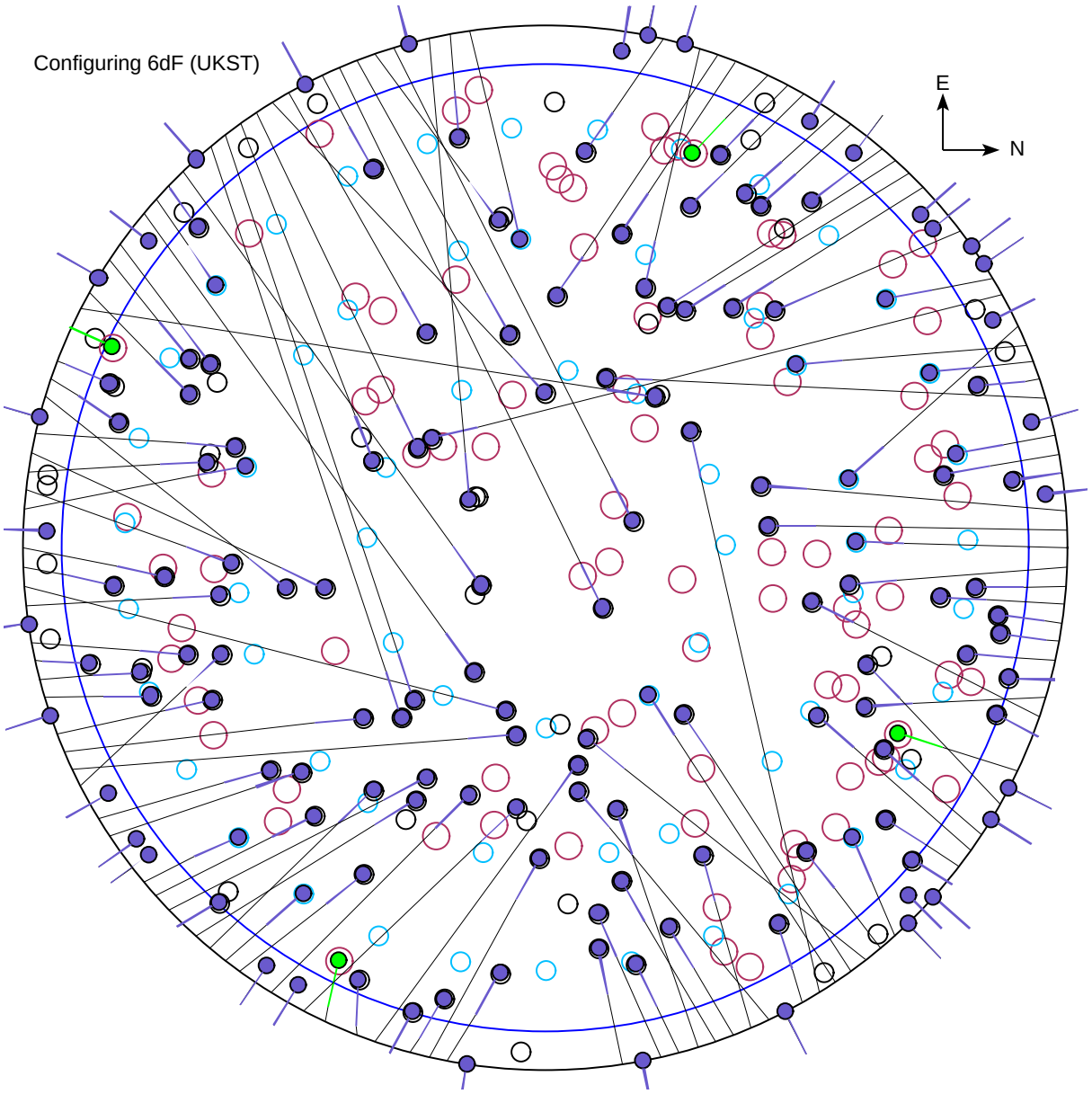

Figure 3.8 The output of the `configure` software for a pilot observation of NVSS selected targets. The black circles are positions from the input list, the red circles are the positions of guide stars and the blue circles are sky positions. 105 fibres were allocated to targets by the software, and 11 fibres were used to observe the sky.

were extended and 48 (30%) were stellar. The 6dF `configure` software allocated 105 fibres out of the 152 targets; 11 of the remaining fibres were used as sky fibres.

The Observation

The observation of this field was made on 2001 May 13 during bright time. Three exposures of 1200 seconds each were made giving a total exposure time of 1 hour. During the galaxy redshift survey each field is observed for a similar amount of time and no observations are made during bright time making this data representative of the worst conditions during survey observing. Seeing was consistently a little above 2″ during the whole exposure time.

Both Ne and Hg-Cd 20 second arc exposures were made before the observation. There were no arc exposures made after the observation. Flat field images were made with dome lights. Spectra were obtained with the 316R grating which provides good coverage in the wavelength range 4500Å-7500Å. This grating is also one of those used in the redshift survey.

Data Reduction

Data were reduced using the IRAF task `dofibres` which combines all of the steps of fibre reduction into one package. The two separate arc observations were co-added to perform the wavelength calibration. The flat field image was used for the fibre throughput correction. On average the spectra obtained were in the wavelength range 4403Å-7437Å with a dispersion of 2.9Å pixel^{-1}.

Sky subtraction of the resultant spectra was problematic. To obtain more sky spectra across the CCD, parked fibres were also used as sky fibres. This resulted in about 30 candidate sky spectra of which about 5 had to be removed due to object contamination. Most of the resultant object spectra had residual peaks due to bad wavelength calibration and in many cases the continuum dropped well below zero counts after subtraction. To alleviate this problem only the 7 weakest sky spectra were averaged to form a combined sky spectrum. All of the stronger sky spectra were to one side of the CCD which in general had a higher level of scattered light than the other. The worst problems with sky subtraction occurred at wavelengths greater than 7000Å due to the sheer number of sky lines. At moderate redshifts the Hα line would appear in this part of the spectrum making it difficult to locate.

Once the object spectra were reduced redshifts were obtained with the `rvsao` package in IRAF (Mink & Kurtz, 1998). This package uses both cross correlation with template spectra and line fitting to obtain redshifts, as in the `runz` package used for reduction of survey data. The template spectra used in the 2dF Galaxy Redshift Survey were used for cross correlation as they have a similar resolution to the spectra in 6dF. A cross-correlation coefficient of R=5 with 2dF spectra was deemed to be sufficient to produce a reliable redshift. However, all spectra with cross-correlation coefficients between R=4 and R=6 were inspected visually to verify the results of `rvsao`. Figure 3.9 shows some examples of reduced spectra from this observation.

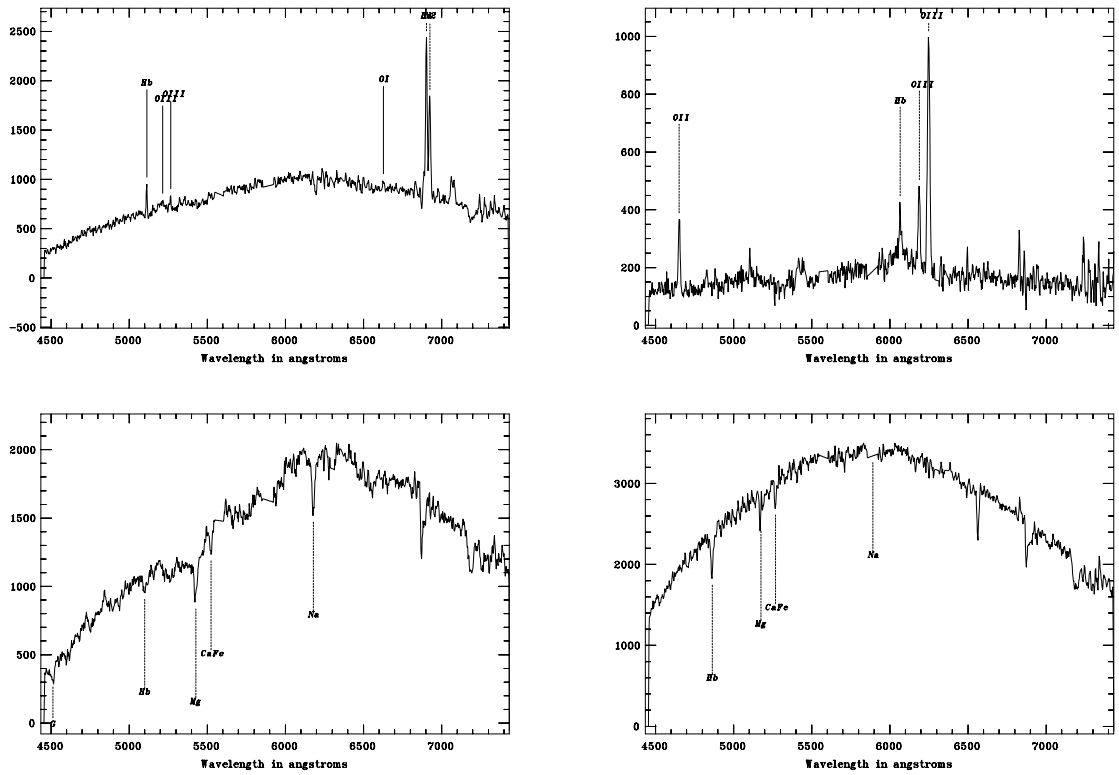

Figure 3.9 Some examples of spectra obtained during the 6dF pilot observation. Due to problematic sky subtraction, residual sky lines at 5577, 5893 and 6300 Å have been removed manually. The redshifted locations of common spectral lines are labelled.

Results

Table 3.3 shows the classifications made from the 105 spectra obtained. A large number of the galaxies were not classifiable due to low signal-to-noise. Most of these were fainter ($b_{\rm J}$ >18) objects well below the magnitude limit of the galaxy survey. No quasar template was used in `rvsao` so the spectra with low R were inspected visually to find QSOs. This search turned up only two candidate quasar spectra.

Table 3.3 Classification of 105 6dF objects in a pilot study.

Classification	N
Stars	22
Galaxies	39
QSO	2
Low S/N or R	42

Figure 3.10 is a histogram of the redshifts obtained from the galaxy spectra. The

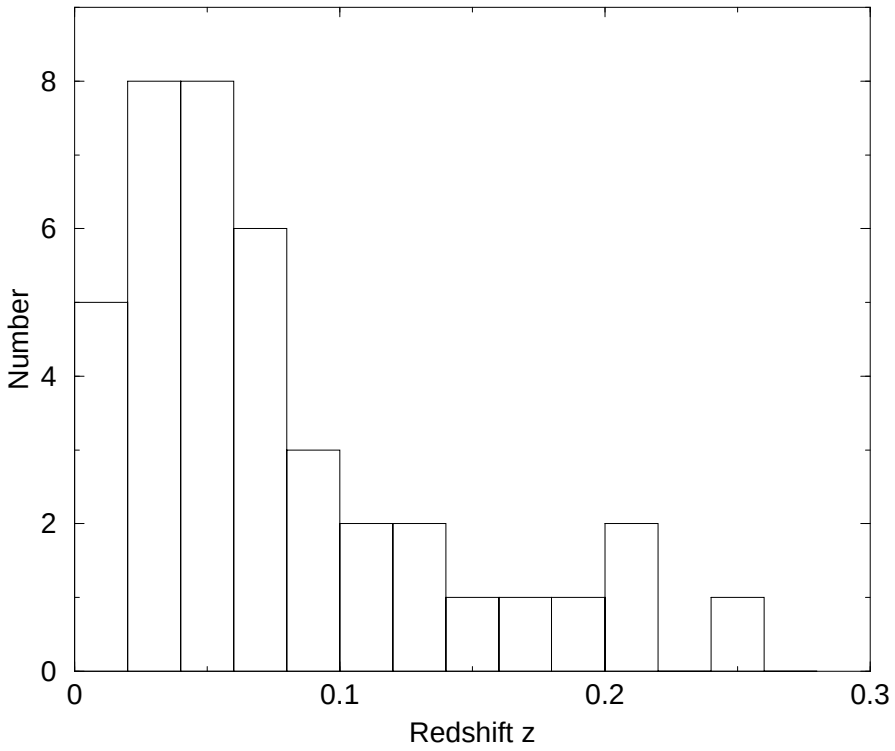

Figure 3.10 A histogram of the redshifts obtained from the 6dF pilot observation. The distribution of these redshifts is similar to that found for all radio sources in the first data release. (see Figure 5.3).

mean redshift obtained was $z = 0.07$ which is in good agreement with the value obtained in the first data release of the 6dFGS. The small number of galaxies with $z > 0.2$ all had very strong emission lines making calculation of redshift possible even at very low signal-to-noise in the continuum.

CCD Counts

Figure 3.11 is a plot of the variation in counts at the blue end of the CCD (4500Å-5000Å) vs b_J from SuperCOSMOS. The sample was separated into stellar and extended objects on the basis of SuperCOSMOS classification. Stellar objects generally have more CCD counts than extended objects for a given magnitude; this is because almost all of the light from a point source will fall down the 6″ fibres while only a fraction of the light in large bright galaxies will. The three extended objects to the left of the plot at around $b_J = 18$ with higher CCD counts are all bright galaxies with incorrect b_J determined by SuperCOSMOS.

At around $b_J = 18$ the CCD counts drop to around 100 and the scatter in the data for both stars and galaxies increases. The increased scatter is due to the sky level becoming dominant at this magnitude. It was decided that a limiting magnitude of $b_J = 18$ was achievable for survey observations. This is the cutoff magnitude applied to the NVSS-SUMSS additional target list.

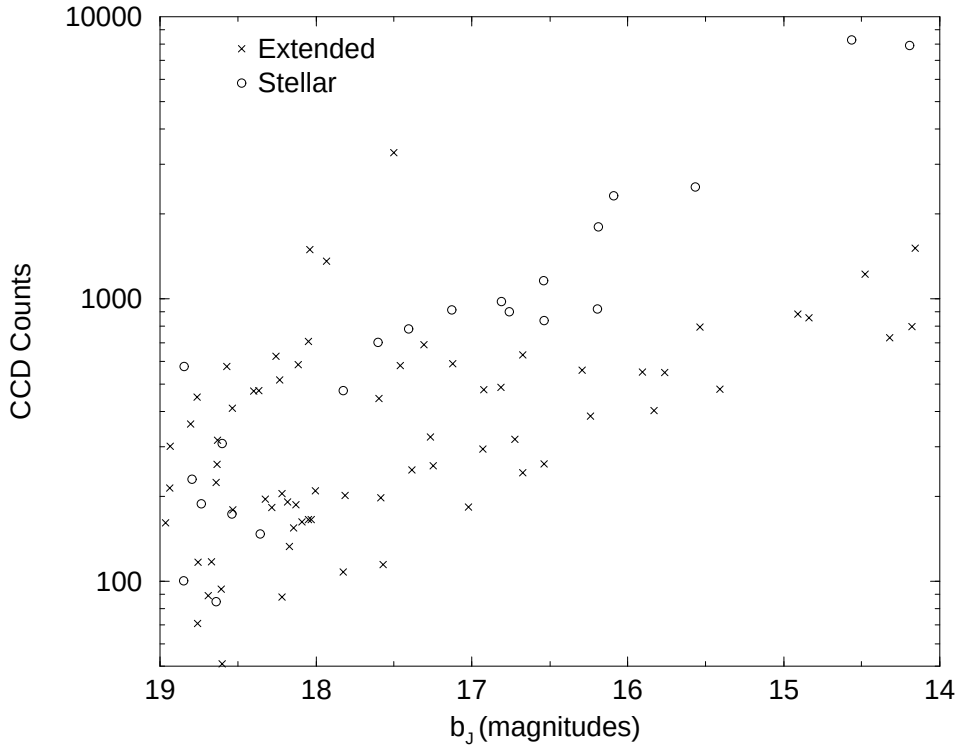

Figure 3.11 A plot of counts at the blue end of the CCD (4500Å-5000Å) vs b_J. The sample is divided by SuperCOSMOS classification, the crosses are for galaxies and the circles are for stars.

3.5.4 Additional targets in the first data release

Table 3.4 shows a breakdown of the various 6dFGS-NVSS/SUMSS additional targets and the fractions which have been observed as part of the first data release. The observational completeness for additional targets is never expected to be 100% as these targets are observed serendipitously. It is expected the observed sample will be an unbiased subset of the complete target list. Very few observations south of $\delta = -50^\circ$ are available as part of the first data release, so as yet only a small number of SUMSS radio sources have been observed. However, the 17% of NVSS additional targets which have been observed represent a sizable enough sample for analysis. Chapter 4 presents an analysis of the 6dFGS-NVSS additional targets found in the first data release.

3.6 The Database

The construction of a useful database of radio source identifications to be studied in this thesis is discussed in this section. After constructing the master list of 6448 candidate radio source identifications observed in the 6dFGS First Data Release, data for each identification were downloaded from the 6dFGS public database at www-wfau.roe.ac.uk/6dFGS/. For each object the data obtained were as follows:

Table 3.4 The Sample of SUMSS/NVSS additional targets observed in the 6dFGS first data release.

Sample	N_{total}			$N_{observed}$			%
Name	Extended[a]	Stellar[b]	Total	Extended[a]	Stellar[b]	Total	Observed
NVSS	3759	3224	6997	580	609	1191	17%
SUMSS	827	1787	2614	3	3	6	0.2%

NOTES:
[a] "Extended" additional targets are those given optical morphology class 1 in the SuperCOSMOS Sky Survey.
[b] "Stellar" additional targets are those given optical morphology class 2 in the SuperCOSMOS Sky Survey.

Table 3.5 Summary of the spectral classes visually assigned to 6dFGS-NVSS objects.

Class	Type of spectrum
Aa	Pure absorption line (early-type) spectrum.
Aae	Absorption lines and narrow LINER-like emission lines.
Ae	Conventional Type I or II emission line AGN.
SF	Star-forming galaxy or extragalactic HII region.
star	Galactic star of any spectral type.
?	Unclassifiable or unknown (usually because of low S/N).

1. A 6dF spectrum of the object.
2. A b_J and r_F image of the object from SuperCOSMOS.
3. J, H & K images of the object from 2MASS (if available).
4. Data for each object, including J2000 position from the 2MASS XSC, redshift, quality flag & b_J, r_F, J, H & K magnitudes.

Images of radio contours overlaid onto SuperCOSMOS b_J images were made and each radio-optical identification was verified by the method discussed in Section 3.4.2 for primary targets and Section 3.5.2 for additional targets, the b_J images were used for verification as not all objects in the database (eg. many of the additional targets) were located in the 2MASS XSC. Removing invalid radio-optical identifications resulted in a list of true radio identifications containing 5571 objects. Next, all spectra of candidate radio sources were inspected visually and classified. The classification scheme used is discussed in Section 3.6.1. Section 3.6.2 outlines how the data were collated into a final database.

3.6.1 Spectral Classification

The 6dFGS spectrum of each of the 5571 accepted radio source identifications was inspected visually both to determine the validity of the redshift and to determine the physical

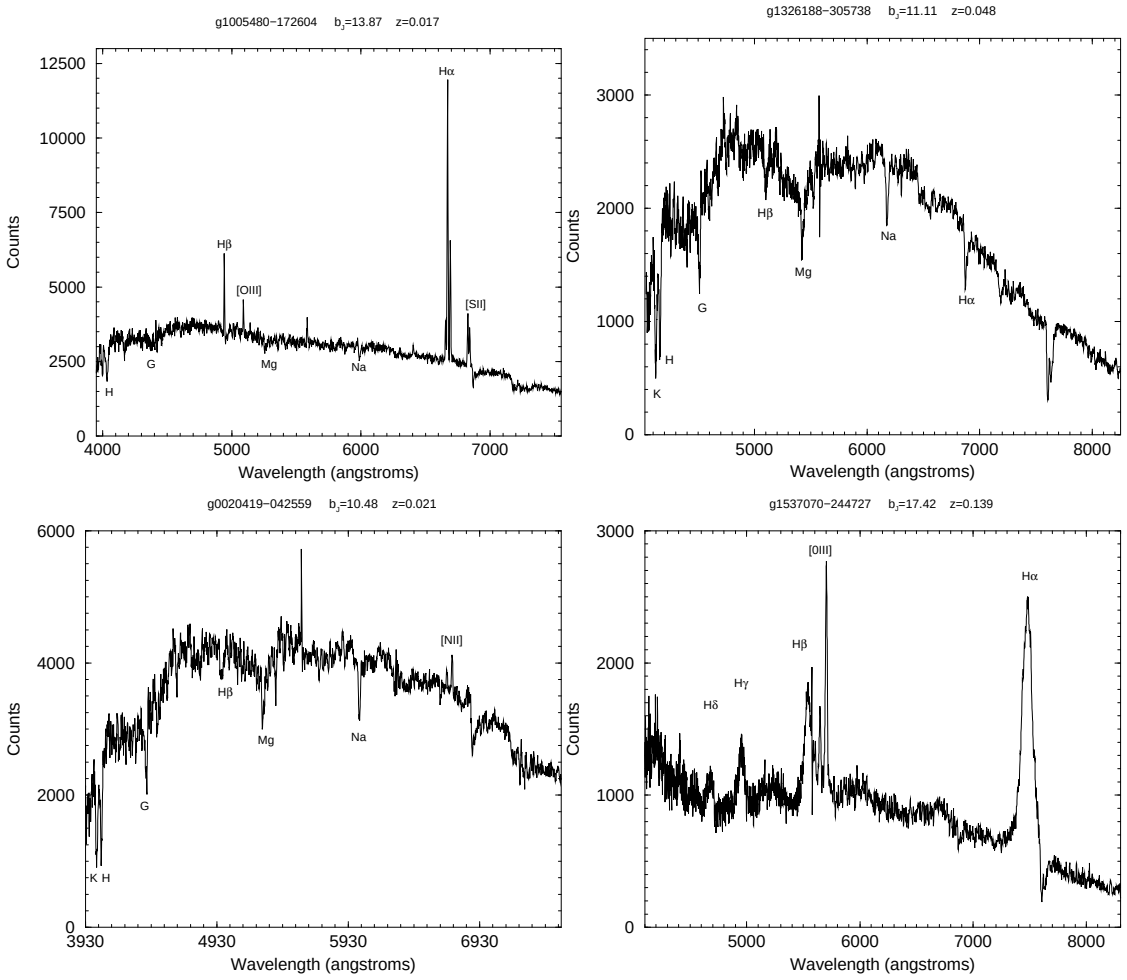

Figure 3.12 Example 6dFGS first data release spectra of 4 spectral classes. In each spectrum common redshifted absorption/emission lines are labelled at the measured redshift, as are the positions of sky emission lines. **Top left:** An 'SF' galaxy, with characteristic strong and narrow Balmer lines. **Top right:** An 'Aa' galaxy, containing broad Mg absorption as well as a distinct break close to the H & K lines at 4100 Å. **Bottom Left:** An 'Aae' galaxy. It looks similar to an 'Aa' galaxy but has a weak [NII] line at 6700 Å. **Bottom right:** An 'Ae' galaxy. This has broad Hα emission and strong [OIII] lines.

Table 3.6 Comparison of spectral classification between two human classifiers for a subset of ~ 1800 6dFGS-NVSS sources. The numbers along the diagonal indicate agreement and those off the diagonal indicate disagreement between the two human classifiers.

		Elaine Sadler									
		SF	SF?	Aa	Aa?	Aae	Aae?	Ae	Ae?	star	?
Thomas Mauch	SF	792	65	2	3	11	19	10	8	2	10
	SF?	15	17	3	1	10	10	8	3	0	5
	Aa	0	2	427	15	18	1	1	0	0	5
	Aa?	0	1	33	9	8	2	0	0	0	9
	Aae	0	0	1	0	6	2	2	0	0	0
	Aae?	0	2	2	0	24	6	7	2	0	3
	Ae	1	0	0	0	2	0	30	0	0	1
	Ae?	1	3	0	0	4	2	18	4	0	1
	star	0	0	1	0	0	0	0	0	55	5
	?	13	8	14	6	2	2	1	5	2	104

process responsible for the radio emission of each galaxy. Each spectrum was classified as either 'AGN' for spectra indicative of galaxies harbouring an active galactic nucleus or 'SF' for spectra indicative of galaxies with ongoing star formation. AGNs can have a pure absorption line spectrum like that of a giant elliptical galaxy (classed as Aa); a spectrum with absorption lines and weak narrow LINER-like emission lines (classed as Aae); a conventional Type II AGN spectrum which has nebular emission lines such as [OII] , [OIII] or [NII] which are stronger than any Hydrogen Balmer emission lines (Hα or Hβ) (classed as Ae); or a conventional Type I AGN spectrum with strong and broad Hydrogen Balmer emission lines (also classed as Ae). Star-forming galaxies have spectra typical of HII regions with strong narrow emission lines of Hα and Hβ dominating the spectrum. Figure 3.12 shows an example of each type of spectrum. Spectra of galactic stars were classified 'star' and spectra for which a classification could not be made (mostly due to a low S/N spectrum) were classed '?'. A '?' was also appended to the end of any classification which was not certain.

To check the reliability of this visual classification scheme a subsample of ~ 1800 spectra was classified by Elaine Sadler and the classifications between us compared. Table 3.6 shows this comparison. On the whole the two human classifiers agreed well, with disagreement in 10% of cases. If only the AGN and SF classes are considered then the two human classifiers disagree only 6% of the time. The main cause for disagreement comes when comparing the classifications of emission-line AGN (Aae and Ae classes) and the SF class, and tends to occur for spectra which have line ratios which are borderline between the AGN and SF. These spectra could indicate a class of galaxy which is a composite source, having ongoing star formation as well as harbouring a radio-loud active galactic nucleus. The spectra for which the two human classifiers were in disagreement were examined in detail before a final decision was made on their class. Results from this table were kept in mind during classification of the remaining ~ 3500 spectra. In their

Table 3.7 The number of spectra of each class outlined in the text for 6dFGS-NVSS primary targets and 6dFGS-NVSS additional targets.

Class	Primary sample	Additional target sample	Total
SF	2644	280	2924
Aa	1268	148	1416
Aae	187	13	200
Ae	162	84	246
star	8	394	402
?	237	146	383

analysis of 2dFGS spectra using the same classification scheme described here, Sadler *et al.* (2002) found that this scheme agreed well with methods such as principal component analysis (PCA; Folkes *et al.*, 1999; Madgwick *et al.*, 2002). This method was also found to agree well with classification based upon diagnostic emission line ratios (Jackson & Londish, 2000).

Spectra covering all 6dFGS quality classes were checked during the classification, and it was found that, in a small fraction of cases ($\sim 1\%$) spectra with $Q < 3$ were classifiable with believable redshifts. These spectra were re-redshifted using the `runz` package and included in the final sample. Classifiable spectra with $Q < 3$ are caused by errors in the redshifting process. Because of this the 6dFGS quality class was generally ignored during the analysis of the data. Table 3.7 shows how the spectra in the 6dFGS-NVSS sample were classified. Spectra of galaxies in the SUMSS sample are discussed in later chapters.

3.6.2 Sample Studied in this Thesis

After classification of all the spectra, data were compiled into a database which was compiled in both ASCII text format and as an `html` table accessible through a web browser for easy access. A search engine was also written to make selecting subsamples of the database simple. The columns of the database are as follows:

1. NVSS or SUMSS catalogue name of the source. NVSS sources start with 'N' and SUMSS sources start with 'S'.
2. 6dFGS database name of the source.
3. J2000 Right Ascension in hours, minutes and seconds.
4. J2000 Declination in degrees, arcminutes and arcseconds.
5. The 6dF measured redshift of the source.
6. The Heliocentric corrected redshift of the source.
7. The 6dFGS database quality flag for the redshift. Some sources had their redshifts remeasured; these were all assigned a redshift quality 3.
8. b_J magnitude from the SuperCOSMOS database.

9. r_F magnitude from the SuperCOSMOS database.
10. J magnitude from the 2MASS XSC. Additional targets are assigned a J magnitude of 0.
11. H magnitude from the 2MASS XSC. Additional targets are assigned an H magnitude of 0.
12. K magnitude from the 2MASS XSC. Additional targets are assigned a K magnitude of 0.
13. $b_J - r_F$ colour.
14. $b_J - K$ colour.
15. Source identification from the NASA extragalactic database.
16. Source classification from the SuperCOSMOS database. 1=Extended, 2=Stellar.
17. Position offset between the NVSS catalogue and the 2MASS XSC for primary targets and between the radio catalogue and the SuperCOSMOS database for additional targets.
18. 1.4 GHz NVSS flux density in mJy. Values were obtained from the NVSS catalogue for point sources and slightly extended sources. The flux densities of very extended sources with complex radio morphology were determined by integrating the radio emission inside a polygon drawn by hand around each source using the `cgcurs` routine in `miriad` (Sault *et al.*, 1995).
19. Position offset between the SUMSS catalogue and the 2MASS XSC for primary target sources and between the radio catalogue and the SuperCOSMOS database for additional targets.
20. 843 MHz SUMSS flux density in mJy. Values of 843 MHz SUMSS flux density were determined using the method described for 1.4 GHz NVSS flux density above.
21. $60\,\mu$m flux density in Jy.
22. Flag denoting if the source is an additional target. 'Y' denotes an additional target and 'N' denotes a primary target.
23. Spectral classification according to the scheme in Section 3.6.1.
24. Flag denoting if the source was accepted as a true radio identification by the method outlined in Section 3.4.2 for primary targets and Section 3.5.2 for additional targets.
25. Comments on the source made during spectral classification and radio-optical identification.

The `html` version of the table also contains links to an image of the 6dF spectrum, 2MASS J,H and K images of each source if available and a SuperCOSMOS b_J image of the source with radio contours overlaid.

3.7 Summary

This chapter has presented an introduction to the 6dF instrument and the 6dF Galaxy Survey and has described the method by which radio sources have been identified in the galaxy survey's primary sample, as well as how radio sources to be observed serendipitously as additional targets have been selected. Radio source spectra were then classified and a database containing data at many wavelengths was created for further analysis. In general, for both crossmatching and spectral analysis, the human eye was found to be preferable and more reliable than machine-based methods for classification. 16% of primary targets in the galaxy survey were identified with NVSS radio sources. These sources comprise 2.5% of the input radio catalogue.

The database described here comprises the largest and most homogeneous set of redshifts and spectra of radio sources in the local universe ever obtained. Results from analysis of this sample are presented in the remaining chapters of this thesis. Chapter 4 contains analysis of the additional targets, Chapter 5 presents analysis of the NVSS identified primary targets including a determination of local 1.4 GHz luminosity function and Chapter 6 presents results from a determination of the 2-point correlation function using a subsample of 6dFGS-NVSS primary targets in the first data release.

Chapter 4

The 6dFGS Additional Targets

This chapter gives an overview of the population of additional targets which have been observed in the 6dFGS first data release. Additional targets are NVSS/SUMSS radio identifications of SuperCOSMOS $b_J < 18$ objects which are not part of the 6dFGS $K < 12.75$ primary sample. The additional targets have been observed so as to quantify the population of NVSS/SUMSS radio sources which were not included in the K-selected primary target sample, either because they were too blue in optical colour, too faint or stellar in optical appearance. 6dF observations of these targets are publicly available from the 6dFGS public database at www-wfau.roe.ac.uk/6dFGS under programme id number 125. The input list of targets for observation was provided by me to the 6dFGS team as part of the work for this thesis. Note that many of these targets overlap with 8 of the 15 other additional target samples of higher priority, as tabulated in Table 4.1. The sky coverage plotted in Figure 4.1 was made using Fortran code kindly provided by Ann Burgess.

4.1 Introduction

This chapter describes the results from investigation of the additional targets observed in the first data release of the 6dF Galaxy Survey. The sample of additional targets was selected by crossmatching all NVSS radio sources with $-40^\circ < \delta < 0^\circ$ within $10''$ of extended sources (SuperCOSMOS class 1) and $5''$ of stellar sources (SuperCOSMOS class 2) brighter than $b_J = 18$ in the SuperCOSMOS database. Stellar objects with Galactic latitude $|b| < 20^\circ$ were excluded to reduce contamination of the sample by Galactic stars. All extended objects with $|b| > 10^\circ$ were included. SUMSS sources with $\delta \leq -50^\circ$ were also selected with the same input criteria as those for the NVSS, i.e. $|b| > 20^\circ$ for stellar identifications and $|b| > 10^\circ$ for extended identifications. As very little of the sky south of declination -50° has been observed in the 6dFGS first data release, discussion in this chapter is primarily about the NVSS additional targets. In Section 4.2.3 the six SUMSS additional targets in the first data release are described in more detail. A complete description of the sample selection of additional targets can be found in Chapter 3.

Additional targets are observed serendipitously as part of regular 6dF Galaxy Survey observations, meaning that a target is only observed if there is a spare fibre in a 6dF field after all higher priority redshift survey targets have been allocated. This provides a randomly selected and incomplete dataset. Study of these additional targets is intended to give an overview of the populations of radio sources which are not in the K-selected primary sample.

Section 4.2 of this chapter will present a general overview of the population of additional targets, including the fraction which were observed serendipitously. Section 4.3 will discuss the stellar objects in more detail and Section 4.4 will discuss the extended objects.

4.2 Sample Classification

The sample of 6dFGS-NVSS additional targets in the 6dF first data release comprises 1191 objects. Plots of NVSS radio contours overlaid on SuperCOSMOS b_J images were inspected for each object. 146 objects were rejected from the sample during visual inspection. This left 1045 6dFGS-NVSS additional targets with verified radio-optical identification, 521 of which were classed as stellar (or class '2' in the SuperCOSMOS catalogue (Hambly *et al.*, 2001a)) and 524 of which were extended (class '1' in the SuperCOSMOS catalogue). Hereafter objects with SuperCOSMOS class 2 will be referred to as 'stellar' and objects with SuperCOSMOS class 1 will be referred to as 'extended'. Figure 4.1 shows the location of these sources on the sky. The surface density of additional targets is greatest in the 6dF Galaxy Survey's central declination strip ($-43^\circ < \delta < -23^\circ$) and steadily decreases north toward the celestial equator. The surface density of observed objects also changes with Right Ascension. This is because additional targets are observed only when a spare 6dF fibre is available. For example, the lack of additional targets observed at 13 hours Right Ascension is because of the increased surface density of galaxies due to the presence of the Shapley Supercluster. This means that more fibres are allocated

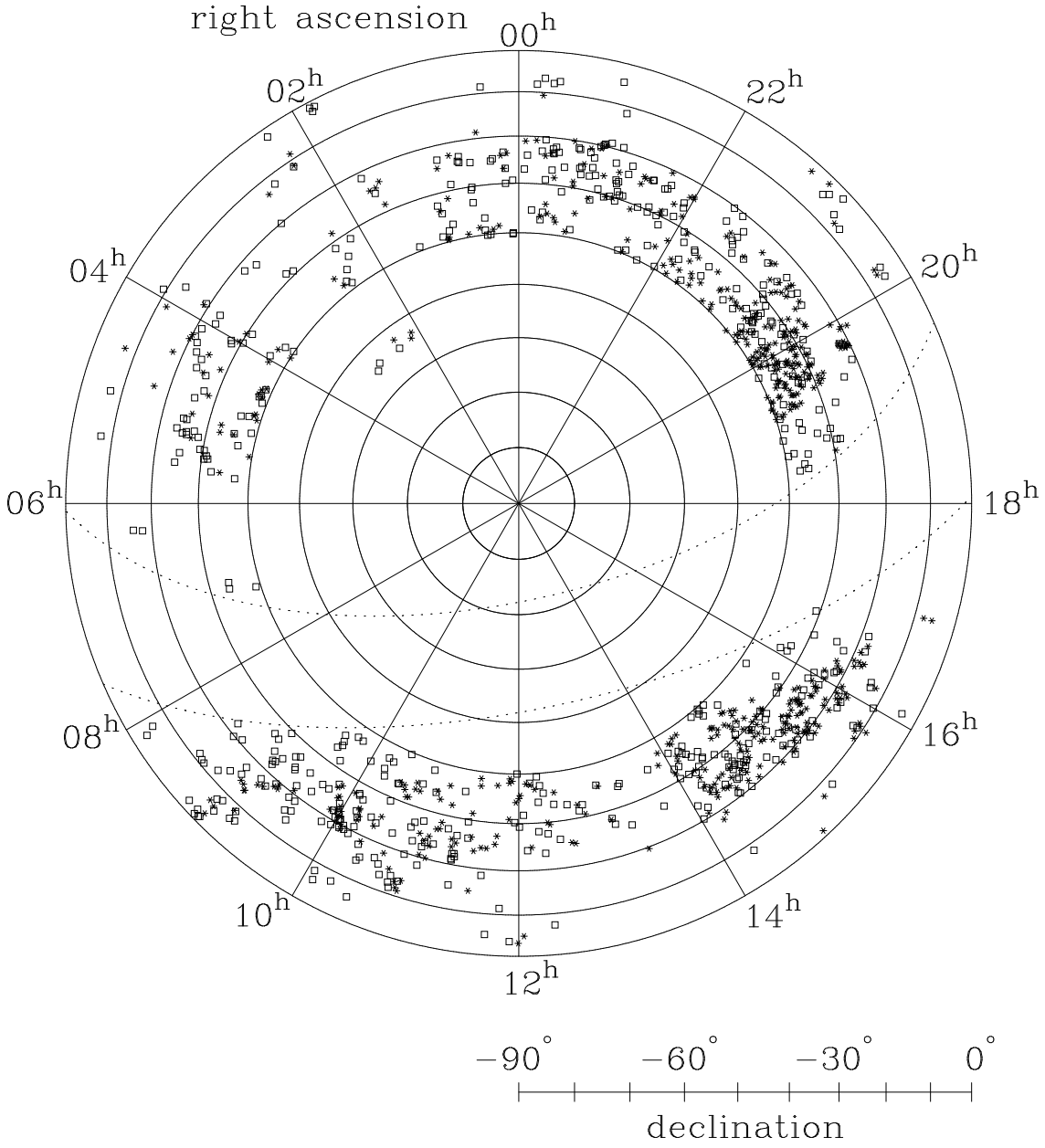

Figure 4.1 The location of the 1045 additional targets in the first data release of the 6dFGS with accepted radio-optical identifications. Stellar identifications are represented by stars and extended identifications are represented by boxes. Dotted lines are plotted at $b = \pm 10^\circ$. An increase in the density of stellar radio identifications close to $b = 20^\circ$ is clearly evident here as is a decrease in observed objects around $\alpha = 13\,h$, because more fibres are given to higher priority samples in the Shapley Supercluster region.

Table 4.1 Higher priority 6dFGS additional target samples in which SUMSS/NVSS additional targets were found.

priority[a]	id[b]	Sample[c]	Stellar	Extended
6	7	SuperCOSMOS $r_F < 15.6$	1	19
6	8	SuperCOSMOS $b_J < 16.75$	0	23
6	90	Shapley Supercluster	0	1
6	113	ROSAT All-Sky Survey	27	11
6	126	IRAS FSC 6σ ($b_J < 20$)	12	122
5	5	DENIS $J < 14.00$	0	2
4	129	Hamburg-ESO Survey QSOs	3	2
4	130	NVSS QSOs ($r_F < 17$)	193	0
1	125	NVSS/SUMSS radio sources	293	344

NOTES:
[a] Priorities are assigned between 1 (lowest) and 8 (highest) for 6dFGS samples. The primary K-selected sample has highest priority of 8. This number is used in the tiling algorithm for 6dF Galaxy survey fields. The lowest priority 1 samples (such as the 6dFGS-NVSS/SUMSS sample) have no effect on the tiling.
[b] The identification number of each additional target sample used to distinguish them in the 6dFGS public database.
[c] A complete description of the 6dF additional target samples is beyond the scope of this thesis, for further information consult the 6dFGS survey description paper (Jones *et al.*, 2004) and the 6dFGS public database at www-wfau.roe.ac.uk/6dFGS/.

to higher priority survey targets and fewer are available serendipitously.

6dFGS-SUMSS/NVSS additional targets are assigned the lowest priority when fibres are allocated to each field for 6dF observing. However, this sample overlaps somewhat with other 6dFGS additional target samples all of which are observed with higher priority. Table 4.1 shows the highest priority sample to which 6dFGS-SUMSS/NVSS additional targets belong. A little over half of the assigned targets are unique to the SUMSS/NVSS sample, the rest are distributed around the various other samples as shown in the table. The largest overlap for stellar identifications occurs with the NVSS QSO sample which has been identified on optical plates in a very similar fashion to the additional targets described here. The largest overlap with extended objects occurs with galaxies in the IRAS Faint Source Catalogue (IRAS FSC; Moshir *et al.*, 1993) sample. This is due to the well established FIR-Radio correlation (see Condon, 1992, and references therein); 110 of these were later spectroscopically identified as star-forming galaxies. There are also a small number of AGN in the IRAS FSC sample; these are believed to be galaxies which have an active nucleus as well as ongoing star formation in the disk. All of the spectroscopically identified galaxies which overlap with the Rosat All-Sky Survey (RASS; Voges, 1993) are AGN of various types.

Table 4.2 Comparison of SuperCOSMOS classification with spectral classification.

SuperCOSMOS Image Classification		Spectral Classification					
		Aa	Aae	Ae	SF	Star	Unknown
	Extended	143	13	27	262	32	60
	Stellar	5	0	57	18	362	86

4.2.1 Image versus Spectral classification

Table 4.2 shows a comparison of the spectral classification made by eye and the image classification made by SuperCOSMOS. Objects classified in optical images as extended are not expected to have the spectrum of a Galactic star, yet 32 stars were found in the extended sample. The reason for this is investigated in Section 4.4. Conversely, objects classified in optical images as stellar may have quasar spectra. 146 (or 14%) of stellar additional targets had spectra which were unclassifiable by eye, many of which had quite high S/N spectra. The fraction of unclassified spectra is much higher for the additional targets than the 5% found for the main survey targets. This is a product of both the fainter magnitude limit of the additional targets and the presence of DC white dwarf stars or BL Lac objects in the additional target sample, both of which have spectra distinguished by the absence of spectral lines. This is discussed further in Section 4.3.

4.2.2 Completeness

As additional targets are observed serendipitously their observational completeness will not be 100%. Here observational completeness is defined as the number of observed additional targets divided by the total number of additional targets in the sample. Knowing the completeness of additional targets in the first data release will allow priorities to be tuned in subsequent survey observations in case a certain class of source is observed more often than is necessary (eg. an abundance of Galactic stars may mean that it is more desirable to observe extended objects throughout the rest of the survey).

There are a total of 6998 additional targets, and of these a total of 1191 have been observed. This implies an observational completeness of 17% for additional targets. However, only 44.2% of the 6dF survey area was observed in the first data release. Assuming then that only 44.2% of the additional targets have been potentially observed the estimated fraction of additional targets being observed is $\frac{17}{0.442} = 38\%$. This implies that an additional target has a 38% chance of being observed, representing a good sample of the complete input list. It should be noted, however, that this completeness is not uniform, as some 6dF fields have more spare fibres than others. Also this fraction is likely to increase in subsequent data releases because the tiling strategy of the 6dFGS means that over-dense regions may be observed up to $\sim$ 3-4 times (Campbell *et al.*, 2004). In subsequent observations, when the density of higher priority targets is reduced, there will be more fibres available for additional targets.

It is also interesting to determine what fractions of different classes of additional targets are being observed as this may influence the priorities in future survey observations.

Table 4.3 SUMSS additional targets in the 6dFGS First Data Release

SUMSS Name	J2000 Position		SCOS	b_J	S_{843}	z	Class
	R.A.	Dec.	Class	mag.	mJy		
J020840−531332	02:08:40.75	−53:13:32.5	2	17.96	123	-	?
J021203−541018	02:12:03.22	−54:10:18.5	2	17.73	62.3	0.421	Ae?
J022925−523221	02:29:25.25	−52:32:21.5	2	17.31	2400	-	?
J022959−542633	02:29:58.96	−54:26:33.3	1	17.22	9.6	0.071	Aa?
J025849−540455	02:58:49.54	−54:04:55.2	1	17.40	10.2	0.093	Aa
J030642−545813	03:06:42.15	−54:58:13.7	1	17.09	20.5	0.074	Ae

Extended objects comprise 3759 sources in the master input list, of which 580 have been observed, an observational completeness of 15%. Stellar objects comprise 3224 sources, of which 609 have been observed meaning the observational completeness for stellar identifications is 19%. Both stellar and extended objects are therefore being selected in a relatively unbiased fashion and no change in priorities is necessary.

4.2.3 SUMSS additional targets

South of declination -50° additional targets are selected from the 843 MHz SUMSS catalogue. Only about 30 6dFGS fields are available in the first data release and only 115 SUMSS sources have been observed so far in the 6dFGS. The vast majority of these are primary targets and are not relevant to this discussion. Only 6 SUMSS additional targets are available in the first data release. Table 4.3 lists the properties of the SUMSS additional targets observed so far.

Redshifts could not be determined for two of the stellar objects in the SUMSS sample as the spectral quality was too low to distinguish any features. J021203-541018 is here tentatively classified as a quasar, but emission lines in the spectrum are very weak so the redshift and spectral classification should be treated with caution. All three extended additional targets are AGN and had good S/N spectra. The redshifts of these objects appear consistent with those found for the AGN in the NVSS selected sample (see Figure 4.12).

4.3 Stellar additional targets

Stellar identifications of NVSS radio sources in the SuperCOSMOS sky survey formed roughly 45% of the total additional target input list. Table 4.2 shows the spectroscopic classification of these sources. The vast majority of these appear to be chance identifications with Galactic stars. However, as expected, a number of radio-loud quasars appear in the sample as well. The high number of unclassifiable (due to their lack of features) spectra, despite quite high S/N, suggests the presence of a population of BL Lac objects in this sample.

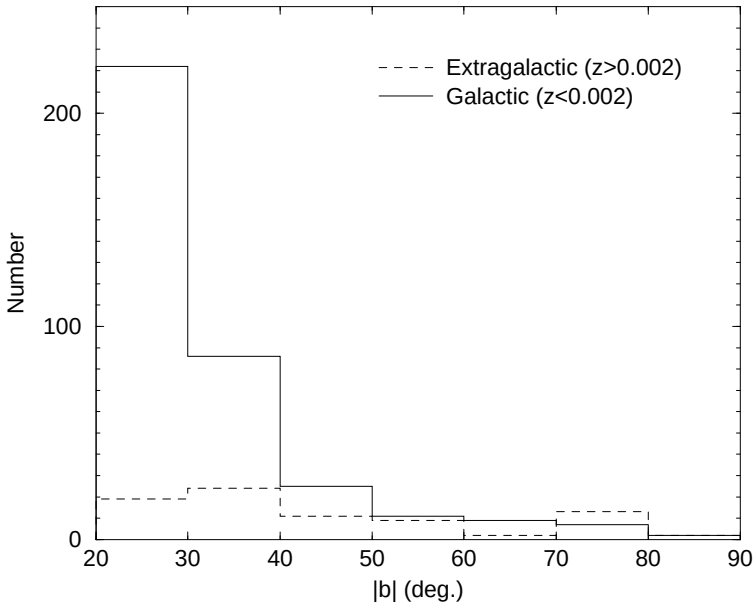

Figure 4.2 The number of Galactic (solid histogram) and extragalactic (dashed histogram) stellar objects vs. Galactic latitude. The fraction of extragalactic objects increases further from the Galactic plane. The increased numbers of objects at lower latitudes is because the bulk of 6dFGS observations in the first data release are in this region.

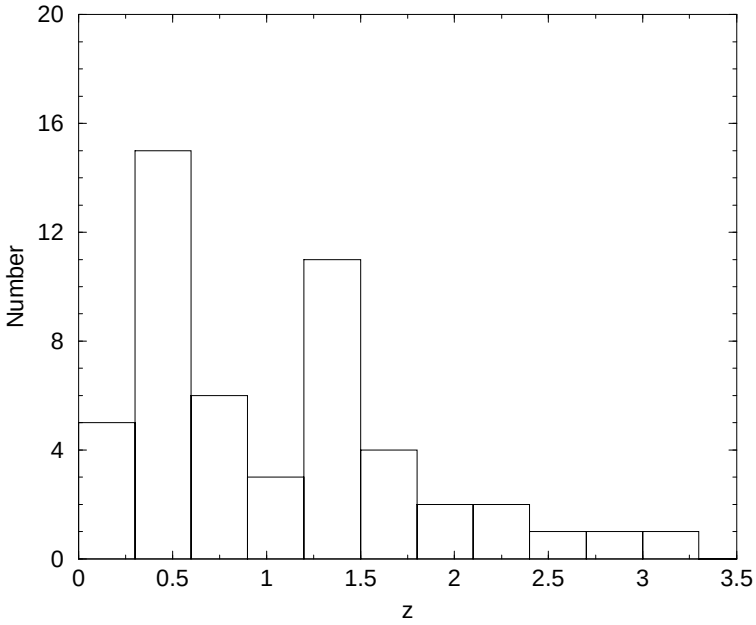

Figure 4.3 The redshift distribution of QSOs in the 6dFGS-NVSS additional target sample.

Table 4.4 A complete list of QSOs identified from the 6dFGS additional target sample.

6dF Name	RA (J2000) $hh:mm:ss$	Dec. (J2000) $^\circ:\prime:\prime\prime$	z	NED id[a]	6dF id[b]	b_J mag.	r_F mag.	$S_{1.4}$ mJy	RBSC X-ray flux ($\frac{\mathrm{mW}}{\mathrm{m}^2}$)
g0008004−233918	00:08:00.36	−23:39:18.3	1.411	[HB89] 0005−239		16.78	16.43	374.8	
g0011556−240439	00:11:55.61	−24:04:39.0	0.768	HE 0009−2421		16.84	16.44	2.6	
g0026320−183947	00:26:31.97	−18:39:46.5	0.694		113	17.41	17.19	35.9	
g0032095−382729	00:32:09.52	−38:27:29.0	0.497		113	17.69	18.05	286.1	
g0041599−392147	00:41:59.89	−39:21:46.9	1.854	[D87] UJ6536P−018		18.00	17.71	4.1	
g0045396−224355	00:45:39.57	−22:43:55.3	1.540	HE 0043−2300	113	16.86	16.28	156.7	
g0058412−390841	00:58:41.20	−39:08:40.8	1.414	[HB89] 0056−394		17.74	17.01	7.6	
g0235404−132111	02:35:40.41	−13:21:11.4	0.277		113	17.86	17.94	51.3	
g0352236−295129	03:52:23.59	−29:51:28.9	1.355		130	17.47	16.74	25.1	
g0422148−384453	04:22:14.79	−38:44:52.8	3.121	[HB89] 0420−388		17.32	16.43	197.9	
g0424422−375621	04:24:42.23	−37:56:20.6	0.781	[HB89] 0422−380	113	17.96	17.59	473.6	
g0428541−374445	04:28:54.07	−37:44:45.0	0.423		113	17.86	18.08	38.3	
g0433567−072131	04:33:56.74	−07:21:31.4	1.557		130	17.85	17.71	201.7	
g0443208−282052	04:43:20.78	−28:20:52.1	0.155	HE 0441−2826	113	15.03	14.53	37.6	2.7×10^{-12}
g0445106−383835	04:45:10.62	−38:38:35.2	0.535		113	16.57	15.97	661.0	2.4×10^{-12}
g0449423−391109	04:49:42.25	−39:11:09.4	1.296	[HB89] 0448−392	113	16.75	16.31	542.7	1.6×10^{-12}
g0458346−261124	04:58:34.59	−26:11:24.0	0.490		130	17.96	17.81	13.1	
g0536284−340111	05:36:28.43	−34:01:11.4	0.682		113	18.00	16.03	652.5	
g0902168−141531	09:02:16.83	−14:15:30.8	1.333	[HB89] 0859−140	113	16.92	16.44	2898.4	
g0927518−203452	09:27:51.82	−20:34:51.5	0.347	[HB89] 0925−203	113	16.59	16.26	849.6	4.9×10^{-12}
g1010053−250130	10:10:05.34	−25:01:30.2	0.743			17.90	17.48	4.9	
g1019463−184338	10:19:46.32	−18:43:38.3	1.597		129	17.44	16.60	110.1	
g1025310−252745	10:25:30.98	−25:27:44.7	0.580			17.68	18.04	16.3	
g1035303−182048	10:35:30.33	−18:20:47.5	0.344		113	17.08	16.24	5.1	
g1047039−130832	10:47:03.93	−13:08:32.3	1.287	HE 1044−1252		17.01	16.47	309.3	
g1103253−264516	11:03:25.30	−26:45:15.9	2.140	[HB89] 1100−264		15.95	15.86	15.4	
g1126217−312358	11:26:21.73	−31:23:58.2	0.322			17.42	16.74	11.0	
g1129149−383731	11:29:14.94	−38:37:30.8	0.233		113	16.40	15.66	5.5	5.7×10^{-12}
g1130071−144927	11:30:07.05	−14:49:27.0	1.182	[HB89] 1127−145	113	16.83	16.04	5622.8	3.0×10^{-12}

Table 4.4 A complete list of QSO's identified from the 6dFGS additional target sample (*continued*).

6dF Name	RA (J2000) $hh:mm:ss$	Dec. (J2000) $^\circ:\prime:\prime\prime$	z	NED id.	6dF id.[1]	b_J mag.	r_F mag.	$S_{1.4}$ mJy	RBSC X-ray flux ($\frac{\mathrm{mW}}{\mathrm{m}^2}$)
g1235378−251217	12:35:37.78	−25:12:16.8	0.355	[HB89] 1232−249		17.27	16.53	2177.7	
g1407549−343128	14:07:54.92	−34:31:28.2	1.122	[HB89] 1404−342		17.96	16.63	441.9	
g1419447−252152	14:19:44.67	−25:21:52.4	1.115			17.37	16.84	12.9	
g1451474−012735	14:51:47.40	−01:27:35.3	1.327	[HB89] 1449−012		17.34	16.65	530.9	
g1512083−302301	15:12:08.30	−30:23:00.8	0.173		113	17.60	17.14	3.7	
g1537070−244727	15:37:06.95	−24:47:27.4	0.139		113	17.42	16.86	3.6	
g1927069−290807	19:27:06.87	−29:08:06.9	0.434			17.76	16.77	6.4	
g1940330−364259	19:40:32.96	−36:42:58.7	1.224			16.69	16.13	48.1	
g1941102−300721	19:41:10.24	−30:07:20.5	2.063			17.78	17.12	315.4	
g1959038−353431	19:59:03.80	−35:34:30.8	0.353			17.91	17.67	1861.3	
g2051196−350001	20:51:19.56	−35:00:01.2	1.322	CTS 0550		17.91	17.44	167.6	
g2103404−384316	21:03:40.44	−38:43:15.9	0.484		130	17.17	16.60	189.0	
g2135117−331242	21:35:11.66	−33:12:41.9	1.287		130	16.63	16.00	221.8	
g2141525−372913	21:41:52.45	−37:29:12.8	0.423	[VCV2001] J214152.4−372912		17.74	17.51	397.3	
g2148484−371541	21:48:48.42	−37:15:41.1	1.287		130	17.77	17.05	11.5	
g2154450−382632	21:54:45.04	−38:26:32.4	2.803			17.83	16.74	760.2	
g2201513−334437	22:01:51.26	−33:44:37.0	2.185	CTS 0369		17.79	17.08	14.5	
g2215160−294423	22:15:16.03	−29:44:23.3	2.700	[HB89] 2212−299		17.65	17.02	467.2	
g2230403−394252	22:30:40.26	−39:42:52.3	0.318	[HB89] 2227−399	113	17.87	16.33	369.7	6.3×10^{-12}
g2236188−252441	22:36:18.79	−25:24:41.4	1.525		130	17.80	17.19	75.9	
g2343137−363753	23:43:13.65	−36:37:52.9	0.621	HE 2340−3654	113	15.98	15.57	10.3	2.7×10^{-12}
g2355330−210309	23:55:33.00	−21:03:08.7	0.429	IRAS F23529−2119	126	17.81	18.39	16.6	

NOTES:

[a] A NED id is only given if the source is identified with something other than NVSS or 6dF which are assumed for this sample. HB89 refers to Hewitt & Burbidge (1993). D87 refers to Drinkwater (1987). HE refers to Wisotzki *et al.* (2000). VCV2001 refers to Véron-Cetty & Véron (2001). CTS refers to Maza *et al.* (1995).

[b] The 6dF id number is taken from Table 4.1 and shows the higest priority sample the object appears in, if it is not unique to this sample.

[c] ROSAT Bright Source Catalogue values from Voges *et al.* (1999) are given here.

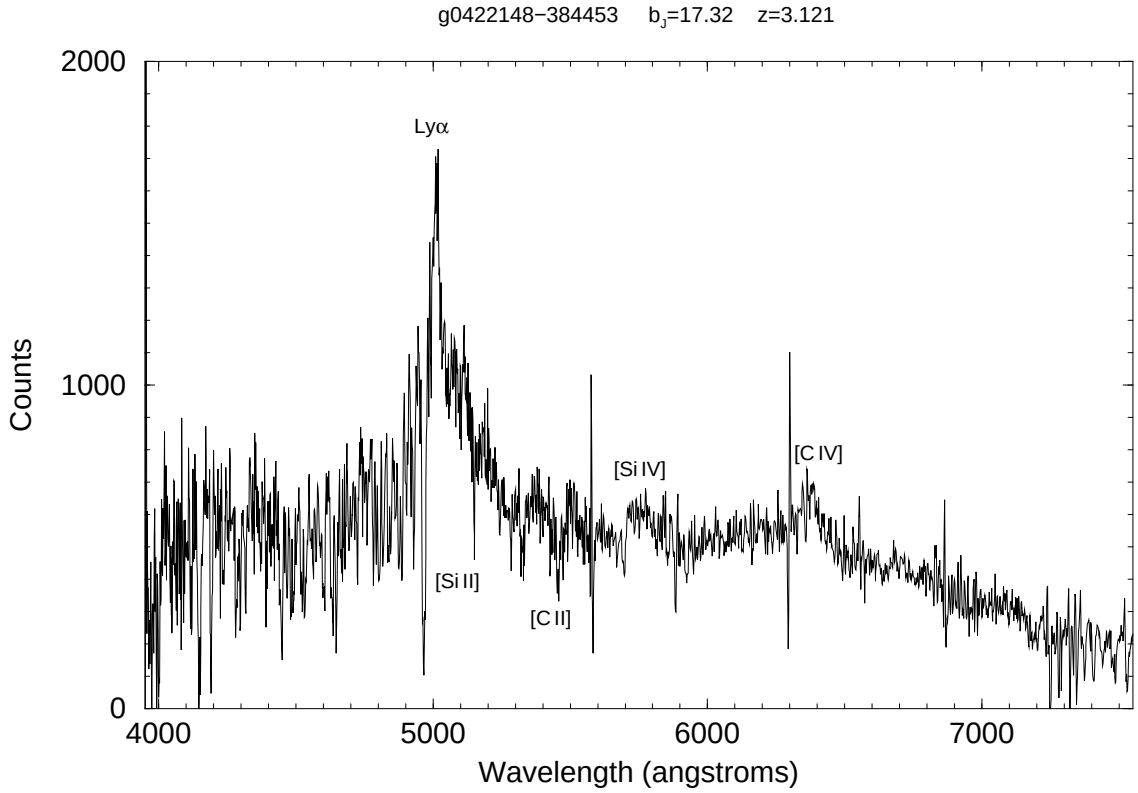

Figure 4.4 A 6dF spectrum of the highest redshift quasar in the 6dFGS-NVSS additional target sample. Broad Lyman α can be seen at ~ 5000Å as well as absorption lines caused by the Lyman α forest and a strong associated absorption in the blue wing of Lyα. This quasar has been well studied and is identified in NED as Q 0422−380 (Hewitt & Burbidge, 1993).

4.3.1 The quasar sample

Of the 55 stellar additional targets classified as Ae, 51 were identified as quasars due to their visually confirmed stellar appearance on digitised optical plates and characteristic broad spectral lines. The remaining 5 were found to be misclassified extended objects in the SuperCOSMOS catalogue. The 51 QSOs represent only 10% of the observed stellar radio identifications. This would tend to imply that searching for QSOs based purely on radio selection will not be very fruitful. However, as Figure 4.2 shows, this fraction changes steeply with Galactic latitude: of the objects with $|b| > 50^\circ$ the QSO detection rate is over 50%, similar to the detection rate of all QSOs in the optical-UV colour-selected 2dF QSO Redshift Survey (2QZ; Croom *et al.*, 2004), and much higher than the detection rate of 2QZ QSOs with the same limit in b_J. The QSOs in this sample span a large range of redshifts all the way up to $z > 3$. Figure 4.3 shows the redshift distribution of the quasar sample. The peak at $z = 1.3$ is probably due to the small numbers of objects in the sample rather than any intrinsic large scale structure.

An example of a 6dF QSO spectrum is shown in Figure 4.4 for the well known QSO Q 0420−388 (Hewitt & Burbidge, 1993). In this spectrum, as for all of the higher redshift

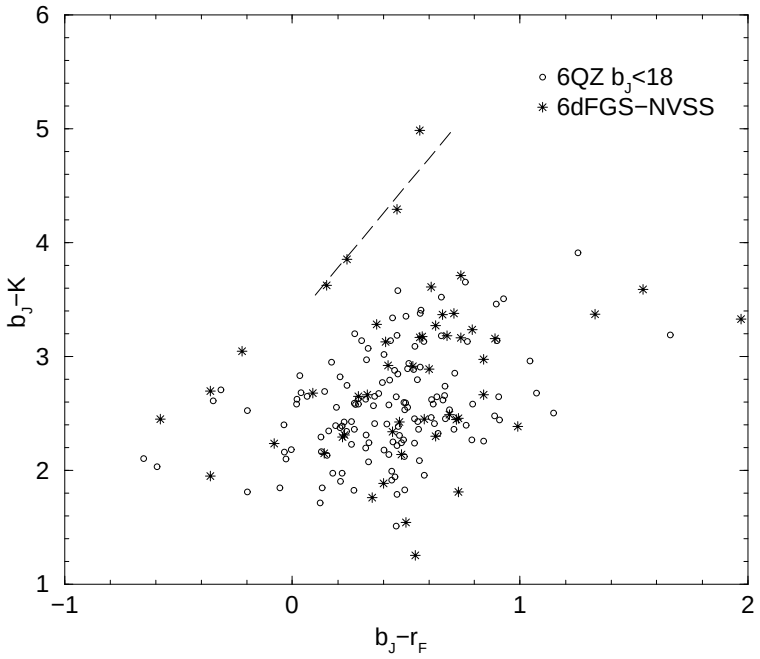

Figure 4.5 A colour-colour plot of the 51 quasars in the 6dFGS-NVSS sample (*) and 151 6QZ targets selected with the same b_J cutoff of 18 (∘). The dashed line shows the direction in which objects would move due to dust extinction in the QSO.

QSOs, broad Hydrogen Lyman α can be seen, with characteristic absorption lines to the blue caused by the Lyman α forest. Table 4.4 lists all of the QSOs in the sample. NASA Extragalactic Database (NED) identifications of previously discovered objects are shown. The QSO sample spans a wide range of radio flux densities, from the NVSS flux density limit of 2.3 mJy to the brightest objects in the entire 6dFGS-NVSS sample. ROSAT Bright Source Catalogue (RBSC) X-ray fluxes are shown for those objects with an identification in the catalogue of NVSS sources associated with the RBSC by Bauer *et al.* (2000). There appears to be no connection between the radio and X-ray properties of this quasar sample.

It is possible to compare this radio-selected sample of QSOs with optical-UV colour-selected QSOs in the 6dF Quasar Redshift Survey (6QZ; Croom *et al.*, 2004) to see if there is a class of objects which may be missed due to optical-UV colour selection. The 6QZ provides spectra and redshifts for 322 QSOs classified by their optical spectra and selected based on their stellar appearance and fulfilling at least one of the following colour criteria: $u - b_J \leq -0.50$; $u - b_J < 0.12 - 0.8(b_J - r_F)$; $b_J - r_F < 0.05$. These colour criteria are chosen to select only those objects which have a significant ultraviolet excess, a product of the non-thermal spectral energy distribution of QSO spectra. It is possible that pure optical-UV selection might miss QSOs whose host galaxies contain excessive amounts of dust which is opaque to ultraviolet light. Recent K-selected quasar samples have revealed a population of such objects (eg. Gregg *et al.*, 2002).

A subsample of the 6QZ which mimics the 6dFGS-NVSS additional target sample was created by only selecting 6QZ quasars with $b_J \leq 18$, the same as the b_J magnitude

cutoff of the radio-selected additional target sample. The 6QZ covers a region of the sky defined by a $75^\circ \times 5^\circ$ declination strip centred on $\delta = -30^\circ$ and extending from $\alpha = 21^h40^m$ to $\alpha = 3^h15^m$ (equinox B1950); this is a subregion of the radio-selected sample presented here. Only high quality QSO identifications in the 6QZ were selected, resulting in a 6QZ subsample of 151 sources to be used for comparison. Only one of the QSOs in the 6dFGS-NVSS additional target sample falls into the 6QZ region and this was also found in the 6QZ sample.

Given the relatively bright ($b_J < 18$) magnitude limit for the QSO samples, most objects should be brighter than the $K = 14.85$ limit of the 2MASS Point Source Catalogue (2MASS PSC; Cutri *et al.*, 2003). K magnitudes were obtained by crossmatching the 51 QSO positions in Table 4.4 and the 151 eligible QSO positions from the 6QZ in the 2MASS PSC. All of the 6dFGS-NVSS QSOs were present in the 2MASS PSC and all but ten from the 6QZ were found. Figure 4.5 shows a $b_J - K$ vs $b_J - r_F$ colour-colour plot for the 6dFGS-NVSS and 6QZ objects with $b_J < 18$ and $K < 14.85$. There are four 6dFGS-NVSS objects (g0458346−261124, g1512083−302301, g1537070−244727 & g1959038-353431) in this figure which lie close to the plotted long-dashed line. These have red $b_J - K$ colours and are separate from the area populated by quasars from the 6QZ. It appears that radio selection has located a population of QSOs which are missing from the optical-UV colour-selected 6QZ sample. The long-dashed line shown in the plot shows the direction an object moves in $b_J - K$ vs $b_J - r_F$ space due to dust reddening in the QSO host galaxy. All of the QSOs in the 6dFGS-NVSS sample close to the line also lie along it which indicates that these objects are from a similar population but are reddened by different amounts of dust in the host galaxy. Though radio-loud quasars form only about 10% of the total quasar population, radio selection yields a sample which is unbiased in relation to the dust content in the host galaxy.

4.3.2 A population of BL Lac objects

Fifteen of the 86 visually unclassifiable spectra of stellar objects listed in Table 4.2 had signal-to-noise of > 10 and yet no discernible emission or absorption features. These fifteen objects form an interesting subsample of spectra as they form a population of candidate BL Lac objects, which are characterised by their featureless optical spectra. A population of BL Lac objects is certainly expected in the sample, as models of the predicted population mix of radio sources at 1.4 GHz indicate the presence of these objects at the 2.3 mJy limit of NVSS (See Figure 1.7; Jackson & Wall, 1999).

A search in the NASA Extragalactic Database (NED) for previous identifications of all the 86 unclassifiable spectra found six previously identified objects. Two of these are known BL Lac objects, one of which had a S/N> 10 spectrum, shown in Figure 4.6. The remaining four NED identifications of unclassifiable spectra are quasars whose 6dF spectra were too low in quality to make a reliable classification or determine a redshift.

The question remains about what the remaining fourteen high S/N featureless continuum objects are. One of them is an X-ray source, often a signature of AGN activity. The spectrum of this object has a S/N of 10.9 and is shown in Figure 4.7. This spectrum is clearly featureless and is therefore identified here as a BL Lac object. A list of all fifteen

Table 4.5 Fifteen featureless optical continuum objects.

6dF Name	α (J2000)	δ (J2000)	b_J	Spec.	$S_{1.4}$	X-ray Flux
	$h:m:s$	$^\circ:\prime:\prime\prime$	mag.	S/N	mJy	mW/m^2
g0054467−245530	00:54:46.73	−24:55:29.5	17.79	10.9	24.3	1.80×10^{-12}
g0100228−334127	01:00:22.83	−33:41:26.5	17.53	13.3	3.6	
g0448376−163243[a]	04:48:37.64	−16:32:42.9	16.76	12.3	59.0	4.83×10^{-12}
g0859076−053956	08:59:07.55	−05:39:55.9	17.03	12.6	63.5	
g1413319−300244	14:13:31.92	−30:02:43.6	16.95	14.4	712	
g1427435−260856	14:27:43.53	−26:08:55.5	17.81	10.8	3.0	
g1441160−231330	14:41:15.95	−23:13:30.1	17.83	10.6	4.6	
g1507297−300648	15:07:29.68	−30:06:48.2	17.45	14.0	9.1	
g1546141−085555	15:46:14.13	−08:55:55.4	17.80	10.5	8.1	
g1619398−192136	16:19:39.75	−19:21:35.5	17.73	13.6	8.6	
g1926301−352904	19:26:30.14	−35:29:03.9	17.63	10.5	81.8	
g2033428−341358	20:33:42.83	−34:13:58.0	17.72	10.2	4.1	
g2035041−263217	20:35:04.14	−26:32:17.1	17.67	10.6	231	
g2316161−350403	23:16:16.08	−35:04:03.3	17.74	10.7	4.2	
g2346049−104046	23:46:04.85	−10:40:45.7	16.66	13.1	2.2	

NOTES:
[a] This is the known BL Lac object identified in NED. Its spectrum is shown in Figure 4.6.

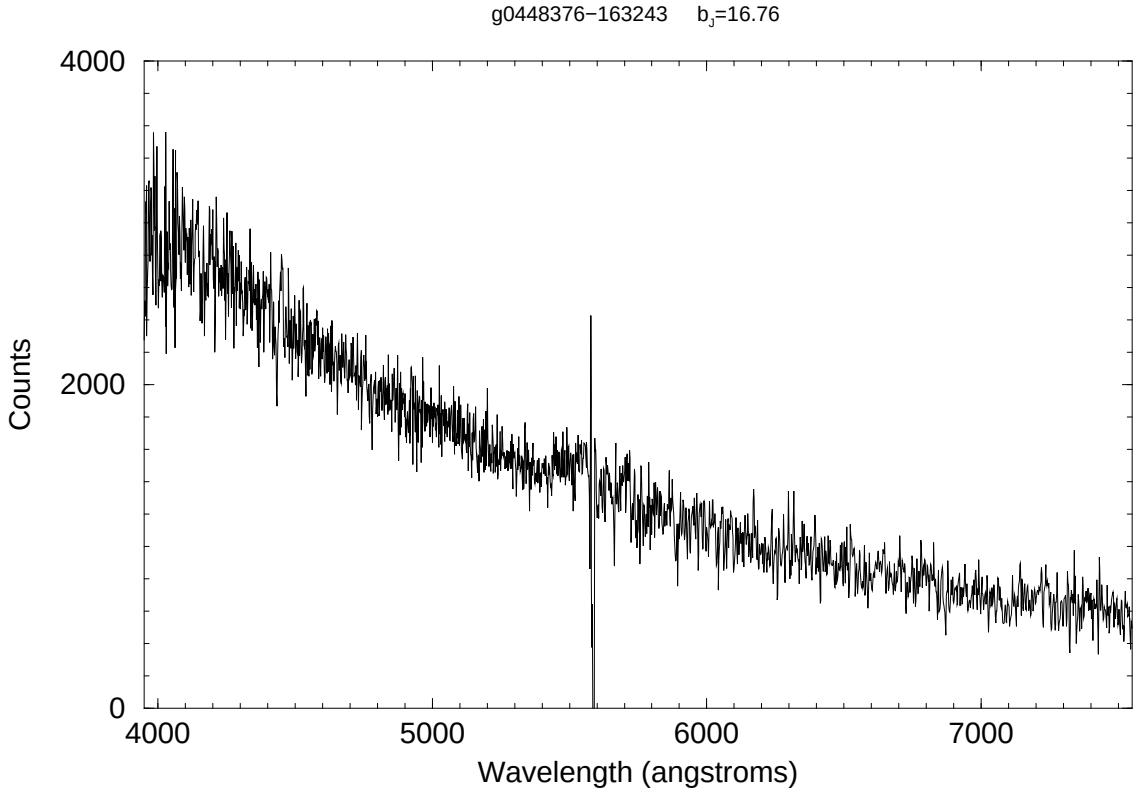

Figure 4.6 Spectrum of a BL Lac object in the 6dFGS-NVSS additional target sample identified in NED (RBS 0589). It has a S/N of 11.80 and NVSS flux density of 59.0 mJy. This object is also an RASS X-ray source.

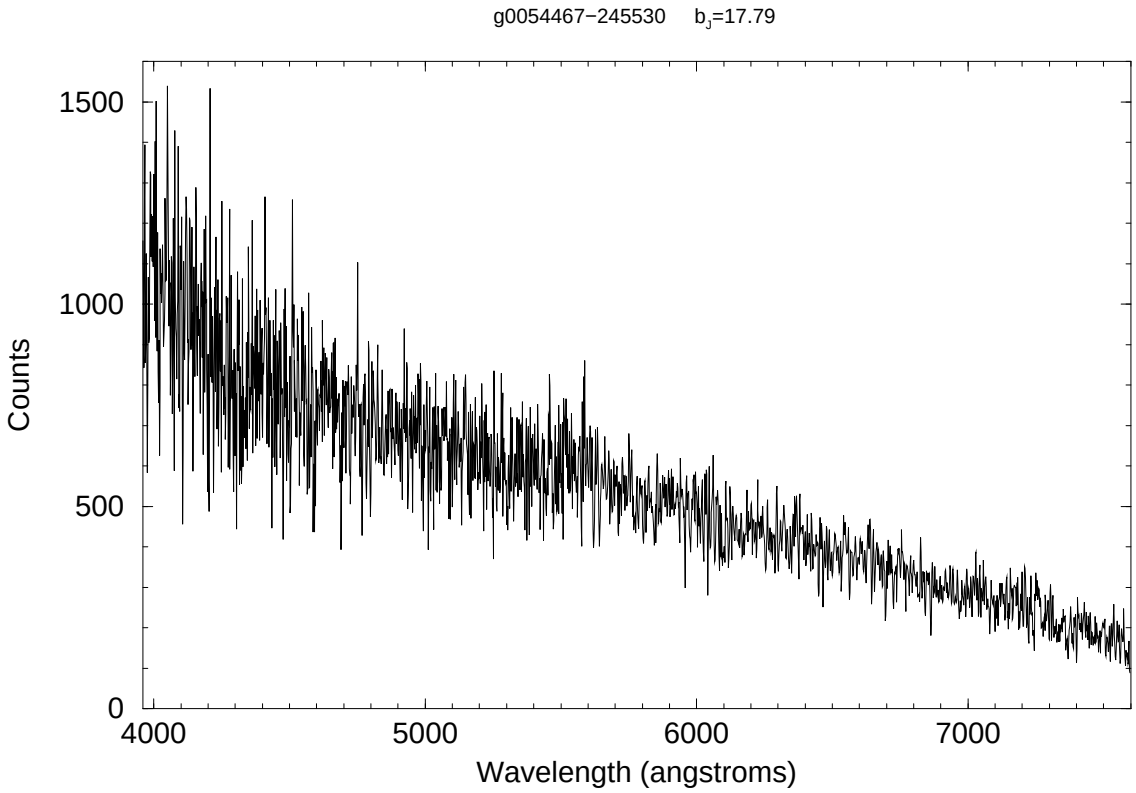

Figure 4.7 The spectrum of a featureless continuum object with both a radio and X-ray identification. It is here identified as a BL Lac objects.

featureless continuum objects which form a candidate BL Lac object population is shown in Table 4.5.

The most likely non-AGN class of objects which could be confused with a BL Lac object on the basis of their optical spectra are DC white dwarfs. Though these are not expected to be NVSS radio sources, chance coincidences are possible at lower Galactic latitudes. Londish *et al.* (2002) describe a method of distinguishing BL Lac objects from DC white dwarfs by measuring their proper motion. The SuperCOSMOS catalogue quotes proper motions for all the objects in the additional target sample. These proper motions are measured by comparing the positions of objects on UKST r_F photographic plates which are observed with an epoch separation of greater than 10 years. This epoch separation corresponds to 3σ proper motions of more than 30 mas year^{-1}.

Galactic stars should have a different distribution of proper motions to extragalactic objects such as QSOs or BL Lac objects, which should exhibit no significant proper motions at all. Figure 4.8 shows the distribution of proper motions divided by their error quoted in the SuperCOSMOS catalogue, for different stellar additional target samples under consideration. Objects with proper motions larger than 3σ are here believed to be Galactic rather than extragalactic as extragalactic objects are expected to have no measurable proper motions. Galactic objects on the other hand may have proper motions less than 3σ, but should form a population which is distributed differently. To explore this

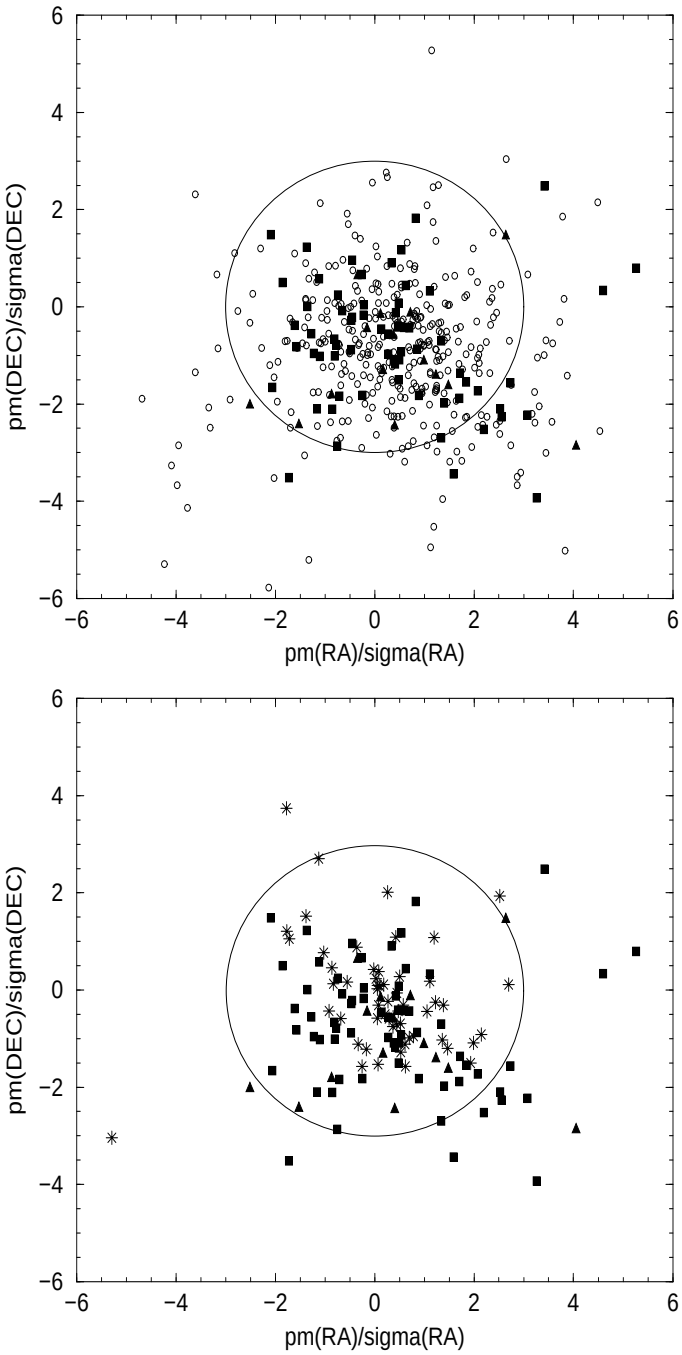

Figure 4.8 **Top:** The distribution of proper motions for the 362 stellar additional targets (open circles), the 14 S/N$\geq$ 10 unclassified objects with no NED identification (filled triangles), and the 65 S/N$<$ 10 unclassified objects with no NED identification (filled squares). A circle is plotted at the 3σ radius. **Bottom:** The distribution of proper motions for the 51 QSOs and 6 objects with NED identifications (asterisks) and the unclassified objects overlaid as in the top plot. The QSOs with proper motions $> 3\sigma$ are due to errors in the SuperCOSMOS catalogue.

Table 4.6 Results from the K-S test comparing the various stellar subsamples to the distribution of stars.

Sample	N	d[b]	P[c]
QSOs + NED[a]	57	0.32	0.0001
Unknowns (S/N$\geq$ 10)	14	0.29	0.15
Unknowns (S/N$<$ 10)	65	0.13	0.29
Unknowns (All)	80	0.12	0.29

NOTES:
[a] The six QSOs and BL Lac objects identified in NED have been removed from the unknowns and added to the QSO sample in this table.
[b] The K-S statistic d is the maximum value of the absolute difference between the cumulative distribution functions of two samples, in this case the radial distribution of proper motions of stars and the radial distribution of proper motions of the sample in the previous column.
[c] The probability derived from the statistic d that the samples come from the same population.

further a one-dimensional Kolmogorov-Smirnov (KS) test was made on the radial distribution of proper motions of the sample of QSOs and stars. The first row of Table 4.6 shows the results of this KS test. The radial proper motion distribution of QSOs is clearly different to that for stars at a $> 99\%$ confidence level.

Table 4.6 also compares the results of the KS test on the radial proper motion distribution of the unclassified spectra. Values of P close to 0 indicate a higher confidence that the two cumulative distributions are different. Whilst the KS test can distinguish between the QSO and star sample with a high degree of confidence, the results for the unknown spectra are inconclusive. More than one of the fifteen objects with S/N$\geq$ 10 spectra listed in Table 4.5 should be BL Lac objects. Validating the radio-optical identification with higher resolution radio observations and obtaining high resolution spectra with better S/N to search for features is required to confirm the identifications presented in this table.

4.3.3 Extragalactic HII regions

There is a population of 16 additional targets which were classified as stellar in the SuperCOSMOS catalogue and were found to have spectra indicative of ongoing star formation. Star formation usually occurs in extended HII regions in galaxies or in galaxy mergers, though the brightest and most compact extragalactic HII regions may appear stellar on optical plates. The radio and optical properties of those identified in the 6dFGS-NVSS additional target sample are tabulated in Table 4.7. Figure 4.9 shows a typical example of the 16 objects; some extended structure is evident in the image and the spectrum is that of a typical star-forming galaxy. These compact regions of emission may be due to a localised burst of star formation within a host dwarf galaxy (Telles *et al.*, 1997). The derived radio powers are generally indicative of moderate to high star-formation rates. These objects are found at higher redshifts than the bulk of the star-forming galaxies in the 6dFGS-NVSS sample. A faint host galaxy can usually be seen in more nearby objects of this type meaning that they do not appear stellar on optical plates.

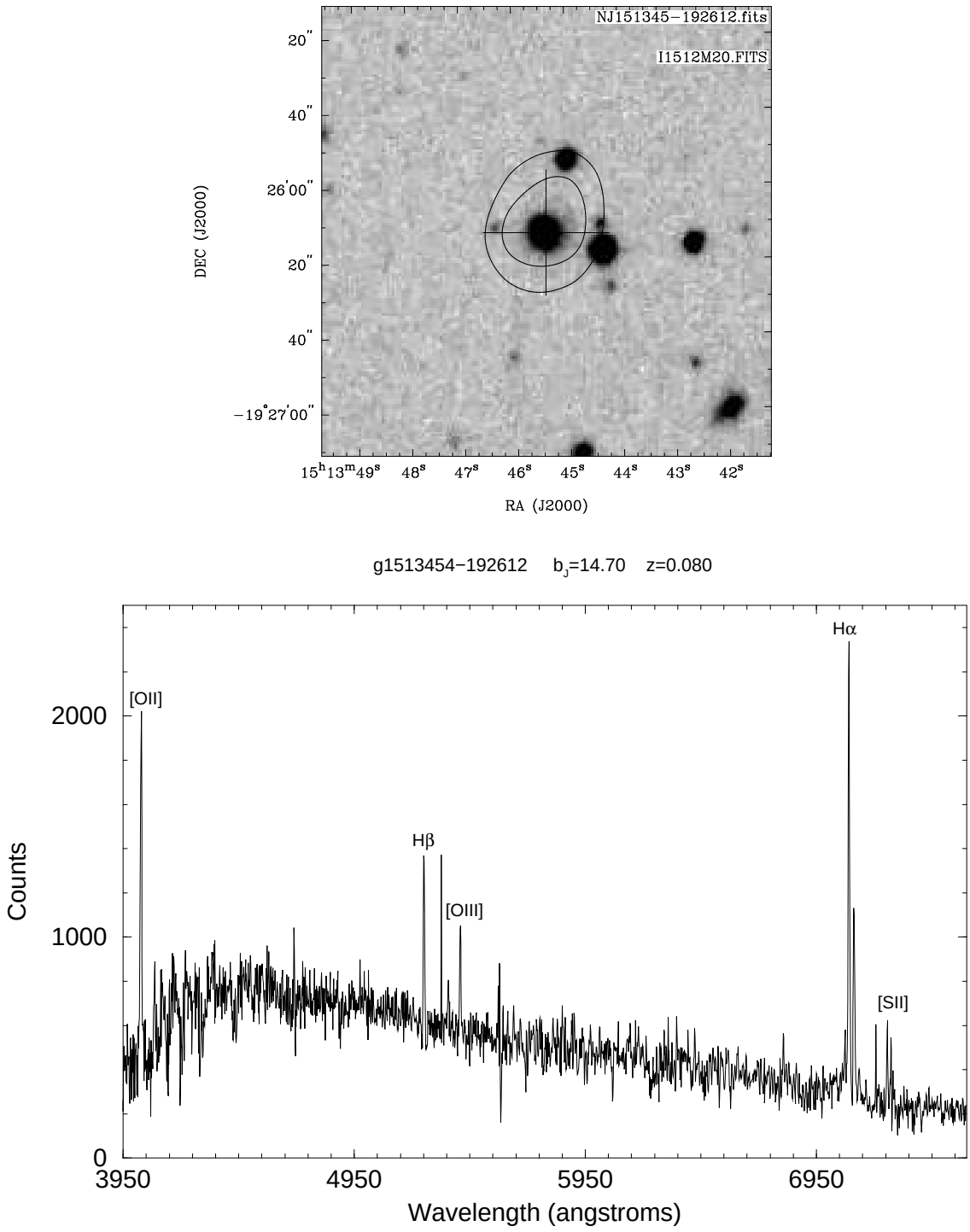

Figure 4.9 Above: SuperCOSMOS image of the galaxy g1513454-192612 with 2 mJy and 2.5 mJy contours from the NVSS overlaid. Crosshairs are shown at the position the 6dF fibre was placed for observing. Below: The 6dF spectrum of the above galaxy, with prominent features labeled.

Table 4.7 The population of extragalactic HII regions in the additional target sample

6dF Name	RA (J2000) $h:m:s$	Dec. (J2000) $^\circ:\prime:\prime\prime$	z	b_J mag.	$S_{1.4}$ mJy	$\log(P_{1.4})$ W Hz^{-1}
g0059190−393933	00:59:19.00	−39:39:32.7	0.056	15.20	4.1	22.45
g0142010−243313	01:42:00.95	−24:33:12.5	0.060	14.53	3.4	22.44
g0349538−400341	03:49:53.75	−40:03:41.4	0.099	15.44	15.8	23.56
g0401596−364055	04:01:59.64	−36:40:54.9	0.100	15.71	3.7	22.94
g0514508−270518	05:14:50.75	−27:05:17.6	0.073	15.05	2.8	22.54
g0520451−392547	05:20:45.10	−39:25:46.7	0.097	14.08	11.3	23.39
g1057181−234259	10:57:18.09	−23:42:59.3	0.085	14.35	2.3	22.58
g1127434−263029	11:27:43.39	−26:30:28.7	0.060	15.54	3.6	22.46
g1152586−304927	11:52:58.60	−30:49:27.0	0.074	14.98	2.5	22.49
g1513454−192612	15:13:45.41	−19:26:12.4	0.080	14.70	3.3	22.69
g2019103−323530	20:19:10.28	−32:35:29.9	0.035	13.94	3.4	21.97
g2041045−320526	20:41:04.45	−32:05:26.0	0.095	14.14	2.5	22.72
g2128194−261325	21:28:19.38	−26:13:24.6	0.110	14.22	3.8	23.03
g2152109−363607	21:52:10.85	−36:36:06.5	0.068	14.85	3.2	22.52
g2216151−285917	22:16:15.07	−28:59:16.8	0.182	17.05	2.6	23.34
g2332144−363532	23:32:14.37	−36:35:32.3	0.073	14.94	2.7	22.51

These radio sources form part of a population of objects which would be missed from most redshift surveys of the local universe. This is because galaxies are usually selected on the basis of extended optical morphology. Given that 16 such radio sources have been observed and that only 38% of all additional targets are being observed, one can expect that approximately 45 such objects are missing from the sample volume of the primary targets. These comprise only 2% of the total population of local star-forming radio sources and should not affect results derived from the primary sample.

4.4 Extended additional targets

The sample of additional targets which were classified as extended by SuperCOSMOS are expected to be either galaxies which are missed from the K-selected 6dFGS input catalogue because they are blue in colour (Seyfert galaxies or starburst galaxies) or fall below the $K = 12.75$ threshold of the primary sample. As can be seen in Figure 4.10, this is what was found on the whole. At b_J magnitudes fainter than 17 the population of additional targets is just a fainter extension of the primary sample with similar mean $b_J - r_F$ colour. The few additional targets brighter than $b_J = 17$ tend to have bluer colours than the primary sample.

The first row of Table 4.2 shows the spectral classification of 6dFGS-NVSS additional targets with extended optical morphology. About 10% of the total list had spectra which were unclassifiable, double the fraction of such spectra in the K-selected primary sample. This can be explained in terms of the fainter magnitude cutoff of the additional target

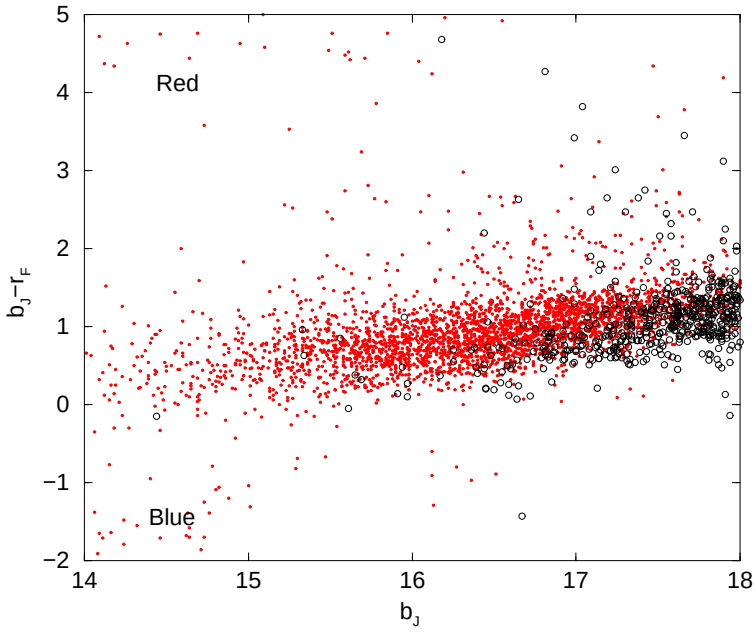

Figure 4.10 The distribution of $b_J - r_F$ colours vs b_J magnitude for observed radio sources in the K-selected galaxy survey (red dots) and additional target galaxies (black circles). The additional targets tend to be slightly bluer at brighter magnitudes.

sample. The average S/N of spectra in the additional target sample is 9.9 which is lower than the average S/N of radio source spectra in the primary sample (12). Lower S/N spectra are more difficult to classify, leading to an increased fraction of unclassified spectra in the additional target sample. All the low S/N spectra in the extended additional target sample had b_J magnitudes fainter than 17.

4.4.1 Blue galaxies

Additional target galaxies brighter than $b_J = 16$ in Figure 4.10 are quite rare. These are objects which have fallen out of the primary sample because their K magnitude is fainter than 12.75, but their bright b_J magnitude indicates these galaxies are extremely blue. The mean $b_J - K$ colour of galaxies in the primary sample is 4.44; additional target galaxies with $b_J < 16$ have $b_J - K_S < 3.25$. Of the 12 additional target galaxies with $b_J < 16$, four are found in the 2MASS XSC. Two of them are AGN (a Seyfert II (Ae) galaxy and an Aae galaxy) and the remainder are all star-forming galaxies. An example of one of the star-forming galaxies is shown in Figure 4.11. Complex structure can be seen in the SuperCOSMOS b_J image (top left) possibly from an interaction between two galaxies or compact HII regions in a single galaxy. The radio source is powered by star formation. In the 2MASS K-band image very little structure can be seen, radio contours from NVSS are overplotted as are cross-hairs at the position where the 6dF fibre was placed to observe the spectrum below. A small K-band source is visible to the west of the cross-hairs in the 2MASS image, and is associated with the brightest object in the b_J image on the

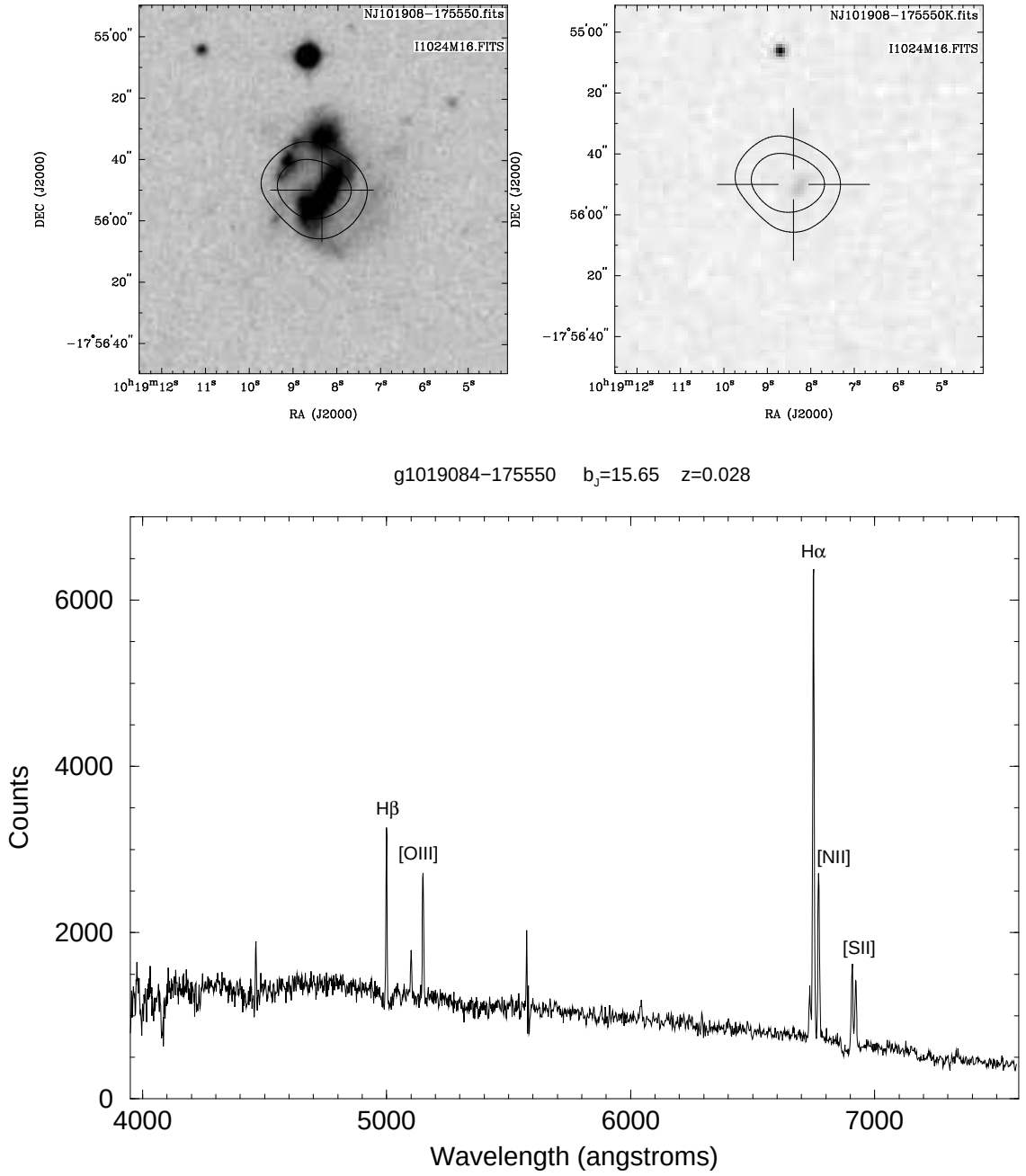

Figure 4.11 Top Left: SuperCOSMOS b_J image of the 6dFGS-NVSS additional target g1019084-175550 with NVSS radio contours overlaid at 2, 2.5 mJy. Top Right: 2MASS K-band image of the same object with same radio contours. Bottom: 6dF spectrum of the object.

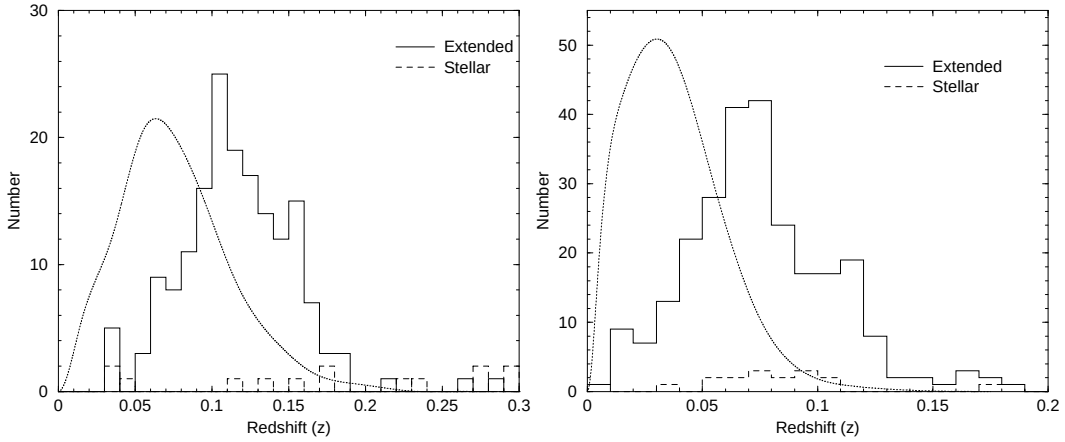

Figure 4.12 The redshift distribution of AGNs (left) and SF galaxies (right) in the additional target sample. The dotted line in each plot shows the redshift distribution of galaxies in the main redshift survey scaled to the same sample size.

left. This object has a K magnitude of 12.9 in the 2MASS XSC, fainter than the 6dFGS primary sample threshold. Its spectrum is that of a typical star-forming galaxy. Much of the optical emission from this galaxy is from very recent star formation, where younger and bluer stars are found. Galaxies such as this are "missed" in the K-selected primary sample because they have little or no old stellar population, but are hosting some of the youngest starbursts in the local universe.

The galaxy in Figure 4.11 is typical of all ten of the star-forming galaxies with $b_J < 16$ in the additional target sample. All of these, as well as the two blue AGN have redshifts compatible with galaxies in the primary sample ($\tilde{z} \sim 0.05$) rather than the additional targets ($\tilde{z} \sim 0.08$). There are ~ 2000 galaxies with $b_J < 16$ in the primary sample. 12 have been found thus far in the additional target sample, which is only 38% complete (see Section 4.2.2), implying that in a 100% complete sample about 30 such galaxies would be found. This means that around 1% of radio sources such as these are being missed from the near-infrared-selected primary sample. These blue galaxies are found even at very low redshift ($z < 0.01$) which implies that there is no redshift for which the near-infrared-selected primary sample can be considered "complete".

4.4.2 Redshift Distribution

Figure 4.12 shows the redshift distribution of both the AGN and star-forming additional targets. The dotted line in each plot shows a fit to the redshift distribution of galaxies in the primary sample scaled to the same number of objects as the additional targets. The median redshift of additional target AGNs is $\tilde{z} = 0.117$, higher than that of AGNs in the K-selected primary sample ($\tilde{z} = 0.073$). For star-forming galaxies the median redshift for additional targets is $\tilde{z} = 0.074$, again higher than that of star-forming galaxies in the primary sample ($\tilde{z} = 0.035$). This can be explained by considering the fainter optical magnitude cutoff of additional target galaxies. Roughly the same population of radio

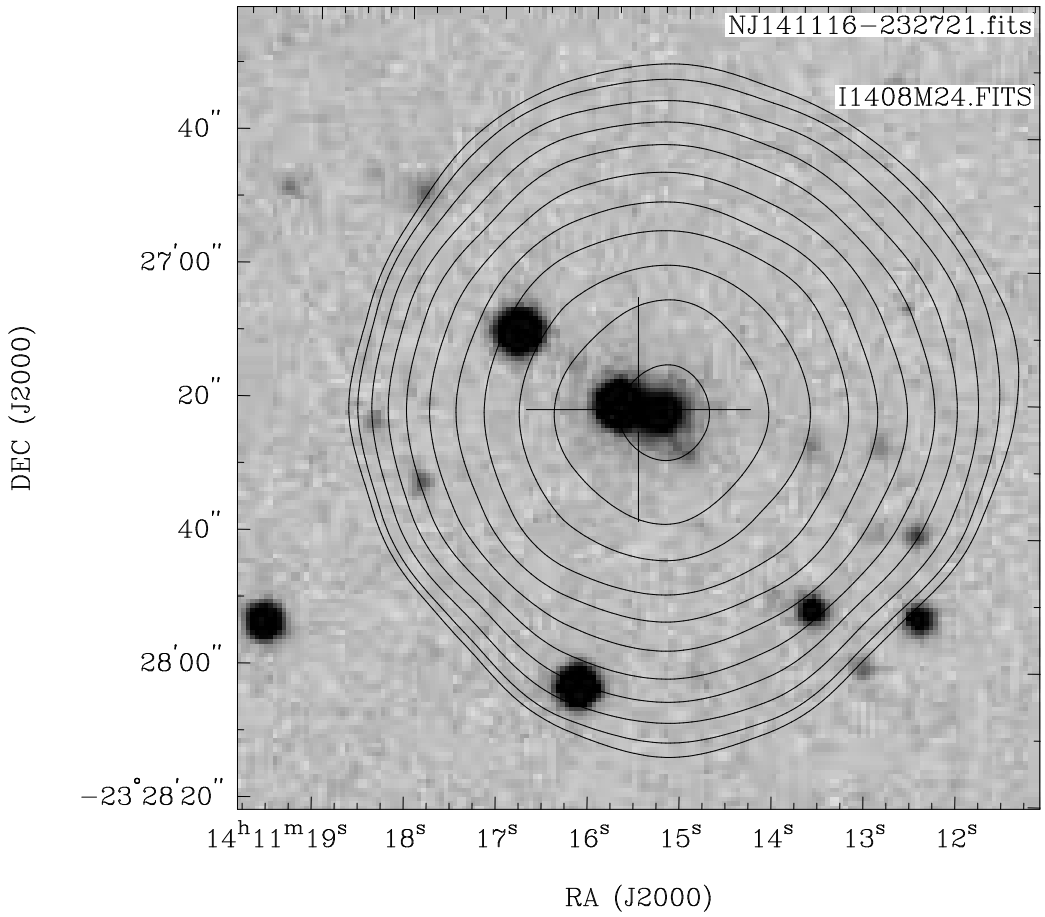

Figure 4.13 An image of the 6dFGS-NVSS additional target g1411155-232721 with NVSS radio contours overlaid. SuperCOSMOS classified this object as extended because the background galaxy is blended with a foreground star.

sources is being probed at a fainter magnitude limit, hence a higher median redshift. The broad low-z wing on the distribution of star-forming additional targets comes from the small population of blue galaxies described in Section 4.4.1.

4.4.3 Stars in the extended object sample

Finally it is worth making brief mention of the spectroscopically identified stars which were classed as extended in the SuperCOSMOS catalogue. 32 such stars were found, representing 6% of the total number of extended additional targets. This is double the fraction of stars contaminating the 6dFGS as a whole (Jones *et al.*, 2004). Figure 4.13 shows an example of a SuperCOSMOS "extended" object which is a blend of a Galactic star and an NVSS radio identification. The radio emission is coming from the background galaxy which can be seen to the right of the cross-hairs in the image. The cross-hairs show the position quoted in the SuperCOSMOS catalogue for this blended object. Unfortunately, light from the star has dominated the spectrum of this object, making it impossible to

distinguish features from the background galaxy. All of the stars with "extended" SuperCOSMOS classification can be attributed to similar limitations in the SuperCOSMOS catalogue.

4.5 Conclusion

This chapter has presented an overview of the population of 1191 6dFGS-NVSS additional targets observed serendipitously as part of the 6dF Galaxy Survey over the period January 2002 and July 2003. These targets give an overview of the population of 'missing' radio source identifications of $b_J < 18$ objects in the main redshift survey. The main results of this study are as follows:

- A SUMSS/NVSS additional target which is observed as part of the 6dF Galaxy Survey had a 38% chance of being observed in the First Data Release. This fraction may increase in subsequent data releases as the density of higher priority targets in fields observed repeatedly decreases.
- There are 16 identifications of 'stellar' objects which have star-forming galaxy spectra indicating a population of 'HII galaxies' missing from radio samples selected from optical galaxy catalogues.
- Galactic stars which are positionally coincident with background galaxies have led to spurious radio source identifications. Such spurious identifications account for $< 3\%$ of all additional targets.
- 69% of identifications of NVSS radio sources with stellar SuperCOSMOS catalogue objects with $b_J < 18$ are chance coincidences with Galactic stars. The fraction of such chance identifications decreases strongly at higher Galactic latitude, with only 45% of objects at $|b| > 50^\circ$ being chance identifications of Galactic stars. This implies that blind radio-selected quasar surveys at high Galactic latitude are as efficient as optical-UV colour-selected quasar surveys.
- Radio selection has identified a population of 'reddened' quasars which are missed in optical-UV colour-selected samples. Such objects represent $10 \pm 4\%$ of the complete radio-selected quasar population.
- A sample of 15 featureless continuum objects has been found. These are here identified as candidate BL Lac objects.
- 1% of extended additional target galaxies are missing from the $K < 12.75$ primary sample because they have blue ($b_J - K < 3.25$) colours. Most of these are star-forming galaxies which form a population of extremely young starbursts in the local universe.
- A population of $16 < b_J < 18$ galaxies is too faint to be in the primary sample. These form a similar population of radio sources to those in the primary sample but have a higher median redshift.

Table 4.8 The population of galaxies "missing" from the primary target sample

Population	$N_{\rm observed}$	$N^{a}_{\rm estimated}$	$\bar{z}$	Space Density (Mpc^{-3})
Stellar				
Star-forming	16	45	0.08	2×10^{-7}
AGN	8	21	0.13	3×10^{-8}
Total	25	66	0.1	1×10^{-7}
Extended $b_J < 16^{b}$				
Star-forming	10	26	0.03	1×10^{-7}
AGN	2	5	0.03	2×10^{-8}
Total	12	32	0.03	1×10^{-7}
Extended $b_J > 16^{b}$				
Star-forming	249	655	0.08	3×10^{-6}
AGN	165	434	0.12	2×10^{-6}
Total	414	1089	0.09	5×10^{-6}

NOTES:
[a] $N_{\rm estimated}$ is calculated by dividing the number of observed additional targets $N_{\rm observed}$ by 0.38 which is the fraction of additional targets which are being observed, as estimated in Section 4.2.2. The number in this column gives an estimate of the *total* number of each population of objects which is missing from the primary K-selected sample.
[b] The extended additional targets are separated by b_J magnitude to delineate the population of objects which is missed from the primary sample because they are too blue in colour ($b_J < 16$ implies $b_J - K < 3.25$) and those that are missed because they are too faint ($b_J > 16$).

The additional targets have identified some interesting classes of radio source in the local universe which are not part of the K-selected primary sample. These are listed in Table 4.8 which shows the number of radio sources of various types restricted to the maximum redshift $z = 0.2$ of the primary sample. Galaxies which appear stellar on optical plates are found at a higher median redshift than galaxies in the primary sample and account for roughly 2% of the complete local radio source population. These radio sources have also been missed from samples selected from other redshift surveys such as the 2dFGRS which only select galaxies that appear extended on optical plates. Galaxies which appear too blue on optical plates account for roughly 1% of the local K-selected radio source population. Though these additional target populations are interesting in themselves they are not large enough to significantly affect the results derived from the primary target sample.

Chapter 5

The local Radio Luminosity Function at 1.4 GHz

In this chapter the 6dFGS-NVSS primary targets are studied in some detail. This includes an investigation of the radio-FIR correlation, the local radio luminosity functions and the fractional radio/K-band luminosity functions of the primary targets. A derivation of the star-formation density at the present epoch is also made.

Work contributed by others:

- Figure 5.18 is a *preliminary* 6dFGS K-band luminosity function which was provided to me by Heath Jones, it will be published shortly (Jones, 2005).

5.1 Introduction

In recent years a new generation of radio surveys have been released covering a large fraction of the celestial sphere down to radio flux density levels of a few mJy (eg. NVSS, Condon *et al.* (1998); SUMSS, Mauch *et al.* (2003); FIRST, Becker *et al.* (1995); WENSS, Rengelink (1998)). The vast majority of the radio sources in these surveys are radio-loud AGN with a median redshift of $z \approx 0.8$ which dominate the radio source population above flux densities of 10 mJy. Below 10 mJy the surveys contain an increasing fraction of nearby ($z < 0.1$) galaxies whose radio emission is fuelled by ongoing star formation. Because radio surveys probe a wide range of redshifts, studying their global properties statistically (eg. through radio source counts or luminosity functions) provides a powerful constraint on the evolutionary properties of galaxies throughout the history of the universe. Unfortunately, radio survey data alone are not sufficient to constrain the current models of radio source counts. These models are strongly dependent on the form of the *local* radio luminosity function from which the measured source counts can be extrapolated via evolutionary models. The current generation of redshift surveys (eg. SDSS, York *et al.* (2000); 2dFGRS, Colless *et al.* (2001); 6dFGS, Jones *et al.* (2004)) provide a useful tool for calculating the local radio luminosity function, as they provide redshifts for thousands of radio sources in the local universe. The host galaxy spectra provide additional value in this context as they can be used to determine the physical cause of the radio emission from galaxies, thereby disentangling the star-forming galaxy population from the AGNs.

Recent derivations have been made of the local radio luminosity function using both the SDSS and 2dFGRS in concert with the current generation of radio surveys. Sadler *et al.* (2002) identified 912 2dFGRS galaxies in the NVSS and derived the local radio luminosity function of both star-forming galaxies and AGNs; this will hereafter be referred to as the 2dFGRS-NVSS sample. Magliocchetti *et al.* (2002) identified 557 optical counterparts to FIRST galaxies in the 2dFGRS and derived the local radio luminosity function of these galaxies; this will hereafter be referred to as the 2dFGRS-FIRST sample. Both the 2dFGRS samples cover a relatively small area of sky to redshifts of $z \approx 0.3$ and are predominantly comprised of AGNs. This is particularly true for the FIRST sample. Its limited UV coverage resolves out much of the extended radio emission in nearby star-forming galaxies. Condon *et al.* (2002) crossmatched the NVSS catalogue with galaxies brighter than $m_p = 14.5$ in the UGC, obtaining a sample of 1966 radio sources in the very nearby ($z < 0.03$) universe in 4.33 sr of the northern sky; this will hereafter be referred to as the UGC-NVSS sample. The wide yet shallow UGC-NVSS sample contained a large population of star-forming galaxies but contained few AGN. Larger numbers of radio-loud AGN in a local volume are found at higher redshifts. Galaxies in the 6dFGS-NVSS primary sample presented in this thesis lie at redshifts intermediate between the more distant 2dFGRS samples and the nearby UGC sample, in a sky area much larger than that of the 2dFGRS derived samples. 6dFGS-NVSS galaxies are therefore contained in a volume of space an order of magnitude larger than any previous *local* radio source sample, with large numbers of both AGNs and star-forming galaxies all contained in the one survey.

In this chapter a derivation is made of the *local* radio luminosity function at 1.4 GHz

of both star-forming galaxies and AGNs in the 6dfGS-NVSS primary sample, the sample selection of which is discussed in detail in Chapter 3. The radio luminosity function derived here has a number of advantages over previous derivations:

- All the input catalogues used for radio source selection are from homogeneous surveys which have been obtained from a single instrument which avoids biases which may result from combining surveys.
- The digital K-band magnitudes from the 2MASS XSC are more accurate than those which have been derived from measurements of photographic plates.
- The near-infrared survey from which the sample is selected is relatively unaffected by dust. This means that the radio selected sample will not be biased with respect to the amount of dust in the host galaxy, which is particularly important in galaxies with higher star-formation rates.
- Near-infrared magnitudes are linked to the old stellar population in galaxies which make them better estimators of stellar mass than optical magnitudes. This means fractional radio luminosity functions in K-band magnitude bins can relate radio properties of star-forming galaxies and AGNs to the mass of the old stellar population in galaxies.
- The 6dFGS-NVSS primary sample presented in this thesis contains twice the number of radio sources than any previous sample.

This sample is therefore the most homogeneous, accurate and largest set of radio source spectra and redshifts ever assembled.

The structure of this chapter is as follows. Section 5.2 outlines the general properties of 6dFGS-NVSS primary target galaxies. Section 5.3 examines the population of primary sample objects which are detected in the IRAS-FSC, both as a consistency check for the spectroscopic classification of the sample and to derive the radio-FIR correlation for a larger sample of star-forming galaxies than any obtained to date. Section 5.4 presents the local radio luminosity function at 1.4 GHz for the AGNs and star-forming galaxies; a derivation of the star-formation density at the present epoch is also made in this section. Section 5.5 presents the fractional luminosity functions of AGNs and star-forming galaxies. Finally, section 5.6 summarises the main results of this chapter. Throughout this chapter, if not explicitly stated, the values adopted for the cosmological parameters are $\Omega_m = 0.3$, $\Omega_\Lambda = 0.7$, and $H_0 = 70\,\mathrm{km\,s^{-1}\,Mpc^{-1}}$.

5.2 The primary sample

Chapter 3 introduced the sample selection criteria and spectral classification method for NVSS and SUMSS radio sources identified with near-infrared objects from the 2MASS XSC which form the 6dFGS primary sample. For the purposes of further analysis only objects north of $\delta = -40^\circ$ have been included, as coverage of 6dFGS primary sample objects in the first data release is extremely sparse south of this. This declination limit leaves a primary 6dFGS-NVSS sample of 4506 radio sources, the largest combined

sample of radio source spectra and redshifts ever obtained. Of these 4506 6dFGS-NVSS objects, 211 are also identified with radio sources in version 1.4 of the SUMSS catalogue south of $\delta = -30^\circ$.

Table 5.1 Spectral classification of primary targets with $\delta > -40^\circ$.

Class	Number
SF	2644
Aa	1268
Aae	187
Ae	162
star	8
?	237
Total	4506

Table 5.1 shows the spectral classification of objects in the sample. The ratio of star-forming galaxies (SF) to AGNs is approximately 60% SF to 40% AGN. The fractions of SF to AGN galaxies in the similarly classified 2dFGRS-NVSS sample (Sadler *et al.*, 2002) are 40% SF to 60% AGN. The difference in these relative fractions can be explained by the fainter magnitude limit ($b_J = 19.4$) of 2dFGRS galaxies, resulting in a larger proportion of detections of more distant AGNs. 228 of the 237 spectra classed as "?" had low S/N and therefore redshift measurements and classifications could not be made. The remaining 9 had high enough S/N to measure a redshift but were deemed unclassifiable; these objects were classified purely on the basis of their measured radio power. Those with $\log[P_{1.4}\,(\mathrm{W\,Hz^{-1}})] < 23$ were classed as star-forming and those with $\log[P_{1.4}\,(\mathrm{W\,Hz^{-1}})] > 23$ were classed as AGN. Contamination of the sample by foreground stars is negligible.

5.2.1 Sky coverage

Figure 5.1 shows the sky coverage of 6dFGS-NVSS galaxies. Filled circles show objects which have been observed in the first data release and open circles show unobserved candidate 6dFGS-NVSS identifications. The completeness (i.e., the percentage of total candidates which have been observed) for all radio sources in this region is 40%. Unobserved candidate identifications in the area of sky studied are the primary cause of incompleteness in the sample. The completeness is about 60% in the region $-40^\circ < \delta < -23^\circ$, which is the 6dF galaxy survey's central declination strip, and the region in which most 6dF observations were targeted in the first year of the survey (Jones *et al.*, 2004). About 30% of radio candidates in the equatorial strip $-23^\circ < \delta < 0^\circ$ have been observed; although the completeness is lower in this region, a fair enough sized sample is available for analysis.

Because the 6dFGS uses a tiling algorithm with variable overlap depending on the underlying galaxy density and because not all tiles in the region north of $\delta = -40^\circ$ were

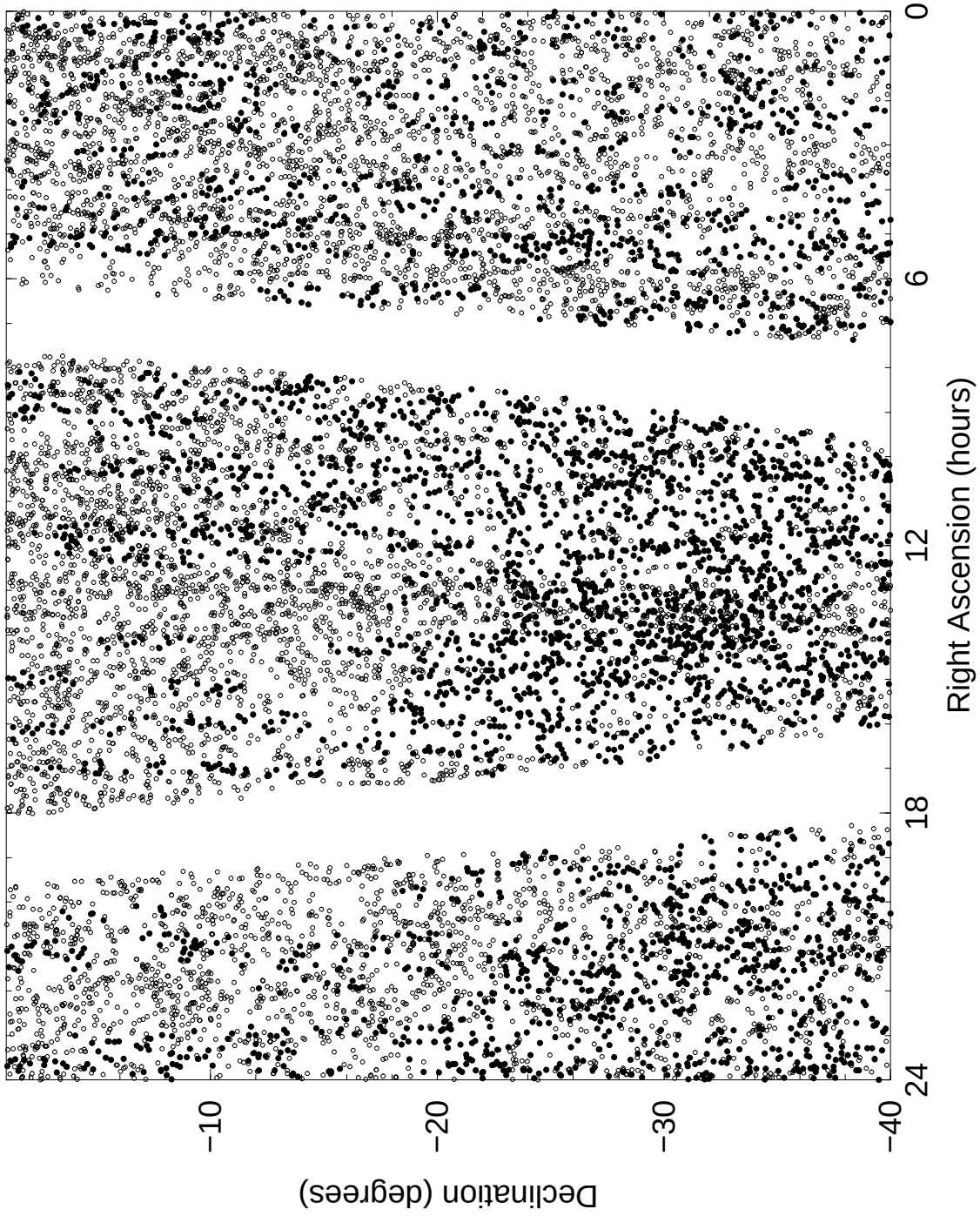

Figure 5.1 Sky coverage of the sample. Filled circles denote the positions of NVSS radio sources identified with 2MASS XSC objects with $K < 12.75$ and observed in the 6dF first data release. Open circles denote the positions of the unobserved candidate 6dFGS-NVSS identifications.

observed in the first data release (~ 479 out of ~ 1097), calculating the exact area of sky surveyed is not straightforward. A method of calculating sky area for incomplete surveys such as the 6dFGS has been described by Folkes *et al.* (1999) and was also applied to a radio source sample matched with 2dFGRS galaxies by Sadler *et al.* (2002). This method estimates the area of sky covered by dividing the number of galaxies observed by the mean surface density of galaxies in the survey target list. There are 113 988 targets in the 6dFGS K-selected primary target list covering 17 046 deg^2 of the sky resulting in a primary target surface density of 6.7 objects deg^{-2}. In the first data release 28 928 primary targets were observed north of -40°. Therefore the effective area of this sample is 4 326 deg^2, or about 10.5% of the celestial sphere. Calculation of the effective area in this way also accounts for the 5% fibreing incompleteness of the 6dFGS. However, it takes no account of incompleteness due to failed observations (eg. low S/N spectra); this is discussed in more detail in Section 5.4.

5.2.2 Radio source counts

The differential source counts of objects in the primary sample are plotted in Figure 5.2. These are plotted in a form in which each bin is weighted by $S^{5/2}$ such that counts in a static Euclidean universe would lie on a horizontal line, as discussed in Section 1.3.4. Counts determined for the AGNs are plotted as filled circles and those for star-forming galaxies are plotted as open circles. The source counts of all 572 777 NVSS catalogue sources in the same region of sky as the primary sample are shown as squares linked by a solid line. The counts follow an approximate power law between 1 Jy and 2.5 mJy, below which they fall sharply; this is because the NVSS catalogue is incomplete below 2.5 mJy. The same falloff can be seen in the counts of the AGN and star-forming subsamples indicating that this 6dFGS-NVSS sample is complete to a flux density limit of 2.5 mJy.

Radio source catalogues such as the NVSS are known to predominantly contain galaxies powered by AGNs with a median redshift of $\tilde{z} \sim 0.8$ (Condon *et al.*, 1998). In the much more nearby ($\tilde{z} \sim 0.05$) 6dFGS-NVSS sample the source counts of AGNs follow roughly the same power-law slope as that of all radio sources but only account for roughly 1-2% of the total number of radio sources. The source counts for star-forming galaxies stay approximately horizontal over the range 2.5 mJy to 1 Jy and therefore account for only 0.1% of all sources at 1 Jy rising to 1-2% of all sources at 2.5 mJy. The counts for star-forming galaxies and AGNs crossover at about 10 mJy, below which star-forming galaxies dominate the population of radio sources. At 1 Jy there are nearly ten times as many AGNs in the sample as star-formers, but the balance changes at lower flux density until at 2.5 mJy there are a little over one-tenth as many AGNs as star-formers.

5.2.3 Redshift distribution

Figure 5.3 shows the redshift distribution of 6dFGS-NVSS radio sources. The redshift distribution of all objects in the sample is shown in the top panel and separate distributions for star-forming galaxies and AGNs are shown in the middle and bottom panels respectively. The median redshift of all radio sources in the 6dFGS-NVSS sample is $\tilde{z} = 0.046$,

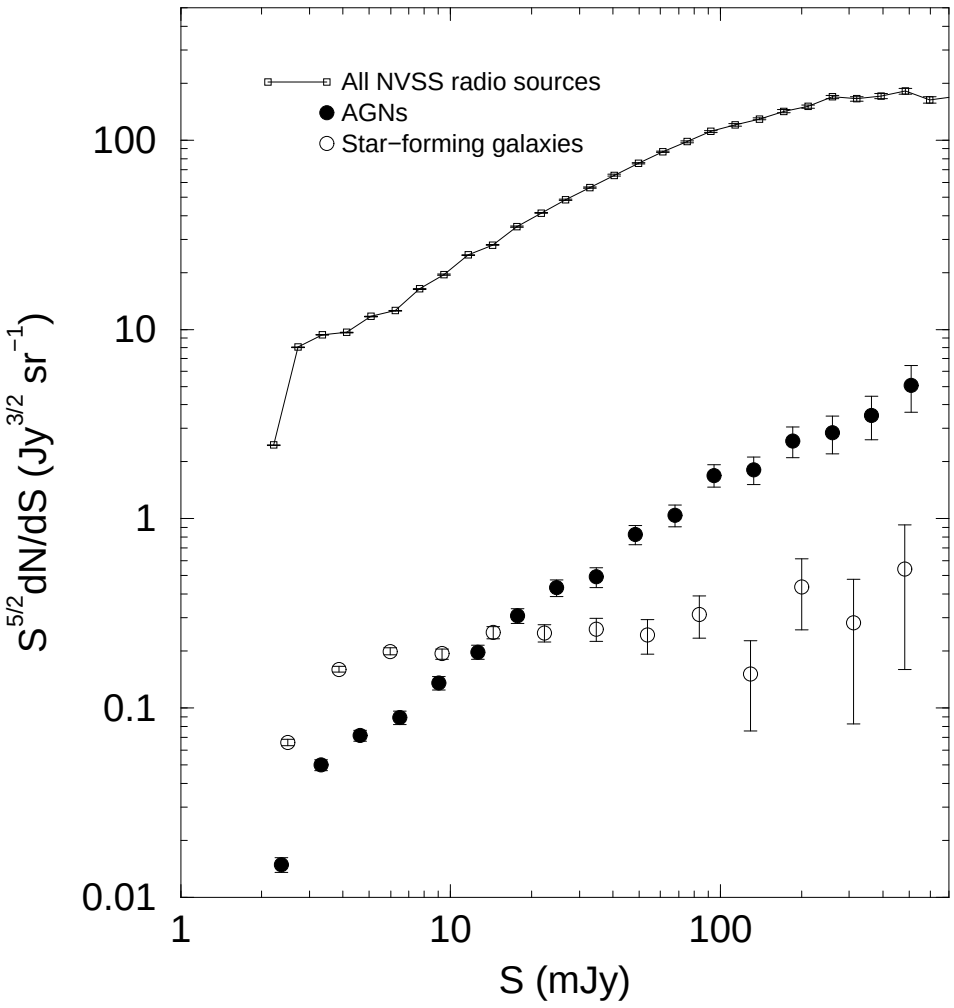

Figure 5.2 Differential source counts of 1.4 GHz NVSS sources multiplied by $S^{\frac{5}{2}}$ such that counts in a Euclidean universe would lie on a horizontal line. The counts of all 572 777 NVSS sources in the region surveyed are shown by open squares linked by a solid line. AGN and SF class galaxies in the 6dFGS-NVSS database are shown as filled and open circles respectively. The error bars shown are the $\sqrt{n}$ counting uncertainties in each bin.

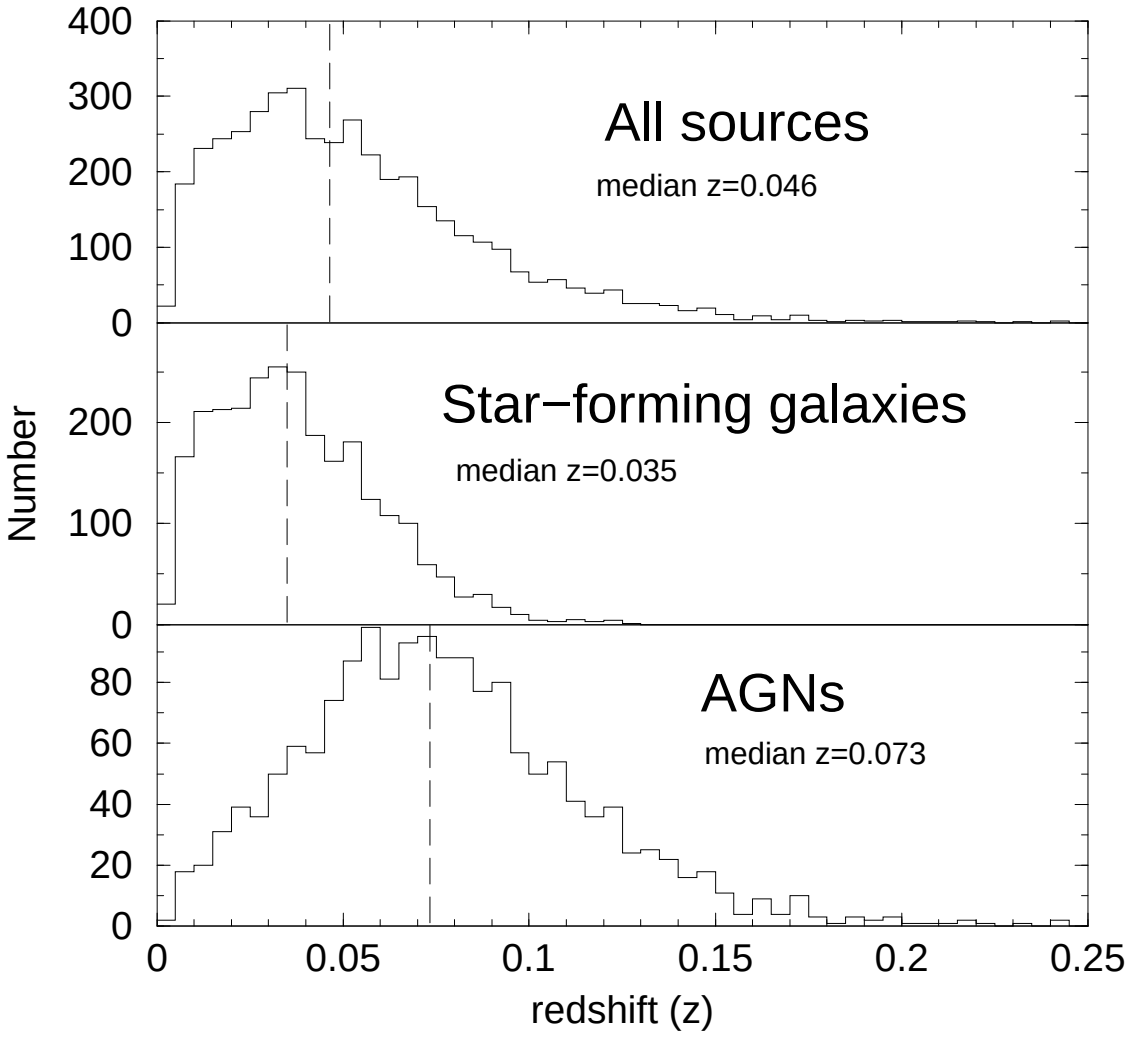

Figure 5.3 The redshift distribution of the 6dFGS-NVSS primary sample in bins of width 0.005 in redshift. *Top panel*: Redshift distribution of all 4269 objects for which a redshift has been measured. *Middle panel*: Redshift distribution of the 2644 Star-forming galaxies. *Bottom panel*: Redshift distribution of the 1617 AGNs. In each panel a vertical dashed line is drawn at the median redshift.

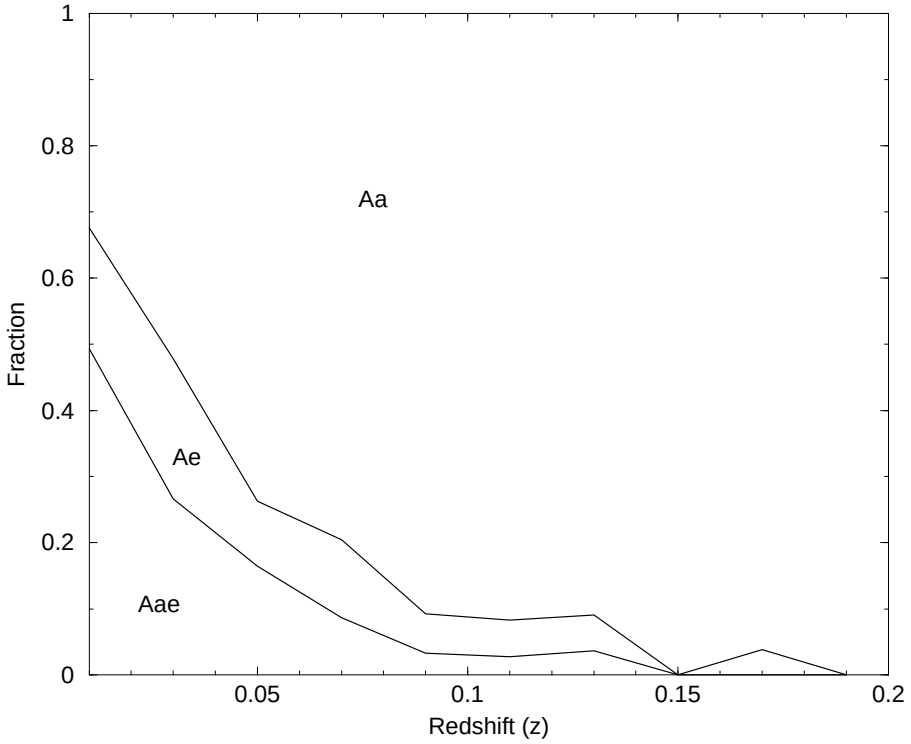

Figure 5.4 The change in the spectral mix of AGN class galaxies with redshift. The zones in the plot defined by the solid lines show the contribution of each spectral class to the total population at a given redshift.

Table 5.2 Median redshifts, flux density limits and magnitude limits for some recent radio samples drawn from redshift surveys.

Sample Name	Band	Mag. limit	$S_{1.4}^{lim}$ (mJy)	$\tilde{z}_{\rm AGN}$	$\tilde{z}_{\rm SF}$
2dFGRS-NVSS[1]	b_J	19.4	2.8	0.14	0.05
2dFGRS-FIRST[2]	b_J	19.4	1	0.15	0.10
UGC-NVSS[3]	M_p	14.5	2.5	0.02	0.02
6dFGS-NVSS	K	12.75	2.5	0.07	0.04

NOTES:
[1] Sadler *et al.* (2002, 1999)
[2] Magliocchetti *et al.* (2002)
[3] Condon *et al.* (2002)

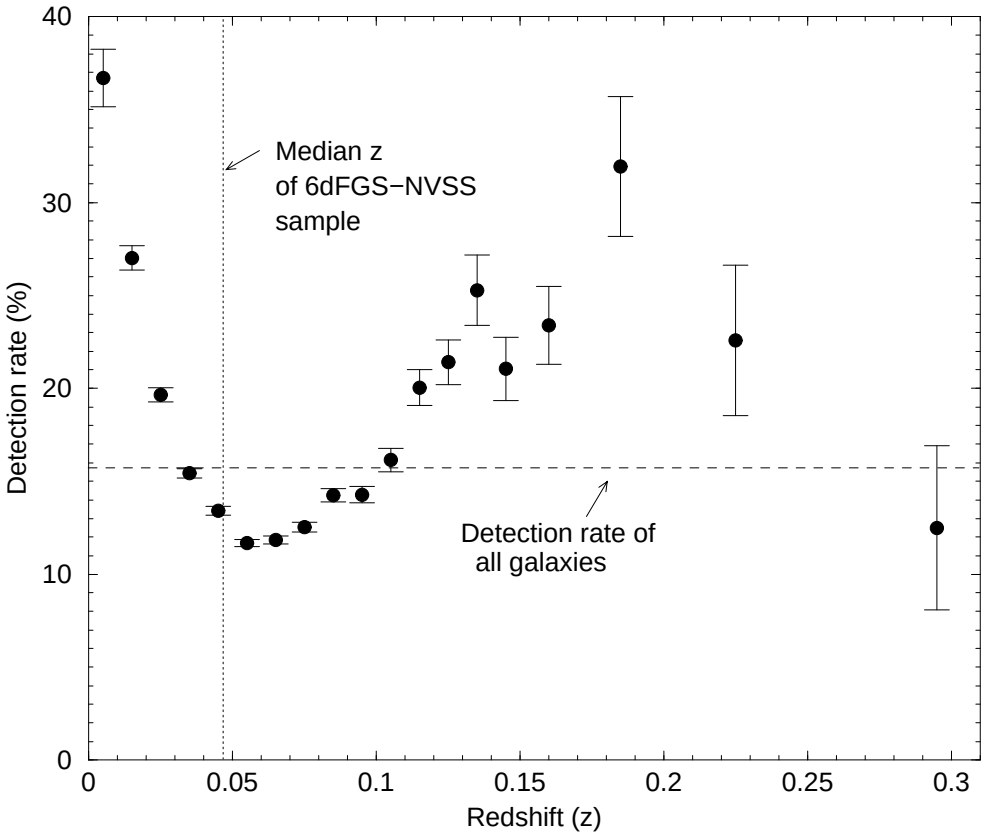

Figure 5.5 The NVSS detection rate of 6dFGS primary target objects observed in the first data release. Here the detection rate is defined as the percentage of radio identifications of observed 6dFGS primary target objects for that bin. The error bars shown correspond to the $\sqrt{n}$ counting error in each bin. A vertical dotted line is plotted at the median redshift of the 6dFGS-NVSS sample and a horizontal dashed line is plotted at the overall radio detection rate of 15.7% for the 6dFGS-NVSS sample.

very close to the median redshift ($\tilde{z} = 0.054$) of the underlying K-selected sample (Jones *et al.*, 2004). Star-forming galaxies dominate the lower redshift radio source population and are found at a median redshift of $\tilde{z} = 0.035$ while AGNs dominate the higher redshift radio source population at a median redshift of $\tilde{z} = 0.073$. Star-forming galaxies have a lower median redshift because these sources tend to have lower radio powers (see Figure 5.6) and therefore start to drop out of the sample at higher redshift because their flux densities fall below the limit of the NVSS catalogue. AGNs have higher radio powers and therefore can be seen at higher redshift; they start to drop out of the sample beyond $z = 0.073$ because of the $K < 12.75$ limit of the 6dFGS.

The optical magnitude limits, radio flux density limits and median redshifts of other radio-optical samples, selected in a similar way to the 6dFGS-NVSS sample, are presented in Table 5.2. In their analysis of $S_{1.4} \geq 2.8\,\mathrm{mJy}$ NVSS radio sources identified with galaxies in the 2dF Galaxy Redshift Survey (2dFGRS; Colless *et al.*, 2001), Sadler *et al.* (1999) found a median redshift of $\tilde{z} = 0.1$ for all 2dFGRS-NVSS galaxies, $\tilde{z} = 0.05$ for star-forming galaxies and $\tilde{z} = 0.14$ for AGNs. The 2dFGRS goes more than two

magnitudes deeper in b_J than the 6dFGS yet the median redshift of 2dFGRS-NVSS star-forming galaxies is only slightly higher than that found here for 6dFGS-NVSS galaxies, which implies that it is primarily the radio flux density limit of optical-radio samples which limits the maximum distance to which star-forming galaxies can be found. In a survey of 1.4 GHz FIRST radio sources with $S \geq 1$ mJy in the 2dFGRS, Magliocchetti *et al.* (2002) found a median redshift for star-forming galaxies of $\tilde{z} = 0.1$, more than twice as distant as NVSS selected samples. Conversely, for AGNs the median redshifts of the 2dFGRS-NVSS and 2dFGRS-FIRST samples are roughly similar ($\tilde{z} = 0.15$) whereas the median redshift of the 6dFGS-NVSS sample is significantly lower. This is a consequence of the different optical magnitude limits of the 6dFGS and the 2dFGRS; radio-loud AGNs fall out of both samples at the optical/near-infrared limit of the spectroscopy.

Figure 5.4 shows the variation in spectral mix for AGNs in 6dFGS-NVSS, showing the contribution from the three AGN spectral types vs. redshift. Though Aa galaxies constitute almost 80% of the entire AGN class, these only dominate the AGN population at higher redshifts. At lower redshifts the combined population of Ae and Aae type galaxies is greater. This effect was noted by Sadler *et al.* (2002) in their analysis of 2dFGRS-NVSS galaxies and they attributed it to an increasing dilution of AGN light by host galaxy light through the 2dF fibre aperture with increasing redshift. The same effect is evident in this sample observed with 6dF. The spatial extent sampled by the $6''$ diameter 6dF fibres increases with increasing redshift and, therefore, spectra of higher redshift AGN include an increasing contribution from stars in the host galaxy. This means that emission line AGN will be easier to recognise at lower redshift than at higher redshift. Because this effect is very difficult to correct for, and because there are very few emission line AGN in the sample, the Aa, Aae and Ae class galaxies are combined into a single AGN class for most of the analysis of this sample.

Figure 5.5 shows the variation in the detection rate of NVSS radio sources in the 6dFGS primary sample as a function of redshift. The detection rates in this plot were calculated by dividing the number of 6dFGS-NVSS galaxies in redshift bins of width 0.01 by the number of the $\sim 29\,000$ 6dFGS first data release primary target galaxies with $Q \geq 3$ in each redshift redshift bin. The average NVSS detection rate of 15.7% is shown as a dashed horizontal line in the plot and the median redshift of the 6dFGS-NVSS sample is shown as a dotted vertical line. The NVSS detection rate drops sharply from 40% at $z = 0.005$ to just over 10% at $z = 0.05$ (the median redshift of the survey). It then rises steadily to over 20% at $z = 0.15$ beyond which results are dominated by counting errors. This fall and subsequent rise in the detection rate with redshift can be explained in terms of the different redshift distributions of the star-forming and AGN radio source populations.

Below $z = 0.05$, where the detection rate is falling with redshift, star-forming galaxies dominate the radio source population. The detection rate is falling at low redshift because of the radio flux density limit of the NVSS. Star-forming galaxies have weaker radio powers. Fewer are found with increasing redshift because the limiting radio power of the 6dFGS-NVSS sample is increasing with redshift (see Figure 5.6). Above $z = 0.05$ where the detection rate is increasing AGNs dominate the radio source population. The population of radio-loud AGNs has a higher average radio power so they tend not to

fall out of the sample because of the flux density limit of the NVSS. The $K \leq 12.75$ cutoff of the 6dFGS means that as redshift increases the galaxies left in the sample are on average more luminous in the near-infrared, this can be understood from Figure 5.6 (*top*) where the K magnitude limit is restricting the survey to brighter absolute magnitudes with increasing redshift. Radio AGNs preferentially reside within the brightest galaxies (see Figure 5.7), and this means that as the underlying galaxy population is getting more luminous they are more likely to host a radio-loud AGN, resulting in an increase in the detection rate of AGN with redshift.

5.2.4 Luminosity distribution

The 1.4 GHz monochromatic radio power (in units of W Hz^{-1}) of each of the objects in the sample is calculated using the relation:

$$P_{1.4} = 4\pi S_{1.4} d_{\rm L}^2 k_{\rm radio}(z) \tag{5.1}$$

where $S_{1.4}$ is the 1.4 GHz NVSS flux density in Jy, d_L is the luminosity distance to the object in m defined by equation 1.11 and $k_{\rm radio}(z)$ is the k-correction which takes account of the effects of redshift on the observed flux density and the observed passband. k_{radio} has been applied in the form specified by Sadler *et al.* (2002):

$$k_{\rm radio}(z) = (1+z)^{-(1+\alpha)} \tag{5.2}$$

where α is the spectral index ($S \propto \nu^{\alpha}$), usually assumed to be $\alpha = -0.7$ for low frequency radio source samples. For this sample median spectral indices were determined separately for the AGN and SF class of galaxies by comparing the flux densities of 211 objects which were also found in version 1.4 of the SUMSS catalogue. For the 114 AGN the median spectral index was $\tilde{\alpha}_{843}^{1400} = -0.62 \pm 0.07$ and for the 97 SF galaxies the median spectral index was $\tilde{\alpha}_{843}^{1400} = -0.86 \pm 0.07$. These values of α have been applied to the k-corrections for all calculations of radio power throughout this work. Both these values are close to the value of $\alpha = -0.7$ normally assumed for radio source samples (eg. Sadler *et al.*, 2002; Condon *et al.*, 2002). For most of the galaxies in this sample these k-corrections are merely a formality as for $z < 0.1$ the value of $k_{\rm radio}$ is very close to 1.

Absolute K-band magnitudes for every object in the sample are derived using the relation

$$M_K = K - 5\log\left(\frac{d_{\rm L}}{10}\right) - k_K(z) \tag{5.3}$$

where K is the measured apparent K-band magnitude from the 6dFGS database, $d_{\rm L}$ is the luminosity distance from equation 1.11 in parsecs and $k_K(z)$ is the K-band k-correction. In the K-band, k-corrections are similar for galaxies of all Hubble types. This is because different amounts of star formation in different galaxy types only affect galaxy spectra at wavelengths shorter than $1\,\mu$m (Cole *et al.*, 2001; Glazebrook *et al.*, 1995). K-band k-corrections for objects in this sample have been calculated using equation 6 of Glazebrook *et al.* (1995) which is a fit to the k-correction derived from the evolutionary synthesis models of Bruzual & Charlot (1993) assuming an instantaneous burst of star formation at

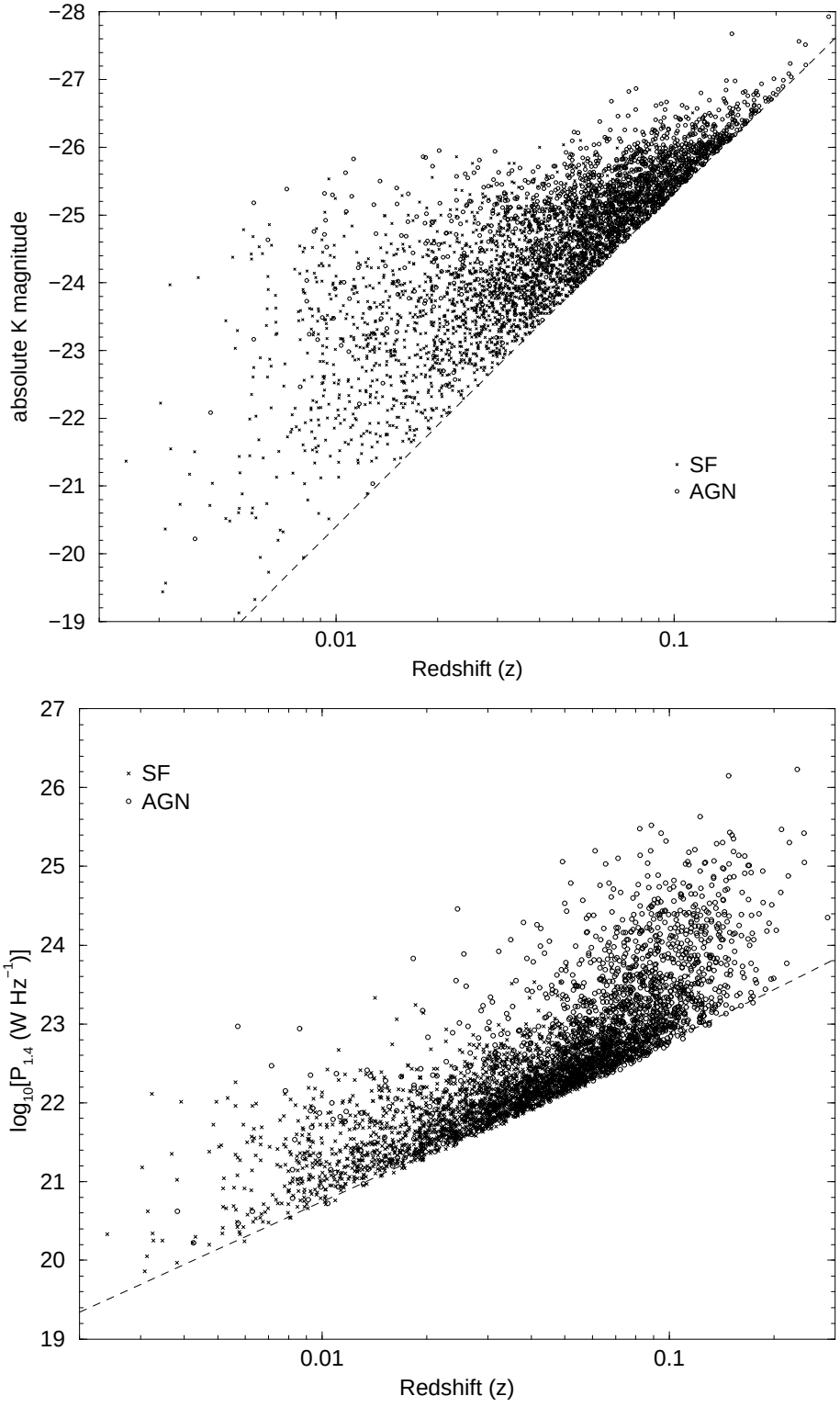

Figure 5.6 *Top*: Absolute K magnitude (calculated via equation 5.3) vs redshift for the star-forming $(\times)$ and AGN $(\circ)$ class galaxies in the sample. A dashed line indicates the $K = 12.75$ limit of the survey. *Bottom*: Monochromatic 1.4 GHz radio power (calculated via equation 5.1) vs redshift for the star-forming galaxies $(\times)$ and AGNs $(\circ)$ in the sample. A dashed line indicates the NVSS 2.5 mJy completeness limit.

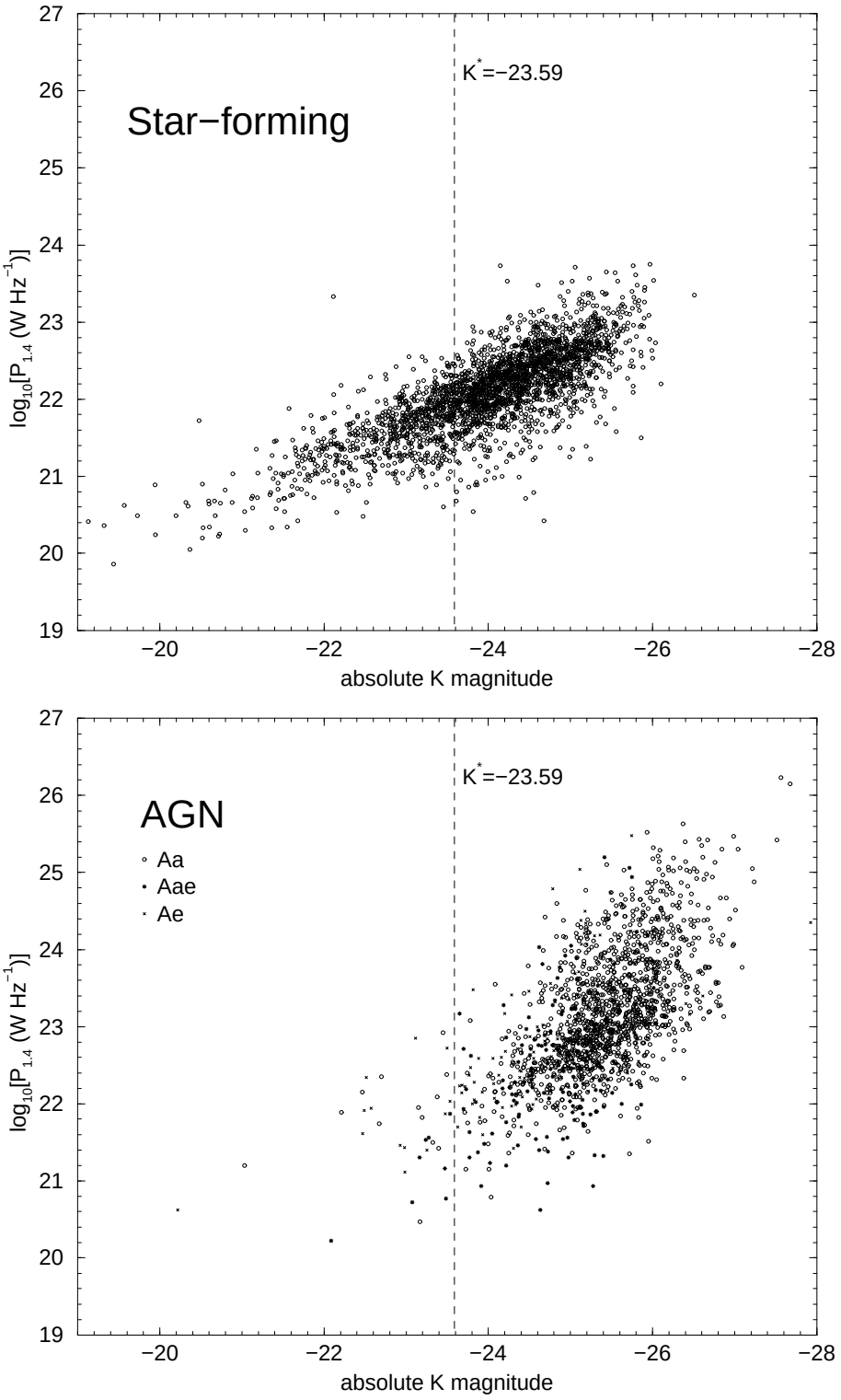

Figure 5.7 *Top*: 1.4 GHz radio power vs. absolute K magnitude for the 2644 star-forming galaxies in the 6dFGS-NVSS sample. *Bottom*: 1.4 GHz radio power vs. absolute K magnitude for the 1617 AGNs in the 6dFGS-NVSS sample. Aa class AGNs are plotted as circles, Aae class AGNs are plotted as stars and Ae class AGNs are plotted as crosses. A dashed vertical line is drawn at the value of $M_K^\star = -23.59$ taken from a Schechter function fit to the luminosity of 2MASS K-band galaxies in the 2dFGRS by Cole *et al.* (2001).

age 5 Gyr. There is almost no variation to the k-correction in their model for ages between 1 and 10 Gyr at $z < 0.5$. The empirical fit to the 5-Gyr model is (Glazebrook *et al.*, 1995)

$$k_K(z) = \frac{-2.58z + 6.67z^2 - 5.73z^3 - 0.42z^4}{1 - 2.36z + 3.82z^2 - 3.53z^3 + 3.35z^4}. \quad (5.4)$$

In the K-band, k-corrections are negative out to large redshift. At the small redshifts probed by this dataset ($z < 0.3$), $k_K(z)$ never changes M_K by more than 0.5 magnitudes.

Figure 5.6 shows plots of $P_{1.4}$ and M_K vs. z for star-forming galaxies and AGNs. The near-infrared or radio limits relevant to each plot are shown as a dashed line. This is calculated from the 2.5 mJy radio completeness limit in the plot of $P_{1.4}$ vs. z and from the $K < 12.75$ limit in the plot of M_K vs. z. In both plots star-forming galaxies dominate at lower redshift and AGNs dominate at higher redshift. The highest radio powers and brightest M_K magnitudes are only seen in AGN at redshift > 0.05. Star-forming galaxies are almost all found at $\log[P_{1.4}\,(\mathrm{W\,Hz^{-1}})] < 23$, and drop out of the sample at higher redshift because of the limiting flux density of the NVSS. A lower flux density limit would pick up a larger number of star-forming galaxies at all redshifts. AGNs are seen at all radio powers in the sample. To obtain a larger sample of low luminosity AGNs, which are found at lower redshift, a larger sample volume would be required rather than a fainter flux density limit.

Figure 5.7 plots 1.4 GHz radio power vs. absolute K-band magnitude separately for the star-forming galaxies and AGNs in the sample. For reference the value of the $M_K^\star = -23.59$ from a Schechter function fit to the K-band luminosity function of 2dFGRS-2MASS galaxies by Cole *et al.* (2001) is shown as a vertical dashed line in both plots. Star-forming galaxies span a range of M_K between -20 and -26, they have median $\tilde{M}_K = -24.12$, only slightly higher than $M_K^\star$. These galaxies tend to have lower radio powers ($P_{1.4} < 10^{23}\,\mathrm{W\,Hz^{-1}}$) than AGNs, with median $\log[\tilde{P}_{1.4}\,(\mathrm{W\,Hz^{-1}})] = 22.13$. AGNs are almost all found in objects brighter than $M_K^\star$, indicative of their preferential location in the brightest elliptical galaxies. The median $\tilde{M}_K$ of AGNs is -25.39. These objects have median radio power $\log[\tilde{P}_{1.4}\,(\mathrm{W\,Hz^{-1}})] = 23.04$, almost an order of magnitude brighter than the median radio power of star-forming galaxies. Though star-forming galaxies tend to have lower radio powers ($P_{1.4} < 10^{23}\,\mathrm{W\,Hz^{-1}}$), AGNs span a very wide range in radio power from 10^{21} to $10^{26}\,\mathrm{W\,Hz^{-1}}$, indicating that there is no clear observational regime in which star-forming galaxies can be separated from AGNs purely on the basis of radio power. The apparent correlation between radio power and M_K seen in both plot is the result of Malmquist bias. The near-infrared apparent magnitude limit and the radio flux density limit have caused the average luminosities of galaxies in the sample to increase with distance.

AGNs in the lower plot of Figure 5.7 have been separated into the three spectral classes Aa (circles), Aae (stars) and Ae (crosses). Both Aae and Ae type AGN seem indistinguishable from the Aa type AGN in this plot, though there is a slight tendency for them to lie at lower radio powers than the Aa class. This is probably because these objects are on average found at lower redshift than the Aa galaxies (see Figure 5.4) and therefore form a population with a lower average radio power.

5.3 Star-forming galaxies and IRAS

It has been well established that a correlation exists between far-infrared (FIR) and radio continuum emission from normal galaxies (see Helou *et al.* (1985); Condon & Broderick (1988); Condon *et al.* (1991); Condon (1992)). This correlation has been attributed to ongoing star formation within the host galaxy, where radio continuum emission is produced by a combination of synchrotron emission from electrons accelerated in the supernova remnants of short-lived massive stars ($M > 8M_{\odot}$ with lifetimes $< 3 \times 10^7$ yr) and free-free emission from HII regions ionised by these same massive stars (Condon, 1992). FIR emission is caused by thermal reradiation of dust in HII regions heated by this same population of massive stars. Though it is understood that recent star formation is the process which drives both the radio continuum and FIR emission of galaxies which lie on the correlation, the actual mechanism that relates non-thermally dominated radio power and thermally dominated FIR luminosity is poorly understood.

The FIR-radio correlation has served as a diagnostic tool for large samples of radio sources, as it can be used to distinguish between galaxies with ongoing star formation and those harbouring an AGN. Sources falling on the correlation derive their radio emission from star formation, whereas sources with a radio "excess" above that expected from the correlation derive their radio emission from the presence of an AGN (eg. Condon *et al.*, 2002; Condon & Broderick, 1988). The correlation also constrains models relating star-formation rate to radio emission (Condon, 1992). In this section results from analysis of the population of radio sources in the 6dFGS-NVSS primary sample with FIR detections in the Infrared Astronomical Satellite (IRAS) Faint Source Catalogue (FSC) (Moshir *et al.*, 1993) are presented, both as a consistency check for the spectral classification of the sample and to examine the correlation for a larger sample of normal galaxies than any hitherto obtained.

5.3.1 Finding IRAS Detections

One of the additional target samples being observed as part of the 6dFGS is $\sim 11\,000$ IRAS-FSC galaxies selected at $60\,\mu\mathrm{m}$ and identified with galaxies with $b_{\mathrm{J}} < 20$ (See Table 4.1 and Jones *et al.*, 2004, for a description of the 6dFGS additional target samples). Unlike the serendipitously observed NVSS additional target sample described in Chapter 4, the FSC additional targets are completely observed. Much of the IRAS-FSC sample overlaps with the $K < 12.75$ primary sample, and because both the FSC targets and the primary targets are completely observed, all IRAS-FSC objects in the 6dFGS primary sample are contained in the FSC additional target list. It is therefore a straightforward matter to find IRAS-FSC detections of 6dFGS-NVSS primary target objects by crossmatching their 6dF target ID names. 2 643 6dFGS-FSC primary targets were included in the first data release. Table 5.3 shows the spectral classification of the 1915 galaxies which are common to the 6dFGS primary sample, the NVSS subsample and the IRAS-FSC subsample. Only emission line galaxies (ie. Ae, Aae, SF) are detected in the far-infrared as has been seen in other spectroscopic studies of far-infrared galaxies (eg. Lawrence *et al.* (1986); de Grijp *et al.* (1992); Sadler *et al.* (2002)).

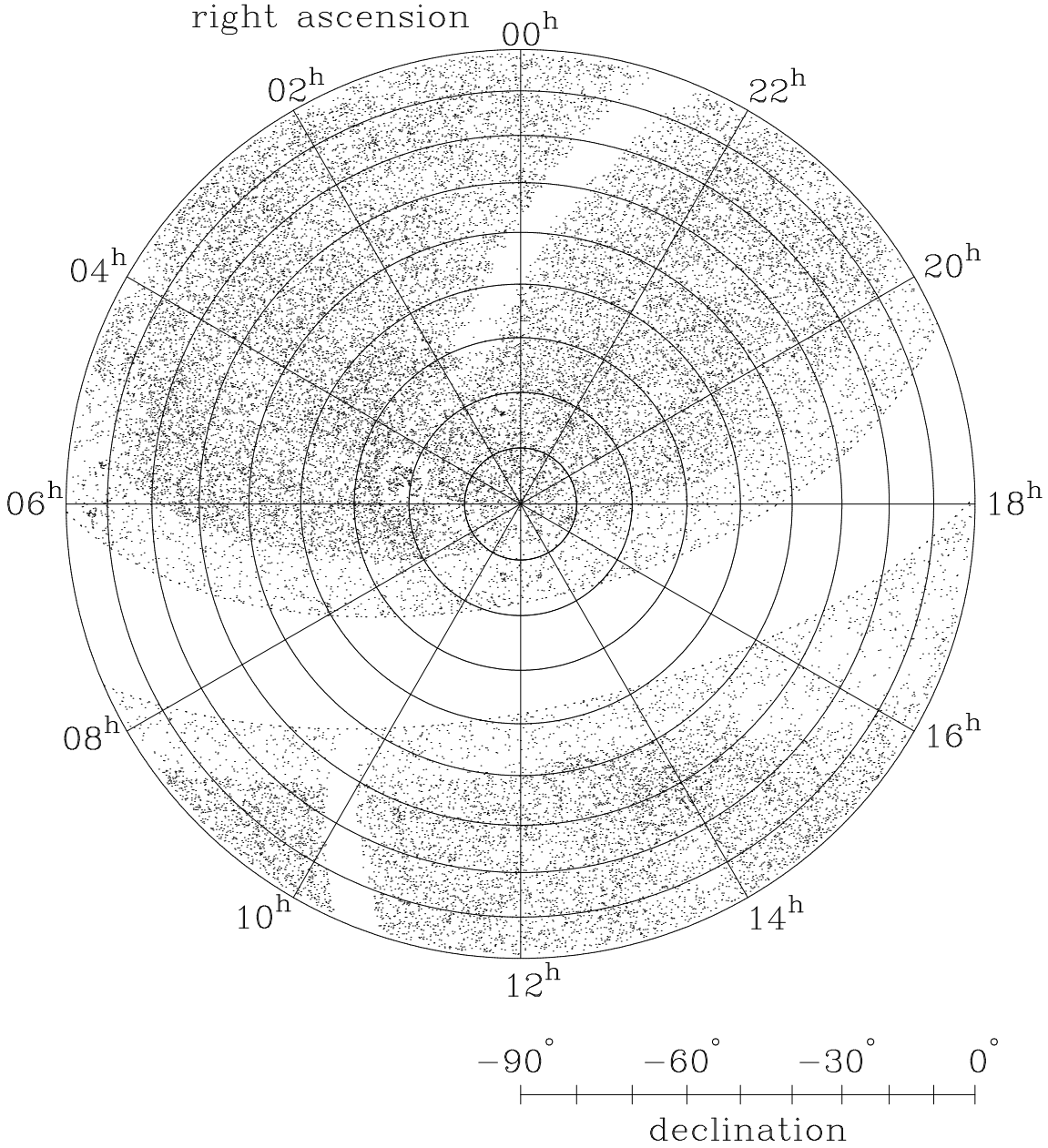

Figure 5.8 The location in B1950 coordinates of the $\sim 39\,000$ IRAS-FSC objects at $\delta < 0°$ which have a $60\,\mu$m detection. Dashed lines are plotted at $b = \pm 10°$.

Table 5.3 Spectral classification of 6dFGS-NVSS objects which are also found in the 6dFGS-FSC sample.

Spectral class	$N_{6\mathrm{dFGS-NVSS}}^{6\mathrm{dFGS-FSC}}$ [1]	$N_{6\mathrm{dFGS-NVSS}}$ [2]	percent of total [3]
SF	1714	2644	64.8
Ae	79	162	48.8
Aae	72	187	38.5
star	3	8	37.5
?	47	237	19.8
Total	1915	4506	42.5

NOTES:
[1] The number of 6dFGS galaxies which are common to both the IRAS-FSC and the NVSS catalogues.
[2] The total number of galaxies in the 6dFGS-NVSS sample.
[3] The percentage of 6dFGS-NVSS galaxies that are also 6dFGS-IRAS galaxies.

Condon *et al.* (2002) noted that the FIR-radio correlation ensures that most far-infrared sources powered by ongoing star formation are also radio sources and vice versa. The FIR/radio ratio $u = \log(S_{60\mu\mathrm{m}}/S_{1.4})$ for nearby spiral galaxies in the UGC has a mean value of $\langle u \rangle = 2.05 \pm 0.02$ with rms width $\sigma_u = 0.2$ (Condon & Broderick, 1988). This value of $\langle u \rangle$ happens to be the ratio between the 280 mJy flux density limit of the IRAS-FSC at $60\,\mu$m and the 2.5 mJy completeness limit of the NVSS at 1.4 GHz ($u = 2.05$). Table 5.3 shows the spectral classes of 6dFGS-NVSS objects which are also found in the 6dFGS-FSC sample. 64.8% of spectroscopically classified star-forming (SF) galaxies have IRAS-FSC detections leaving 929 SF galaxies with no detection. Conversely, 725 IRAS-FSC galaxies in the primary sample have no NVSS detection. Reasons for these missing star-forming galaxies are outlined in the following paragraphs.

Figure 5.8 shows the positions of all 60μm IRAS-FSC detections south of $\delta = 0°$. There are obvious gaps in the coverage and the surface density of 60μm objects also changes strongly with position. The gaps in the coverage are because there are no 60μm IRAS observations in these regions of sky and the changes in surface density are due to the nonuniformity of the IRAS-FSC. Some regions of sky were scanned fewer times than others. Images in these areas are noisier, resulting in a higher IRAS-FSC limit than 280 mJy. These non-uniformities in the IRAS-FSC have resulted in many brighter star-forming NVSS radio sources not being detected by IRAS.

Figure 5.9 shows how the fraction of 6dFGS-FSC galaxies detected in the 6dFGS-NVSS sample varies with $60\,\mu$m flux density. This fraction rises from 50% at $S_{60\,\mu\mathrm{m}} = 0.3$ Jy to 100% at 1.2 Jy. The fall in detection rate below 1 Jy is a product of both incompleteness in the IRAS-FSC and the scatter in the average FIR/radio ratio u. Taking the value of $u = 2.05$ with $\sigma_u = 0.2$ from (Condon & Broderick, 1988) the $60\,\mu$m flux density above which $\sim 100\%$ of radio sources will be detected above the NVSS completeness limit of 2.5 mJy (ie. the value of $S_{60\,\mu\mathrm{m}}$ for which $u + 3\sigma_u$ is reached for a 2.5 mJy radio source) is 1.12 Jy, this is very close to the value of 1.2 Jy at which the detection rate in the plot reaches 100%. Therefore, many 6dFGS-FSC galaxies are not detected in the 6dFGS-

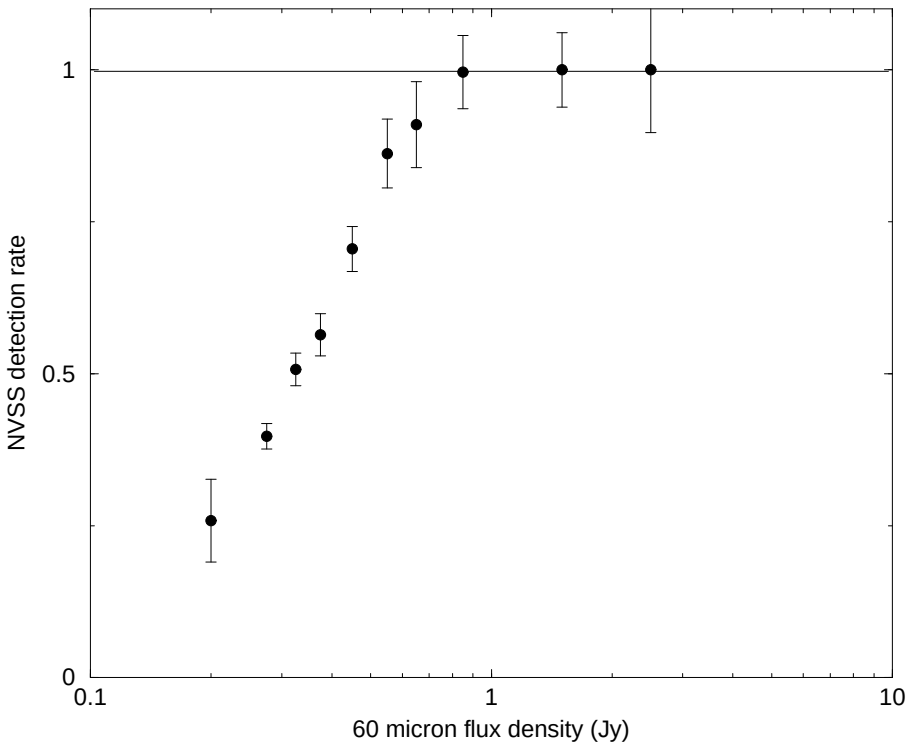

Figure 5.9 The fraction of 6dFGS-FSC galaxies which are detected in the 6dFGS-NVSS sample vs. $60\,\mu$m flux density. A horizontal line is shown at the point at which all sources are detected. Errors shown are the $\sqrt{n}$ counting error of each bin.

NVSS sample because of scatter in the measured FIR-radio correlation. This scatter is caused by a mixture of uncertain NVSS and IRAS-FSC flux densities at the survey limits as well as intrinsic dispersion in the FIR-radio correlation itself. There are about 150 6dFGS-NVSS galaxies not detected in the IRAS-FSC due to incomplete coverage, the remaining ~ 750 objects are missing because of scatter at the detection limit.

$100\,\mu$m flux densities from the IRAS-FSC were also obtained when available for each source with a $60\,\mu$m detection. For the $\sim 20\%$ of objects which did not have a $100\,\mu$m detection the $100\,\mu$m flux density was assumed to be twice the $60\,\mu$m flux density as has been done with similar FIR-radio samples (eg. Condon *et al.* (2002); Sadler *et al.* (2002)) based on the calculated average $\langle \log(S_{100\,\mu\mathrm{m}}/S_{60\,\mu\mathrm{m}}) \rangle = 0.3$ with a scatter of 0.2 from the bright galaxy sample of Soifer *et al.* (1989). 60 and $100\,\mu$m flux densities are then converted into the quantity FIR (in units of W m^{-2}) defined by

$$\mathrm{FIR} = 1.26 \times 10^{-14}\,(2.58 S_{60\,\mu\mathrm{m}} + S_{100\,\mu\mathrm{m}}) \tag{5.5}$$

where $S_{60\,\mu\mathrm{m}}$ and $S_{100\,\mu\mathrm{m}}$ are in Janskys (Helou *et al.*, 1985). FIR is a measure of the total far-infrared flux between 42.5 and 122.5 μm. and is easily converted to L_{FIR}, the FIR luminosity in units of $L_\odot$ using

$$L_{\mathrm{FIR}} = 3.65 \times 10^5 d_L^2 \mathrm{FIR} \tag{5.6}$$

Table 5.4 12 star-forming galaxies with $q < 1.8$.

6dF Name	α (J2000)	δ (J2000)	z	$S_{1.4}$ mJy	$\log_{10}(\mathrm{FIR})$ W m^{-2}	q
g0001558-273738	00:01:55.82	−27:37:38.0	0.028	29.8	-13.49	1.46
g0056374-225612	00:56:37.36	−22:56:11.8	0.057	10.4	-13.74	1.67
g0102009-383127	01:02:00.91	−38:31:26.7	0.055	11.8	-13.60	1.76
g0113367-103446	01:13:36.73	−10:34:45.8	0.053	8.0	-13.73	1.79
g0451118-293903	04:51:11.77	−29:39:03.3	0.061	6.8	-13.89	1.70
g0517397-292334	05:17:39.70	−29:23:33.6	0.064	8.0	-13.80	1.73
g1119349-224712	11:19:34.93	−22:47:12.4	0.070	25.3	-13.37	1.65
g1129159-342703	11:29:15.88	−34:27:02.5	0.048	13.7	-13.53	1.76
g1201012-351255	12:01:01.19	−35:12:55.4	0.033	22.2	-13.33	1.75
g1308420-242258	13:08:42.01	−24:22:57.9	0.014	474.5	-13.18	0.57
g1413373-175901	14:13:37.25	−17:59:00.8	0.0049	101.6	-13.17	1.25
g2141259-315612	21:41:25.90	−31:56:11.6	0.090	11.8	-13.86	1.50

where d_L in m is defined by equation 1.11. Similarly to Sadler *et al.* (2002) no k-correction is made to L_{FIR} because all of the FIR detected galaxies studied here are at low redshift ($z < 0.05$) and the k-correction will have almost no effect.

5.3.2 The FIR/radio ratio q

The radio-FIR correlation is often parametrised by the FIR/radio flux ratio parameter q (Helou *et al.*, 1985). This is defined by

$$q = \log\left(\frac{\mathrm{FIR}/(3.75\times10^{12})}{S_{1.4}}\right) \tag{5.7}$$

where FIR (defined by equation 5.5) is divided by the factor 3.75×10^{12} Hz (the frequency at $80\,\mu$m) to convert FIR to W m^{-2} Hz^{-1}. The mean value of $\langle q\rangle = 2.28$ with rms scatter $\sigma_q = 0.23$ for all 1520 objects with measured fluxes at both 60 and $100\,\mu$m. σ_q is somewhat larger than the value found by Condon *et al.* (2002) for a more nearby sample of UGC-NVSS galaxies. This discrepancy probably reflects the large uncertainties associated with fainter IRAS-FSC flux densities as well as the larger AGN population contained in the 6dFGS-NVSS-FSC sample. For the subset of 1386 star-forming galaxies with measured 60 and $100\,\mu$m flux densities $\langle q_{\mathrm{SF}}\rangle = 2.3$ with rms scatter $\sigma_{\mathrm{SF}} = 0.18$, in close agreement with Condon *et al.* (2002) for the UGC-NVSS sample. This value also agrees well with results from samples of stronger IRAS sources in spiral galaxies (Condon *et al.*, 1991). For the subset of 94 AGNs with measured 60 and $100\,\mu$m flux densities $\langle q_{\mathrm{AGN}}\rangle = 2.0$ with rms scatter $\sigma_{\mathrm{AGN}} = 0.5$. The larger scatter is expected for AGNs as these are not expected to be correlated as strongly and the smaller average q value reflects the fact that AGNs tend to be more radio "loud" than star-forming galaxies.

A cutoff of $q = 1.8$ is often used as a diagnostic to distinguish between star-forming galaxies and AGN (eg. Condon *et al.* (2002)), and it appears that the spectroscopic clas-

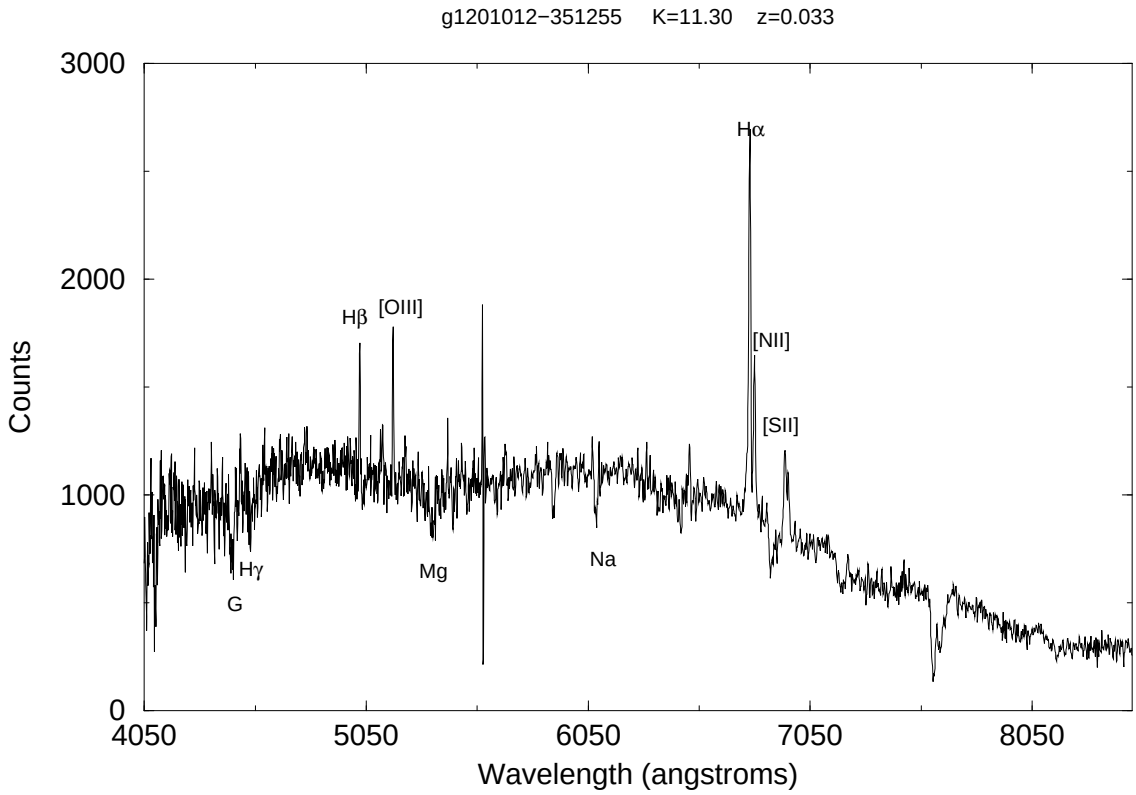

Figure 5.10 A 6dF spectrum of g1201012-351255. Though this spectrum was visually classified as SF, it has a q value of 1.75 making it more than three times more radio "loud" than the mean for star-forming galaxies.

sification of radio sources used in this work agrees well with this diagnostic. Only 12 ($< 1\%$) of the star-forming galaxies in this sample have $q < 1.8$, the value below which a galaxy is 3 times more radio "loud" than the mean for star-forming galaxies. These 12 galaxies possibly come from a class of "composite" radio source, whose radio emission is a mixture of both star-forming and AGN activity. An example spectrum of one of these objects (g1201012-351255) is shown in Figure 5.10 and a list of the radio/FIR properties of all of them is shown if Table 5.4. The "SF" spectral classification of these objects is retained in further analysis.

5.3.3 Far-infrared colours

Another common diagnostic which is often used to distinguish between AGN and star-forming radio galaxies is the far-infrared spectral index between 60 and 25 μm, $\alpha_{\rm IR} = \log(S_{25\,\mu{\rm m}}/S_{60\,\mu{\rm m}})/\log(60/25)$. $\alpha_{\rm IR}$ is a measure of the temperature of the FIR emitting dust. Star-forming galaxies tend to have cooler ($T < 50\,{\rm K}$) dust emission because of their extended star and gas distributions and therefore have values of $\alpha_{\rm IR} < -1.5$. The central engines in AGNs heat the dust to warmer temperatures ($T > 100\,{\rm K}$) and have values of $\alpha_{\rm IR} > -1.5$ (de Grijp *et al.*, 1992).

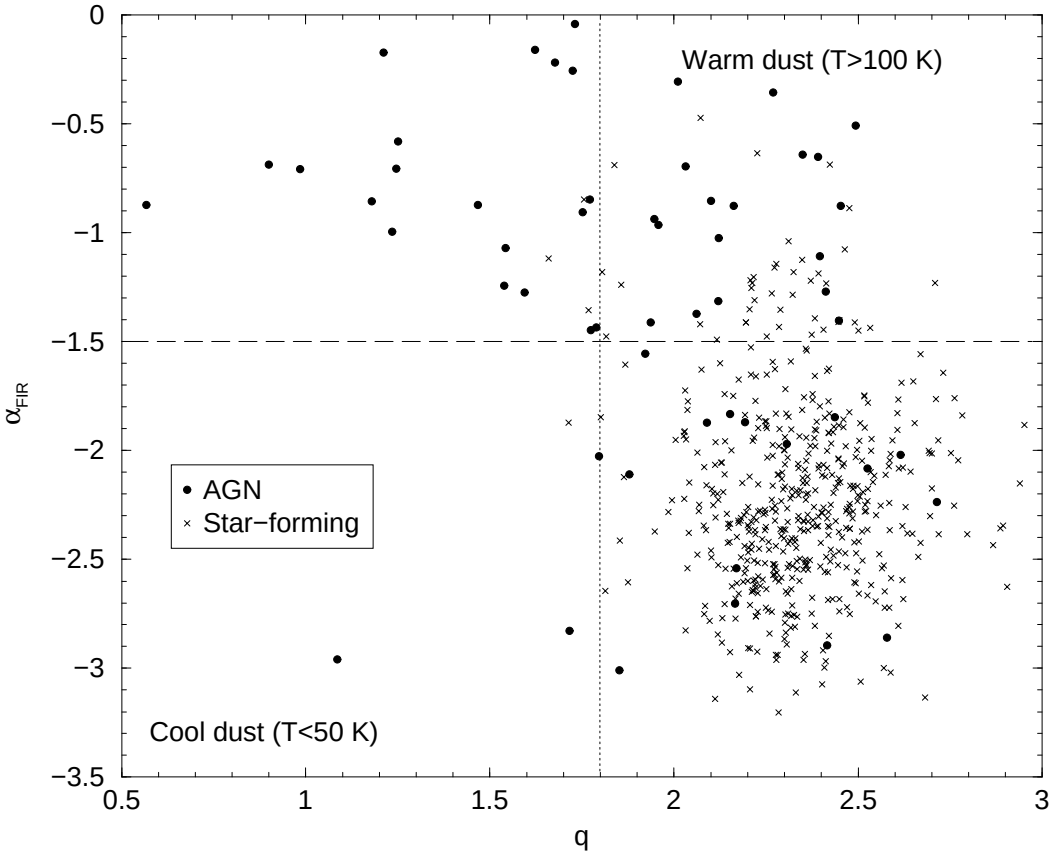

Figure 5.11 $\alpha_{\rm FIR}$ vs. q (defined by equation 5.7) for the 528 star-forming galaxies (crosses) and the 56 AGNs in the 6dFGS-NVSS-FSC sample which also had a detection in the FSC at 25 μm. A dashed horizontal line is shown at $\alpha_{\rm FIR} = -1.5$ do delineate the regions occupied by "warm" ($\alpha_{\rm FIR} > -1.5$) and "cool" ($\alpha_{\rm FIR} < -1.5$) IRAS galaxies. The canonical value of $q = 1.8$, used to distinguish between star-forming galaxies and AGNs in other surveys (eg. Condon *et al.*, 2002) is shown as a dotted vertical line. The single AGN in the lower left of the plot is a typical looking star-forming galaxy with a large radio excess. Its radio excess has led to the AGN classification here.

Fifty-six AGNs and 528 star-forming galaxies in the sample had detections in the IRAS-FSC at 25 μm. Figure 5.11 plots $\alpha_{\rm IR}$ vs. q for these galaxies, comparing the dust temperature of the galaxy with its degree of radio excess. The vast bulk of star-forming galaxies lie in the lower right of the plot as expected from the radio-FIR correlation. The majority of AGNs have $\alpha_{\rm IR} > -1.5$ indicating that the FIR spectral index, used in concert with the radio-FIR correlation agrees well with spectral classification as a discriminator of star-forming and AGN type radio sources.

Fifteen spectroscopically classified AGNs in the 6dFGS-NVSS sample lie in the lower right region of Figure 5.11 which is occupied by star-forming galaxies; this represents a very small fraction ($\sim 1\%$) of the complete AGN population. As noted in the previous section, less than 1% of spectroscopically classified star-forming galaxies had classifications which disagreed with the radio-FIR correlation diagnostic. It can therefore be concluded

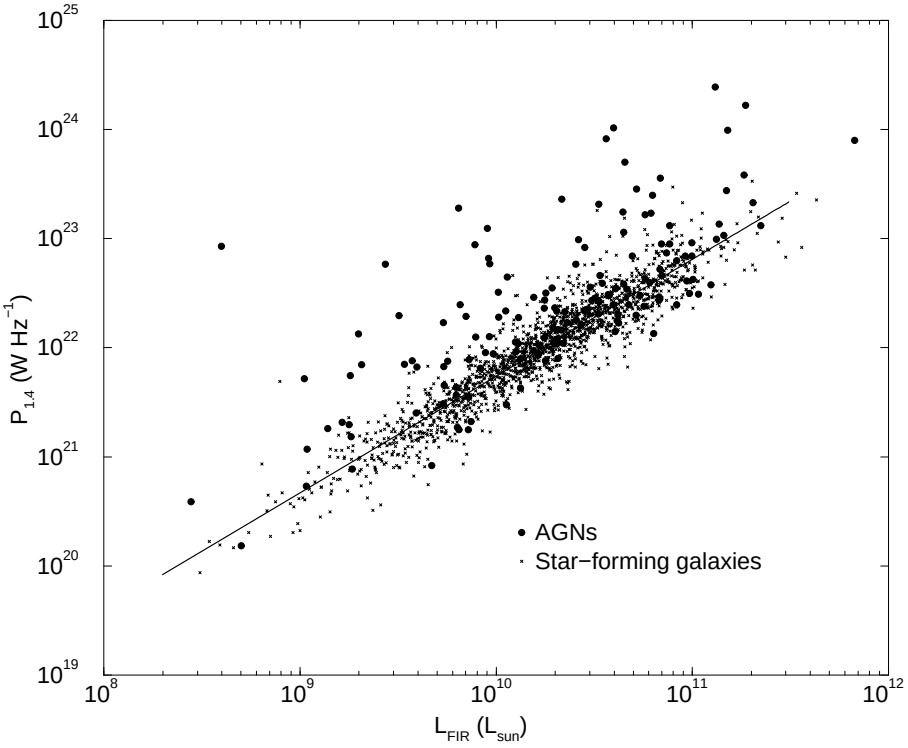

Figure 5.12 The radio-FIR correlation of all 1714 star-forming galaxies (crosses) and 152 AGNs (filled circles) in the 6dFGS-NVSS-FSC sample. A best fit line (equation 5.8 in the text) based on a subsample of 1386 star-forming galaxies with accurate 60 and 100 μm flux densities is also shown. $H_0 = 70\,\mathrm{km\,s^{-1}\,Mpc^{-1}}$, $\Omega_M = 0.3$ and $\Omega_\Lambda = 0.7$ were used to derive both $L_{\rm FIR}$ and $P_{1.4}$.

that the (vastly different) spectral classification technique and radio-FIR correlation techniques yield very similar results. It should be noted, however, that only 40% of objects in the 6dFGS-NVSS sample were detected in the IRAS-FSC. This makes the radio-FIR correlation diagnostic unsuitable for radio-optical samples such as the one presented in this thesis because a non-detection of a galaxy in the IRAS FSC does not preclude it from being a star-forming galaxy in the 6dFGS-NVSS sample. Deeper far-infrared surveys are required to detect star-forming galaxies out to the redshifts probed by optical redshift surveys.

5.3.4 The FIR-Radio correlation of 6dFGS galaxies

Figure 5.12 shows a plot of the radio-FIR correlation ($P_{1.4}$ vs. $L_{\rm FIR}$) of all radio sources in the 6dFGS with a 60 μm detection in the IRAS-FSC. Spectroscopically classified AGNs are plotted as filled circles and star-forming galaxies are plotted as crosses. There is a strong correlation between radio power and FIR luminosity extending over 4 orders of magnitude though the scatter tends to increase above $L_{\rm FIR} = 10^{11}\,L_\odot$ as was seen for IRAS-FSC detected galaxies in the 2dFGRS-NVSS sample of Sadler *et al.* (2002). The FIR luminosities show weaker correlation with radio power for spectroscopically classi-

fied AGNs which are found across the whole range of FIR luminosity sampled. Many of them have "excess" radio powers, causing them to lie above the correlation defined by the star-forming galaxies. These radio-excess IRAS galaxies are of interest for understanding the connection between star-forming galaxies and AGNs (Drake *et al.*, 2003). Ultra-luminous IRAS galaxies (ULIRGs) with $L_{\rm FIR} > 10^{12}\,L_{\odot}$ are also of interest for understanding the relationship between starbursts and AGNs in galaxies (Sanders & Mirabel, 1996). There are no ULIRGs in the sample presented here; such objects are extremely rare in the local universe, with the nearest known being at redshift 0.02. The ULIRG space density, estimated from the FIR luminosity function of Saunders *et al.* (1990), is $\sim 10^{-8}\,{\rm Mpc}^{-3}$. The enclosed volume of the 6dFGS-NVSS sample (see Table 5.7) is $\sim 2.4 \times 10^{8}\,{\rm Mpc}^{3}$, meaning that ~ 2 ULIRGs are expected in the 6dFGS-NVSS volume. Interestingly, Sadler *et al.* (2002) found 10 ULIRGs in the 2dFGRS-NVSS sample, in a volume of $5.8 \times 10^{7}\,{\rm Mpc}^{3}$ which implies a space density of ULIRGs of $2 \times 10^{-7}\,{\rm Mpc}^{-3}$ within the 2dFGRS redshift range of $0 < z < 0.3$. This suggests that these objects evolve very strongly with redshift.

A least-squares line of best fit to the subsample of 1386 star-forming galaxies for which accurate 60 and 100 μm flux densities are available in the IRAS-FSC is also shown in Figure 5.12. The line has the form

$$\log(P_{1.4}) = (1.07 \pm 0.01)\log(L_{\rm FIR}) + (11.04 \pm 0.1). \tag{5.8}$$

which is similar to that found in other derivations of the radio-FIR correlation for brighter galaxies (eg Condon *et al.* (1991); Condon & Broderick (1988); Devereux & Eales (1989)). The radio-FIR correlation derived from the 60 μm flux limited ($S \geq 5.24\,{\rm Jy}$) IRAS Bright Galaxy Sample by Condon *et al.* (1991) was parametrised by the equation

$$\log(P_{1.4}) = (1.11 \pm 0.02)\log(L_{\rm FIR}) + 10.50 \tag{5.9}$$

where $P_{1.49}$ has been converted to $P_{1.4}$ assuming a spectral index $\alpha_{1400}^{1490} = -0.86$ as derived in Section 5.2.4 and H_0 has been converted to 70 from $50\,{\rm km\,s^{-1}\,Mpc}$. The slope ($m = 1.07 \pm 0.01$) for the 6dFGS-NVSS-FSC sample is within 2σ of that derived by Condon *et al.* (1991) ($m = 1.11 \pm 0.02$). The difference in the value of the intercepts between the two samples is probably caused by uncertainties in the luminosities of fainter sources.

5.4 The local Radio Luminosity Function

The luminosity function (Φ) of a sample of astronomical objects is a measure of the variation in their space density with luminosity. Luminosity functions are a powerful statistic as they can be used to constrain source count models, evolution and also give some understanding of the physics underpinning the emission from different types of objects. The *local* luminosity function of radio sources is the global average space density of radio sources at the present epoch (Auriemma *et al.*, 1977; Condon, 1989). An accurate derivation of the local luminosity function is important as a present epoch benchmark for studies of radio sources at higher redshift so that their cosmological evolution can be determined.

In this section the local radio luminosity function is derived both for the 6dFGS-NVSS sample as a whole and for the star-forming and AGN subgroups separately. The $\sim 4\,000$ objects all have redshift errors of less than 1% (Jones *et al.*, 2004) meaning that small radio flux density and K-magnitude errors dominate the errors in the calculation of radio power and absolute K magnitude. NVSS flux densities have errors up to $\sim 20\%$ for the faintest sources but this decreases rapidly to 3% for sources with $S_{1.4} > 20\,\mathrm{mJy}$ (Condon *et al.*, 1998). K-band magnitudes from the 2MASS XSC are nearly always accurate to better than 0.2 for objects with $K < 12.75$, the magnitude limit of the 6dFGS primary sample (Jarrett *et al.*, 2000). Systematic errors introduced from combining samples taken from different instruments are minimised in the 6dFGS-NVSS sample because all measurements have been obtained from a single instrument with high accuracy.

5.4.1 Completeness

The luminosity function can be calculated directly but requires a sample which is complete to the limits of all the surveys from which it is derived. It is therefore necessary to define a subsample of the 6dFGS-NVSS primary sample which is complete to both its K-band magnitude limit and radio flux density limit. In the K-band, the 2MASS XSC from which the 6dFGS primary sample is selected is highly complete and reliable down to $K < 13.5$ (Jarrett *et al.*, 2000). This is well below the $K = 12.75$ limit of the 6dFGS, indicating that the near-infrared sample from which radio sources are selected is complete. The NVSS catalogue contains sources as faint as 2 mJy at 1.4 GHz but it is not complete to this limit. Figure 5.2 shows the source counts for NVSS catalogue sources in the region $-40^\circ < \delta < 0^\circ, |b| > 10^\circ$. These drop sharply below 2.5 mJy due to incompleteness, so a radio completeness limit of 2.5 mJy was applied to the 6dFGS-NVSS sample. This is the sample limit used by Condon *et al.* (2002) in determining the luminosity function of UGC-NVSS radio sources and is the completeness limit quoted on the NVSS webpage (www.cv.nrao.edu/nvss/). There are 4076 6dFGS-NVSS galaxies with $S_{1.4} > 2.5\,\mathrm{mJy}$ and 6dFGS measured redshifts. Of these, 2500 were assigned spectral class SF, 1568 were assigned AGN and 8 were unclassified; the spectral classification technique is outlined in detail in Chapter 3. The 8 unclassified spectra with measured redshifts were assigned a class on the basis of their measured radio power: those with $P_{1.4} < 10^{23}\,\mathrm{W\,Hz^{-1}}$ (7) were classed as SF and the one with $P_{1.4} > 10^{23}\,\mathrm{W\,Hz^{-1}}$ was classed as AGN. This results in a final sample of 2507 star-forming galaxies and 1569 AGN from which the local radio luminosity function is derived.

To account for incomplete sampling of the celestial sphere in the 6dFGS first data release, calculated volumes were normalised by the effective area of the 6dFGS-NVSS sample. As derived in Section 5.2.1 the effective sky area of the 6dFGS-NVSS sample is $4\,326\,\mathrm{deg}^2$ or $1.318\,\mathrm{sr}$;this means that the 6dFGS-NVSS sample effectively covers 10.49% of the celestial sphere and all volumes calculated in deriving the luminosity function are therefore multiplied by 0.1049.

A correction is also made to the luminosity function to account for spectroscopic incompleteness of the sample. Of the 4506 NVSS radio sources identified with 6dFGS primary sample galaxies observed in the first data release, 228 had spectra which were too

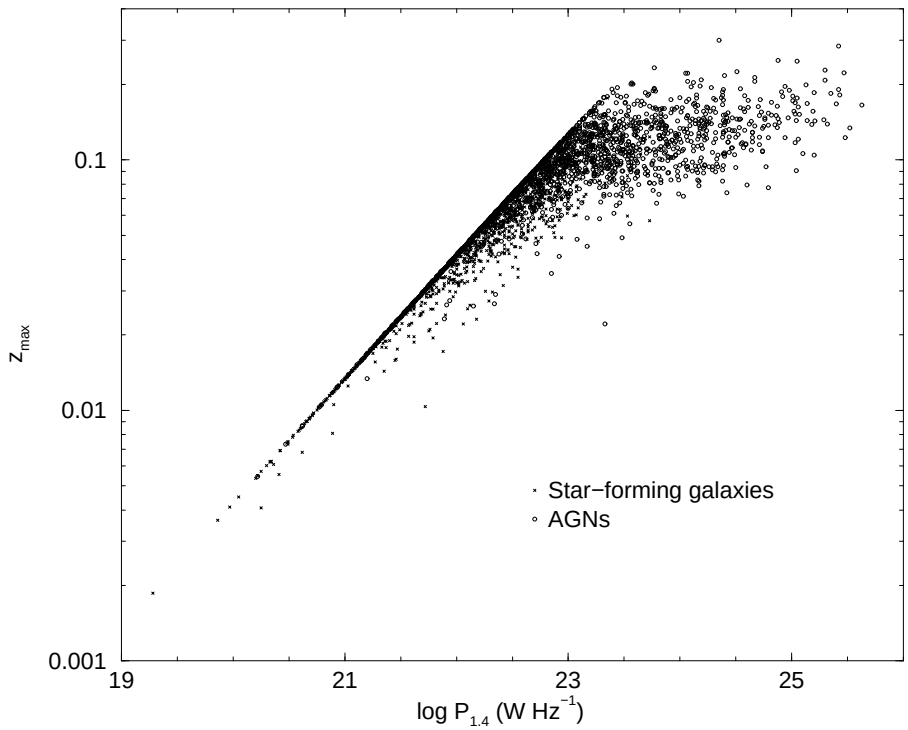

Figure 5.13 The maximum redshift to which sources in the 6dFGS-NVSS sample can be moved and still remain in the sample ($z_{\max}$) vs 1.4 GHz radio power. Star-forming galaxies are plotted as crosses and AGNs as open circles. $H_0 = 70\,\mathrm{km\,s^{-1}\,Mpc^{-1}}$, $\Omega_M = 0.3$ and $\Omega_\Lambda = 0.7$ were used to calculate both $z_{\max}$ and $P_{1.4}$.

poor in quality to determine a redshift. These poor quality spectra arose for a myriad of reasons which were primarily instrumental (eg. broken fibres, misplaced buttons etc.) and are therefore a random subset of the data. There are no known systematic variations in spectroscopic completeness (Jones *et al.*, 2004). The spectroscopic incompleteness of 5% causes the luminosity function to be underestimated, so values of Φ have been increased by 5% to compensate.

5.4.2 Calculating the luminosity function

The radio luminosity function is a measure of the space density of radio sources ($\Phi(P)dP$) between P and $P + dP$. It is more common to write this in the form

$$\Phi_m(P) = \ln(m) P \Phi(P) \tag{5.10}$$

where $\Phi_m(P)$ is the equivalent density of sources per unit $\log_m(P)$ and $m = \mathrm{dex}(0.4)$ which is equivalent to 1 magnitude. The luminosity function is then calculated using the $(1/V_{\max})$ method of Schmidt (1968). Assuming galaxies are randomly distributed in the local universe, the value of Φ_m is estimated from the number of sources N in a bin of

width m centred on L from

$$\Phi_m(P) = \sum_{i=1}^{N} \left[\frac{1}{V_{\rm max}}\right]_i \tag{5.11}$$

where $V_{\rm max}$ is the maximum volume in which a galaxy will satisfy all the sample selection criteria. In the case of the 6dFGS-NVSS sample these selection criteria are $S_{1.4} \geq 2.5$ mJy and $K < 12.75$. $V_{\rm max}$ is calculated in practice for each source by first calculating its radio power and absolute K magnitude from its measured redshift using equations 5.1 and 5.3. Then the measured redshift is increased in steps of $\Delta z = 10^{-6}$. At each increment the radio flux density and apparent K magnitude the source would have at the new redshift is calculated from its radio power and absolute K magnitude using the inverse of the k-correction. The increments Δz continue until either the object's radio flux density drops below 2.5 mJy or its apparent K magnitude is fainter than 12.75, the redshift at which this occurs is the maximum redshift at which the source can still remain in the survey ($z_{\rm max}$). $V_{\rm max}$ is then calculated from $z_{\rm max}$ using equation 1.14.

Figure 5.13 shows a plot of $z_{\rm max}$ vs. radio power for star-forming galaxies (crosses) and AGNs (circles). The points which form an upper envelope show the locus at which galaxies drop out of the sample because of the radio flux density limit of 2.5 mJy. It is primarily star-forming galaxies which lie along this line. The higher radio power AGNs in the survey mainly drop out because of the K-magnitude limit. Most of the AGNs in the sample have an accessible redshift below $z = 0.2$ which corresponds to a lookback time of $\tau \sim 2$ Gyr and the star-forming galaxies have accessible redshifts below $z = 0.1$, a lookback time of $\tau \sim 1$ Gyr. Some evolution might be possible over these lookback times.

The rms statistical error in each bin of $\Phi_m(P)$ is given by

$$\sigma_\Phi = \left(\sum_{i=1}^{N} \left[\frac{1}{V_{\rm max}}\right]_i^2\right)^{\frac{1}{2}}. \tag{5.12}$$

This error is based on the assumption underpinning the $1/V_{\rm max}$ determination of the luminosity function that objects are randomly distributed within the sample volume. To test if this is indeed the case, one examines the distribution of $V/V_{\rm max}$ values of the sample. If the objects are randomly distributed in space then the distribution of $V/V_{\rm max}$ values should be uniform in the interval [0, 1] and have mean

$$\left\langle \frac{V}{V_{\rm max}} \right\rangle \equiv \frac{\sum_{i=1}^{N} \left[\frac{V}{V_{\rm max}}\right]_i}{N} = 0.5. \tag{5.13}$$

The standard deviation of a uniform distribution on the interval [0, 1] is $1/\sqrt{12}$ and the rms error of $\langle V/V_{\rm max}\rangle$ is therefore $1/\sqrt{12N}$. A statistically significant departure from a uniform distribution could indicate some clustering or evolution in the sample volume.

The local luminosity function can be corrected for galaxy clustering at a distance s centred on our own Galaxy using the equation

$$\frac{\rho_P}{\rho} = 1 + \frac{3}{3-\gamma_s}\left(\frac{s_0}{s}\right)^{\gamma_s} \tag{5.14}$$

(Peebles, 1980), as discussed by Condon *et al.* (2002). Here ρ_P/ρ is the expected overdensity near our own Galaxy, or the space density (ρ_P) of *local* galaxies divided by the average space density (ρ) of *all* galaxies, γ_s is the slope and s_0 the correlation scale length from a power-law fit, $\xi(s) = (s/s_0)^{-\gamma_s}$, of the two-point correlation function in redshift space. The two-point correlation function of local radio sources is derived in Chapter 6 and is adequate to describe clustering of radio sources centred on our own galaxy. Derivations of γ_s and s_0 for radio sources in the 6dFGS-NVSS sample are shown in Table 6.5; the relevant values are $\gamma_s = 1.57$ and $s_0 = 10.07$. $\xi(s)$ has a power-law form for distances $s < 30$ Mpc, and $\xi(s) \approx 0$ for $s > 30$ Mpc. Therefore to correct for the local overdensity, the volume within s is multiplied by the expression in equation 5.14 in calculating $V_{\max}$ for $s < 30$ Mpc and is left unchanged for $s > 30$ Mpc. In practise, $V_{\max}$ is almost always much larger than the local clustering volume, and so this correction has made little or no difference to the results.

5.4.3 Results

Table 5.5 shows the derived local radio luminosity function for the star-forming galaxies, AGNs and the 6dFGS-NVSS sample as a whole. The 2507 star-forming galaxies have $\langle V/V_{\max}\rangle = 0.507 \pm 0.006$, the 1569 AGNs have $\langle V/V_{\max}\rangle = 0.508 \pm 0.007$ and all the 4076 galaxies in the sample have $\langle V/V_{\max}\rangle = 0.508 \pm 0.005$. These values all lie within 2σ of the expected value of $\langle V/V_{\max}\rangle = 0.5$ which indicates little systematic large-scale clustering or evolution within the sample over its $\tau \sim 1 - 2$ Gyr lookback times. Radio sources of the highest luminosities are predominantly found at the highest redshifts where evolutionary effects may dominate the luminosity function. It is possible that the calculation of $\langle V/V_{\max}\rangle$ above allows low luminosity sources in each class to dilute the possible evolutionary effects of the higher luminosity sources (particularly for AGN). To check for this, Table 5.5 shows values of $\langle V/V_{\max}\rangle$ in each bin of radio power. There is a slight tendency toward higher $\langle V/V_{\max}\rangle$ at higher radio powers. The value is never more than 3σ from 0.5, which indicates little or no significant evolution over the sample volume.

The local radio luminosity function of all 6dFGS-NVSS galaxies is plotted in Figure 5.14; its statistical errors are of order 1% or less over 5 decades of radio luminosity. Separate local radio luminosity functions for both star-forming galaxies and AGNs are shown in Figure 5.15. These cross over at $P_{1.4} = 10^{23}$ W Hz^{-1}, star-forming galaxies dominate the population of radio sources below this power and AGNs dominate the population above it.

The luminosity function of active galaxies maintains a power-law form for about 5 orders of magnitude before turning over above $P_{1.4} > 10^{24.5}$ W Hz^{-1}. This power-law form of AGN luminosity function can only continue to fainter flux densities if it does not exceed

Table 5.5 Local radio luminosity functions at 1.4 GHz for the AGNs, star-forming galaxies and for all galaxies.

	All galaxies			Star-forming galaxies			AGNs		
$\log L_{1.4}$ (W Hz^{-1})	N	$\log \Phi$ (mag^{-1} Mpc^{-3})	$\langle V/V_{\rm max}\rangle$	N	$\log \Phi$ (mag^{-1} Mpc^{-3})	$\langle V/V_{\rm max}\rangle$	N	$\log \Phi$ (mag^{-1} Mpc^{-3})	$\langle V/V_{\rm max}\rangle$
20.0	4	$-2.80^{+0.19}_{-0.33}$	0.44 ± 0.17	4	$-2.80^{+0.19}_{-0.33}$	0.44 ± 0.17			
20.4	23	$-2.51^{+0.09}_{-0.12}$	0.48 ± 0.06	21	$-2.56^{+0.10}_{-0.13}$	0.49 ± 0.06	2	$-3.53^{+0.24}_{-0.59}$	0.43 ± 0.20
20.8	66	$-2.67^{+0.06}_{-0.06}$	0.51 ± 0.04	60	$-2.71^{+0.06}_{-0.07}$	0.52 ± 0.04	6	$-3.64^{+0.16}_{-0.26}$	0.48 ± 0.12
21.2	219	$-2.77^{+0.03}_{-0.03}$	0.44 ± 0.02	201	$-2.80^{+0.03}_{-0.03}$	0.44 ± 0.02	18	$-3.91^{+0.10}_{-0.13}$	0.53 ± 0.07
21.6	432	$-3.02^{+0.03}_{-0.03}$	0.49 ± 0.01	394	$-3.06^{+0.03}_{-0.03}$	0.49 ± 0.01	38	$-4.11^{+0.07}_{-0.08}$	0.53 ± 0.05
22.0	783	$-3.34^{+0.02}_{-0.02}$	0.51 ± 0.01	681	$-3.39^{+0.02}_{-0.02}$	0.51 ± 0.01	102	$-4.25^{+0.05}_{-0.06}$	0.51 ± 0.03
22.4	926	$-3.78^{+0.02}_{-0.02}$	0.53 ± 0.01	692	$-3.88^{+0.02}_{-0.02}$	0.54 ± 0.01	234	$-4.46^{+0.04}_{-0.04}$	0.51 ± 0.02
22.8	669	$-4.34^{+0.02}_{-0.02}$	0.50 ± 0.01	357	$-4.55^{+0.03}_{-0.03}$	0.51 ± 0.02	312	$-4.76^{+0.04}_{-0.04}$	0.49 ± 0.02
23.2	385	$-4.80^{+0.09}_{-0.11}$	0.49 ± 0.01	78	$-5.17^{+0.18}_{-0.31}$	0.49 ± 0.03	307	$-5.05^{+0.04}_{-0.04}$	0.49 ± 0.02
23.6	229	$-5.17^{+0.04}_{-0.05}$	0.51 ± 0.02	19	$-6.06^{+0.13}_{-0.18}$	0.52 ± 0.07	210	$-5.23^{+0.04}_{-0.05}$	0.51 ± 0.02
24.0	155	$-5.48^{+0.04}_{-0.05}$	0.52 ± 0.02				155	$-5.48^{+0.04}_{-0.05}$	0.52 ± 0.02
24.4	104	$-5.74^{+0.05}_{-0.06}$	0.56 ± 0.03				104	$-5.74^{+0.05}_{-0.06}$	0.56 ± 0.03
24.8	44	$-6.26^{+0.08}_{-0.10}$	0.60 ± 0.04				44	$-6.26^{+0.08}_{-0.10}$	0.60 ± 0.04
25.2	28	$-6.55^{+0.10}_{-0.13}$	0.52 ± 0.06				28	$-6.55^{+0.10}_{-0.13}$	0.52 ± 0.06
25.6	7	$-7.33^{+0.17}_{-0.29}$	0.46 ± 0.10				7	$-7.33^{+0.17}_{-0.29}$	0.46 ± 0.10
26.0	1	$-9.09^{+0.30}_{-1.00}$					1	$-9.09^{+0.30}_{-1.00}$	
26.4	1	$-9.04^{+0.30}_{-1.00}$					1	$-9.04^{+0.30}_{-1.00}$	
Total	4076		0.508 ± 0.005	2507		0.507 ± 0.006	1569		0.508 ± 0.007

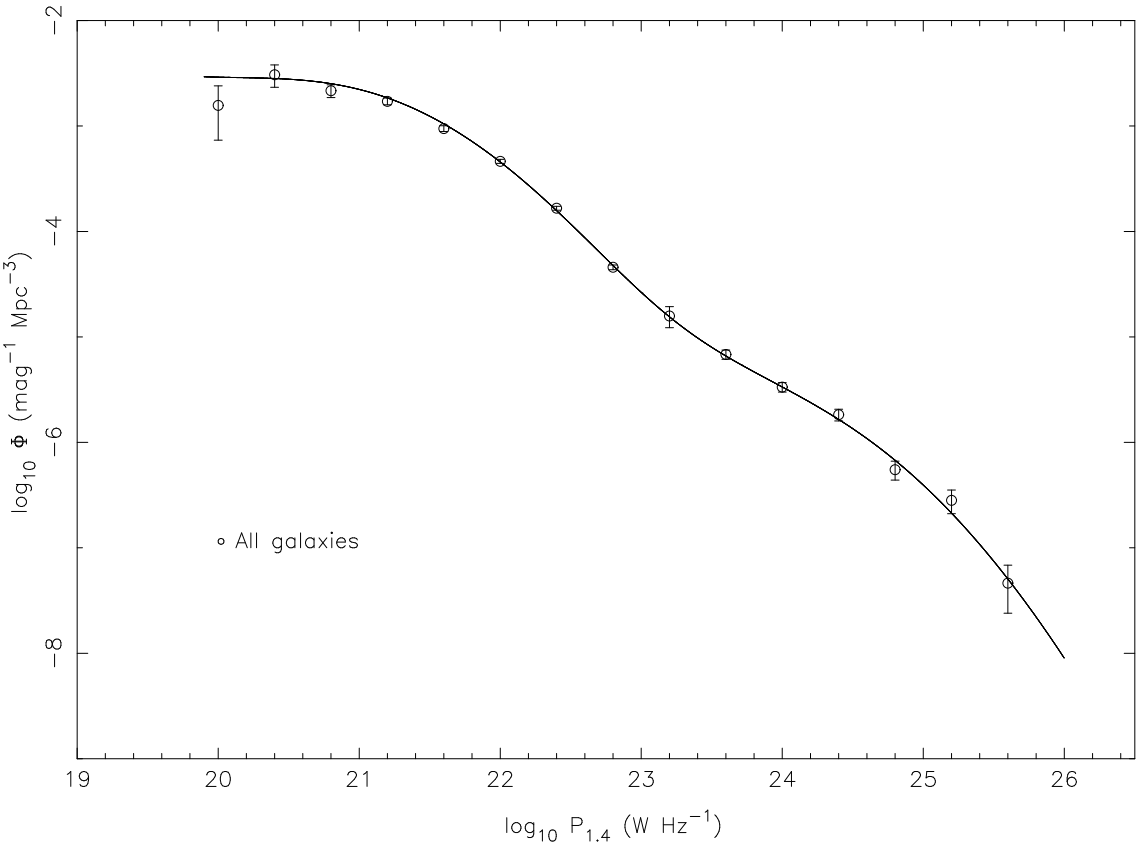

Figure 5.14 The local luminosity function at 1.4 GHz for all the radio sources in the 6dFGS-NVSS sample. All volumes and luminosities have been calculated using $H_0 = 70\,\mathrm{km\,s^{-1}\,Mpc^{-1}}$, $\Omega_M = 0.3$ and $\Omega_\Lambda = 0.7$. Error bars have been calculated using equation 5.12. The curve plotted is the sum of the contributions to the luminosity function from fits of equation 5.15 to the AGN and SF data separately (Table 5.6).

the space density of the luminous galaxies in which AGN preferentially reside. Taking the best fit Schechter function to the B-band luminosity for early type galaxies in the 2dFGRS from Madgwick *et al.* (2002), and assuming that radio AGN typically live in the brightest early type galaxies (see Figure 5.7, *bottom*), the space density of early type elliptical galaxies with ($L_B > L_B^\star$) is $(9.3 \pm 0.3) \times 10^{-4}\,\mathrm{Mpc^{-3}}$ (for $H_0 = 70\,\mathrm{km\,s^{-1}\,Mpc^{-1}}$). The space density of radio-loud AGNs from the 6dFGS-NVSS luminosity function of Figure 5.15 is $\approx 8 \times 10^{-4}\,\mathrm{Mpc^{-3}}$. If the power-law form for AGN continues to fainter radio powers a maximum must be reached at $P_{1.4} \approx 10^{19.5}\,\mathrm{W\,Hz^{-1}}$, just beyond the limit of the present data, although there is some evidence (eg. from Figure 5.7) that AGNs of lower radio power may live in less luminous host galaxies which have higher space density. In a recent radio AGN model, in which strong variability in the radio power in AGNs is related to the heating of cooling flows in galaxies and clusters, the AGN radio luminosity function is interpreted as the lognormal distribution of the time spent by an AGN at a given radio luminosity (Nipoti & Binney, 2005). From a fit to the radio luminosity function of 2dFGRS-FIRST radio sources (Magliocchetti *et al.*, 2002), Nipoti & Binney (2005)

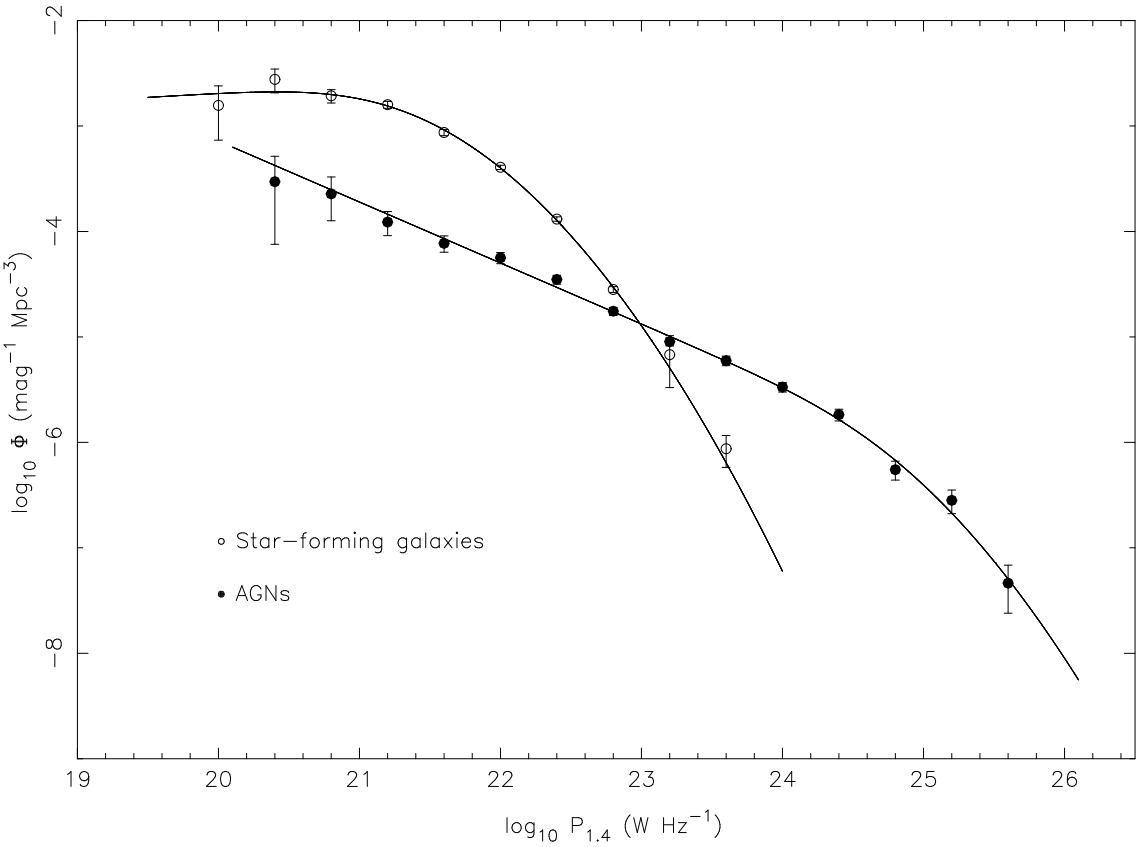

Figure 5.15 The local luminosity function at 1.4 GHz derived separately for the AGNs (*filled circles*) and Star-forming galaxies (*open circles*) in the 6dFGS-NVSS sample. All volumes and luminosities have been calculated using $H_0 = 70\,\mathrm{km\,s^{-1}\,Mpc^{-1}}$, $\Omega_M = 0.3$ and $\Omega_\Lambda = 0.7$. Error bars have been calculated using equation 5.12 in the text. The two curves plotted are the fits of equation 5.15 to the AGN and SF data.

predict that the AGN luminosity function will turn over at $P_{1.4} = 10^{20.4\pm0.1}\,\mathrm{W\,Hz^{-1}}$ (for $H_0 = 70\,\mathrm{km\,s^{-1}\,Mpc^{-1}}$). This is just at the faint limit of the 6dFGS-NVSS luminosity function and no such turnover can be seen. The model of Nipoti & Binney (2005) is poorly constrained by observational data at present. It requires further constraints on the relationship between the mechanical luminosity of heating of cooling flows by radio jets in AGN as well as a more detailed understanding of the X-ray luminosity function of AGN. It should also be noted that if the power-law form of the AGN luminosity function continues to fainter radio powers, AGNs would start to dominate the faint radio source population over star-forming galaxies below $P_{1.4} = 10^{19}\,\mathrm{W\,Hz^{-1}}$.

Optical luminosity functions are commonly fit by the Schechter function (Schechter, 1976). This function turns over more steeply toward high luminosities than radio luminosity functions. Instead the radio luminosity function is commonly fitted by the parametric form given by

$$\Phi(L) = C\left(\frac{L}{L_\star}\right)^{1-\alpha} \exp\left\{-\frac{1}{2}\left[\frac{\log_{10}(1+L/L_\star)}{\sigma}\right]^2\right\} \tag{5.15}$$

Table 5.6 Fits of equation 5.15 to the local radio luminosity function of both AGNs and star-forming galaxies for 6dFGS-NVSS galaxies and 2dFGRS-NVSS galaxies.

Parameter	Star-forming	AGN	Units
	6dFGS-NVSS		
$\log_{10} L_\star$	20.56 ± 0.01	24.06 ± 0.02	$\mathrm{W\,Hz^{-1}}$
α	0.919 ± 0.005	1.578 ± 0.010	
σ	0.728 ± 0.002	0.758 ± 0.046	
$\log_{10} C$	-2.64 ± 0.01	-5.49 ± 0.01	$\mathrm{mag^{-1}\,Mpc^{-3}}$
χ^2_{red}	0.68	0.97	
	2dFGRS-NVSS		
$\log_{10} L_\star$	19.26 ± 0.03	24.30 ± 0.03	$\mathrm{W\,Hz^{-1}}$
α	0.840 ± 0.020	1.58 ± 0.02	
σ	0.940 ± 0.004	1.00 ± 0.13	
$\log_{10} C$	-1.97 ± 0.04	-5.45 ± 0.02	$\mathrm{mag^{-1}\,Mpc^{-3}}$
χ^2_{red}	1.86	0.91	

as was used to fit the luminosity function of IRAS galaxies by Saunders *et al.* (1990). Table 5.6 shows the results of least-squares fits to the data for star-forming galaxies and AGNs and the curves plotted in Figure 5.15 also show equation 5.15 for star-forming galaxies and AGNs. The luminosity function of all galaxies is just the sum of the two contributions from star-forming galaxies and AGNs, this can be seen in Figure 5.14, the curve in this figure is just the sum of the two separate fits to the radio luminosity function for the star-forming galaxies and AGNs.

The Saunders *et al.* (1990) parametric form for the luminosity function was also fitted to the radio luminosity function of 2dFGRS-NVSS galaxies by Sadler *et al.* (2002). The values presented here generally agree well with Sadler *et al.* (2002) given the differences in the two surveys. The fits to the 2dFGRS-NVSS luminosity function were supplemented by data from other surveys at the faint and bright ends of the luminosity function. The fits to the 6dFGS-NVSS sample presented here are made purely with the available data. Though the fits to the 6dFGS-NVSS radio luminosity function are from a more homogeneous sample, inadequate sampling at both the bright and faint ends of the luminosity function presented here have affected the results of the fitting.

Figure 5.16 shows a comparison of the radio luminosity function of 6dFGS-NVSS galaxies with those of UGC-NVSS galaxies (Condon *et al.*, 2002) and 2dFGRS-NVSS galaxies (Sadler *et al.*, 2002) for star-forming galaxies and AGNs. Values of the 2dFGRS-NVSS luminosity function have been shifted from their published values to $H_0 = 70\,\mathrm{km\,s^{-1}\,Mpc^{-1}}$. The properties of these three surveys are shown in Table 5.7. The 6dFGS-NVSS sample presented here samples a larger volume of space by an order of magnitude than any previous radio source sample and probes lookback times intermediate between the very nearby UGC-NVSS sample and the more distant 2dFGRS-NVSS sample. These three luminosity functions are all drawn from the same radio source catalogue and differ only in the optical/near-infrared samples from which they are selected. The agreement between the three samples is striking.

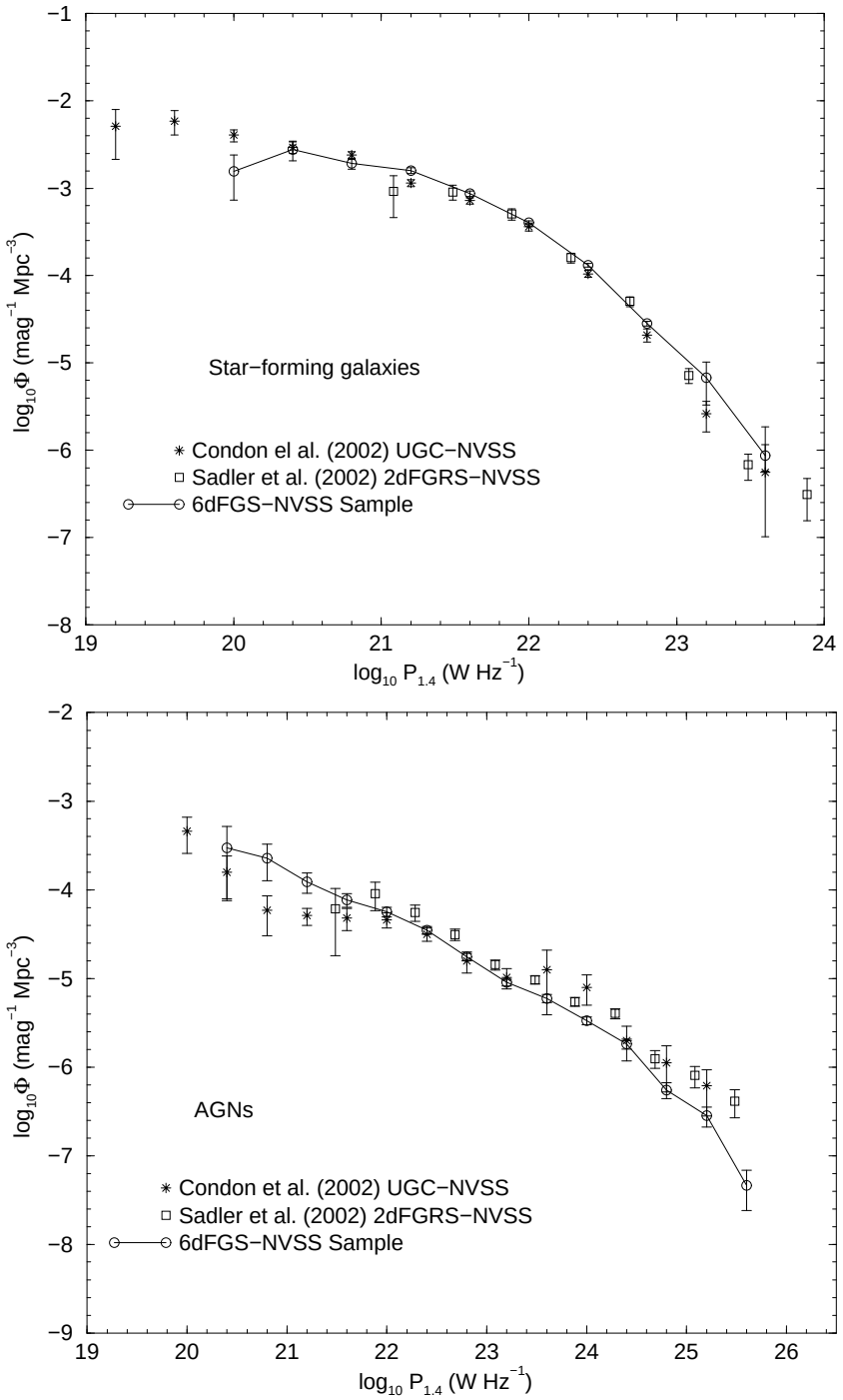

Figure 5.16 The local radio luminosity function at 1.4 GHz for star-forming galaxies (top) and AGNs (bottom), comparing results from three different samples. All volumes and luminosities have been calculated using $H_0 = 70\,\mathrm{km\,s^{-1}\,Mpc^{-1}}$. The UGC-NVSS luminosity functions of Condon *et al.* (2002) are shown as stars. The 2dFGRS-NVSS luminosity functions of Sadler *et al.* (2002) are shown as boxes and have been modified from $H_0 = 50$ to $H_0 = 70$ by the scaling factors $P_{1.4} \propto H_0^{-2}$ and $\Phi \propto H_0^3$. The 6dFGS-NVSS luminosity functions are shown as circles with a line linking the points to highlight their position.

Table 5.7 Comparison of recent radio surveys of the local universe.

	UGC-NVSS	2dFGRS-NVSS	6dFGS-NVSS
	Star-forming Galaxies		
No. Galaxies	1672	242	2507
Mag. limit	$m_p < 14.5$	$14.0 \leq b_J \leq 19.4$	$K_S < 12.75$
$S_{\rm lim}$	2.5 mJy	2.8 mJy	2.5 mJy
Area(Sr.)[a]	4.33	0.10	1.32
z range[b]	$\lesssim 0.04$	$\lesssim 0.15$	$\lesssim 0.1$
median z	0.012	0.043	0.035
Volume (10^6Mpc^3)[c]	7	8	33
τ (Gyr)[d]	0.543	1.89	1.30
$\rho_{\rm SF}(M_\odot\,{\rm yr}^{-1}\,{\rm Mpc}^{-3})$	0.018 ± 0.001	0.031 ± 0.006	0.021 ± 0.001
	AGNs		
No. Galaxies	294	420	1569
Mag. limit	$m_p < 14.5$	$14.0 \leq b_J \leq 19.4$	$K_S < 12.75$
$S_{\rm lim}$	2.5 mJy	2.8 mJy	2.5 mJy
Area(sr.)[a]	4.33	0.10	1.32
z range[b]	$\lesssim 0.04$	$\lesssim 0.3$	$\lesssim 0.2$
median z	0.019	0.140	0.073
Volume (10^6Mpc^3)[c]	7	58	240
τ (Gyr)[d]	0.543	3.44	2.44

NOTES:
[a] For the 2dFGRS-NVSS and 6dFGS-NVSS samples the area is the "effective" area as defined in Section 5.1.
[b] The maximum redshift of each survey has been estimated from the redshift histogram.
[c] Volumes are calculated to the maximum redshift of each survey and reduced by the fraction of sky surveyed.
[d] τ is the lookback time in Gyr and is calculated from the maximum redshift of each survey.

The 6dFGS-NVSS luminosity function for star-forming galaxies in the upper plot of Figure 5.16 agrees very well with the other two over the range $10^{20.5} < P_{1.4} < 10^{22.5}\,{\rm W\,Hz^{-1}}$. The falloff at the $P_{1.4} = 10^{20}\,{\rm W\,Hz^{-1}}$ point is due to the small numbers of less luminous star-forming galaxies in the 6dFGS sample volume and can also be seen at the lowest radio powers in the luminosity function of 2dFGRS-NVSS galaxies. The UGC-NVSS luminosity function extends about an order of magnitude lower in radio power for star-forming galaxies, reflecting the larger number of low-luminosity radio sources detected in a flux density limited sample covering a larger solid angle. The 6dFGS-NVSS radio luminosity function does not fall as steeply as the other two at the highest radio powers ($P_{1.4} > 10^{22.5}\,{\rm W\,Hz^{-1}}$). This might be due to the near-infrared selection of the 6dFGS-NVSS sample. Galaxies contributing to these points have the highest star-formation rates probed by radio surveys, and might not be detected in optically selected samples because of their higher rates of dust extinction.

The AGN luminosity function of 6dFGS-NVSS galaxies generally agrees well with the UGC-NVSS AGN luminosity function. The UGC-NVSS AGN sample consists of only 294 objects and is therefore not as well constrained. Most of the large error bars in the UGC-NVSS AGN luminosity function overlap with the 6dFGS-NVSS points. A power-law fit to the 6dFGS-NVSS luminosity function gives

$$\log_{10}[\Phi(P_{1.4})] = (-0.60 \pm 0.02)\log[P_{1.4}] + (8.84 \pm 0.39) \tag{5.16}$$

and to the 2dFGRS-NVSS luminosity function is

$$\log_{10}[\Phi(P_{1.4})] = (-0.62 \pm 0.03)\log[P_{1.4}] + (9.42 \pm 0.70). \tag{5.17}$$

The 2dFGRS-NVSS luminosity function has the same power-law slope as the 6dFGS-NVSS luminosity function over about 5 orders of magnitude in radio power but the two have a constant offset. This offset may be due to evolution over the narrow redshift range between $z = 0.07$ and $z = 0.14$ between the two samples, though the offset is small enough that normalisation errors may be responsible.

5.4.4 The star-formation density at the present epoch

Radio emission from star-forming galaxies in the sample is the product of massive ($M \geq 8M_{\odot}$) stars which have short lifetimes ($\tau \sim 10^7$ yr). Roughly 90% of this radio emission comes from non-thermal synchrotron electrons, which have been accelerated in the remnants of type II supernovae, and the remainder comes from HII regions heated by the most massive stars. This means that the radio luminosity of star-forming galaxies is roughly proportional to the rate of recent ($\tau \sim 10^8$ yr) star-formation (Condon, 1992). It is therefore possible to use the star-forming galaxies in this sample to estimate the present epoch star-formation density of the universe, which is the zero point of the Madau diagram (Madau *et al.*, 1996). Estimates of the local star-formation density made from radio surveys are particularly robust as they are free from the effects of dust extinction. The 6dFGS-NVSS represents an almost entirely extinction-free sample, as the radio selection is made from a near-infrared sample. Radio surveys selected from optical samples can miss extremely dusty galaxies with higher star-formation rates because dust extinction can cause these galaxies to fall out of optical samples.

It is possible to estimate the local star-formation density as a function of star-formation rate directly from the radio luminosity function using a method described by Cram (1998) and Haarsma *et al.* (2000). Assuming a typical Salpeter-like initial mass function of the form

$$\Psi(M) \propto M^{-2.35} \tag{5.18}$$

between 0.1 and $100M_{\odot}$, the star-formation rate of stars more massive than $0.1M_{\odot}$ (in $M_{\odot}$ yr^{-1}) can be calculated from the 1.4 GHz radio power by the relation

$$\mathrm{SFR(P_{1.4})} = \frac{P_{1.4}}{8.85 \times 10^{20}} \tag{5.19}$$

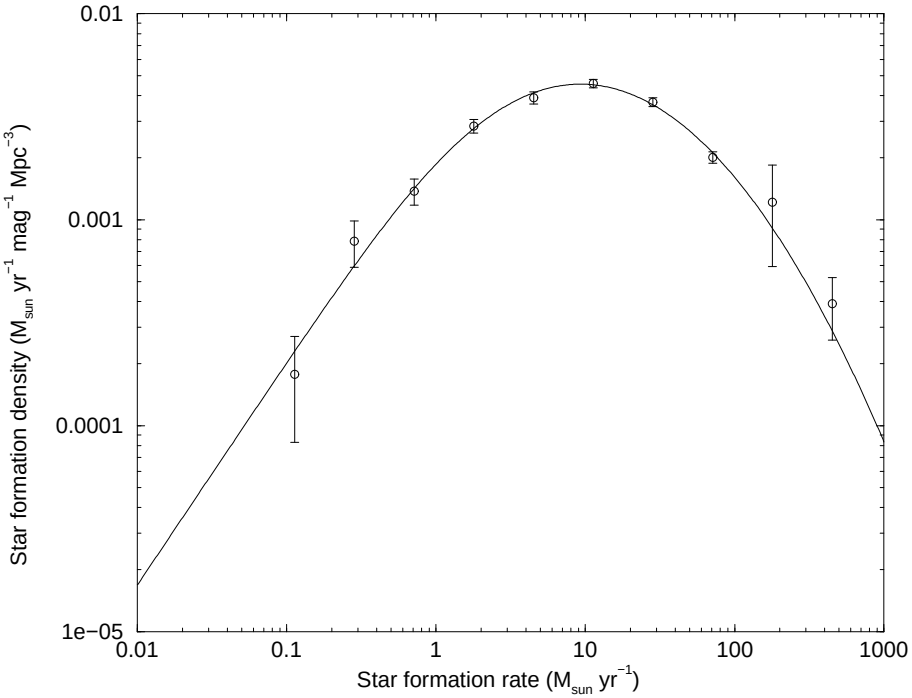

Figure 5.17 The variation in star-formation density ($\rho_{\rm SF}({\rm SFR})$) with star-formation rate for galaxies with star-formation rates between 0.1 and 100 $M_\odot$ yr^{-1} as derived from equation 5.20. Values of Φ have been taken from Table 5.5 for star-forming galaxies with the errors scaled appropriately. The curve is derived from the fit of equation 5.15 to the luminosity function of star-forming galaxies.

(Sullivan *et al.*, 2001). The star-formation density can then be determined as a function of star-formation rate by multiplying the star-formation rate by the space density of radio sources, or simply

$$\rho_{SF}({\rm SFR}) = {\rm SFR}(P_{1.4}) \times \Phi(P_{1.4}) \tag{5.20}$$

in $M_\odot$ yr^{-1} mag^{-1} Mpc^{-3}. Figure 5.17 plots equation 5.20 for the luminosity function of 6dFGS-NVSS star-forming galaxies. Star-forming galaxies in the 6dFGS-NVSS sample trace star-formation rates between 0.1 and 500 $M_\odot$ yr^{-1}, though the major contribution to the local star-formation density comes from galaxies with star-formation rates between 1 and 100 $M_\odot$ yr^{-1} as has been seen in other determinations of the star-formation density of the local universe (eg. Sadler *et al.* (radio; 2002), and Gallego *et al.* (Hα; 1995)).

Integrating underneath the curve in Figure 5.17 gives an estimate of the global star-formation density at the present epoch ($\rho_{\rm SF}$). The vast majority of radio sources in this sample contribute to the integral around its maximum at 10 $M_\odot$ yr^{-1}; the less certain points below this maximum make little contribution to the integral. This implies that the global star-formation density will be accurately constrained by the data. Rather than compute the global star-formation density from the plot in Figure 5.17 it is preferable to compute $\rho_{\rm SF}$ directly from a sum over each sample galaxy. This is done by computing the local power density function ($u(P_{1.4})$), which by analogy with equations 5.10 and 5.11

for ($\Phi(P_{1.4})$) is computed in dex(0.4) logarithmic luminosity bins and defined by

$$u_m(P_{1.4}) = \sum_{i=1}^{N} \left[\frac{P_{1.4}}{V_{\rm max}}\right]_i \tag{5.21}$$

for the N galaxies in each bin. $u(P_{1.4})$ is a measure of the total radio power produced per unit volume in each bin of radio power (it has units of $\mathrm{W\,Hz^{-1}\,mag^{-1}\,Mpc^{-3}}$). The total radio power produced per unit volume of space U (in units of $\mathrm{W\,Hz^{-1}\,Mpc^{-3}}$) is just the integral over all radio powers of the power density function

$$U = \int_0^\infty u(P_{1.4}) dP_{1.4}. \tag{5.22}$$

This can be calculated directly as the sum over all galaxies of $P_{1.4}/V_{\rm max}$. The statistical error in U is

$$\sigma_U = \left(\sum_{i=1}^{N} \left[\frac{P_{1.4}}{V_{\rm max}}\right]_i^2\right)^{\frac{1}{2}} \tag{5.23}$$

$U_{\rm SF}$ is directly proportional to the star-formation rate density $\rho_{\rm SF}$ and is computed using the relation

$$\rho_{\rm SF} = 1.13 \times 10^{-21} U_{\rm SF} \tag{5.24}$$

the factor 1.13×10^{-21} comes from the conversion between star-formation rate and radio power in equation 5.19. The shape of the distribution of $\rho_{\rm SF}(\mathrm{SFR})$ shown in Figure 5.17 ensures that the global $\rho_{\rm SF}$ will be well determined, as galaxies with lower and higher star-formation rates than those in the sample contribute little to the integral (assuming no drastic changes in the shape of $\rho_{\rm SF}(\mathrm{SFR})$).

The global power density of star formation at the present epoch implied by the 6dFGS-NVSS sample is $U_{\rm SF} = (1.84 \pm 0.09) \times 10^{19}\,\mathrm{W\,Hz^{-1}\,Mpc^{-3}}$. This translates to a global star-formation density

$$\rho_{\rm SF} = (0.021 \pm 0.001) \quad M_\odot\,\mathrm{yr^{-1}\,Mpc^{-3}} \tag{5.25}$$

The uncertainty in $\rho_{\rm SF}$ quoted here comes from equation 5.23 and takes no account of the errors arising from the conversion from $P_{1.4}$ to star-formation rate in equation 5.19. Errors in this conversion may come from predicting the star-formation rate from the Type II SNe rate, which contributes 90% of the radio power at 1.4 GHz (Sullivan *et al.*, 2001), from models of the total radio spectral energy per Type II supernova or from the assumption of a Salpeter-like initial mass function in equation 5.18.

Values for $\rho_{\rm SF}$ from the UGC-NVSS and 2dFGRS-NVSS samples are shown in table 5.7. The value of $\rho_{\rm SF}$ for 6dFGS-NVSS galaxies is intermediate between those for the other samples. Condon *et al.* (2002) derived $\rho_{\rm SF} = 0.018 \pm 0.001\,M_\odot\,\mathrm{yr^{-1}\,Mpc^{-3}}$ for the UGC-NVSS sample of 1672 star-forming galaxies, about two standard deviations lower than the value derived here. Sadler *et al.* (2002) derived $\rho_{\rm SF} = 0.031 \pm 0.006\,M_\odot\,\mathrm{yr^{-1}\,Mpc^{-3}}$ (converted to $H_0 = 70\,\mathrm{km\,s^{-1}\,Mpc^{-1}}$) for 242 star-forming galaxies from the 2dFGRS-NVSS sample, about 2 standard deviations higher than the value

derived here. UGC-NVSS sample galaxies have a median redshift of $\tilde{z} = 0.012$, the 6dFGS-NVSS sample has median $\tilde{z} = 0.035$ and 2dFGRS-NVSS sample has median $\tilde{z} = 0.043$. The apparent increase in star-formation rate density over the narrow redshift range between the UGC-NVSS sample and the 6dFGS-NVSS sample is larger than that expected from the commonly accepted evolution of the form $(1+z)^3$. A partial explanation may be that the UCG-NVSS sample is selected from galaxies in the m_p band which is subject to strong dust extinction and may have led to a small under-estimation of the local star-formation density.

The uncertainty in star-formation rates derived from radio luminosities comes primarily from inadequate models describing the relationship between the rate of type II supernovae and the rate of massive star formation in galaxies. Such uncertainties do not affect models describing the relationship between star-formation rate and luminosities at shorter wavelengths (eg. Hα or UV). However, dust extinction within the HII regions where star formation occurs contributes increasingly to the model uncertainties at these shorter wavelengths. Radio emission is an extinction-free estimator of the star-formation rate, and it is therefore of interest to compare estimates of the star-formation density in the local universe between different wavebands as a consistency check for models of star formation. From a calculation of the extinction corrected Hα luminosity function at $z \leq 0.045$, Gallego *et al.* (1995) determined $\rho_{\rm SF} = 0.018^{+0.010}_{-0.007}\, M_\odot\,{\rm yr}^{-1}\,{\rm Mpc}^{-3}$ (for $H_0 = 70\,{\rm km\,s^{-1}\,Mpc^{-1}}$). Based on H$\alpha$ imaging of a subsample of the Gallego *et al.* (1995) sample, Pérez-González *et al.* (2003) argued that this value should be $\sim 60\%$ higher because of uncertainties in the aperture corrections applied to the spectroscopic Hα luminosities. The Pérez-González *et al.* (2003) result corresponds to $\rho_{\rm SF} = 0.025^{+0.015}_{-0.010}\, M_\odot\,{\rm yr}^{-1}\,{\rm Mpc}^{-3}$, close to the value presented here but with much larger error margins. From a sample of 273 galaxies selected in the far-UV (Wyder *et al.*, 2005) found $\rho_{\rm SF} = 0.013^{+0.016}_{-0.010}\, M_\odot\,{\rm yr}^{-1}\,{\rm Mpc}^{-3}$ assuming an extinction correction of $A_{\rm FUV} \approx 1\,{\rm mag}$. The far-UV results are strongly dependent on the choice of extinction correction, and are slightly lower than those at all other wavelengths. However they agree within the quoted error with the value derived here. The general agreement between values of $\rho_{\rm SF}$ at different wavebands is very reassuring.

5.5 Fractional luminosity functions

The local radio luminosity functions of star-forming galaxies and AGNs presented in the previous section contain large numbers of galaxies in most bins of radio power. This enables the luminosity functions to be binned into statistically significant subclasses which may be studied in more detail. In particular, the local radio luminosity functions can be broken into bins of absolute K magnitude to examine the variation in the radio properties of galaxies of different near-infrared luminosities. The near-infrared selection of the 6dFGS-NVSS sample is of particular importance here, as the K-band galaxy luminosity is an extinction-free estimator of the mass of the old stellar population in galaxies, which can be related to the star-formation rate derived from radio power in the case of the luminosity function of star-forming galaxies. For the 6dFGS-NVSS AGNs, the vast majority

of which are in early type galaxies, absolute K magnitudes give an indication of a host galaxy's bulge mass which in turn is correlated with the black hole mass of the AGN (eg. Marconi & Hunt, 2003). This means it is possible to examine how the radio properties of AGNs vary with black-hole mass.

A luminosity function broken up into different subclasses of near-infrared absolute magnitude is known as a fractional, or bivariate luminosity function $F_K(P_{1.4})$, the derivation of which is described in Section 5.5.1. Results from a determination of $F_K(P_{1.4})$ for star-forming galaxies and AGNs are given in Sections 5.5.2 and 5.5.3 respectively.

5.5.1 Calculating the fractional luminosity function

Apart from the general radio luminosity function $\Phi(P_{1.4})$ defined in Section 5.4.2 which includes all kinds of radio source, it is also possible to define $\phi_i(P_{1.4})$, which is the luminosity function of radio sources of a particular class i. This is calculated by finding all objects in the sample of a desired class and then calculating the luminosity function for those objects using the method outlined in Section 5.4.2. The separate star-forming ($\phi_{\rm SF}(P_{1.4})$) and AGN ($\phi_{\rm AGN}(P_{1.4})$) luminosity functions presented in Table 5.5 are an example of luminosity functions broken into different classes. When separating the radio luminosity function into absolute K-magnitude bins it is preferable to define a normalised, or fractional, luminosity function

$$F_K(P_{1.4}) = \frac{\phi_K(P_{1.4})}{\rho_K} \tag{5.26}$$

which is the radio luminosity function of galaxies in absolute K-magnitude bin $M_K \pm \Delta M_K$ ($\phi_K(P_{1.4})$ in Mpc^{-3}) divided by the volume density (ρ_K in Mpc^{-3}) of *all* galaxies with absolute magnitude in the M_K-magnitude bin $M_K \pm \Delta M_K$. The radio luminosity function in each K magnitude bin $\phi_K(P_{1.4})$ is calculated using the $1/V_{\rm max}$ method (Schmidt, 1968) in 1-magnitude radio luminosity bins of width 0.4 in $\log(P_{1.4})$ by analogy with equation 5.11. This gives $\phi_K(P_{1.4})$ in units of mag^{-1} Mpc^{-3}. Errors of $\phi_K(P_{1.4})$ in each bin of radio power are calculated by analogy with equation 5.12. With this definition $F_K(P_{1.4})dP_{1.4}$ represents the fraction of all galaxies in the absolute near-infrared magnitude bin $M_K \pm \Delta M_K$ that have radio power between $P_{1.4}$ and $P_{1.4} + dP_{1.4}$.

To determine ρ_K, the volume density of galaxies with absolute near-infrared magnitude M_K, it is convenient to use the K-band galaxy luminosity function Φ_K, which is the space density of galaxies in the K-band in units of mag^{-1} Mpc^{-3}. It is important that the K-band luminosity function used be subject to the same selection criteria as the radio sample, so as not to introduce biases into the data. Biases may arise from variations in the clustering of objects in different regions of space, or from different amounts of evolution in samples with different median redshifts. The most natural K-band luminosity function to compare with the 6dFGS-NVSS sample is that calculated from the 6dFGS itself. A *preliminary* 6dFGS K-band luminosity function has been calculated using 69 585 galaxies in the 5.19 sr of sky of the second data release of the 6dFGS (Jones, 2005). Though the radio subsample present in this thesis was drawn from the first data release, the 6dFGS second data release covers the same region of sky as the first data release but fills in much

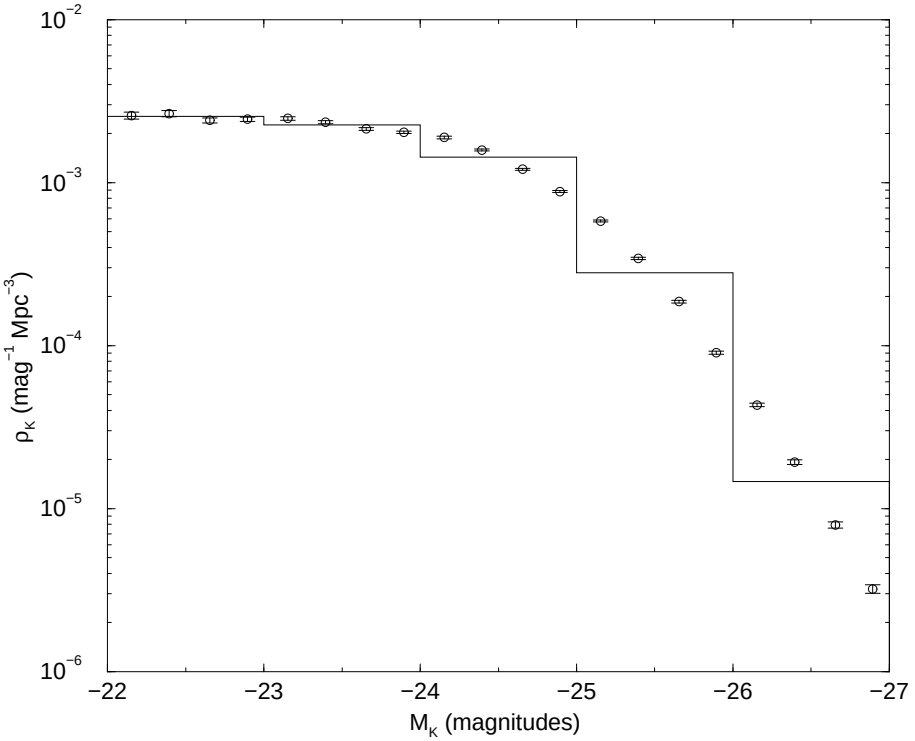

Figure 5.18 Open circles show the *preliminary* K-band luminosity function of 69 585 galaxies observed in the 5.19 sr of sky of the 6dFGS second data release (Jones, 2005). The step function shows the values of ρ_K derived from this luminosity function in the 1 magnitude bins described in the text which have been used to calculate $F_K(P_{1.4})$ as per equation 5.26.

of the incompleteness north of $\delta = -23^\circ$. The *preliminary* 6dFGS K-band luminosity function derived by Jones (2005) is shown in Figure 5.18. Its error bars are much smaller than those in the 6dFGS-NVSS luminosity function and are therefore ignored when calculating $F_K(P_{1.4})$.

The procedure used for calculating $F_K(P_{1.4})$ is as follows. First the AGN and star-forming samples are split into 5 intervals which are 1 magnitude wide in absolute K magnitude. In each M_K bin, $\phi_K(P_{1.4})$ is calculated in radio power bins of width 0.4 in $\log P_{1.4}$ which are also equivalent to 1 magnitude. This is done to ensure that the units are consistent between the M_K bins and the radio-power bins. Values of $\phi_K(P_{1.4})$ (in $\mathrm{mag}^{-1}\,\mathrm{Mpc}^{-3}$) are divided by the adopted value of ρ_K (also in $\mathrm{mag}^{-1}\,\mathrm{Mpc}^{-3}$) for each M_K bin. ρ_K values in each M_K bin are shown in the step function in Figure 5.18.

Table 5.8 shows the number of radio sources, the median redshift and the average value of $\langle V/V_{\rm max}\rangle$ separately for star-forming galaxies and AGNs in each M_K bin. For both classes of radio source the median redshift of the sample increases with increasing M_K. However there is no need to correct for this effect here because each M_K bin has been normalised by the 6dFGS K-band luminosity function which comes from the same underlying galaxy population as the radio sample. For the star-forming galaxies, values of $\langle V/V_{\rm max}\rangle$ stay within $1-2\sigma$ of 0.5 in all bins of M_K except the brightest one, which

Table 5.8 $\langle V/V_{\rm max}\rangle$ values for different M_K bins.

	SF galaxies			AGNs		
M_K bin	N	$\tilde{z}$	$\langle V/V_{\rm max}\rangle$	N	$\tilde{z}$	$\langle V/V_{\rm max}\rangle$
$-22 \geq M_K > -23$	255	0.017	0.49 ± 0.02	12	0.020	0.42 ± 0.08
$-23 \geq M_K > -24$	737	0.028	0.50 ± 0.01	52	0.026	0.46 ± 0.04
$-24 \geq M_K > -25$	1047	0.044	0.52 ± 0.01	334	0.051	0.52 ± 0.02
$-25 \geq M_K > -26$	355	0.066	0.50 ± 0.02	897	0.078	0.50 ± 0.01
$-26 \geq M_K > -27$	4	0.070	0.19 ± 0.14	263	0.127	0.55 ± 0.02
All	2507	0.035	0.51 ± 0.01	1569	0.073	0.51 ± 0.01

only contains 4 galaxies and is ignored in subsequent analysis. For the AGNs, values of $\langle V/V_{\rm max}\rangle$ are within 1σ of 0.5 in all but the brightest bin of M_K. The median redshift of 0.127 in this brightest bin for AGNs indicates some evolution of the population. The faintest M_K bin for AGNs contains only 12 galaxies and is therefore ignored in much of the subsequent analysis.

5.5.2 Fractional luminosity function of Star-forming galaxies

Figure 5.19 shows $F_K(P_{1.4})$ for star-forming galaxies in four bins of M_K. There are too few star-forming galaxies in the $(-26 : -27)$ bin to make a determination of $F_K(P_{1.4})$ so this bin is not plotted. In all the M_K bins the fraction of galaxies detected as star-forming radio sources flattens at the lowest radio powers before turning over above a certain critical radio power. The radio power at which this turn-over occurs increases with increasing K-band luminosity. For star-forming galaxies the 1.4 GHz radio power can be interpreted as a star-formation rate, as prescribed by equation 5.19 which is plotted on the upper abscissa of Figure 5.19, and M_K is related here to the mass of the old stellar population of the host galaxy. The data therefore support the idea that increasingly massive galaxies support increasingly higher star-formation rates.

5.5.3 Fractional luminosity function of AGN

Figure 5.20 plots $F_K(P_{1.4})$ for the AGNs in the four M_K bins $(-23, -24)$ $(-24, -25)$ $(-25, -26)$ $(-26, -27)$. The $(-22, -23)$ bin has been omitted as there are too few AGNs to determine $F_K(P_{1.4})$. The fractional luminosity function of AGNs has a power-law form in all four bins of M_K. Which therefore implies that there is a decrease with radio power in the fraction of galaxies which are radio-loud AGNs, reflecting the decrease in space density of AGN with increasing radio power. The power-law becomes flatter with increasing K-band luminosity, which implies that radio AGN of all powers are more common in the brightest galaxies. For a given radio power, there is a strong increase in the fraction of galaxies which are AGN with increasing K-band luminosity. More luminous galaxies are therefore more likely to host a radio-loud AGN as has been seen in previous determinations of the fractional radio-optical luminosity function of elliptical

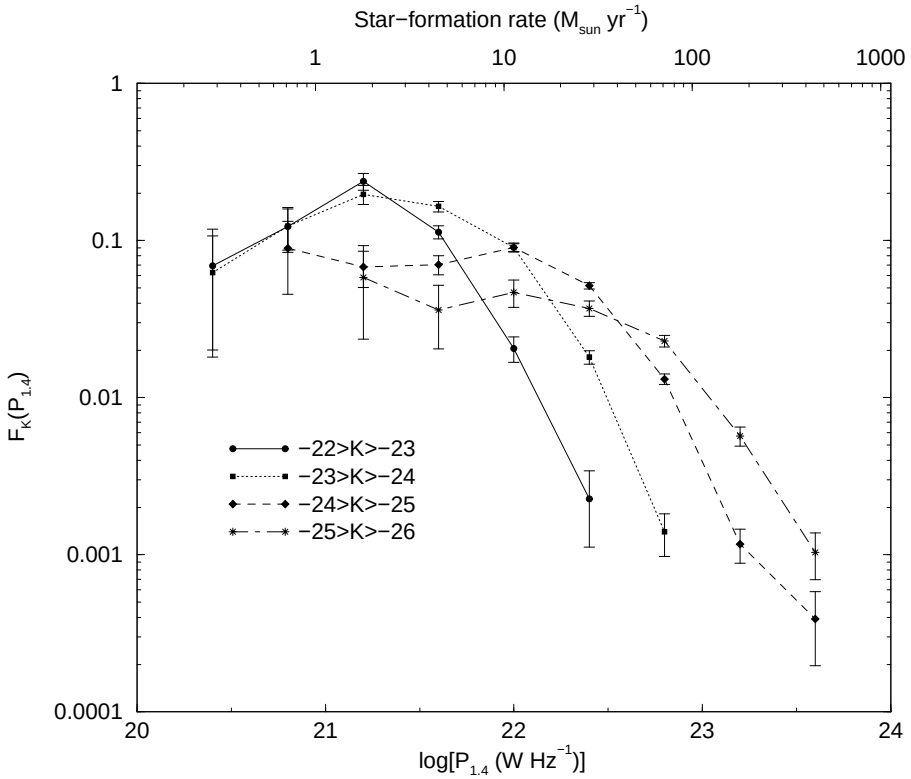

Figure 5.19 The fractional luminosity function of star-forming galaxies calculated using the procedure described in Section 5.5.1. $F_K(P_{1.4})$ is calculated in 4 bins of absolute K magnitude, in the $(-22:-23)$ M_K bin it is denoted by filled circles linked by a solid line, in the $(-23:-24)$ M_K bin it is denoted by filled squares linked by a short dashed line, in the $(-24:-25)$ M_K bin it is denoted by filled diamonds linked by a long dashed line and in the $(-25:-26)$ M_K bin it is denoted by stars linked by a long-short dashed line. The star-formation rate corresponding to the radio power on the lower abscissa derived according to equation 5.19 is shown on the upper abscissa. Error bars shown are purely statistical from equation 5.12.

galaxies (Sadler *et al.*, 1989; Auriemma *et al.*, 1977). To properly quantify this effect it is necessary to determine the fractional luminosity function in its integral form.

The integral form of the fractional luminosity function at a particular radio power ($F_K(> P_{1.4})$) is calculated in each M_K bin from the sum of $F_K(P_{1.4})$ between the largest bin of radio power ($P_{1.4}^{\max}$) to $P_{1.4}$, as defined by

$$F_K(> P_{1.4}) = \sum_{i=P_{1.4}^{\max}}^{P_{1.4}} [F_K(i)]\,. \tag{5.27}$$

The integral fractional luminosity function $F_K(> P_{1.4})$ gives the fraction of all galaxies which are radio sources with powers greater than $P_{1.4}$ in each M_K bin. It is not straightforward to calculate the error at each point of $F_K(> P_{1.4})$ because the points are not independent. For this reason errors in each radio power bin of $F_K(> P_{1.4})$ are calculated using the bootstrap method. Bootstrap errors are calculated by resampling the data under consideration at random, with replacement, to create a new dataset which has a popula-

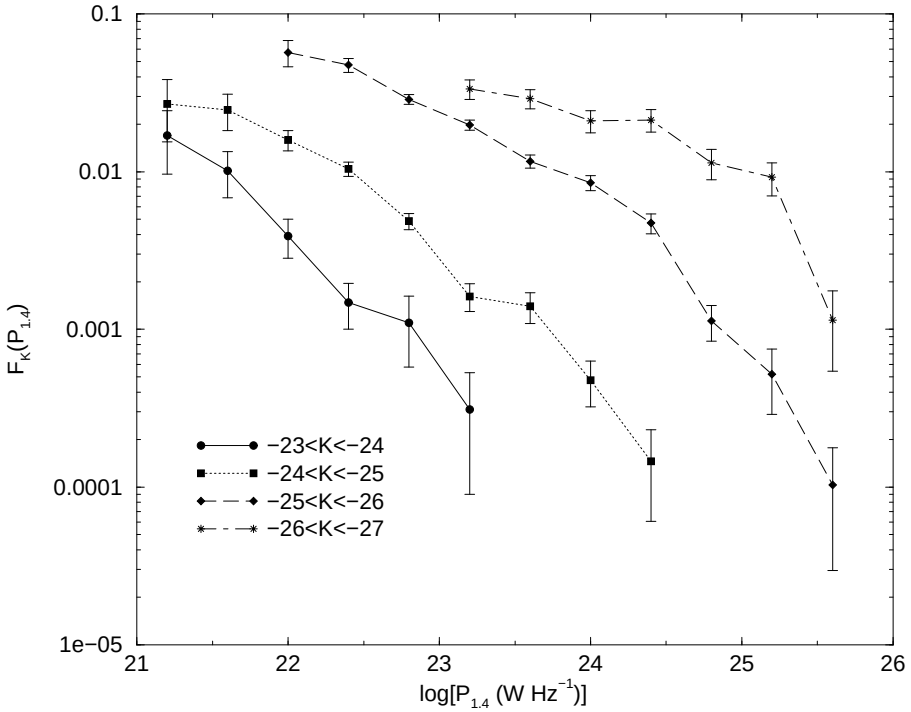

Figure 5.20 The fractional luminosity function of AGNs calculated using the procedure described in Section 5.5.1 of the text. $F_K(P_{1.4})$ is calculated in 4 bins of absolute K magnitude, in the $(-23:-24)$ M_K bin it is denoted by filled circles linked by a solid line, in the $(-24:-25)$ M_K bin it is denoted by filled squares linked by a short dashed line, in the $(-25:-26)$ M_K bin it is denoted by filled diamonds linked by a long dashed line and in the $(-26:-27)$ M_K bin it is denoted by stars linked by a long-short dashed line. Error bars shown are purely statistical from equation 5.12.

tion distribution identical to that of the original dataset. $F_K(> P_{1.4})$ is then recalculated from the resampled dataset to obtain $F_K(i)^b$. This process is then repeated $N = 10^6$ times and the standard deviation in each bin of $F_K(> P_{1.4})$ is determined from the bootstrap estimates using

$$\sigma_i^2 = \sum_{k=1}^{N} \frac{(F_K(i)_k^b - \left\langle F_K(i)^b \right\rangle)^2}{N-1} \tag{5.28}$$

where $\left\langle F_K(i)^b \right\rangle$ is the average value of the bootstrap estimates for the $i^{\rm th}$ bin of radio power. In practice with 10^6 bootstrap iterations $\left\langle F_K(i)^b \right\rangle$ recovers the calculated value of $F_K(i)$ from the actual data to one part in 10^4.

Figure 5.21 shows the fractional luminosity function of AGNs in integral form in all five bins of M_K, with bootstrap errors. With the available data, radio powers at which 30-40% of galaxies are detected as radio-loud AGNs are reached at the brightest M_K bins. Extending the radio luminosity function of AGNs to fainter radio powers will require surveys of a large volume of space at extremely low flux densities. This can be done either with a large sky area with brighter optical apparent magnitude limits or a smaller sky area with fainter optical apparent magnitude limits.

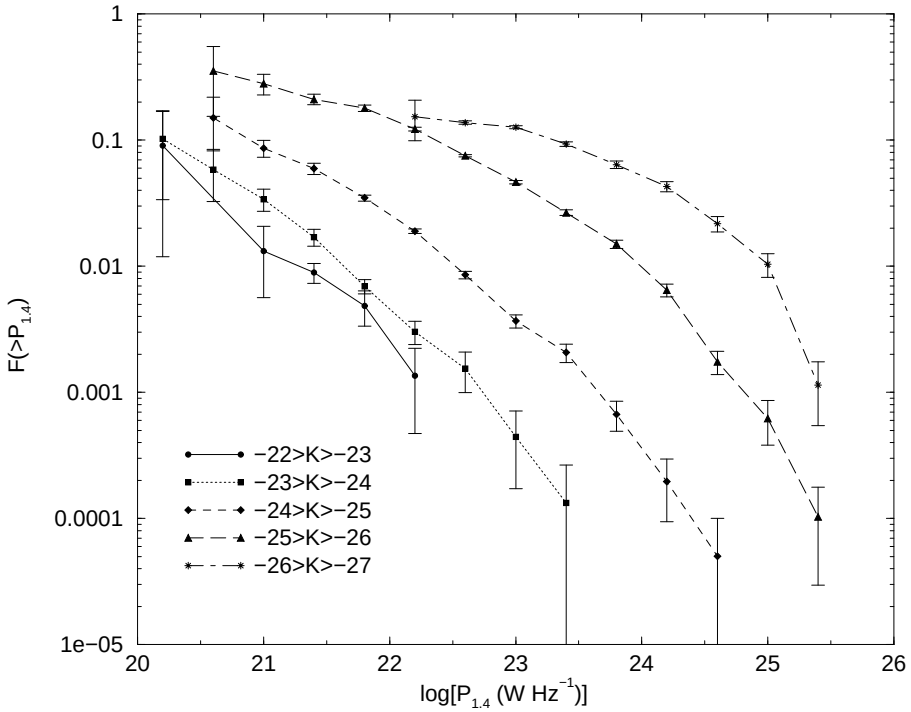

Figure 5.21 The fractional luminosity function of AGNs in integral form calculated according to equation 5.21 of the text. $F_K(> P_{1.4})$ denotes the fraction of all galaxies which are AGNs and have radio power greater than $P_{1.4}\,\mathrm{W\,Hz^{-1}}$. $F_K(> P_{1.4})$ is calculated in 5 bins of absolute K magnitude, in the $(-22:-23)$ M_K bin it is denoted by filled circles linked by a solid line, in the $(-23:-24)$ M_K bin it is denoted by filled squares linked by a dotted line, in the $(-24:-25)$ M_K bin it is denoted by filled diamonds linked by a short dashed line in the $(-25:-26)$ M_K bin it is denoted by triangles linked by a long dashed line and in the $(-26:-27)$ M_K bin it is denoted by stars linked by a long-short dashed line. Error bars have been calculated using the bootstrap method described in the text with 10^6 iterations.

One can define a characteristic 1.4 GHz radio power $P_{1.4}(n)$, which is the radio power above which n percent of galaxies radiate. It is simple to calculate this merely by drawing horizontal line at a given fraction in the integral plot of Figure 5.21. Figure 5.22 shows a plot of the characteristic radio power exceeded by 1%, 5% and 10% of galaxies versus M_K. The shape of the distribution of $P_{1.4}(n)$ versus M_K is almost independent of n: the characteristic radio power merely decreases as n increases. Given that the vast majority ($> 90\%$) of the radio AGNs in the sample reside in early-type galaxies, their M_K magnitude should be close to or equal to their near-infrared bulge luminosity. Assuming this, the K-band luminosities of AGNs in this sample are indicative of the AGNs black-hole mass via the $M_{\rm bulge} - M_{\rm BH}$ correlation (eg. Marconi & Hunt, 2003).

A fit of a power-law to $P_{1.4}(n)$ vs. M_K yields the relation

$$P_{1.4}(n) \propto {M_K}^{-1.25\pm0.10} \tag{5.29}$$

Clearly the characteristic radio power is an increasing function of K-band luminosity, which confirms that radio AGNs live preferentially in the brightest host galaxies. These

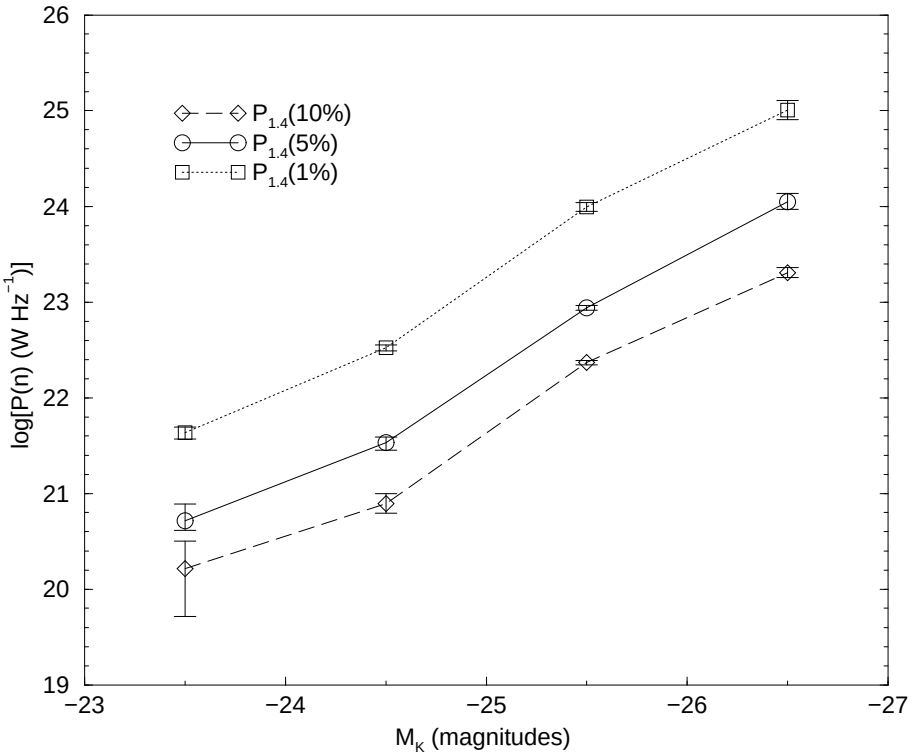

Figure 5.22 The variation of characteristic radio powers $P_{1.4}(n)$ in $\mathrm{W\,Hz^{-1}}$ exceeded by $n = 1\%$ of galaxies (squares linked by a dotted line), $n = 5\%$ of galaxies (circles linked by a solid line) and $n = 10\%$ of galaxies (diamonds linked by a dashed line) in four absolute magnitude bins.

are also the galaxies with the largest black-hole masses. Only a very small fraction of all galaxies with M_K fainter than -23 are detected as radio sources in the 6dFGS-NVSS sample which implies there is a minimum black-hole mass of around $10^8\,\mathrm{M}_\odot$ for the onset of an AGN, similar to that found in other studies of radio-loud AGN (eg. Magliocchetti *et al.* (2002)). Above this minimum black-hole mass, it appears that more massive black holes support increasingly more powerful radio sources.

5.6 Conclusion

In this chapter the 4506 radio sources in an effective area of 1.32 sr north of $\delta = -40°$, which comprise the 6dFGS-NVSS primary sample, have been examined in detail. The main results of this chapter are:

- The median redshift of all radio sources in the sample is $\tilde{z} = 0.046$, similar to that of the $\sim 30\,000$ K-band selected galaxies from which the radio sources were selected. 60% of 6dFGS-NVSS primary targets are spectroscopically identified as star-forming galaxies which form a much more nearby population ($\tilde{z} = 0.035$) and 40% of 6dFGS-NVSS primary targets are spectroscopically identified with AGNs which form a more distant population ($\tilde{z} = 0.073$).

- Star-forming galaxies and AGNs have quite distinct distributions in the plane of radio power vs. absolute K magnitude. Star-forming galaxies tend to have radio powers $P_{1.4} < 10^{23}\,\mathrm{W\,Hz^{-1}}$, though they have a wide range of absolute K magnitudes. The AGNs are found over the entire range of radio powers surveyed but are almost all found in the most luminous near-infrared galaxies with $M_K > M_K^\star$.

- 1714 star-forming galaxies and 151 AGNs were detected at 60 μm in the IRAS Faint Source Catalogue. One would expect all star-forming galaxies in the sample to be detected in the IRAS-FSC because they all should lie on the radio-FIR correlation. However, incompleteness in the IRAS-FSC as well as the intrinsic dispersion in the measured radio-FIR correlation has meant that only 65% of spectroscopically classified star-forming galaxies in the 6dFGS-NVSS sample have detections in the IRAS-FSC.

- All of the star-forming galaxies with IRAS-FSC detections in the 6dFGS-NVSS sample are found to lie on the radio-FIR correlation, with average FIR-radio flux ratio parameter $\langle q_{\mathrm{SF}} \rangle = 2.3$ with rms scatter $\sigma_{\mathrm{SF}} = 0.18$, in close agreement with the results of other recent radio-FIR surveys (UGC-NVSS; Condon *et al.*, 2002). Many of the 151 AGNs with IRAS-FSC 60 μm detections also lie on the radio-FIR correlation. However, these tend to have hotter IRAS 60-25 μm colours. The combination of the radio-FIR correlation and the 60-25 μm colour as a means of AGN/Star-forming classification for radio sources agrees with spectroscopic classification for $\sim 95\%$ of all galaxies, which is reassuring considering the differences in these classification techniques.

- The most accurate and homogeneous local radio luminosity functions at 1.4 GHz of star-forming galaxies and AGNs has been presented. The AGN luminosity function maintains a power-law form for over 5 orders of magnitude down to $P_{1.4} = 10^{20}\,\mathrm{W\,Hz^{-1}}$ and must turn over before $P_{1.4} = 10^{19}\,\mathrm{W\,Hz^{-1}}$ so as not to exceed the space density of luminous elliptical galaxies. The luminosity functions presented here agree well with recent determinations of the local radio luminosity function derived from different optical samples (eg. UGC-NVSS; Condon *et al.* (2002), 2dFGRS-NVSS; Sadler *et al.* (2002)). A small shift in the position of the power-law section of the AGN radio luminosity function derived from the higher redshift 2dFGRS-NVSS sample may be the result of evolution. However, the shift does not have the statistical significance to make a quantitative measurement of this evolution.

- The star-formation density at the present epoch has been measured from the 6dFGS-NVSS sample and was found to be $\rho_{SF} = (0.021 \pm 0.001)\,\mathrm{M_\odot\ yr^{-1}\ Mpc^{-3}}$, a value which is 2σ greater than the more nearby UGC-NVSS sample (Condon *et al.*, 2002) and 2σ smaller than the more distant 2dFGRS-NVSS sample (Sadler *et al.*, 2002). The star-formation density measured from the 6dFGS-NVSS sample is greater than that expected from $(1+z)^3$ evolution over the narrow redshift range and is attributed to a slight under-estimation in the UGC-NVSS sample due to dust extinction in the optically-selected host galaxies.

- The radio luminosity function of both star-forming galaxies and AGNs has been split into five M_K bins and combined with the *preliminary* K-band luminosity function of 6dFGS galaxies to calculate the fractional luminosity functions $F_K(P_{1.4})$ of 6dFGS-NVSS star-forming galaxies and AGNs. The derivation of $F_K(P_{1.4})$ for AGNs has shown that the fraction of AGN fuelled radio sources increases strongly as a function of near-infrared luminosity, which in turn is indicative of an increasing probability for a galaxy to host a radio-loud AGN with increasing black-hole mass.

Chapter 6

Clustering of 6dFGS Radio Sources

In this chapter a brief analysis of the clustering properties of radio sources in the primary 6dFGS-NVSS sample is presented. Clustering properties are determined via the two-point correlation function in both redshift space and real space and are calculated for a subsample of 2090 6dFGS-NVSS galaxies where coverage of the 6dFGS first data release is most uniform. This work was undertaken during a four month stay at Oxford University from July to November 2004 under the supervision of Professor Steve Rawlings. The code used to calculate the two-point correlation function was entirely written by me but was modelled upon code kindly provided to me by Dr Kate Brand.

6.1 Introduction

With the recent release of mJy level radio surveys covering large fractions of the sky (eg. NRAO VLA Sky Survey (NVSS; Condon *et al.*, 1998), Westerbork Northern Sky Survey (WENSS; Rengelink, 1998), Sydney University Molonglo Sky Survey (SUMSS; Mauch *et al.*, 2003) and Faint Images of the Radio Sky at Twenty cm (FIRST; Becker *et al.*, 1995)) it has become possible to study the large-scale structure in the spatial distribution of radio galaxies down to a limiting flux density of a few mJy over large fractions of the celestial sphere. The population of radio sources at these flux densities includes a mix of galaxies whose dominant source of radio emission is powered by super-massive black holes (AGNs) and those which are powered by ongoing star formation. Radio-loud AGN are believed to be excellent probes of large scale structure over the large range of redshift in which they are found in radio surveys. This is because they are extremely biased tracers of the underlying matter distribution (as discussed in Section 1.3.2). Measurements of the angular two-point correlation function $\omega(\theta)$ have been made for all of these surveys and the results are in excellent agreement (eg. Blake *et al.*, 2004). However, de-projecting the angular two-point correlation function to estimate the spatial two-point correlation function $\xi(r)$ is difficult as the redshift distribution $N(z)$ of mJy radio sources is poorly determined out to the median redshift of most radio source surveys ($z \sim 0.8$). This results in widely conflicting determinations of the clustering scale length r_0 for radio sources.

A simple way to alleviate the problem of poorly-determined $N(z)$ is to measure a 'characteristic' $N(z)$ using a homogeneous subsample of radio sources. Early work of this kind was done by Peacock & Nicholson (1991) in which the authors obtained redshifts for a sample of 329 radio sources throughout the celestial sphere with $|b| > 15^\circ$ and $S_{1.4\,\mathrm{GHz}} > 0.5\,\mathrm{Jy}$ to calculate the redshift-space two-point correlation function of radio sources in the local universe.

Obtaining redshifts for larger samples of radio sources has recently become possible with the release of large optical redshift surveys such as the 2 degree Field Galaxy Redshift Survey (2dFGRS; Colless *et al.*, 2001), Sloan Digitised Sky Survey (SDSS; York *et al.*, 2000) and 6 degree Field Galaxy Survey (6dFGS; Jones *et al.*, 2004). All of these surveys provide redshifts for large numbers of galaxies over large areas of sky and can be used in concert with the large-area radio surveys mentioned above to obtain redshifts of many radio sources in the local universe. Magliocchetti *et al.* (2004) have done this by crossmatching FIRST radio sources down to 1 mJy in the 2dFGRS. They obtained a sample of 826 radio sources with optical spectra and redshifts from which they determined the two-point correlation function in both redshift space and real space. Having the source spectra also allows the physical cause of radio emission to be determined and then correlation functions of different types of galaxies can be studied separately (eg. AGNs and star-forming galaxies). This chapter presents preliminary clustering results for over 2000 radio sources from the 6dFGS first data release studied in concert with the NVSS.

A cosmology is assumed throughout with $\Omega_M = 0.3, \Omega_\Lambda = 0.7$ and $h = 0.7 = H_0/100$ consistent with the latest WMAP CMB and 2dF results (eg. Spergel *et al.*, 2003). All distances and separations are calculated in comoving units unless otherwise stated.

Table 6.1 Spectral classification of the subsample used to calculate the two-point correlation function.

Class	Number
Aa	633
Aae	67
Ae	76
SF	1314

6.2 Sample Selection

The sample selection of the 6dFGS-NVSS primary targets is fully described in Chapter 3. The 6dFGS first data release primarily covers the survey's central declination strip ($-42^\circ < \delta < -23^\circ$) and includes additional fields at other declinations. For this analysis only 6dFGS-NVSS primary target galaxies which lie in the approximately 2000 deg.^{2} of sky bounded by $8h < \alpha < 24h$ and $-40^\circ < \delta < -20^\circ$ with $|b| > 10^\circ$ were used since coverage was most uniform in this region. An NVSS 1.4 GHz flux density threshold of 3 mJy was applied to maximise the completeness and reliability of the sample.

Table 6.1 shows the spectral mix of the 6dFGS-NVSS subsample used for analysis. Two galactic stars in the region studied were removed from the dataset. Aa, Aae and Ae galaxies are all grouped together and referred to as the AGN sample and star-forming galaxies as the SF sample. About 1% of galaxies with emission line spectra were difficult to visually distinguish between the SF and AGN classes. As described in Chapter 5 these sources were classified on the basis of their observed radio power. Galaxies with $P_{1.4} < 10^{23}\,\mathrm{W\,Hz^{-1}}$ were classed as star-forming and those with $P_{1.4} > 10^{23}\,\mathrm{W\,Hz^{-1}}$ were classed as AGNs.

Figure 6.1 shows the sky coverage of the sample. Filled circles indicate observed galaxies and open circles indicate unobserved galaxies. The numbers in the overplotted grid of 4.5 deg^2 cells show the completeness in each cell. The completeness in this region is fairly uniform except in the most over-dense regions (eg. The Shapley supercluster). Lower completeness in these regions is caused by the tiling strategy of the 6dFGS (Campbell *et al.*, 2004). Over-dense regions require a greater number of overlapping observations for all galaxies to be observed. The overall completeness of the area in this analysis is 60%. Corrections for incompleteness in the sample are discussed in Section 6.3.1.

6.3 The two-point correlation function in redshift space

The redshift-space two-point correlation function $\xi(s)$ was calculated using the 2090 galaxies from Table 6.1. $\xi(s)$ was calculated separately for both the AGN and SF classes of galaxy and for the combined sample of all galaxies. The two-point correlation function is calculated by counting the numbers of pairs in comoving separation bins in the data. These are compared to the number of pairs in a random catalogue which has the same selection function as the data under consideration. A random catalogue is constructed

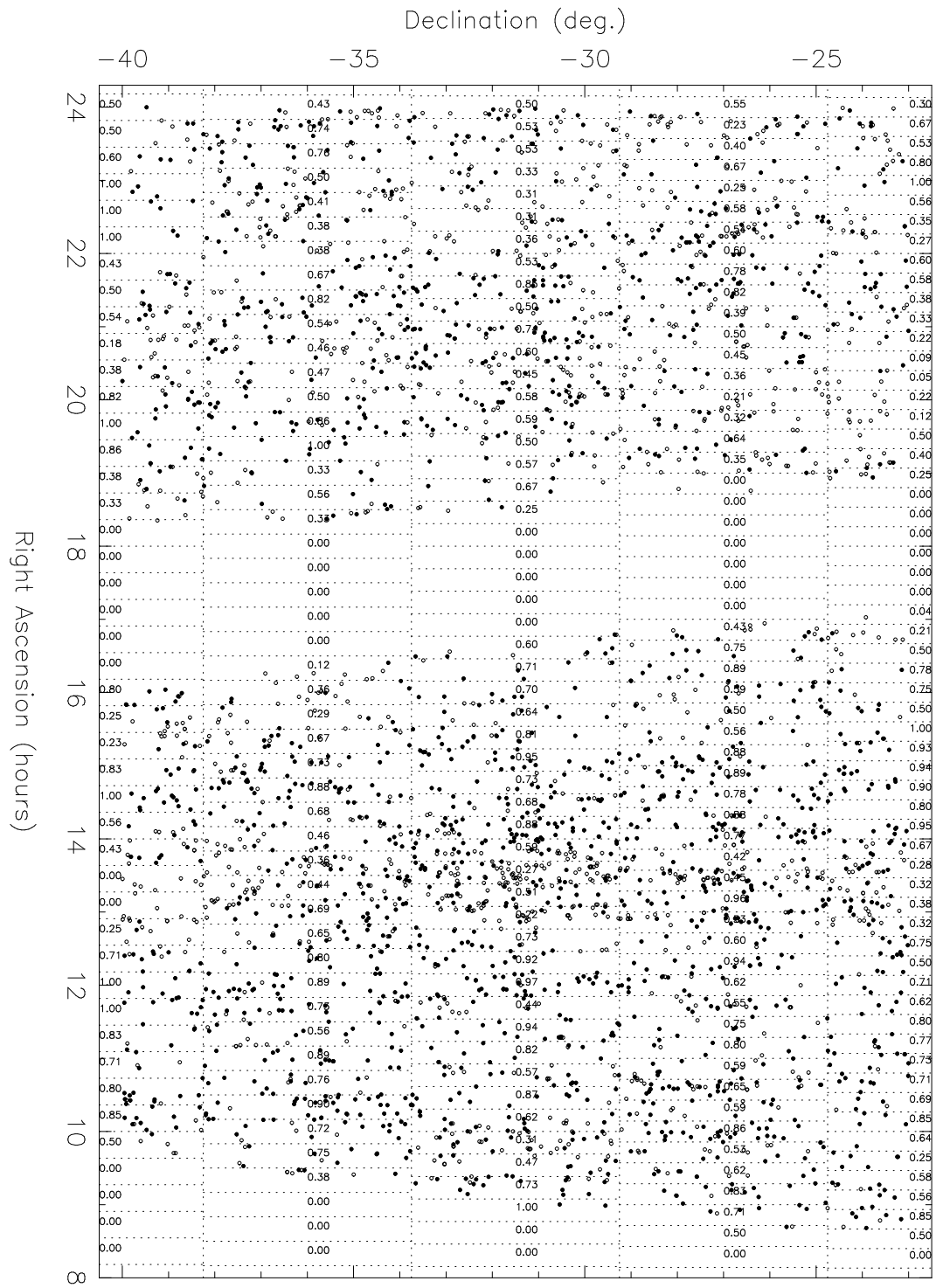

Figure 6.1 A completeness map of the 6dFGS-NVSS subsample used to calculate the two-point correlation function. Filled circles indicate galaxies which have been observed as part of the 6dFGS first data release and empty circles are identified radio sources which have not yet been observed. A grid of 4.5deg.^{2} boxes is overplotted and and the completeness in each box is shown. This is used when generating a random catalogue such that the local completeness will not bias the true clustering signal. No galaxies are observed within $b = \pm 10^\circ$ of the galactic plane hence the completeness in this region drops to 0.0.

which mimics both the angular completeness and the radial selection function of the real data.

6.3.1 Selection function

Redshift incompleteness due to broken fibres or bad quality data as well as the incomplete coverage of the first data release mean that the completeness is not uniform over the area of sky chosen for this analysis. Varying completeness can affect the determination of the two-point correlation function as areas which are more complete can appear more clustered than areas which are not. The number in each cell of the overplotted grid in Figure 6.1 shows the completeness in that cell. Completeness is defined simply as the ratio of the number of NVSS radio galaxies for which a 6dFGS redshift has been obtained in a cell divided by the total number of 6dFGS-NVSS identifications in the same cell.

6dFGS-NVSS primary targets are contained within a volume of about $2 \times 10^8\,\mathrm{Mpc}^3$, a representative fraction of the local universe (see Table 5.7). This means that the redshift distribution of this sample tends to be smoothed out and is unaffected by smaller scale structure due to clustering. Therefore, to obtain a model redshift distribution for constructing a random catalogue the redshift distribution of the available data is used as the model $N(z)$. A model curve was determined by interpolating between selected points in the redshift histogram of each sample with a cubic spline. The points were chosen so as to minimise the χ^2 value of the fit to the histogram. Interpolating points were placed no more than four bins apart to ensure as good a fit as possible to the data available. Figure 6.2 shows cubic spline fits to the redshift distributions of the SF, AGN and the combined sample. These fits were subsequently used as the model redshift distribution in constructing random catalogues.

To construct a random catalogue a position is chosen at random in the same region of sky as the real data (i.e. $8h < \alpha > 12h$, $-40^\circ < \delta < -20^\circ$ and $|b| > 10^\circ$). The completeness near this random position is obtained from the completeness map in Figure 6.1. This measured local completeness is then used as a probability that the chosen position be kept in the random catalogue. If the position is kept, it is then assigned a redshift from the measured redshift distribution $N(z)$ in Figure 6.2. The process is repeated until the number of objects in the random catalogue equals the number of objects in the real data.

6.3.2 The two-point correlation function

The most common statistic used to measure the clustering properties of a catalogue is the two-point correlation function. The two-point correlation function measures the excess chance dP of finding a pair of objects in two volume elements dV_1 and dV_2 with a comoving separation r over the chance a pair would be found if the objects were distributed at random. It is defined by

$$dP = \rho_0^2[1 + \xi(r)]dV_1 dV_2 \tag{6.1}$$

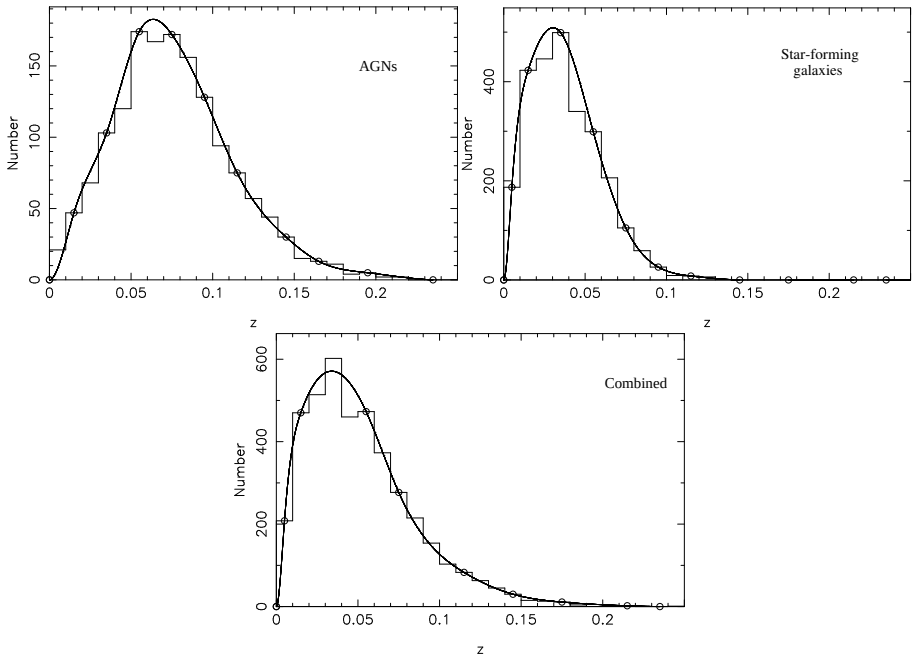

Figure 6.2 Cubic spline fits to the redshift distributions of AGN (*top left*), SF (*top right*) and all galaxies (*bottom*) in the 6dFGS-NVSS primary target sample. Circles are plotted on each histogram at the interpolating points of the cubic spline fits.

where ρ_0^2 is the average number density of objects in the survey. See Peacock (1999) for a detailed description. The correlation function is often fitted by a power-law

$$\xi(s) = \left(\frac{s}{s_0}\right)^{-\gamma} \tag{6.2}$$

in which γ is the slope of the correlation function and s_0 is the intrinsic correlation scale length (actually the value for which $\xi(s) = 1$). s is used instead of r in this section to denote separations in redshift space. Because s_0 is a measure of the overall clustering properties of any sample, it is the most often used value for comparison of the clustering of different datasets.

The correlation function is calculated using an estimator which is computed by counting the number of pairs at a given separation in the catalogue under consideration and comparing this to the number of pairs in a random catalogue with the same angular completeness and radial selection function as the real catalogue. There are many estimators which can be used for calculating the correlation function (see Kerscher *et al.* (2000) for a description), for this analysis the estimator described by Landy & Szalay (1993) was used and is defined by

$$\xi(s) = \frac{DD(s) - 2DR(s) + RR(s)}{RR(s)}, \tag{6.3}$$

where $DD(s)$, $RR(s)$ and $DR(s)$ are the number of data-data, random-random and data-random pairs at separation s. This estimator was chosen because it has been found to

Table 6.2 The least-squares best fitting parameters of a power-law to the redshift-space correlation function.

Sample	γ	s_0 (Mpc)	$\chi^2_{\rm reduced}$
AGN	1.68 ± 0.06	13.03 ± 0.36	0.37
SF	1.48 ± 0.13	9.59 ± 0.48	1.09
All	1.45 ± 0.08	10.18 ± 0.31	1.02

outperform others at large separations ($s \sim 115h^{-1}\,$Mpc) whilst being comparable on small ($s \sim 4h^{-1}\,$Mpc) scales (Kerscher *et al.*, 2000).

In order to overcome statistical variations within the random samples, one-thousand random catalogues were generated with the same number of sources as the input catalogues. Random catalogues had the angular completeness and radial selection function as determined in Section 6.3.1 applied to them. This procedure was applied to all of the three samples under consideration (ie., the AGN, SF and combined samples).

Figure 6.3 shows the results for the correlation function in redshift space for the three samples. Data points in a plot of $\xi(s)$ are not independent (ie. single galaxies can contribute pairs in more than one bin), therefore standard Poisson error bars underestimate the true error in each bin. Error bars in the plots were calculated by bootstrap resampling the data 50 times. The bootstrap method involves resampling the data with replacement and at random to construct a new dataset which has a population distribution identical to that of the original dataset. The correlation function is then recomputed using this resampled dataset to obtain $\xi^b(s)$. This process is then repeated N times and the standard deviation in each bin of $\xi(s)$ is determined from the bootstrap sample using

$$\sigma_i^2 = \sum_{k=1}^{N} \frac{(\xi_i^{b_k} - \langle \xi_i^b \rangle)^2}{N-1} \tag{6.4}$$

where $\langle \xi_i^b \rangle$ is the average value of ξ for the bin i.

The points in Figure 6.3 suggest that a power-law fit is not good over all the range of values for $\xi(s)$. The redshift-space correlation function tends to steepen for $s > 30\,$Mpc and flatten on scales $s < 3\,$Mpc. This effect has been seen in previous determinations of $\xi(s)$ (eg. Magliocchetti *et al.*, 2004; Hawkins *et al.*, 2003), and on small scales can be attributed to high peculiar velocities in over-dense regions stretching galaxies in redshift space (the 'fingers-of-god' effect). Because of these deviations a power-law fit is only made between separations $3\,\mathrm{Mpc} < s < 60\,\mathrm{Mpc}$ for the AGN sample and between $4\,\mathrm{Mpc} < s < 40\,\mathrm{Mpc}$ for the SF and combined samples. The line shown in each plot of Figure 6.3 is a least-squares fit of equation 6.2 to the binned data as a function of s. Table 6.2 shows the best fitting values of the parameters s_0 and γ for the three samples under consideration.

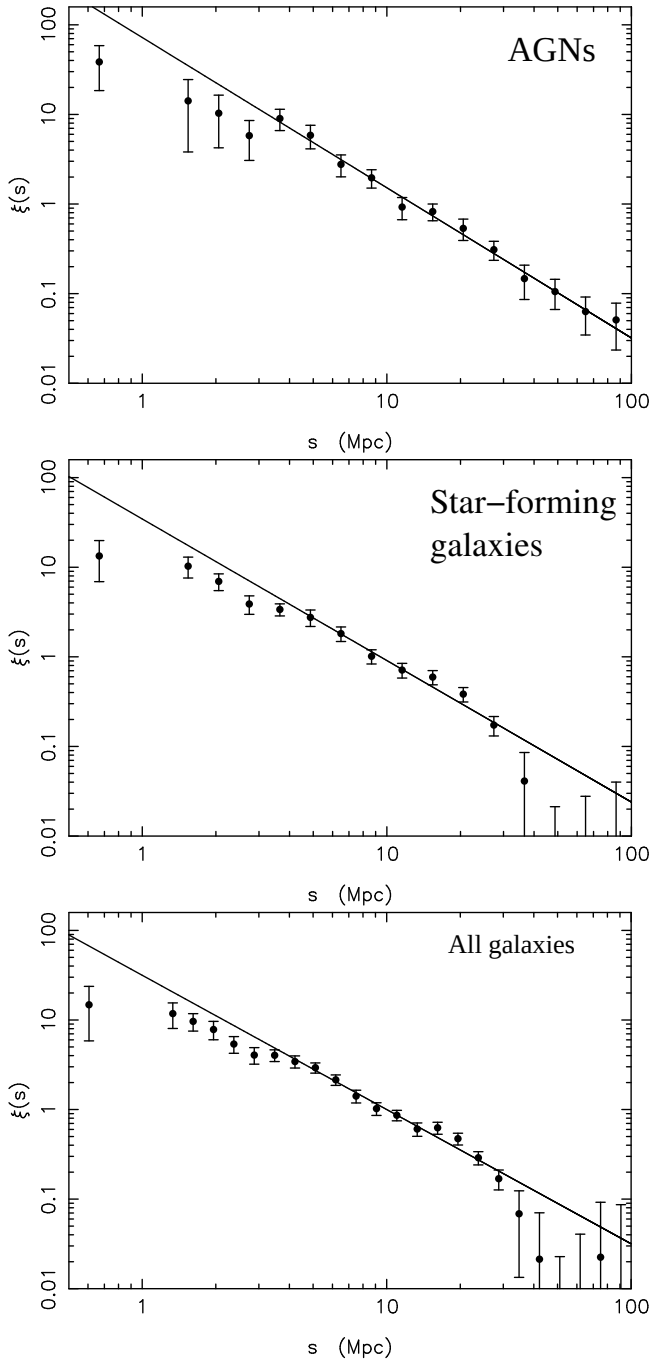

Figure 6.3 The redshift-space correlation function for AGNs (*top*), star-forming galaxies (*middle*) and the combined sample (*bottom*). The line shown is a least-squares fit to the data. In the top figure only points between $3\,\mathrm{Mpc} \leq s < 60\,\mathrm{Mpc}$ and in the middle and bottom figures only points between $4\,\mathrm{Mpc} \leq s < 40\,\mathrm{Mpc}$ were fitted. These regions were deemed to be those in which a power law is a good fit to the data. The error bars were obtained by bootstrap resampling the data 50 times.

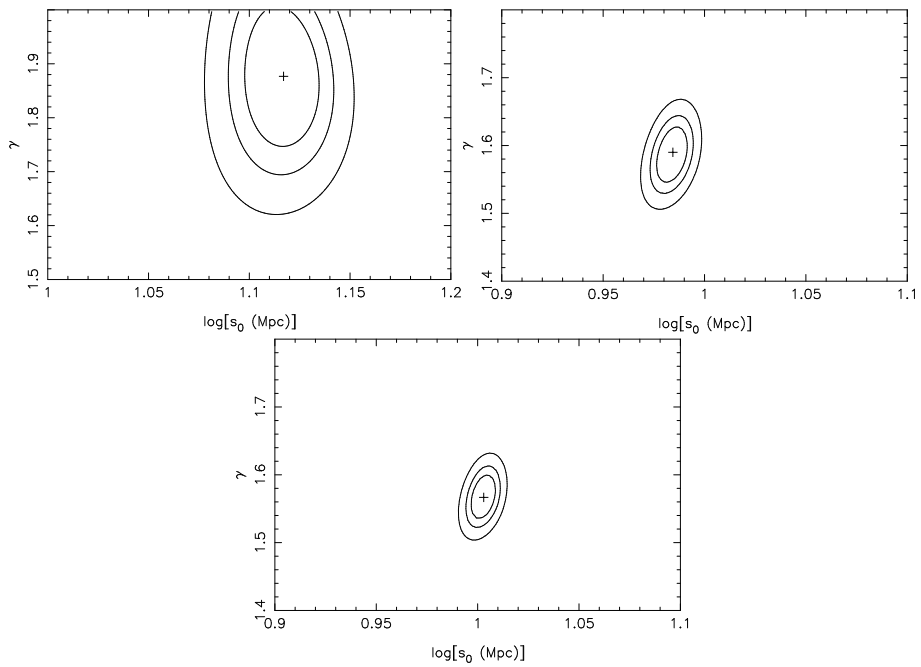

Figure 6.4 Best fitting values for s_0 and γ obtained by applying the maximum likelihood method described in Section 6.3.3. Top right shows the results for SF galaxies, top left for AGNs and the bottom for the combined sample. The contours shown are plotted at 1,2 and 3 σ and were directly determined from the probability distribution obtained from equation 6.6

.

Table 6.3 Values for γ and s_0 obtained by the maximum likelihood method.

Sample	γ	s_0 (Mpc)
AGN	$1.87^{+0.07}_{-0.09}$	$13.07^{+0.38}_{-0.41}$
SF	1.59 ± 0.03	$9.65^{+0.12}_{-0.13}$
All	1.57 ± 0.03	10.07 ± 0.11

6.3.3 Maximum likelihood estimator

It is possible to determine the values of γ and s_0 using a more direct (unbinned) method than least-squares fitting the binned data. Each galaxy can contribute to close pairs in multiple bins in Figure 6.3. This can cause the correlation function in neighbouring bins to be correlated. Binning the data can also introduce uncertainties as the calculated value of $\xi(s)$ can depend on the binning interval used. Croft *et al.* (1997) describe a method of maximising the likelihood that the observed pair separations can be described by the power-law form of equation 6.2. Using this method it is possible to determine the parameters γ and s_0 without binning and compute confidence limit contours in γ-s_0 parameter space.

To construct a maximum likelihood estimator a catalogue of random points is constructed with the same angular completeness and radial selection function described in Section 6.3.1. Then, if the number of cluster–random pairs in an interval ds is $g(s)ds$

then the predicted mean number of cluster–cluster pairs in that interval ($h(s)ds$) can be written as (Croft *et al.*, 1997),

$$h(s)ds = \left[1 + \left(\frac{s}{s_0}\right)^{-\gamma}\right] fg(s)ds, \tag{6.5}$$

where f is a normalisation calculated from the number of data points divided by the number of random points. Random catalogues with 10^5 points were constructed so that the number of data–random pairs could be binned into 400 intervals between 0–100 Mpc.

A likelihood function ($\mathcal{L}$) is then determined using the separations (s_i) of the N data–data pairs. $\mathcal{L}$ is the product of the probabilities in a chosen range (s_a to s_b; or the range over which we expect $\xi(s)$ to have the power-law form) that there is a pair in the interval ds at each of the data–data pair separations s_i and the probability that there are no pairs in the other intervals ds. For more information see both Croft *et al.* (1997) and Marshall *et al.* (1983).

The best fitting values of γ and s_0 are then obtained by minimising the quantity $S = -2\ln\mathcal{L}$ which is given by

$$S = 2\int_{s_a}^{s_b} h(s)ds - 2\sum_{i}^{N} \ln\left[h(s_i)\right] \tag{6.6}$$

this allows a direct determination of the probability distribution for both γ and s_0 by working out $\mathcal{L} = e^{-\frac{S}{2}}$.

Figure 6.4 shows 1,2 and 3 sigma contours of the parameters γ and s_0 for the three samples and Table 6.3 shows the best fitting parameters with 1 σ error bars. The results presented here are the most accurate ever determination of the two-point correlation function of radio galaxies in the local universe. γ and s_0 are much better constrained for the SF and complete samples than for the AGN which is a product of different sample sizes. As has been seen in previous determinations of $\xi(r)$ for radio sources the larger correlation scale length (s_0) as well as the steeper power-law slope for AGNs implies these objects cluster more strongly than SF galaxies. SF galaxies have very similar clustering properties to the combined sample, these tend to dilute the clustering signal of the AGNs.

6.4 The real-space correlation function

The redshift-space correlation function $\xi(s)$ plotted in Figure 6.3 differs from the real-space correlation function $\xi(r)$ because of peculiar velocities which can lead to redshift space distortions. For example fingers of god stretching effects can lead to a suppression of clustering signal on small scales because galaxies' peculiar velocities make them appear at larger comoving separations. Both the slope and amplitude of the real-space correlation function will then differ from the values measured in the previous section (Hawkins *et al.*, 2003; Saunders *et al.*, 1992). The difference between real and redshift-space correlation functions is that the redshift-space correlation function yields information about "measured" clustering from redshift surveys whereas the real-space two-point correlation function is related to the physical clustering of galaxies in the universe.

6.4.1 Calculating $\Xi(r_T)$

It is straightforward to recover $\xi(r)$ by computing the two-point correlation function as a function of separations parallel r_P and transverse r_T to the observers' line of sight $\xi(r_P, r_T)$ and then calculating the projected correlation function $\Xi(r_T)$ using:

$$\Xi(r_T) = 2\int_0^\infty \xi(r_P, r_T) dr_P. \tag{6.7}$$

To calculate the separation for a pair of galaxies with redshift-position vectors $\mathbf{v_1}$ and $\mathbf{v_2}$ we define the redshift separation vector $\mathbf{s} \equiv \mathbf{v_1} - \mathbf{v_2}$ and the line of sight vector $\mathbf{l} \equiv \frac{1}{2}(\mathbf{v_1} + \mathbf{v_2})$. The parallel and perpendicular separations are then calculated by

$$r_P \equiv \frac{\mathbf{s}\cdot\mathbf{l}}{|\mathbf{l}|}, \;\; r_T^2 \equiv \mathbf{s}\cdot\mathbf{s} - r_P^2. \tag{6.8}$$

In practice $\xi(r_P, r_T)$ is estimated by means of the estimator given by equation 6.3 where pairs are calculated in a grid of separation bins $\Delta r_P, \Delta r_T$ and then Ξ is derived by means of equation 6.7. The integral in equation 6.7 is only calculated out to separations of $r = 70\,$Mpc, this value was chosen as a compromise between including as much real data as possible while not including noise from results at higher separations.

The projected correlation function $\Xi(r_T)$ is related to the real-space correlation function $\xi(r)$ by (Davis & Peebles, 1983)

$$\Xi(r_T) = 2\int_{r_T}^\infty \xi(r)\frac{r dr}{(r^2 - r_T^2)^{1/2}}. \tag{6.9}$$

Although it is possible to directly invert this integral by a method described by Saunders *et al.* (1992) the data are too sparse to make this inversion. However the integral can be solved analytically assuming the power law form $\xi(r) = (r/r_0)^\gamma$ leading to

$$\Xi(r_T) = r_0^\gamma r_T^{1-\gamma}\frac{\Gamma(\frac{1}{2})\Gamma(\frac{\gamma-1}{2})}{\Gamma(\frac{\gamma}{2})} \tag{6.10}$$

where $\Gamma(x)$ is the usual Euler gamma function evaluated at x.

Results for the projected correlation are shown in Figure 6.5. The error bars on all three plots are obtained by bootstrap resampling the data 50 times (as described in Section 6.3.2). In all three samples the flattening seen in the redshift-space correlation function on small scales is no longer evident, though the correlation function still steepens on scales larger than 30 Mpc. Results of fitting equation 6.10 to the data are shown in Table 6.4.

6.4.2 Comparison with the clustering of other local galaxy populations

Table 6.5 shows a comparison of the results presented here with other determinations of $\xi(r)$ in the local universe. It can immediately be seen from this table that AGNs have

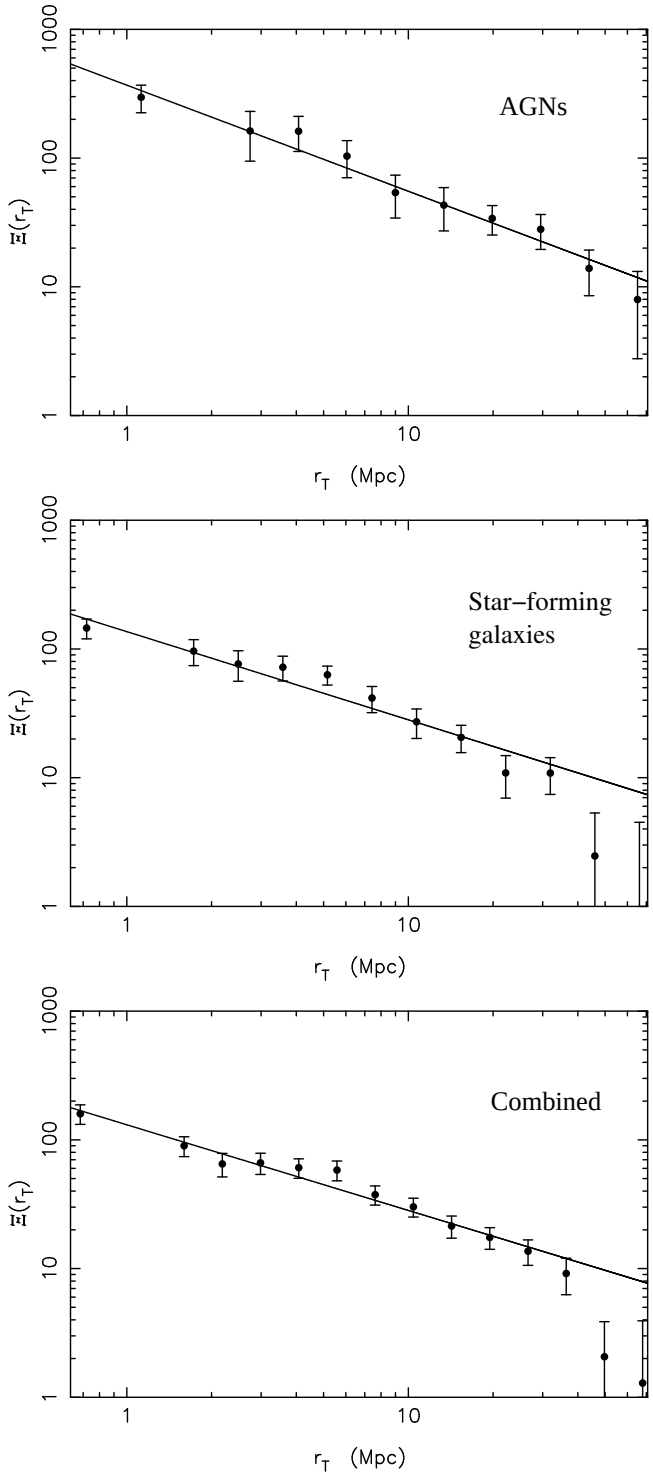

Figure 6.5 The projected real-space correlation function for AGN class galaxies (*top*), star-forming galaxies (*middle*) and the combined sample (*bottom*). The line shown is a fit of equation 6.10 to the data for r_T values between 0 Mpc and 70 Mpc for AGN's and 0 Mpc and 40 Mpc for the SF and combined samples.

Table 6.4 The χ^2 best fitting parameters of equation 6.10 to the projected correlation function.

Sample	γ	r_0 (Mpc)	$\chi^2_{\rm reduced}$
AGN	1.80 ± 0.05	12.96 ± 0.44	0.23
SF	1.67 ± 0.06	8.23 ± 0.39	1.20
All	1.66 ± 0.04	8.01 ± 0.27	0.83

a clustering amplitude intermediate between that found by Croft *et al.* (1997) for rich clusters and that of normal galaxies, which is consistent with their preferential location in small galaxy groups. The redshift-space clustering of the combined sample is very similar to that found for the entire population of 2dFGRS galaxies by Hawkins *et al.* (2003) which implies that radio sources at mJy flux density levels trace the underlying host galaxy population from which they come in an unchanged fashion.

The results in redshift space for this sample agree strikingly well with those of Magliocchetti *et al.* (2004) given the different selection properties of the two databases (optical for the 2dFGRS sample and near-infrared for the 6dFGS sample). It appears that both the FIRST and NVSS samples trace the underlying b_J-selected 2dFGRS and K-selected 6dFGS galaxy populations in a very similar manner. The real space clustering amplitudes determined here are somewhat higher than those determined by Magliocchetti *et al.* (2004). It is probable that this arises from differences between the 2dFGRS-FIRST and 6dFGS-NVSS samples. The 2dFGRS-FIRST sample probes a fainter galaxy population than that presented here and fainter host galaxies are known to be less strongly clustered (Norberg *et al.*, 2002), as they are less biased tracers of the underlying mass. Also, the Magliocchetti *et al.* (2004) real-space correlation function is very sparsely sampled and may be in error by more than the quoted uncertainties.

The AGNs in the 6dFGS-NVSS sample cluster similarly to the brightest early-type galaxies in the 2dFGRS whose clustering properties were determined by Norberg *et al.* (2002). The SF galaxies seem to cluster on an intermediate scale between the brightest and faintest late-type galaxies. This is consistent with Figure 5.7 from which it could be seen that AGNs preferentially reside in bright early-type galaxies whereas SF galaxies mostly reside in late-type galaxies which span a wide range in K magnitude. Radio sources cluster similarly to the host galaxy populations in which they reside.

6.5 Conclusion

This chapter has presented a brief introduction to the clustering properties of a sample of 2090 NVSS radio sources in the 6dFGS primary sample. The clustering analysis presented here is the most accurate determination of the two-point correlation function for radio sources ever made. This analysis has confirmed the result that radio-loud AGN cluster on scales intermediate between that of rich clusters and normal galaxies, and that these objects are biased tracers of the underlying mass. Star-forming galaxies cluster in a similar fashion to all radio sources in the sample, meaning that these galaxies dilute the strong clustering signal coming from the AGNs. Power-law fits of the two-point correla-

Table 6.5 Comparison of results with previous work on local galaxy populations.

Sample	γ_s	s_0 (Mpc)	γ_r	r_0 (Mpc)
6dFGS-NVSS AGN	$1.87^{+0.07}_{-0.09}$	$13.07^{+0.38}_{-0.41}$	1.80 ± 0.05	12.96 ± 0.44
6dFGS-NVSS SF	1.59 ± 0.03	$9.65^{+0.12}_{-0.13}$	1.67 ± 0.06	8.23 ± 0.39
6dFGS-NVSS combined	1.57 ± 0.03	10.07 ± 0.11	1.66 ± 0.04	8.01 ± 0.27
Magliocchetti *et al.* (2004) (2dFGRS-FIRST AGN)	$1.8^{+0.1}_{-0.2}$	13 ± 0.9	2.0 ± 0.1	$10.9^{+1.0}_{-1.2}$
Magliocchetti *et al.* (2004) (2dFGRS-FIRST All)	1.5 ± 0.1	$10.7^{+0.8}_{-0.7}$	1.6 ± 0.1	$6.7^{+0.9}_{-1.1}$
Croft *et al.* (1997) (APM AR$\geq$ 2 Clusters)	$3.2^{+1.6}_{-1.1}$	$30.4^{+15.9}_{-13.3}$	-	-
Peacock (1999) (Radio galaxies $S_{1.4\,\mathrm{GHz}} > 0.5\,\mathrm{Jy}$)	1.8 ± 0.3	15.7 ± 1.7	-	-
Brand *et. al.* (2004) (TONS radio galaxies)	1.8	11.0 ± 2.0	-	-
Hawkins *et al.* (2003) (2dFGRS complete)	1.57 ± 0.07	9.74 ± 0.4	1.72 ± 0.04	7.07 ± 0.36
Norberg *et al.* (2002) (2dFGRS bright early-type galaxies)	-	-	1.87 ± 0.1	13.85 ± 1.7
Norberg *et al.* (2002) (2dFGRS faint late-type galaxies)	-	-	1.76 ± 0.1	5.2 ± 1.1
Norberg *et al.* (2002) (2dFGRS bright late-type galaxies)	-	-	1.76 ± 0.1	9.0 ± 1.4
Fisher *et al.* (1994) (1.2 Jy IRAS galaxies)	$1.28^{+0.06}_{-0.02}$	$6.47^{+0.30}_{-0.31}$	$1.66^{+0.12}_{-0.09}$	$5.37^{+0.29}_{-0.33}$

tion function in both redshift space and real space agree well with previous determinations at radio wavelengths. By comparison with the results of clustering of 2dFGRS galaxies separated by optical morphology and brightness (Norberg *et al.*, 2002) it has also been shown that radio sources of both AGN and SF class cluster in much the same way as the optical host galaxy populations from which they are selected, even though radio sources sample the galaxy population very sparsely.

There is some evidence of deviation from a simple power-law in the clustering of both SF and AGN galaxies, though the present data are not sufficient to fully determine these deviations. There are a further 4000 radio sources in the 6dFGS second data release which was made publicly available in April 2005. Correlation functions calculated from these data should allow further constraints on the precise form of $\xi(r)$ to which a more accurate dark matter halo occupation model can be fitted, giving a direct determination of the way in which radio galaxies trace the underlying distribution of dark matter.

Chapter 7

Conclusion

In this chapter the thesis is concluded with a restatement of its main results. Prospects for further work on local radio source populations and for studies of evolution by locating more distant radio source populations are also outlined.

7.1 Summary of main results

In 2001 this thesis project was begun with the goal of combining large area mJy sensitivity radio source surveys with spectra from the 6dF Galaxy Survey to study the population of radio sources in the local universe as a benchmark for later studies of their cosmological evolution.

The main results of this thesis are:

- A catalogue of almost 200 000 843 MHz radio sources has been constructed from the Sydney University Molonglo Sky Survey, the deepest radio catalogue covering a substantial solid angle in the southern sky. A novel technique involving a decision tree was used to remove spurious sources at the catalogue limit and make it $> 95\%$ complete and reliable above 8 mJy beam^{-1} for sources with $\delta < -50^\circ$ and equally complete and reliable above 18 mJy beam^{-1} for sources with $\delta > -50^\circ$. (Chapter 2)
- A large and homogeneous set of 6dF spectra has been obtained for radio sources identified with 16% of $K \leq 12.75$ galaxies in the 2MASS XSC. Only 2.5% of radio sources in the NVSS catalogue are identified with such galaxies showing that local galaxies are rare objects in mJy-level radio source surveys. Pushing the sample to a deeper near-infrared magnitude limit would mainly identify galaxies with a higher median redshift. (Chapter 3)
- A population of blue ($b_J - K < 3.25$) star-forming galaxies in the local universe is not found in the K-selected population of radio sources. Such objects are extremely rare, making up less than 1% of the K-selected primary sample. These missing blue galaxies have had little effect on statistical properties determined from the K-selected primary sample. (Chapter 4)
- Another population of nearby star-forming galaxies is not found in the primary K-selected sample because the galaxies are stellar in appearance. The radio powers of these "Extragalactic HII regions" imply that these galaxies are forming stars at moderate rates of $\sim 10\,\mathrm{M}_\odot\,\mathrm{yr}^{-1}$, similar to the majority of star-forming galaxies in the primary sample. The fraction of these objects is less than 2% of the K-selected sample. (Chapter 4)
- About 60% of identifications of radio sources with objects in SuperCOSMOS which were stellar in appearance and had $b_J < 18$ were spurious identifications of foreground stars. The majority of the remainder are quasars. Foreground star contamination decreases strongly with galactic latitude and at $|b| > 40^\circ$ is only 30%. The detection rate of quasars at $|b| > 40^\circ$ is 60% which is roughly the equivalent fraction of quasars detected in the optical-UV colour-selected 2dF Quasar Survey (2QZ; Croom *et al.*, 2004). Therefore a blind radio-selected quasar survey at high galactic latitude would be as efficient as an optical-UV colour-selected one.
- The radio selected quasar population presented here has revealed a population of "reddened" AGN which are missed from optical-UV colour-selected samples. These are objects in which either light from the quasar host galaxy dominates the

spectrum at near-infrared wavelengths or dust in or near the AGN is obscuring their UV emission. These galaxies make up $10 \pm 4\%$ of all radio selected quasars. (Chapter 4)

- Crossmatching primary target galaxies with the IRAS-FSC has allowed a redetermination of the radio-FIR correlation for 1714 star-forming galaxies. This redetermination agrees well with previous studies of the radio-FIR correlation (eg. Condon *et al.*, 1991; Condon & Broderick, 1988; Devereux & Eales, 1989). Using the correlation as a diagnostic to separate star-forming galaxies from AGNs has been found to agree in over 95% of cases with spectral classification. (Chapter 5)
- Accurate and homogeneous local radio luminosity functions at 1.4 GHz of star-forming galaxies and AGNs have been measured. The AGN luminosity function maintains a power-law form for over 5 orders of magnitude in radio power down to $P_{1.4} = 10^{20}\,\mathrm{W\,Hz^{-1}}$. It must turn over below $P_{1.4} = 10^{19}\,\mathrm{W\,Hz^{-1}}$ so as not to exceed the space density of luminous elliptical galaxies. The radio luminosity function of star-forming galaxies has been used to derive a local star-formation density of $\rho_{\mathrm{SF}} = (0.021 \pm 0.001)\,M_{\odot}\,\mathrm{yr^{-1}\,Mpc^{-3}}$, in agreement with determinations from shorter wavelengths. (Chapter 5)
- The fractional luminosity function of both star-forming galaxies and AGNs shows that more massive galaxies have higher star-formation rates and that the probability that a galaxy will host a radio-loud AGN increases with brightening absolute K-band magnitude as $M_K^{-1.25 \pm 0.1}$. (Chapter 5)
- The 2-point correlation function has been calculated in both redshift space $\xi(s)$ and real space $\xi(r)$ separately for star-forming galaxies and AGNs. Radio-loud AGNs are found to cluster more strongly than the overall galaxy population but cluster similarly to bright early-type galaxies which are their parent population. Radio-loud AGN are biased tracers of the mass distribution. Star-forming galaxies cluster in much the same way as the underlying optical host galaxy population in which they reside. (Chapter 6)

7.2 Further work

7.2.1 Future 6dFGS data releases

The data presented in this thesis represent roughly 40% of the total 6dFGS survey area that overlaps with the NVSS. In April 2005 the second data release of the 6dFGS was made publicly available online (Jones *et al.*, in press). It contains spectra of a further 40 000 primary target galaxies of which 6 500 should be identified with radio sources in the NVSS at $\delta > -40^{\circ}$ (assuming a 16% dectection rate) this would yield radio source spectra and redshifts of over 10 000 radio sources in the local volume out to $z \sim 0.1$.

The inclusion of the 6dFGS second data release will double the volume of space sampled by the first data release. A larger sample volume will allow a more accurate determination of both the faint and bright ends of the radio luminosity function. As the 6dFGS-

NVSS sample is flux-density limited, less luminous radio-sources are only found at the lowest redshifts (eg. Figure 5.6) and are therefore rare inside a small sampled volume. The larger solid angle probed by the 6dFGS DR2 will detect more of these low luminosity radio sources. This is of particular interest for the AGNs as a turnover at the faint end of the 1.4 GHz radio luminosity function of AGNs is expected at low radio power so that their measured space density does not exceed the space density of luminous elliptical galaxies in which they preferentially reside. A detection of the location of this turnover is useful for constraining models of radio-loud AGN (eg. Nipoti & Binney, 2005) and in furthering understanding of the demographics of the local radio source population.

Possible deviations from the power-law form of the two-point correlation function of radio-loud AGN and star-forming galaxies are not well constrained by the present data. The second data release will allow a more accurate determination of the two-point correlation function in a much larger volume of the local universe than that studied in Chapter 6. An accurate determination of the clustering properties of radio sources will allow a detailed study of the way in which radio-loud AGN trace the underlying matter distribution. With more data, the two-point correlation function can also be determined as a function of galaxy environment. This would allow studies of how triggering of radio-loud AGN and the rate of star formation in galaxies are affected by environment.

Combining the complete 6dFGS-NVSS sample with the complete 2dFGRS-NVSS sample described by Sadler *et al.* (2002) will yield spectra and redshifts for more than 10 000 1.4 GHz radio sources over the redshift range $0 < z < 0.3$. The present data are not sufficient to detect evolution with any statistical significance over this redshift range but larger 2dFGRS-NVSS and 6dFGS-NVSS datasets will allow a detailed study of the evolution of both star-forming galaxies and AGNs. Further afield, about 3% of Luminous Red Galaxies (LRGs) in the 2dF-SDSS LRG and QSO survey (2SLAQ; Richards *et al.*, 2005) are detected at 1.4 GHz in the FIRST catalogue. To date about 300 radio detected LRGs have been observed by 2dF. These are all radio-loud AGN with early-type spectra and median redshift $z = 0.6$, the 2SLAQ-FIRST sample directly probes the radio source population at this redshift. Comparison of these galaxies with the 6dFGS-NVSS population presented in this thesis will allow a direct measurement of the evolution of radio-loud AGN to redshifts of $z = 0.6$.

Furthermore there are 3 152 SUMSS/NVSS additional targets in the second data release of the 6dFGS. Figure 7.1 shows the location of these targets on the sky. The larger sample of additional targets in the second data release should yield greater numbers of the radio source populations discussed in Chapter 4. In particular a larger population of reddened QSOs should be found in the 6dFGS second data release. These objects are of much interest as they are not seen in many of the recent large quasar surveys such as the SDSS and the 2QZ. The high detection rate of stars in the additional target sample is also of interest. Sadler *et al.* (2002) suggested from studying the 2dFGRS-NVSS sample that there might be an unknown population of radio sources in the NVSS which are hosted by Galactic stars. It is possible to test for such a population using the 6dFGS-NVSS sample by comparing how many radio source identifications are expected by chance via Monte Carlo simulations to the distribution of radio source identifications of stars found in the additional target sample.

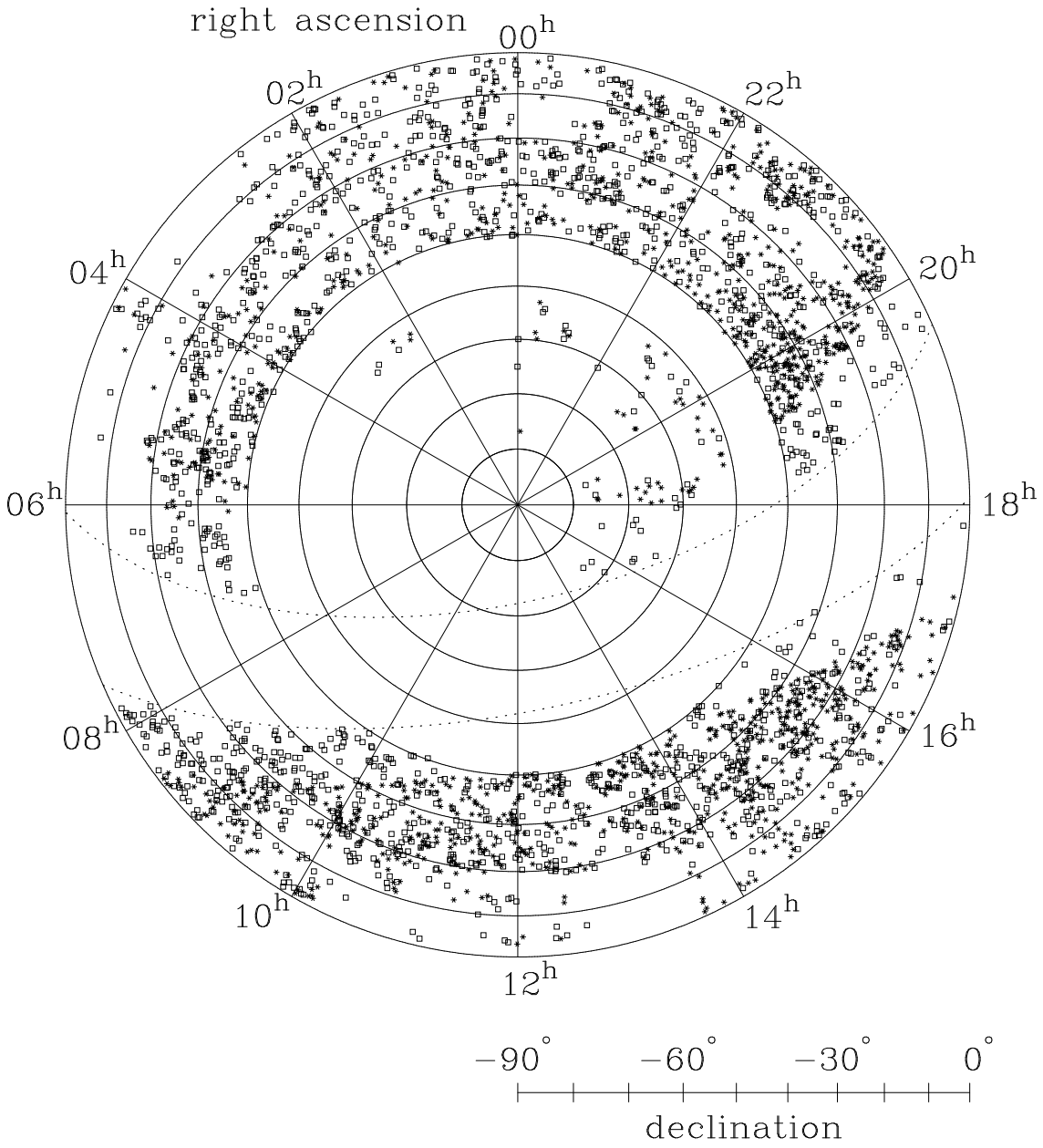

Figure 7.1 The sky coverage of 6dFGS-NVSS/SUMSS additional targets in the 6dFGS second data release. Stellar identifications are plotted as stars and extended identifications are plotted as squares. Dotted lines are plotted at $b = \pm 10°$.

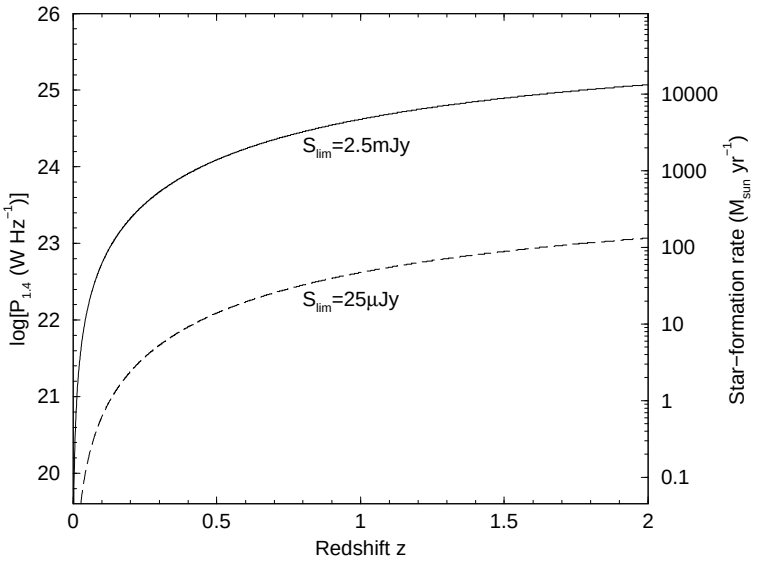

Figure 7.2 The radio power limits at high redshift for 2.5 mJy limit of the NVSS (*solid curve*) and for a hypothetical all-sky SKA survey with 100 times the sensitivity of the NVSS (*dashed curve*). The limiting star-formation rate corresponding to a given radio power derived according to equation 5.19 is shown on the right ordinate.

With the full 6dFGS data release in 2006, a sample of more than 2000 radio source spectra and redshifts of the galaxies in the 843 MHz selected 6dFGS-SUMSS sample will be available. The full 843 MHz luminosity function calculated from these objects will allow an accurate study of how the spectral index distribution of source populations vary with radio power. In particular it is expected that core dominated AGN with flat spectral indices will dominate the radio-loud AGN population at low radio powers with an increasing population of AGN of steeper spectral indices at higher radio power. Such a study would be valuable in understanding the properties of the radio-loud AGN population which dominate the SUMSS and NVSS catalogues.

7.2.2 Deeper radio surveys

Figure 7.2 shows the 1.4 GHz radio luminosity range probed at different redshifts for a detection limit of 2.5 mJy (NVSS) and 25 μJy. The 25 μJy detection limit is an estimated limit which would be reached by a Square Kilometre Array (SKA; www.skatelescope.org) telescope undertaking a similar radio source survey to either the NVSS or SUMSS. Such a telescope should have 100 times the sensitivity of the Very Large Array as used for the NVSS or the Molonglo Observatory Synthesis Telescope as used for SUMSS. Results from the local radio luminosity function have shown that the radio source population is a mixture of both star-forming galaxies and AGNs over all radio powers surveyed implying that a mixture of both AGNs and star-forming galaxies will be seen in radio surveys at all redshifts. Extrapolating the local luminosity function of 6dFGS-NVSS AGNs implies that these galaxies may again dominate the faint radio source population below 10^{19} W Hz^{-1}.

This means that optical spectroscopy will always be important as a means of disentangling the star-forming galaxy population from the AGN population in deeper radio surveys.

Future radio surveys will play an important role in studies of the evolution of star-forming galaxies. The right ordinate of Figure 7.2 shows the corresponding star-formation rates derived from radio power according to equation 5.19. As Figure 5.17 has shown, it is star-forming galaxies with star-formation rates of around $10\,\mathrm{M}_{\odot}\,\mathrm{yr}^{-1}$ which contribute the most to the star-formation density at the present epoch. The NVSS can only detect such galaxies out to redshifts of $z \approx 0.05$, which is about the median redshift of the 6dFGS. A future all sky SKA survey will be able to detect such galaxies to redshifts of $z \approx 0.5$ allowing a detailed understanding of the star-formation history of the universe to lookback times of $\tau \sim 5\,\mathrm{Gyr}$. Smaller area SKA surveys with longer integration times will probe to even fainter flux densities and should detect moderate star-formation rates in galaxies at any redshift they might exist (Garrett, 2002).

7.3 Conclusion

Combining large-area radio surveys (SUMSS and NVSS) with the 6dFGS has provided an accurate picture of the demographics of the population of radio sources in the local universe. Radio sources are not rare or exotic objects as once thought but are quite common in the local universe. From this perspective, a study of the radio properties of galaxies is a powerful tool for understanding the galaxy population as a whole, not just the population of radio sources. About 10% of all galaxies in the 6dFGS are forming stars at a rate of $> 1\,\mathrm{M}_{\odot}\,\mathrm{yr}^{-1}$ and it is these galaxies which are making the greatest contribution to the star-formation density at the present epoch. About 6% of all galaxies in the 6dFGS are radio-loud AGNs powered by a supermassive black hole. These radio-loud AGNs inhabit almost all of the bright elliptical galaxies in the local universe. Radio-loud AGNs must have been more luminous in the past rather than having higher space density as the bright elliptical galaxies in which they preferentially reside were less common.

In summary, this thesis has been successful in its goal of characterising the radio source population of the local universe by assembling a database of NVSS radio sources detected in the 6dFGS. This work provides an accurate benchmark for future studies of the evolution of radio sources which will be done by combining data from next-generation radio source surveys with data from future redshift surveys.

References

Antonucci, R., 1993. ARA&A, **31**, 473–521.

Auriemma, C., Perola, G. C., Ekers, R. D., Fanti, R., Lari, C., Jaffe, W. J., & Ulrich, M. H., May 1977. A&Ap, **57**, 41–50.

Baldwin, J. E., Boysen, R. C., Hales, S. E. G., Jennings, J. E., Waggett, P. C., Warner, P. J., & Wilson, D. M. A., Dec. 1985. MNRAS, **217**, 717–730.

Bauer, F. E., Condon, J. J., Thuan, T. X., & Broderick, J. J., Aug. 2000. ApJS, **129**, 547–562.

Becker, R. H., White, R. L., & Helfand, D. J., Sept. 1995. ApJ, **450**, 559–577.

Beichman, C. A., Neugebauer, G., Habing, H. J., Clegg, P. E., & Chester, T. J., 1988, *Infrared astronomical satellite (IRAS) catalogs and atlases. Volume 1: Explanatory supplement*, **1**, NASA RP–1190, Washington, DC:GPO.

Bennett, C. L., Bay, M., Halpern, M., Hinshaw, G., Jackson, C., Jarosik, N., Kogut, A., Limon, M., Meyer, S. S., Page, L., Spergel, D. N., Tucker, G. S. a nd Wilkinson, D. T., Wollack, E., & Wright, E. L., Jan. 2003. ApJ, **583**, 1–23.

Best, P. N., Kauffmann, G., Heckman, T. M., Brinchmann, J., Charlot, S., Ivezic, Z., & White, S. D. M., June 2005a. arXiv:astro-ph/0506269.

Best, P. N., Kauffmann, G., Heckman, T. M., & Ivezic, Z., June 2005b. arXiv:astro-ph/0506268.

Blake, C., Mauch, T., & Sadler, E. M., Jan. 2004. MNRAS, **347**, 787–794.

Blake, C., & Wall, J., Jan. 2002. MNRAS, **329**, L37–L41.

Bock, D. C.-J., Large, M. I., & Sadler, E. M., Mar. 1999. ApJ, **117**, 1578–1593.

Bolton, J. G., Stanley, G. J., & Slee, O. B., 1949. Nature, **164**, 101.

Brand, K., Rawlings, S., Hill, G. J., & Lacy, M., Sept. 2003. New Astronomy Review, **47**, 325–328.

Brand, K., Rawlings, S., Hill, G. J., & Tufts, J. R., Mar. 2005. MNRAS, **357**, 1231–1254.

Bruzual, A. G., & Charlot, S., Mar. 1993. ApJ, **405**, 538–553.

Campbell, L., Saunders, W., & Colless, M., June 2004. MNRAS, **350**, 1467–1476.

Campbell-Wilson, D., & Hunstead, R. W., Apr. 1994. PASA, **11**, 33–38.

Cannon, R. D., 1984. In *ASSL Vol. 110: IAU Colloq. 78: Astronomy with Schmidt-Type Telescopes*, page 25.

Carroll, S. M., Press, W. H., & Turner, E. L., 1992. ARA&A, **30**, 499–542.

Cohen, A. S., Lane, W. M., Kassim, N. E., Lazio, T. J. W., Cotton, W. D., Perley, R. A., Condon, J. J., & Erickson, W. C., Dec. 2004. American Astronomical Society Meeting Abstracts, 205.

Cole, S., Norberg, P., Baugh, C. M., Frenk, C. S., Bland-Hawthorn, J., Bridges, T., Cannon, R., Colless, M., Collins, C., Couch, W., Cross, N., Dalton, G., De Propris, R., Driver, S. P., Efstathiou, G., Ellis, R. S., Glazebrook, K., Jackson, C., Lahav, O., Lewis, I., Lumsden, S., Maddox, S., Madgwick, D., Peacock, J. A., Peterson, B. A., Sutherland, W., & Taylor, K., Sept. 2001. MNRAS, **326**, 255–273.

Colless, M., Dec. 2000. Publications of the Astronomical Society of Australia, **17**, 215–226.

Colless, M., Dalton, G., Maddox, S., Sutherland, W., Norberg, P., Cole, S., Bland-Hawthorn, J., Bridges, T., Cannon, R., Collins, C., Couch, W., Cross, N., Deeley, K., De Propris, R., Driver, S. P., Efstathiou, G., Ellis, R. S., Frenk, C. S., Glazebrook, K., Jackson, C., Lahav, O., Lewis, I., Lumsden, S., Madgwick, D., Peacock, J. A., Peterson, B. A., Price, I., Seaborne, M., & Taylor, K., Dec. 2001. MNRAS, **328**, 1039–1063.

Condon, J. J., Mar. 1989. ApJ, **338**, 13–23.

Condon, J. J., 1992. ARA&A, **30**, 575–611.

Condon, J. J., Feb. 1997. PASP, **109**, 166–172.

Condon, J. J., Anderson, M. L., & Helou, G., July 1991. ApJ, **376**, 95–103.

Condon, J. J., & Broderick, J. J., July 1988. AJ, **96**, 30–61.

Condon, J. J., Broderick, J. J., & Seielstad, G. A., Apr. 1989. AJ, **97**, 1064–1073.

Condon, J. J., Cotton, W. D., & Broderick, J. J., Aug. 2002. AJ, **124**, 675–689.

Condon, J. J., Cotton, W. D., Greisen, E. W., Yin, Q. F., Perley, R. A., Taylor, G. B., & Broderick, J. J., May 1998. AJ, **115**, 1693–1716.

Condon, J. J., & Yin, Q. F., July 1990. ApJ, **357**, 97–104.

Cram, L. E., Oct. 1998. ApJL, **506**, L85–L88.

Croft, R. A. C., Dalton, G. B., Efstathiou, G., Sutherland, W. J., & Maddox, S. J., Oct. 1997. MNRAS, **291**, 305–313.

Croom, S. M., Smith, R. J., Boyle, B. J., Shanks, T., Miller, L., Outram, P. J., & Loaring, N. S., Apr. 2004. MNRAS, **349**, 1397–1418.

Cutri, R. M., Skrutskie, M. F., van Dyk, S., Beichman, C. A., Carpenter, J. M., Chester, T., Cambresy, L., Evans, T., Fowler, J., Gizis, J., Howard, E., Huchra, J., Jarrett, T., Kopan, E. L., Kirkpatrick, J. D., Light, R. M., Marsh, K. A., McCallon, H., Schneider, S., Stiening, R., Sykes, M., Weinberg, M., Wheaton, W. A., Wheelock, S., & Zacarias, N., June 2003. VizieR Online Data Catalog, 2246.

Davis, M., & Peebles, P. J. E., Apr. 1983. ApJ, **267**, 465–482.

De Breuck, C., van Breugel, W., Röttgering, H. J. A., & Miley, G., Apr. 2000. A&AS, **143**, 303–333.

de Grijp, M. H. K., Keel, W. C., Miley, G. K., Goudfrooij, P., & Lub, J., Dec. 1992. A&ApS, **96**, 389–428.

Devereux, N. A., & Eales, S. A., May 1989. ApJ, **340**, 708–712.

Drake, C. L., McGregor, P. J., Dopita, M. A., & van Breugel, W. J. M., Nov. 2003. AJ, **126**, 2237–2267.

Drinkwater, M. J., 1987. Ph.D. Thesis.

Edge, D. O., Shakeshaft, J. R., McAdam, W. B., Baldwin, J. E., & Archer, S., 1959. MemRAS, **68**, 37–60.

Elvis, M., Wilkes, B. J., McDowell, J. C., Green, R. F., Bechtold, J., Willner, S. P., Oey, M. S., Polomski, E., & Cutri, R., Nov. 1994. ApJS, **95**, 1–68.

Fanaroff, B. L., & Riley, J. M., May 1974. MNRAS, **167**, 31P–36P.

Fisher, K. B., Davis, M., Strauss, M. A., Yahil, A., & Huchra, J., Jan. 1994. MNRAS, **266**, 50–64.

Folkes, S., Ronen, S., Price, I., Lahav, O., Colless, M., Maddox, S., Deeley, K., Glazebrook, K., Bland-Hawthorn, J., Cannon, R., Cole, S., Collins, C., Couch, W., Driver, S. P., Dalton, G., Efstathiou, G., Ellis, R. S., Frenk, C. S., Kaiser, N., Lewis, I., Lumsden, S., Peacock, J., Peterson, B. A., Sutherland, W., & Taylor, K., Sept. 1999. MNRAS, **308**, 459–472.

Gaensler, B. M., & Hunstead, R. W., Apr. 2000. PASA, **17**, 72–82.

Gallego, J., Zamorano, J., Aragon-Salamanca, A., & Rego, M., Dec. 1995. ApJL, **455**, L1–L4.

Garrett, M. A., Mar. 2002. A&Ap, **384**, L19–L22.

Glazebrook, K., Peacock, J. A., Miller, L., & Collins, C. A., July 1995. MNRAS, **275**, 169–184.

Glikman, E., Helfand, D., Becker, R., & White, R., 2004. In *ASP Conf. Ser. 311: AGN Physics with the Sloan Digital Sky Survey*, page 351.

Gower, J. F. R., Scott, P. F., & Wills, D., 1967. MmRAS, **71**, 49–144.

Green, A. J., 1999. In *ASP Conf. Ser. 168: New Perspectives on the Interstellar Medium*, page 43.

Green, A. J., Bunton, J. D., Campbell-Wilson, D., Cram, L. E., Davison, R. G., Hunstead, R. W., Mitchell, D. A., & Parfitt, A. J., 2001. In *SKA: Defining the Future, Berkeley, U.S.A., www.skatelescope.org/skaberkely/*.

Gregg, M. D., Lacy, M., White, R. L., Glikman, E., Helfand, D., Becker, R. H., & Brotherton, M. S., Jan. 2002. ApJ, **564**, 133–142.

Griffith, M. R., & Wright, A. E., May 1993. AJ, **105**, 1666–1679.

Haarsma, D. B., Partridge, R. B., Windhorst, R. A., & Richards, E. A., Dec. 2000. ApJ, **544**, 641–658.

Hambly, N. C., Irwin, M. J., & MacGillivray, H. T., Oct. 2001a. MNRAS, **326**, 1295–1314.

Hambly, N. C., MacGillivray, H. T., Read, M. A., Tritton, S. B., Thomson, E. B., Kelly, B. D., Morgan, D. H., Smith, R. E., Driver, S. P., Williamson, J., Parker, Q. A., Hawkins, M. R. S., Williams, P. M., & Lawrence, A., Oct. 2001b. MNRAS, **326**, 1279–1294.

Hartley, M., & Dawe, J. A., 1981. Proceedings of the Astronomical Society of Australia, **4**, 251–254.

Hawkins, E., Maddox, S., Cole, S., Lahav, O., Madgwick, D. S., Norberg, P., Peacock, J. A., Baldry, I. K., Baugh, C. M., Bland-Hawthorn, J., Bridges, T., Cannon, R., Colless, M., Collins, C., Couch, W., Dalton, G., De Propris, R., Driver, S. P., Efstathiou, G., Ellis, R. S., Frenk, C. S., Glazebrook, K., Jackson, C., Jones, B., Lewis, I., Lumsden, S., Percival, W., Peterson, B. A., Sutherland, W., & Taylor, K., Nov. 2003. MNRAS, **346**, 78–96.

Heckman, T. M., Aug. 1980. A&Ap, **88**, 311–316.

Helou, G., Soifer, B. T., & Rowan-Robinson, M., Nov. 1985. ApJL, **298**, L7–L11.

Hewitt, A., & Burbidge, G., Aug. 1993. ApJS, **87**, 451–947.

Hill, G. J., & Lilly, S. J., Jan. 1991. ApJ, **367**, 1–18.

Høg, E., Fabricius, C., Makarov, V. V., Urban, S., Corbin, T., Wycoff, G., Bastian, U., Schwekendiek, P., & Wicenec, A., Mar. 2000. A&Ap, **355**, L27–L30.

Hogg, D. W., May 1999. arXiv:astro-ph/9905116.

Hunstead, R. W., 1991. Australian Journal of Physics, **44**, 743.

Huynh, M. T., Jackson, C. A., Norris, R. P., & Prandoni, I., June 2005. arXiv:astro-ph/0506047.

Ivezić, Ž., Menou, K., Knapp, G. R., Strauss, M. A., Lupton, R. H., Vanden Berk, D. E., Richards, G. T., Tremonti, C., Weinstein, M. A., Anderson, S., Bahcall, N. A., Becker, R. H., Bernardi, M., Blanton, M., Eisenstein, D., Fan, X., Finkbeiner, D., Finlator, K., Frieman, J., Gunn, J. E., Hall, P. B., Kim, R. S. J., Kinkhabwala, A., Narayanan, V. K., Rockosi, C. M., Schlegel, D., Schneider, D. P., Strateva, I., SubbaRao, M., Thakar, A. R., Voges, W., White, R. L., Yanny, B., Brinkmann, J., Doi, M., Fukugita, M., Hennessy, G. S., Munn, J. A., Nichol, R. C., & York, D. G., Nov. 2002. AJ, **124**, 2364–2400.

Jackson, C. A., & Londish, D. M., Dec. 2000. Publications of the Astronomical Society of Australia, **17**, 234–240.

Jackson, C. A., & Wall, J. V., Mar. 1999. MNRAS, **304**, 160–174.

Jarrett, T. H., Chester, T., Cutri, R., Schneider, S., Skrutskie, M., & Huchra, J. P., May 2000. AJ, **119**, 2498–2531.

Jones, D. H., June 2005. In prep.

Jones, D. H., Saunders, W., Colless, M., Read, M. A., Parker, Q. A., Watson, F. G., Campbell, L. A., Burkey, D., Mauch, T., Moore, L., Hartley, M., Cass, P., James, D., Russell, K., Fiegert, K., Dawe, J., Huchra, J., Jarrett, T., Lahav, O., Lucey, J., Mamon, G. A., Proust, D., Sadler, E. M., & Wakamatsu, K., Dec. 2004. MNRAS, **355**, 747–763.

Jones, H. D., Saunders, W., Read, M., & Colless, M., in press. Publications of the Astronomical Society of Australia.

Kerscher, M., Szapudi, I., & Szalay, A. S., May 2000. ApJL, **535**, L13–L16.

Kleinmann, S. G., Lysaght, M. G., Pughe, W. L., Schneider, S. E., Skrutskie, M. F., Weinberg, M. D., Price, S. D., Matthews, K., Soifer, B. T., & Huchra, J. P., July 1994. Ap&SS, **217**, 11–17.

Landy, S. D., & Szalay, A. S., July 1993. ApJ, **412**, 64–71.

Large, M. Notes on Radio Source Counts. Technical Report MTR 90.003, Molonglo Observatory, 1990.

Large, M. I., Campbell-Wilson, D., Cram, L. E., Davison, R. G., & Robertson, J. G., Apr. 1994. PASA, **11**, 44–49.

Large, M. I., Cram, L. E., & Burgess, A. M., Apr. 1991. The Observatory, **111**, 72–75.

Large, M. I., Mills, B. Y., Little, A. G., Crawford, D. F., & Sutton, J. M., Feb. 1981. MNRAS, **194**, 693.

Lawrence, A., Walker, D., Rowan-Robinson, M., Leech, K. J., & Penston, M. V., Apr. 1986. MNRAS, **219**, 687–701.

Ledlow, M. J., & Owen, F. N., Mar. 1995. AJ, **109**, 853–873.

Leibundgut, B., 2001. ARA&A, **39**, 67–98.

Lewis, I. J., Cannon, R. D., Taylor, K., Glazebrook, K., Bailey, J. A., Baldry, I. K., Barton, J. R., Bridges, T. J., Dalton, G. B., Farrell, T. J., Gray, P. M., Lankshear, A., McCowage, C., Parry, I. R., Sharples, R. M., Shortridge, K., Smith, G. A., Stevenson, J., Straede, J. O., Waller, L. G., Whittard, J. D., Wilcox, J. K., & Willis, K. C., June 2002. MNRAS, **333**, 279–299.

Londish, D., Croom, S. M., Boyle, B. J., Shanks, T., Outram, P. J., Sadler, E. M., Loaring, N. S., Smith, R. J., Miller, L., & Maxted, P. F. L., Aug. 2002. MNRAS, **334**, 941–957.

Lortet, M.-C., Borde, S., & Ochsenbein, F., Oct. 1994. A&AS, **107**, 193–218.

Machalski, J., & Condon, J. J., July 1999. ApJS, **123**, 41–78.

Madau, P., Ferguson, H. C., Dickinson, M. E., Giavalisco, M., Steidel, C. C., & Fruchter, A., Dec. 1996. MNRAS, **283**, 1388–1404.

Madgwick, D. S., Lahav, O., Baldry, I. K., Baugh, C. M., Bland-Hawthorn, J., Bridges, T., Cannon, R., Cole, S., Colless, M., Collins, C., Couch, W., Dalton, G., De Propris, R., Driver, S. P., Efstathiou, G., Ellis, R. S., Frenk, C. S., Glazebrook, K., Jackson, C., Lewis, I., Lumsden, S., Maddox, S., Norberg, P., Peacock, J. A., Peterson, B. A., Sutherland, W., & Taylor, K., June 2002. MNRAS, **333**, 133–144.

Magliocchetti, M., Maddox, S. J., Hawkins, E., Peacock, J. A., Bland-Hawthorn, J., Bridges, T., Cannon, R., Cole, S., Colless, M., Collins, C., Couch, W., Dalton, G., de Propris, R., Driver, S. P., Efstathiou, G., Ellis, R. S., Frenk, C. S., Glazebrook, K., Jackson, C. A., Jones, B., Lahav, O., Lewis, I., Lumsden, S., Norberg, P., Peterson, B. A., Sutherland, W., & Taylor, K., June 2004. MNRAS, **350**, 1485–1494.

Magliocchetti, M., Maddox, S. J., Jackson, C. A., Bland-Hawthorn, J., Bridges, T., Cannon, R., Cole, S., Colless, M., Collins, C., Couch, W., Dalton, G., de Propris, R., Driver, S. P., Efstathiou, G., Ellis, R. S., Frenk, C. S., Glazebrook, K., Lahav, O., Lewis, I., Lumsden, S., Peacock, J. A., Peterson, B. A., Sutherland, W., & Taylor, K., June 2002. MNRAS, **333**, 100–120.

Marconi, A., & Hunt, L. K., May 2003. ApJL, **589**, L21–L24.

Marshall, H. L., Tananbaum, H., Avni, Y., & Zamorani, G., June 1983. ApJ, **269**, 35–41.

Mauch, T., Feb. 2002. Anglo-Australian Observatory Epping Newsletter, **99**, 10–11.

Mauch, T., Murphy, T., Buttery, H. J., Curran, J., Hunstead, R. W., Piestrzynski, B., Robertson, J. G., & Sadler, E. M., July 2003. MNRAS, **342**, 1117–1130.

Maza, J., Wischnjewsky, M., Antezana, R., & Gonzalez, L. E., Oct. 1995. Revista Mexicana de Astronomia y Astrofisica, **31**, 119–129.

McLure, R. J., & Jarvis, M. J., Oct. 2004. MNRAS, **353**, L45–L49.

Metcalf, R. B., & Magliocchetti, M., May 2005. arXiv:astro-ph/0505194.

Mills, B. Y., 1981. PASA, **4**, 156–159.

Mills, B. Y., Aitchison, R. E., Little, A. G., & McAdam, W. B., 1963. Proc. Inst. Radio Engrs Aust., **24**, 156.

Mink, D. J., & Kurtz, M. J., 1998. In *ASP Conf. Ser. 145: Astronomical Data Analysis Software and Systems VII*, page 93.

Morgan, D. H., Tritton, S. B., Savage, A., Hartley, M., & Cannon, R. D., 1992. In *ASSL Vol. 174: Digitised Optical Sky Surveys*, page 11.

Moshir, M., Copan, G., Conrow, T., McCallon, H., Hacking, P., Gregorich, D., Rohrbach, G., Melnyk, M., Rice, W., & Fullmer, L., Feb. 1993. VizieR Online Data Catalog, 2156.

Murdoch, H. S., Crawford, D. F., & Jauncey, D. L., July 1973. ApJ, **183**, 1–14.

Nilson, P., 1973, *Uppsala general catalogue of galaxies*, Acta Universitatis Upsaliensis. Nova Acta Regiae Societatis Scientiarum Upsaliensis - Uppsala Astronomiska Observatoriums Annaler, Uppsala: Astronomiska Observatorium, 1973.

Nipoti, C., & Binney, J., May 2005. arXiv:astro-ph/0505060.

Norberg, P., Baugh, C. M., Hawkins, E., Maddox, S., Madgwick, D., Lahav, O., Cole, S., Frenk, C. S., Baldry, I., Bland-Hawthorn, J., Bridges, T., Cannon, R., Colless, M., Collins, C., Couch, W., Dalton, G., De Propris, R., Driver, S. P., Efstathiou, G., Ellis, R. S., Glazebrook, K., Jackson, C., Lewis, I., Lumsden, S., Peacock, J. A., Peterson, B. A., Sutherland, W., & Taylor, K., June 2002. MNRAS, **332**, 827–838.

Norris, R. P., Roy, A. L., Allen, D. A., Kesteven, M. J., Troup, E. R., & Reynolds, J. E., 1992. In *ASP Conf. Ser. 31: Relationships Between Active Galactic Nuclei and Starburst Galaxies*, page 71.

Oort, M. J. A., Steemers, W. J. G., & Windhorst, R. A., Apr. 1988. AAS, **73**, 103–123.

Pérez-González, P. G., Zamorano, J., Gallego, J., Aragón-Salamanca, A., & Gil de Paz, A., July 2003. ApJ, **591**, 827–842.

Peacock, J. A., 1999, *Cosmological physics*, Publisher: Cambridge, UK: Cambridge University Press, 1999. ISBN: 0521422701.

Peacock, J. A., & Nicholson, D., Nov. 1991. MNRAS, **253**, 307–319.

Peebles, P. J. E., 1980, *The large-scale structure of the universe*, Research supported by the National Science Foundation. Princeton, N.J., Princeton University Press, 1980. 435 p.

Perlmutter, S., Aldering, G., Goldhaber, G., Knop, R. A., Nugent, P., Castro, P. G., Deustua, S., Fabbro, S., Goobar, A., Groom, D. E., Hook, I. M., Kim, A. G., Kim, M. Y., Lee, J. C., Nunes, N. J., Pain, R., Pennypacker, C. R., Quimby, R., Lidman, C., Ellis, R. S., Irwin, M., McMahon, R. G., Ruiz-Lapuente, P., Walton, N., Schaefer, B., Boyle, B. J., Filippenko, A. V., Matheson, T., Fruchter, A. S., Panagia, N., Newberg, H. J. M., Couch, W. J., & The Supernova Cosmology Project, June 1999. ApJ, **517**, 565–586.

Pilkington, J. D. H., & Scott, P. F., 1965. MmRAS, **69**, 183.

Quinlan, J., 1993, *C4.5: Programs for Machine Learning*, Morgan Kaufmann, San Mateo, CA USA.

Rees, N., May 1990. MNRAS, **244**, 233–246.

Reid, I. N., Brewer, C., Brucato, R. J., McKinley, W. R., Maury, A., Mendenhall, D., Mould, J. R., Mueller, J., Neugebauer, G., Phinney, J., Sargent, W. L. W., Schombert, J., & Thicksten, R., July 1991. PASP, **103**, 661–674.

Rengelink, R., 1998. Ph.D. Thesis.

Ricci, R., Sadler, E. M., Ekers, R. D., Staveley-Smith, L., Wilson, W. E., Kesteven, M. J., Subrahmanyan, R., Walker, M. A., Jackson, C. A., & De Zotti, G., Oct. 2004. MNRAS, **354**, 305–320.

Richards, G. T., Croom, S. M., Anderson, S. F., Bland-Hawthorn, J., Boyle, B. J., De Propris, R., Drinkwater, M. J., Fan, X., Gunn, J. E., Ivezić, Ž., Jester, S., Loveday, J., Meiksin, A., Miller, L., Myers, A., Nichol, R. C., Outram, P. J., Pimbblet, K. A., Roseboom, I. G., Ross, N., Schneider, D. P., Shanks, T., Sharp, R. G., Stoughton, C., Strauss, M. A., Szalay, A. S., Vanden Berk, D. E., & York, D. G., July 2005. MNRAS, **360**, 839–852.

Robertson, J. G., 1991. Australian Journal of Physics, **44**, 729.

Ryle, M., 1968. ARA&A, **6**, 249–266.

Sadler, E. M., Jackson, C. A., Cannon, R. D., McIntyre, V. J., Murphy, T., Bland-Hawthorn, J., Bridges, T., Cole, S., Colless, M., Collins, C., Couch, W., Dalton, G., De Propris, R., Driver, S. P., Efstathiou, G., Ellis, R. S., Frenk, C. S., Glazebrook, K., Lahav, O., Lewis, I., Lumsden, S., Maddox, S., Madgwick, D., Norberg, P., Peacock, J. A., Peterson, B. A., Sutherland, W., & Taylor, K., Jan. 2002. MNRAS, **329**, 227–245.

Sadler, E. M., Jenkins, C. R., & Kotanyi, C. G., Oct. 1989. MNRAS, **240**, 591–635.

Sadler, E. M., McIntyre, V. J., Jackson, C. A., & Cannon, R. D., Dec. 1999. Publications of the Astronomical Society of Australia, **16**, 247–256.

Sanders, D. B., & Mirabel, I. F., 1996. ARA&A, **34**, 749–792.

Saripalli, L., Hunstead, R. W., Subrahmanyan, R., & Boyce, E., July 2005. arXiv:astro-ph/0507055.

Sault, R. J., Teuben, P. J., & Wright, M. C. H., 1995. In *ASP Conf. Ser. 77: Astronomical Data Analysis Software and Systems IV*, **4**, page 433.

Saunders, W., Oliver, S., Keeble, O., Rowan-Robinson, M., Maddox, S., McMahon, R., Efstathiou, G., Sutherland, W., Tadros, H., White, S. D. M., & Frenk, C. S., 2000. In *ASP Conf. Ser. 201: Cosmic Flows Workshop*, page 223.

Saunders, W., Rowan-Robinson, M., & Lawrence, A., Sept. 1992. MNRAS, **258**, 134–146.

Saunders, W., Rowan-Robinson, M., Lawrence, A., Efstathiou, G., Kaiser, N., Ellis, R. S., & Frenk, C. S., Jan. 1990. MNRAS, **242**, 318–337.

Schechter, P., Jan. 1976. ApJ, **203**, 297–306.

Schmidt, B. P., Suntzeff, N. B., Phillips, M. M., Schommer, R. A., Clocchiatti, A., Kirshner, R. P., Garnavich, P., Challis, P., Leibundgut, B., Spyromilio, J., Riess, A. G., Filippenko, A. V., Hamuy, M., Smith, R. C., Hogan, C., Stubbs, C., Diercks, A., Reiss, D., Gilliland, R., Tonry, J., Maza, J., Dressler, A., Walsh, J., & Ciardullo, R., Nov. 1998. ApJ, **507**, 46–63.

Schmidt, M., Feb. 1968. ApJ, **151**, 393–409.

Schoenmakers, A. P., de Bruyn, A. G., Röttgering, H. J. A., & van der Laan, H., Aug. 2001. A&Ap, **374**, 861–870.

Shectman, S. A., Landy, S. D., Oemler, A., Tucker, D. L., Lin, H., Kirshner, R. P., & Schechter, P. L., Oct. 1996. ApJ, **470**, 172–188.

Soifer, B. T., Boehmer, L., Neugebauer, G., & Sanders, D. B., Sept. 1989. AJ, **98**, 766–797.

Spergel, D. N., Verde, L., Peiris, H. V., Komatsu, E., Nolta, M. R., Bennett, C. L., Halpern, M., Hinshaw, G., Jarosik, N., Kogut, A., Limon, M., Meyer, S. S., Page, L., Tucker, G. S., Weiland, J. L., Wollack, E., & Wright, E. L., Sept. 2003. ApJS, **148**, 175–194.

Sullivan, M., Mobasher, B., Chan, B., Cram, L., Ellis, R., Treyer, M., & Hopkins, A., Sept. 2001. ApJ, **558**, 72–80.

Tegmark, M., Hamilton, A. J. S., & Xu, Y., Oct. 2002. MNRAS, **335**, 887–908.

Telles, E., Melnick, J., & Terlevich, R., June 1997. MNRAS, **288**, 78–107.

Urry, C. M., & Padovani, P., Sept. 1995. *PASP*, **107**, 803–845.

Véron-Cetty, M.-P., & Véron, P., July 2001. A&A, **374**, 92–94.

Visser, A. E., Riley, J. M., Roettgering, H. J. A., & Waldram, E. M., May 1995. A&ApS, **110**, 419–439.

Voges, W., Dec. 1993. Advances in Space Research, **13**, 391–397.

Voges, W., Aschenbach, B., Boller, T., Bräuninger, H., Briel, U., Burkert, W., Dennerl, K., Englhauser, J., Gruber, R., Haberl, F., Hartner, G., Hasinger, G., Kürster, M., Pfeffermann, E., Pietsch, W., Predehl, P., Rosso, C., Schmitt, J. H. M. M., Trümper, J., & Zimmermann, H. U., Sept. 1999. A&A, **349**, 389–405.

Wall, J. V., Pearson, T. J., & Longair, M. S., Dec. 1980. MNRAS, **193**, 683–706.

Watson, F. G., & Parker, Q. A., June 1994. In *Proc. SPIE Vol. 2198, p. 65-74, Instrumentation in Astronomy VIII, David L. Crawford; Eric R. Craine; Eds.*, 65–74.

White, R. L., Becker, R. H., Helfand, D. J., & Gregg, M. D., Feb. 1997. ApJ, **475**, 479.

Wild, J. P., 1970. Australian Journal of Physics, **23**, 113–115.

Windhorst, R., Mathis, D., & Neuschaefer, L., 1990. In *ASP Conf. Ser. 10: Evolution of the Universe of Galaxies*, 389–403.

Wisotzki, L., Christlieb, N., Bade, N., Beckmann, V., Köhler, T., Vanelle, C., & Reimers, D., June 2000. A&A, **358**, 77–87.

Wyder, T. K., Treyer, M. A., Milliard, B., Schiminovich, D., Arnouts, S., Budavári, T., Barlow, T. A., Bianchi, L., Byun, Y., Donas, J., Forster, K., Friedman, P. G., Heckman, T. M., Jelinsky, P. N., Lee, Y., Madore, B. F., Malina, R. F., Martin, D. C., Morrissey, P., Neff, S. G., Rich, R. M., Siegmund, O. H. W., Small, T., Szalay, A. S., & Welsh, B. Y., Jan. 2005. ApJL, **619**, L15–L18.

Yentis, D. J., Cruddace, R. G., Gursky, H., Stuart, B. V., Wallin, J. F., MacGillivray, H. T., & Collins, C. A., 1992. In *ASSL Vol. 174: Digitised Optical Sky Surveys*, page 67.

York, D. G., Adelman, J., Anderson, J. E., Anderson, S. F., Annis, J., Bahcall, N. A., Bakken, J. A., Barkhouser, R., Bastian, S., Berman, E., Boroski, W. N., Bracker, S., Briegel, C., Briggs, J. W., Brinkmann, J., Brunner, R., Burles, S., Carey, L., Carr, M. A., Castander, F. J., Chen, B., Colestock, P. L., Connolly, A. J., Crocker, J. H., Csabai, I., Czarapata, P. C., Davis, J. E., Doi, M., Dombeck, T., Eisenstein, D., Ellman, N., Elms, B. R., Evans, M. L., Fan, X., Federwitz, G. R., Fiscelli, L., Friedman, S., Frieman, J. A., Fukugita, M., Gillespie, B., Gunn, J. E., Gurbani, V. K., de Haas, E., Haldeman, M., Harris, F. H., Hayes, J., Heckman, T. M., Hennessy, G. S., Hindsley, R. B., Holm, S., Holmgren, D. J., Huang, C., Hull, C., Husby, D., Ichikawa, S., Ichikawa, T., Ivezić, Ž., Kent, S., Kim, R. S. J., Kinney, E., Klaene, M., Kleinman, A. N., Kleinman, S., Knapp, G. R., Korienek, J., Kron, R. G., Kunszt, P. Z., Lamb, D. Q., Lee, B., Leger, R. F., Limmongkol, S., Lindenmeyer, C., Long, D. C., Loomis, C., Loveday, J., Lucinio, R., Lupton, R. H., MacKinnon, B., Mannery, E. J., Mantsch, P. M., Margon, B., McGehee, P., McKay, T. A., Meiksin, A., Merelli, A., Monet, D. G., Munn, J. A., Narayanan, V. K., Nash, T., Neilsen, E., Neswold, R., Newberg, H. J., Nichol, R. C., Nicinski, T., Nonino, M., Okada, N., Okamura, S., Ostriker, J. P., Owen, R., Pauls, A. G., Peoples, J., Peterson, R. L., Petravick, D., Pier, J. R., Pope, A., Pordes, R., Prosapio, A., Rechenmacher, R., Quinn, T. R., Richards, G. T., Richmond, M. W., Rivetta, C. H., Rockosi, C. M., Ruthmansdorfer, K., Sandford, D., Schlegel, D. J., Schneider, D. P., Sekiguchi, M., Sergey, G., Shimasaku, K., Siegmund, W. A., Smee, S., Smith, J. A., Snedden, S., Stone, R., Stoughton, C., Strauss, M. A., Stubbs, C., SubbaRao, M., Szalay, A. S., Szapudi, I., Szokoly, G. P., Thakar, A. R., Tremonti, C., Tucker, D. L., Uomoto, A., Vanden Berk, D., Vogeley, M. S., Waddell, P., Wang, S., Watanabe, M., Weinberg, D. H., Yanny, B., & Yasuda, N., Sept. 2000. *AJ*, **120**, 1579–1587.